Biocompatible Nanocarriers

Dorothée Margret Dollenmayer

(geborene Gößl)

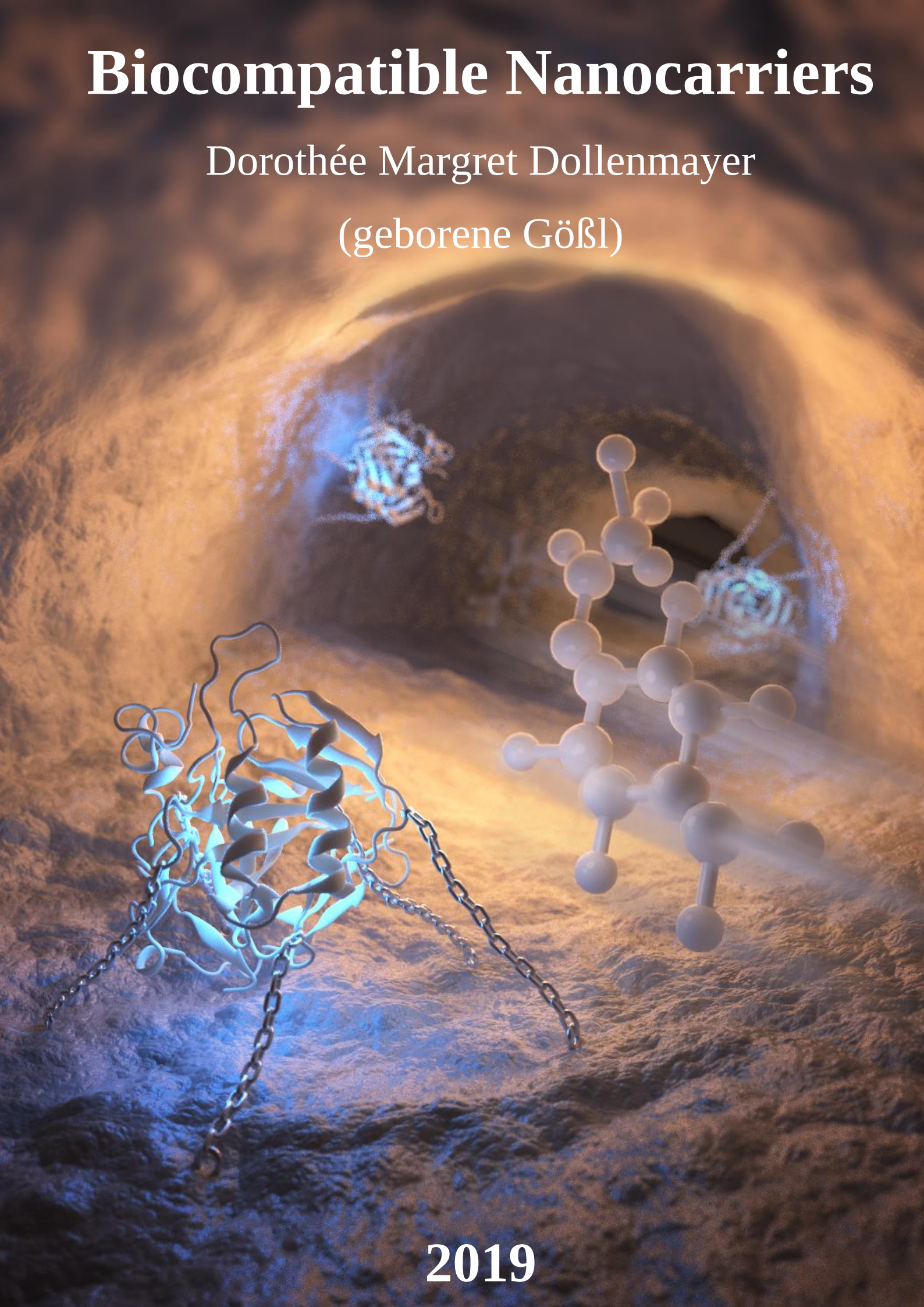

2019

Dissertation zur Erlangung des Doktorgrades

der Fakultät für Chemie und Pharmazie

der Ludwig-Maximilians-Universität München

Biocompatible Nanocarriers

Dorothée Margret Dollenmayer (geborene Gößl)

aus

München, Deutschland

2019

Erklärung

Diese Dissertation wurde im Sinne von § 7 der Promotionsordnung vom 28. November 2011 von Herrn Prof. Dr. Thomas Bein betreut.

Eidesstattliche Versicherung

Diese Dissertation wurde eigenständig und ohne unerlaubte Hilfe bearbeitet.

München, den 28. August 2019

Dorothée Dollenmayer

Dissertation eingereicht am 15. April 2019

1. Gutachter: Prof. Dr. Thomas Bein
2. Gutachterin: Prof. Dr. Carole Bourquin

Mündliche Prüfung am 16. Mai 2019

Danksagung

Als Erstes möchte ich meinem Doktorvater Prof. Dr. Thomas Bein einen großen Dank aussprechen für die Unterstützung und Betreuung während meiner Zeit als Doktorandin. Danke, dass du mich herzlich in deine wunderbare Gruppe aufgenommen hast und mir das Arbeiten in einem Umfeld junger, motivierter Wissenschaftler und hervorragend ausgestatteter Labore ermöglicht hast. Vielen Dank für die zahlreichen Gelegenheiten meine Ergebnisse auf nationalen und internationalen Konferenzen und Workshops vorstellen zu dürfen und somit auch einen Austausch mit anderen Wissenschaftlern zu erfahren. Deine gute Vernetzung mit CeNS und NIM erlaubte es an vielen interessanten Workshops und Summer/Winter Schools teilnehmen zu können.

Liebe Hanna, dir möchte ich ebenso für die wunderbare Betreuung in den vergangenen Jahren danken. Bei sämtlichen Fragen und Korrekturen konnte ich dich immer erreichen, sei es ein normaler Dienstagvormittag oder ein später Freitagabend… Vielen Dank dafür! Danke, dass du dich mit mir aufgeregt und gefreut hast und mich immer wieder ermutigt und gestärkt hast! Ich wünsche dir nur das Beste für die Zukunft und hoffe, dass du noch vielen weiteren DoktorandInnen eine super Chefin sein wirst.

Bei Frau Prof. Dr. Carole Bourquin möchte ich mich herzlich für die erfolgreichen und sehr interessanten Kooperationen bedanken sowie für die Erstellung des Zweitgutachtens.

Im Zuge dessen möchte ich mich auch herzlich bei Simon Heidegger für die schöne Zusammenarbeit bedanken und bei Inès Mottas für das anfängliche Weiterführen des Projekts. Mein allergrößter Dank geht hier aber an Julia Wagner. Danke für die wunderbare Kooperation in den letzten drei Jahren! Danke für die produktiven Skypemeetings, die unglaublich zuverlässige und schnelle Zusammenarbeit, deine Geduld beim Erklären der sehr

komplexen Immunologie, deine große Hilfe beim Erstellen unseres Manuskripts und deine wertvollen Anmerkungen!

Ich möchte mich auch herzlich bei PD Dr. Markus Rehberg und Dr. Katharina Nekolla für die gute Zusammenarbeit bedanken. Trotz harter Arbeit wurde uns leider der fast greifbare Erfolg verwehrt…

Ich möchte mich bei den Werkstätten und der zentralen Analytik sowie bei Christian Minke für die Festkörper-NMR Messungen bedanken. Ein großer Dank geht auch an Dr. Steffen Schmidt für die Aufnahme sämtlicher schöner TEM- und REM-Bilder! Dann möchte ich drei sehr wichtigen Personen des AK Beins danken: Liebe Tina, danke für sämtliche Sorptions- und TGA-Messungen und einfach für alles, dass du tagtäglich erledigst, um uns das Arbeiten im Labor unglaublich zu erleichtern! Liebe Regina und liebe Corinna, euch beiden danke ich ebenso herzlich für Eure großartige Arbeit! Danke, dass ihr stets den Überblick über sämtliche Papier-Angelegenheiten behalten und uns immer unterstützt habt!

Dann möchte ich mich noch bei den lieben Leuten aus dem fünften Stock des Physikgebäudes in der Innenstadt bedanken. Mein Dank geht an Dr. Susanne Hennig und Claudia Leonhardt vom CeNS Team, an das gesamte NIM Team insbesondere an Christoph Hohmann für die 3D DesignWorkshops und die Gestaltung des super Covers sowie an das SFB1032 Team insbesondere an Marilena Pinto. Danke Euch allen für viele interessante Workshops, Seminare und tolle Summer/Winter Schools!

Dann möchte ich dem ganzen Arbeitskreis Bein für die schöne Zeit danken! Ein großer Dank geht natürlich an alle MesoBios für den kooperativen und familiären Zusammenhalt in der Subgroup! Danke an Christian und Alex für die Einarbeitung am Anfang. Einen großen Dank auch an dich, liebe Karin, für deine Hilfe und Unterstützung in der ganzen Zeit! Danke dir, Cindy, für die gute Zusammenarbeit und das Bestehen unserer Freundschaft auch über die

Distanz Deutschland-Taiwan! Ein sehr großer Dank geht auch an Euch, Stefan und Noggi, für die Beantwortung sämtlicher Fragen und Eure Unterstützung über all die Jahre! Danke Stefan für deinen Optimismus, das Radeln und die schöne Zeit! Danke Noggi für deine Hilfe vor allem jetzt auch am Schluss! Danke Lisa, Noggi und Andi, für die lustigen Erinnerungen und den Spaß in unserem Büro! Danke Andi für deine Unterstützung und beste Verpflegung! Lisa, danke für deine stets gute Laune und die wunderbaren Erinnerungen an sämtliche Konferenzen, Workshops und Summer/Winter Schools! Sabrina, dir ebenso ein riesengroßes Danke für die gesamte wunderschöne gemeinsame Zeit! Euch beiden ein großes Danke an die besten Zimmernachbarinnen! Danke natürlich auch an dich, Niklas, für die guten gemeinsam erlebten Zeiten! Danke auch an Tina, Cindy, Laura, Maria und Erika sowie Stephan, Michi, Wascht und Niklas für die schöne und lustige Zeit im HelloKitty-Office! Ich danke auch ganz herzlich meinen Studentinnen Helena, Betty und Olga! Ein riesengroßes Danke geht auch an dich, Natasha, für deinen unermüdlichen Einsatz die Synthese zu optimieren und die schöne Zeit!

Danke an meine Mädels aus dem Studium, vor allem meine Laborpartnerin Luisi, ohne die die erste Hürde, das Chemiestudium, wohl nicht so leicht und mit so viel guter Laune zu nehmen gewesen wäre! Danke Susi, Margit, Rebecca, Luisa, Cecile und Andi für die Riesenunterstützung aus der Ferne und Eure langjährige, wunderschöne Freundschaft!

Mein allergrößter Dank gilt meiner Familie, vor allem meinen Eltern und meinen wunderbaren Schwestern Mimi und Sophie.

Mama und Papa, Danke für Eure Unterstützung, Euren Rückhalt, Euren Optimismus und Eure Überzeugung, dass ich das alles schaffen kann!

Und Danke Dir, Marcus, einfach für alles.

Abstract

Novel nanoscale materials with advanced functionalities have attracted increasing attention in the fields of drug delivery, diagnostics and medical imaging. Nanoparticles possess sizes in the range of cellular compartments and are therefore capable to enter living cells *via* mechanisms like endocytosis. This allows them to function as carrier systems to locally deliver fragile, water-insoluble or harmful cargo to the respective target site and thus overcome degradation, permeation or toxicity problems. In addition, a targeted delivery of the cargo can achieve higher local drug dosages while preventing severe side effects. These positive characteristics of nanoparticle-based therapies are extensively studied in the field of cancer treatment. Mesoporous silica nanoparticles (MSNs) have been widely reviewed as promising delivery system for chemotherapeutics. They also hold great promise as nanocarriers for immune-modulating drugs which are applied in cancer immunotherapy to induce an augmented antitumor T cell response of the immune system. MSNs possess very large surface areas which enable high drug loading contents and thus an overall reduced dosage to be effective. Furthermore, their particle and pore size can be easily tuned allowing them to accommodate a wide variety of different guest molecules. In addition, they are easily functionalized on their in- and outside, thus allowing perfectly tailored host-guest as well as particle-cell interactions. Due to this spatial control, guest molecules can be trapped inside the pores until the capping system opens up upon a certain stimulus. Here, a wide variety of stimuli-responsive capping systems exists, ranging from polymers over metal oxides to protein caps or complete coatings by supported lipid bilayers. Furthermore, to enhance passive or active targeting, (bio) polymer shells like polyethylene glycol can be added around the particles to achieve a so-called stealth effect and thus enable passive accumulation in the tumor *via* the enhanced permeability and retention (EPR) effect. On the other hand, targeting ligands covalently attached to the outer surface of the MSNs may enable active receptor-

mediated uptake into tumor cells. Lastly, the surface of the particles can be modified in a way that they are specifically taken up by innate immune cells which is the goal of cancer vaccines belonging to the field of cancer immunotherapy. Nevertheless, there is still a great need for improvement of well-established systems like mesoporous silica nanoparticles (MSNs) as well as for the synthesis of novel biomaterials. Aspects like the successful loading and controlled release of drugs, stability and degradation issues of the delivery system in biological fluids, favoured particle-cell interactions especially successful targeting versus rapid clearance of the nanocarrier and of course safety and toxicity profiles of the hosts have to be carefully evaluated *in vitro* and specifically *in vivo*.

This thesis focuses on the implementation of well-known MSNs as delivery vehicles for various types of cargo. The impact of fine-tuning the inner surface of the particles on the loading and release behaviour of the respective drug is shown with *in cuvette* and *in vitro* cellular delivery experiments. Furthermore, the choice of the capping system also has a tremendous influence on the release performance. In addition, the impact of surface functionalization, e.g. through capping systems, on particle-cell interactions is especially discussed for the indirectly active targeting approach of MSNs to antigen-presenting cells (APCs). The biocompatibility and toxicity of the carrier system is evaluated *in vitro* and *in vivo* as it is a crucial aspect for future clinical applications. Furthermore, the possibilities of the nanocarrier to deliver more than one guest at a time and the associated enhanced performance of the system are reported. To underline the flexibility of MSNs, not only small molecules are chosen as cargo but also the encapsulation of large biomolecules is discussed. In addition, different binding strategies of cargoes to the inside of the pores are described with regard to the intended application of the carrier system. At last a novel biomaterial with a different host-guest interaction is introduced and applied in cellular delivery experiments.

The first part of this thesis focuses on the evaluation of mesoporous silica nanoparticles as appropriate carrier for immune-stimulant cargo. For this purpose, amine-functionalized MSNs with and without pH-responsive polymer capping system are assessed regarding their biocompatibility, toxicity, and immune-modulatory properties, all aspects of great relevance for future clinical applications. It is shown that MSNs are rapidly and efficiently taken up by specialized antigen-presenting cells (APCs) such as dendritic cells (DCs). This preferred uptake of MSNs by APCs is the target in nanoparticle-based cancer vaccines. By enhanced uptake into DCs, the key players of the innate immune system, a successful DC maturation can be achieved followed by a potent tumor-specific T cell activation. Another important requirement is that the carrier system exhibits no toxicity and no immune-modulatory properties itself. It is shown that MSNs possess a favourable toxicity profile and induce marked apoptosis only when used in very high concentrations of 200 $\mu g\, mL^{-1}$. Further, unloaded MSNs initiated only a slight immune response in primary murine immune cells, meaning they did not upregulate any activation markers such as co-stimulatory molecules or proinflammatory cytokines. Summarizing, the particles represent a non-toxic and non-inflammagenic delivery system which is preferentially taken up by specialized antigen-presenting cells. To assess if this MSN system can principally function as carrier for immune-modulatory cargo with regard to cancer immunotherapy applications, the particles were loaded with Resiquimod (R848) and coated with the pH-responsive polymer PVP as capping system. The MSN-PVP system was internalized *via* endocytosis into the acidic environment of the APCs' lysosome, which triggered pH-dependent R848 release. R848 is a synthetic Toll-like receptor agonist and is capable of inducing a potent immune response by activating dendritic cells and thus starting the cascade of a successful T cell response and tumor cell killing. The release of delivered R848 caused significant upregulation of the above mentioned

activation markers. In summary, it was demonstrated that MSNs possess indeed the appropriate characteristics for an optimal carrier system of immune-modulatory cargo.

To implement the gained knowledge and explore the possibilities of MSNs as drug delivery system, MSNs are investigated in detail as pH-responsive carrier system for R848 in the succeeding chapter. To examine the full potential of the drug delivery system, the aforementioned polymer cap was compared to a protein-based one with respect to their R848 loading and release behaviour. The two different capping systems differ in their opening and closure mechanisms. Whereas the polymer system works reversibly upon pH-dependent (de-) protonation of the PVP group, the biotin-avidin complex is irreversibly detached through pH-dependent cleavage of the connecting acetal linker. Time-based fluorescence release measurements *in cuvette* demonstrated that the R848 release of the avidin-capped system is superior to that of the PVP-coated MSNs. This was further confirmed in a cell-based assay. The easy functionalization of MSNs allows for choosing the most efficient capping system as well as the optimal pore interior for each cargo. To optimize the loading behaviour of R848 into MSN-avidin, we incorporated phenyl moieties inside the pores and compared them with amine-functionalized particles. The latter showed electrostatic repulsion and thus hampered cargo uptake whereas phenyl functionalized MSNs showed great loading in the correct buffer. To allow the hydrophobic effect to act between cargo and pore wall, the SSC20x buffer with the kosmotropic citrate ions was determined to be the best loading buffer. Due to the fact that MSNs will be injected subcutaneously into mice in future applications, they only reach the draining lymph node (LN) with dendritic cells (DCs), after being taken up by them. This implies that particles have to prove a long-term stability until they are all ‘picked up’ by DCs and delivered to the LN to avoid systemic distribution of R848 due to premature release. This long-term stability of the capping system was examined with a time-based release experiment over 60 h at 37 °C. Avidin coated MSNs proved to achieve tight capping under physiological

pH and showed strong release of the R848 cargo when the environmental pH was decreased to 5.5 or lower. It was shown that MSNs are rapidly taken up by APCs and mainly accumulated in migratory DCs in the draining LN after subcutaneous injection into mice. Particles loaded with R848 induced a potent DC activation as shown in the upregulation of co-stimulatory and MHC molecules as well as cytokine production. Remarkably, the supernatant of the loaded particles did not induce an immune response, proving the tightness of the capping system. To explore the possibilities of the MSN system further, simultaneous delivery of antigen and adjuvant was monitored. The co-delivery of both agents in the same particles showed superior T cell activation. In sum, it was demonstrated that MSNs hold indeed great promise as carrier system for immune-stimulant R848 to antigen-presenting cells. In addition, they show high potential to be used in further cancer vaccine applications to achieve a locally induced immune activation while preventing adverse systemic effects.

Besides these small molecules, also larger biomolecules rely on transporting systems for an improved performance in various application fields. Here, large-pore mesoporous silica nanoparticles (LP-MSNs) are promising nanocarriers for the targeted delivery of macromolecules. Chapter 5 of this thesis discusses the diversity of multifunctional stellate large-pore MSNs regarding the impact of different incorporated organosilanes on the mesopore structure and the particle morphology. Furthermore, an adapted version of the delayed co-condensation method for small-pore particles was transferred to create spatially-segregated core-shell large pore MSNs. The particles were further functionalized with stimuli-responsive linkers, namely the pH-responsive acetal linker described in chapter 4 and a redox-sensitive disulfide linker, to enable controlled cargo release. This was followed by attachment of DBCO derivatives allowing for mild cargo conjugation *via* copper free click chemistry. The successful release of the model cargo TAMRA dye was triggered with specific buffer or redox conditions and monitored *via* time-based fluorescence measurements as well as *in vitro*

fluorescence microscopy experiments. The covalent conjugation of the cargo described here *via* mild click-chemistry can be of high importance in application fields of biocatalysis. Here, it is of interest to immobilize enzymes to allow for continuous industrial processes. The potential of the stellate LP-MSNs as enzyme support is described in chapter 6 of this thesis.

Silica-based supports for enzyme immobilization are widely used, as their porous system can protect the fragile cargo from external degradation forces. Furthermore, covalent immobilization into MSNs allows for easy recovery of the 'biocatalyst' in comparison to the tedious work-up of free enzymes. Here, mild copper-catalyzed click chemistry was applied to immobilize two different enzymes, namely horseradish peroxidase and carbonic anhydrase, into the large pores of azide-functionalized stellate MSNs. The concave shape of the pores allowed for easy diffusion of the large biomolecules into the pores prior to covalent attachment. In addition, this pore shape also enables the quick diffusion of substrates to the immobilized enzymes and thus enhances the overall catalytic performance. The successful immobilization of the biomolecules inside the silica support was characterized with several methods including IR-spectroscopy, gas sorption, and TGA measurements. In addition, their potential as biocatalysts was investigated with model catalytic activity measurements. Here, colorimetric assays were applied for the respective enzymes to monitor the catalytic activity over several cycles with simple washing and centrifugation steps of the particles in between. It was shown that the enzymes remained stable and active in the pores, thus proving the benefits of covalent immobilization inside mesoporous silica nanoparticles.

Besides the above-mentioned successful implementations of already existing mesoporous silica nanoparticles for various applications, the last chapter of this thesis is concerned with the synthesis of a novel biomaterial. Here, a completely organic and covalently crosslinked material based on β-cyclodextrins (CDs) is introduced. This soft material consists of small

nanoparticles with sizes of ~ 150 nm, which are highly water-dispersible. Covalently labeled CD nanoparticles showed rapid uptake in HeLa cells within 30 minutes, whereas lipid bilayer coating of the particles inhibited the uptake in this short period of time. This suggests that CD NPs are endocytosed *via* a sugar-receptor mediated pathway. Their ability to form inclusion complexes between the cyclodextrin rings and various cargos was demonstrated with the loading of the nuclei staining dye Hoechst and the chemotherapeutic doxorubicin, respectively. Both cargos were efficiently delivered without notable premature leakage. Upon acidification in the endosomes both cargos were successfully released, as seen in strong nuclei staining or potent cell killing, respectively. Thus, the novel sugar-based material holds great promise as alternative biocompatible drug carriers.

In summary, the great potential of multifunctional MSNs as carrier system in various fields was demonstrated in this work. MSNs with different pore sizes, morphologies, and post-synthetic functionalizations were tailored to meet the requirements of a non-toxic and non-inflammagenic carrier system as well as a support material for large biomolecules. Their promising potential as stimuli-responsive delivery systems was demonstrated *in vitro* and *in vivo*. To expand the spectrum of talented biocompatible carriers, a novel sugar-based nanomaterial was introduced with promising cellular delivery characteristics. The future aim is to implement these functionalization methods and materials further to enable delivery of multiple drugs in one carrier and thus combine different synergistic cancer treatments as for example chemotherapy and cancer immunotherapy.

Table of contents

CHAPTER 1

Introduction

1. Introduction

1.1 Mesoporous silica nanoparticles

Mesoporous silica nanoparticles (MSNs) represent a class of promising inorganic drug carriers. They are well-known for their large surface areas, their high thermal stability and their tunable pore sizes and shapes.[1] Furthermore, they can be functionalized easily on their inside with spatial control to perfectly tune the interaction between cargo and host to achieve very high loading and release efficiencies. Not only the interior of the MSNs can be modified but also the outside of the spatially segregated core-shell bifunctional particles. The exterior surface can be equipped with matching functionalities to allow covalent binding of targeting ligands, endosomal escape agents and most importantly different capping systems to ensure tight sealing of the pores. Those closure mechanisms are always chosen in a way to open up upon certain stimuli. The stimuli can be either external ones like light, heat, a magnetic field or the like or the opening of the pores can be evoked by internal stimuli, like changes of pH, redox reactions or enzyme mediated degradations.

Those characteristics make MSNs a promising material that meets many requirements of a successful drug delivery vehicle.

The description mesoporous is defined by the International Union of Pure and Applied Chemistry (IUPAC) as a term describing porous materials with pore sizes between 2 and 50 nm.[2] Furthermore, the term ‘nanoparticles’ is strictly speaking only to be used for particles with sizes in at least one dimension smaller than 100 nm.[3] The MSNs used in this thesis are spherical and show sizes between 50 nm and 200 nm. Due to the fact that in this size range the properties of the particles do not change as drastically as they change from a nanoparticle in comparison to bulk material, we will still call them mesoporous silica nanoparticles.

The story of MSNs begins almost 30 years ago in 1990/1992, when two independent groups, namely Yanagisawa et al. and Kresge et al., reported surfactant-templated periodic mesoporous materials for the first time.[4-5] The need for larger pores was great due to the arising restrictions in the use of microporous zeolites, especially in the field of catalysis.[6] Larger pores would enable a faster diffusion of larger reactants into the catalytic material.[7] Especially the work of the Kresge group with their invention to use quaternary ammonium salts as templating molecules paved the way for MSNs. With their new templating approach in micellar form, they achieved either hexagonal (MCM-41) or cubic (MCM-48) pore structures with pore sizes around 3 nm (MCM: Mobil Crystalline Material). Furthermore, they were able to show the positive effect of pore swelling agents leading to expanded pore sizes of up to 10 nm. As time would show it should take some years until the control over the synthesis of colloidally stable solutions would be gained.[8]

Besides the MCM family, a couple of years later, the SBA family (Santa Barbara Amorphous) emerged.[9-10] Whereas, MCMs are synthesized under basic conditions and with the use of cationic surfactants, SBAs are produced in acidic media with the help of templating non-ionic triblock copolymers. The change of pH and surfactant results in thicker pore walls and higher thermal stability. Nowadays, MCM-41 with its 2D hexagonal pore structure, MCM-48 with its 3D cubic pore structure and SBA-15 with its likewise 2-dimensional hexagonal mesostructure represent the most studied and commonly used mesoporous silica materials.[11]

To date, there is a large number of different synthesis and functionalization routes available resulting in particles with size ranges from about 20 nm to 500 nm and pore size ranges between about 2 nm and 30 nm.[12-14]

1.1.1. Small-pore MSNs

In the beginning of research on mesoporous materials, the particle sizes were in the micrometer range. In the biomedical field, one of the main research areas of MSNs nowadays, the use of micrometer-sized particles is limited due to a size-dependent efficiency in cellular uptake since their size is too big.[15-16] In 2001, the new potential property of MCM-41 particles to act as drug delivery vehicles was shown for the first time by means of loading and release studies with ibuprofen.[17] After this discovery, efforts were being made to achieve controlled nanometre-sized, spherical mesoporous silica nanoparticles. Grün and co-workers achieved sub-micrometer sized spherical MCM-41 particles by addition of cationic surfactant in a modified Stöber synthesis.[18-19] In the classical picture, the template enables micelle formation and electrostatic interaction between negatively charged silicates and positively charged template. The following base-catalyzed hydrolysis and condensation of the tetraalkyl silicates then takes place on the surface of the micelles and therefore leads to a mesopore formation.[20] Cai *et al*. as well as Ostafin and co-workers gained particles in the nanometre range due to extremely low silicate and surfactant concentrations.[21-22] Lin and Tsai also worked with very diluted solutions resulting in even smaller nanoparticles at a low pH of 5.6.[23] Furthermore, the group of Mann achieved nanoparticles by a quenching and dilution method of the reaction mixture after very short reaction times with subsequent neutralization.[24] These developments all show the production of mesoporous silica nanoparticles *via* a simple synthesis route. The drawback though is the used large reaction volume to avoid particle agglomeration. This can lead to a difficult product isolation and therefore results in low product yields. To overcome this hurdle, a synthesis route developed in our group employs the chelating base triethanolamine (TEA) instead of the commonly applied NaOH.[25] Employing this polyalcohol in the synthesis as a weak base, enables the use of lower pH values in the synthesis. This leads, in combination with the complexing behaviour of TEA, to well-defined non-

agglomerated MSNs.[26] As a templating agent CTAC (cetyltrimethylammonium chloride) is employed and ammonium fluoride is added to achieve spherically shaped MSNs. The resulting colloidally stable, spherical nanoparticles show sizes of around 80 nm and pore diameters of 4 nm. The porous system shows a wormlike structure suggesting a seed-growth mechanism, which is possibly induced through the reduced reaction rate in the condensation step through the chelating effects of TEA. Tuning the ratio between TEA and TEOS leads to a range of available particle sizes between 50 and 100 nm.[27] To actually access and open up the mesopore system, the template has to be removed. This can be either achieved *via* calcination or by extraction methods. Calcination is typically performed at elevated temperatures for a certain period of time. It can lead to agglomeration and pore shape deformation and can only be applied for unfunctionalized silica particles. Therefore, extraction is the method of choice used in our group. For this, the particles are redispersed in a basic ethanolic solution and heated under reflux at 90 °C for 45 min. Subsequently, the particles are centrifuged and redispersed in an acidic ethanolic solution and heated a second time under the same conditions. This very mild extraction method can also be applied for silica particles functionalized with organic moieties. The resulting small-pore MSNs were already successfully used by Bein and co-workers to deliver small molecules, chemotherapeutics and dyes as model cargoes *in vitro*.[28-31]

Additionally to the making of the above described silica particles, recently the 'breaking' process attracted also attention. Degradation products play, besides other parameters as size, surface charge etc. (discussed below), also an important role in the toxicity profile of the particles. The silica framework consists mainly of –Si-O- bonds, which represent quite stable chemical connections with a bond energy of 452 kJ/mol. Nevertheless, hydrolytic breakage through nucleophilic attack can occur in aqueous media. The resulting silicic acid ($Si(OH)_4$) can leach out from the silica matrix. It is non-toxic and can be easily excreted by urine.[32-33] As

shown by Möller and Bein, the conditions chosen for the synthesis of the mesoporous silica nanoparticles strongly affect their degradation behaviour (see Figure 1-1).[34] MSNs produced under acidic pH show a very high stability in aqueous media due to the thicker pore walls resulting from this synthesis route. The higher the pH chosen in the reaction, the thinner and less condensed are the resulting pore walls and the faster does degradation occur. Notably, unfunctionalized particles are significantly more stable than core-shell functionalized particles produced *via* a site-specific delayed co-condensation approach (described below). This can be explained with the lower amount of fully condensed –Si-O- building blocks due to the introduction of organic moieties. The resulting –Si-R or –Si-OH bonds apparently offer more opportunity for nucleophilic attack.

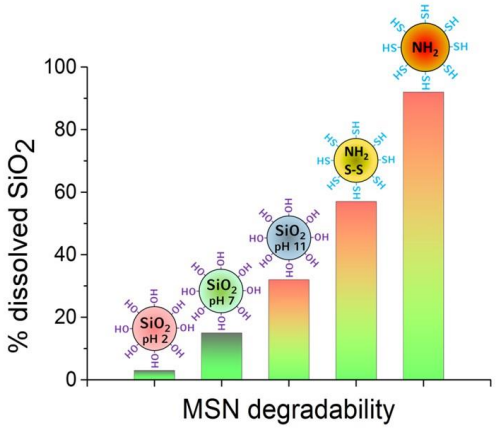

Figure 1-1. Differences in degradation behaviour depending on the synthesis conditions of (un-) functionalized mesoporous silica nanoparticles. Adapted with permission from "Degradable Drug Carriers: Vanishing Mesoporous Silica Nanoparticles" by K. Möller and T. Bein, *Chem. Mater.* 2019, *31* (12), 4364-4378. Copyright 2019 by the American Chemical Society.[34]

Concluding, the degradation behaviour can be fine-tuned by choosing the respective reaction conditions and (organo-)silanes. Altogether, MSNs represent tunable, multifunctional and well-tailored host systems for a variety of guests, as will be discussed below. The successful use of small-pore MSNs as carrier system for immunostimulant cargo is described in chapters 3 and 4 in this thesis.

1.1.2. Large-pore MSNs

Besides the above mentioned small-sized cargoes, there is the need to delivery larger guests. Especially fragile molecules like siRNA and other biomolecules like proteins and enzymes may be degraded fast and easily in biological media. Therefore, encapsulation in a carrier system is needed. To be able to accommodate those larger guests, great efforts have been made towards achieving silica particles with larger pores. The different approaches can be summarized in two general pathways: (a) Using additional swelling agents in combination with commonly used surfactants, or (b) applying amphiphilic copolymers or larger surfactants (commonly with a prolonged alkyl chain).[35] As mentioned above, already the Kresge group showed the effect of a pore-swelling agent resulting in pore sizes of up to 10 nm.[27] Stucky *et al.* achieved SBA-15 with pore sizes of up to 30 nm by using amphiphilic block copolymers poly(ethylene oxide)-poly(propylene oxide)-poly(ethylene oxide) (PEO-PPO-PEO) in addition with the pore-expanding mesitylene (1,3,5-trimethylbenzene, TMB).[10, 36] In both cases the pore sizes are enlarged, but in particles of micrometer size. Especially for the listed fragile biomolecules above, the particle size is again a crucial factor for efficient cellular delivery. Han and Ying reported in 2004 a fluorocarbon-surfactant-mediated synthesis yielding nanometer-sized particles (50-300 nm) with large pores (tunable between 5-30 nm).[37] They applied pH values between 1.6 and 1.8, which resulted in a slow hydrolysis of silica precursors, followed by their co-assembly with nonionic triblock copolymer surfactant ($EO_xPO_yEO_x$; ethylene oxide (EO) and propylene oxide (PO)) into well-defined mesophases. Cationic fluorocarbon surfactant FC-4, which was added simultaneously, remained at the periphery of the forming particles due to its immiscibility with the copolymer surfactant. This surrounding of the silica particles by FC-4 limited their growth and led to nano-sized large-pore MSNs (LP-MSNs). By choosing different copolymers and partial addition of pore

swelling agent TMB in the FC-4-supported synthesis, they were able to achieve five different mesostructures as shown in Figure 1-2.

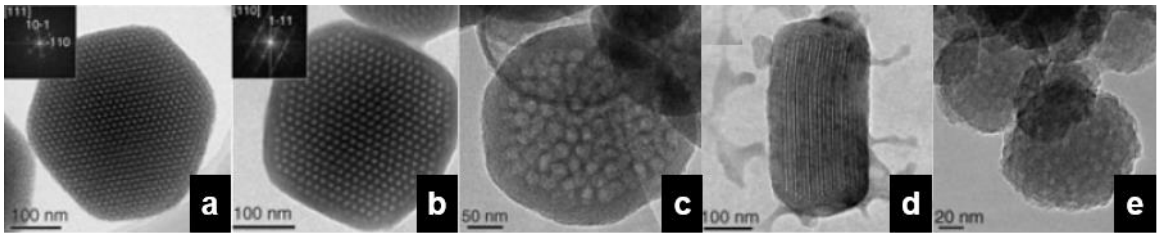

Figure 1-2: Five different mesostructures resulting from fluorocarbon-surfactant-mediated synthesis. (a) IBN-1 (3D cubic (*Im3m*) with template F127). (b) IBN-2 (3D cubic (*Fm3m*) with template F127+TMB). (c) IBN-3 (mesocellular foam with template P65+TMB). (d) IBN-4 (2D hexagonal (*p6m*) with template P123). (e) IBN-5 (disordered with template F108). Adapted with permission from "Generalized Fluorocarbon-Surfactant-Mediated Synthesis of Nanoparticles with Various Mesoporous Structures" by Y. Han and J. Y. Ying, *Angew. Chem. Int. Ed.* 2004, *44* (2), 288-292. Copyright 2004 by John Wiley & Sons, Inc.[37]

This fluorocarbon-assisted approach was further developed by Gao *et al.* using low temperatures (10 °C) during the synthesis and a subsequent hydrothermal treatment to gain MSNs with pore entrances of 17 nm.[38] This modified method was adapted by our group to introduce organic functionalities *via* a co-condensation approach.[27] In this quite tedious synthesis approach, challenges were encountered when chargeable functional groups like amino or mercapto groups were co-reacted. By applying 5 mol% instead of 1 mol% of mercapto groups the particles became nearly dense and lost their large porous system. These limitations and the harsh conditions restrict the use of this synthesis route.

Besides the fluorocarbon-surfactant-mediated approach, there is also the possibility to use pore swelling agents in combination with commonly used templating molecules. The organic auxiliary molecules can be accommodated in the hydrophobic interior of the surfactant micelles. Commonly used pore expanding agents are triisopropyl benzene (TIPB), mesitylene (TMB), trioctylamine (TOA), decane, N,N-dimethylhexadecylamine (DMHA) and tri-octylmethylammoniumbromide (TOMAB).[27, 39-43] With the use of these agents or even combinations thereof, pore sizes can be enlarged up to 5 nm. For larger biomolecules and,

e.g., plasmid-DNA these pores may still be too small. It has to be mentioned that work in our group showed that particles with 5 nm pores are sufficient for the efficient delivery of fragile siRNA.[44] In comparison to the above described large-pore MSNs synthesized under acidic conditions, particles with medium-sized pores even showed a higher efficiency.[27]

Besides the need to synthesize MSNs with larger pores (> 5 nm), a very simple approach is useful for possible upscaling of the reaction. Recently, Zhang *et al.* published a synthesis route using mild conditions yielding large-pore MSNs at the kilogram scale.[45] The sol-gel synthesis uses cetyltrimethylammonium (CTA^+) as a template and small organic amines (SOAs) as additives. By use of tosylate (Tos^-) counterions and almost neutral pH, they achieved a stellate pore morphology with pore mouth sizes of 10-15 nm. Changing the counterion to Br^- leads to a quasi-spherical raspberry-like morphology as can be seen in Figure 1-3.

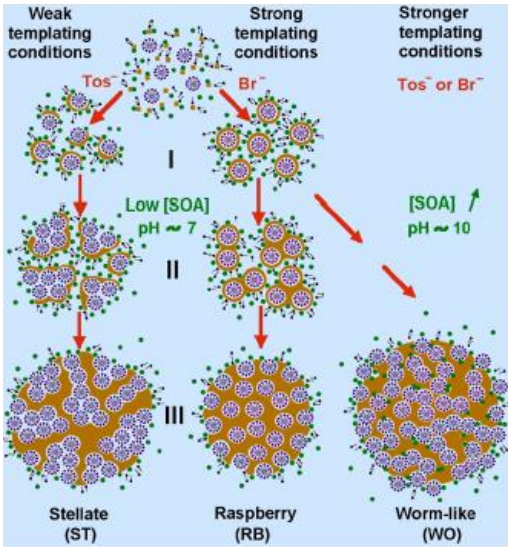

Figure 1-3: Synthesis routes at low and high pH with resulting different templating conditions are shown. Reprinted with permission from "Facile Large-Scale Synthesis of Monodisperse Mesoporous Silica Nanospheres with Tunable Pore Structure" by Zhang, K.; Xu, L.-L.; Jiang, J.-G.; Calin, N.; Lam, K.-F.; Zhang, S.-J.; Wu, H.-H.; Wu, G.-D.; Albela, B.; Bonneviot, L.; Wu, P., *J. Am. Chem. Soc.* 2013, *135* (7), 2427-2430. Copyright 2013 by the American Chemical Society.[45]

The authors explain this difference by either weak or strong templating conditions. This means the counterion tosylate competes more with the negatively charged silanol groups in regard of the adsorption onto the positively charged micelles (CTA^+) than Br^- does. This effect is even stronger at low concentrations of SOAs (= low pH) and leads to an increase of Tos^- anions in the MSNs, resulting in an unorganized stellate structure. Contrary at higher pH values, the silanolate density is high enough to replace the Tos^- anions efficiently and therefore leading to a more organized worm-like structure, as shown on the right side of Figure 1-3.

The resulting conical pore shape of stellate large-pore MSNs can be successfully loaded with larger biomolecules. An adapted synthesis recipe developed in our group enables functionalization of stellate LP-MSNs in a co-condensed way as discussed in chapter 5. Moreover, the use of large-pore particles as successful enzyme support is shown in chapter 6

of this thesis. A general overview of enzyme immobilization in large-pore mesoporous silica nanoparticles is given below.

1.1.3. Functionalization of mesoporous silica nanoparticles

One of the great advantages of mesoporous silica nanoparticles is the simple functionalization of the interior and exterior surface. Besides PMOs, periodic mesoporous organosilicas, which were reported by three independent groups in 1999, in which Si atoms are bridged by applied ethane groups or the like,[46-48] there are generally two possible ways to introduce organic functionalities into the silica framework. One distinguishes between a post-synthetic grafting process and a co-condensation approach. Whereas, grafting with template molecules still present in the MSNs may lead to functionalization only or predominantly on the surface of the particles, co-condensed MSNs show a homogenous distribution of the organic moieties. The grafting process of the exterior surface can take place with the template-filled particles right after the synthesis. This is followed by template removal and functionalization of the pore interior with another group.[49] However, due to the fact that mesopores are large enough to allow diffusion of grafting agents into the template-filled pores, a spatial control of functionalities is difficult to achieve with this method.[50] Particles used in this thesis are therefore prepared by a site-selective co-condensation approach developed in our group (Figure 1-4).[51] This method gives great control over the amount and density of the incorporated functionalities. Depending on the time of addition to the reaction mixture, functionalities can be solely attached to the inside of the pores or exclusively found on the external surface as shown in Figure 1-5. The resulting systems are called core-shell particles.

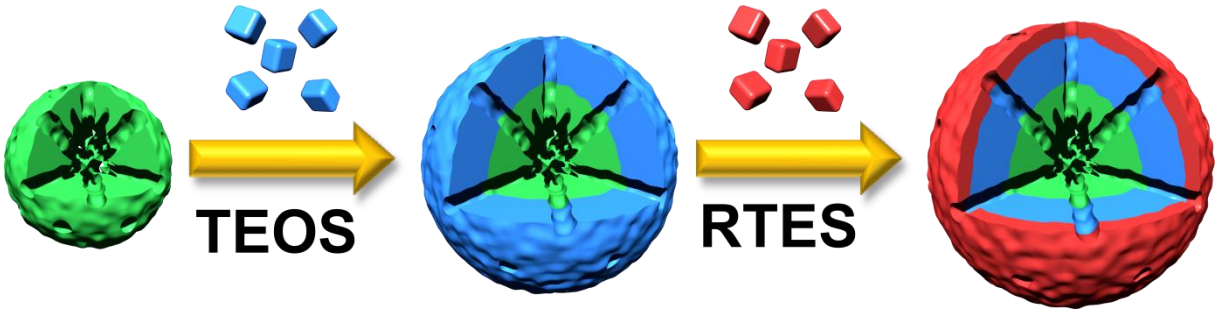

Figure 1-4: Schematic depiction of sequential co-condensation reactions leading to core-shell MSNs. Shown in green is the synthesized core of the MSNs with an incorporated organic moiety R_1. In a second step an interlayer of pure tetraethyl orthosilicate (TEOS) is added (shown in blue). And in the final step the second organic moiety (R_2, shown in red) is placed on the exterior of the particles. Reprinted with permission from "Multifunctional Mesoporous Silica Nanoparticles as Universal Platform for Drug Delivery" by C. Argyo, V. Weiss, C. Bräuchle and T. Bein, *Chem. Mater.* 2014, *26* (1), 435-451. Copyright 2014 by the American Chemical Society.[1]

To prove that this approach leads to spatial control of functionalization, Cauda *et al.* performed fluorescence quenching studies with dye-functionalized MSNs (fluorescein isothiocyanate, FITC) and external gold nanoparticles.[50] It could be shown that the energy transfer between FITC and the gold NPs takes only place when FITC was added to the external surface of amine-functionalized MSNs. In the case of aminopropyltriethoxy silane (APTES) added to the core of the particles, no quenching occurred due to the greater distance between FITC, attached inside, and external Au NPs. This great possibility of spatially-controlled functionalization can be used to accommodate guest molecules on the one hand, and optimize the external surface on the other hand by means of attachment of targeting ligands, endosomal escape agents and capping systems to ensure desired interactions with cells and membranes in biological systems.[1] The variety of possible functionalizations is depicted in Figure 1-5.

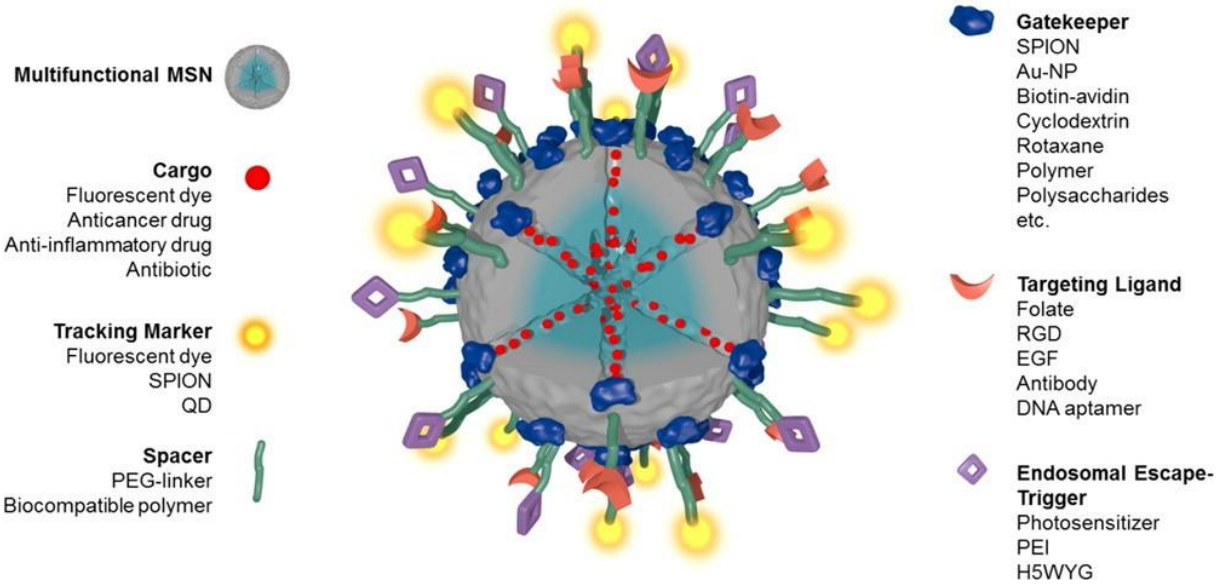

Figure 1-5: Multifunctional MSNs. Reprinted with permission from "Multifunctional Mesoporous Silica Nanoparticles as Universal Platform for Drug Delivery" by C. Argyo, V. Weiss, C. Bräuchle and T. Bein, *Chem. Mater.* 2014, *26* (1), 435-451. Copyright 2014 by the American Chemical Society.[1]

The attachment of gatekeepers to the external surface of the particles enables tight pore sealing and prevents premature release of the cargo. The first example of a successful capping system was shown by Victor Lin and his group in 2003.[52] They applied a CdS-cap and showed stimuli-responsive release of vancomycine and adenosine triphosphate (ATP) loaded MSNs upon addition of disulfide-bond reducing agents like dithiotreitol (DTT). Other examples of pore capping groups are bulky molecules such as proteins, superparamagnetic iron oxide nanoparticles (SPIONs), ZnO nanolids, β-cyclodextrins or gold nanoparticles.[53-60] A second, very efficient pore sealing method is the coating of the complete particle. Examples hereof are supported lipid bilayers (SLB), (bio-) polymers, calcium carbonate and oligonucleotides.[28, 61-70] The attachment of the polymer polyethylene glycol (PEG) additionally brings a stealth effect, leading to longer circulation times in the blood stream instead of rapid clearance. This is a crucial factor when the nanoparticles are supposed to accumulate passively in the tumor *via* the enhanced permeability and retention (EPR) effect which is described below.

Concluding, functionalization of MSNs leads to multifunctional nanoparticles which can be applied in different areas. In the following, their use in enzyme immobilization as well as in drug delivery is discussed.

1.1.4. Enzyme immobilization in mesoporous silica systems

Enzymes possess very interesting characteristics for the application in biocatalysis. They show a high catalytic efficiency even under mild reaction conditions, which makes them user and bio-friendly. Furthermore, they possess a high stereo- and regio-selectivity, which simplifies processes and is important in the production of chiral and optically active compounds.[71] However, there are certain drawbacks, which limit the use of native, unprotected enzymes in biocatalysis. If harsher conditions are applied in the reactions, enzymes commonly degrade very quickly and become therefore inactive. Furthermore, the reuse of enzymes involves the tedious purification and separation thereof, limiting their use in a continuous or large-scale process due to high costs. Consequently, encapsulation of the enzymes leads to better protection of the fragile cargo and a simplified work-up. There are different ways to immobilize enzymes onto solid supports. One of the very early examples of using a silica support was shown in 1970 by Johnson and Whateley.[72] They incorporated the enzyme trypsin into a polymerizing silica gel system and could show enhanced long-term stability. After the discovery of mesoporous silica particles in the early 90ies, Diaz and Balkus were the first to show actual immobilization of cytochrome c, papain and trypsin into the pores of MCM-41 *via* physical adsorption. Furthermore, they proved the limited use of the small-pore particles for larger enzymes, as they could not load peroxidase successively onto the pores. This immobilization technique relies on very weak interactions and leads therefore easily to leaching phenomena.[71] Another non-covalent immobilization method is to incorporate positively charged amine groups into the silica framework and immobilize

negatively charged enzymes *via* electrostatic interactions. This was shown by Ackerman *et al.* by immobilizing negatively charged glucose oxidase (GOX) in the above mentioned amine-functionalized particles, as well as, positively charged organophosphorus hydrolase (OPH) in respectively carboxylic-functionalized SBA-15 MSNs.[73] Besides the already mentioned methods, there are also different forms of covalent enzyme immobilization present. Covalent attachment to the support occurs *via* reaction between certain groups of the protein chains and respective functional groups of modified particles as shown in Figure 1-6.

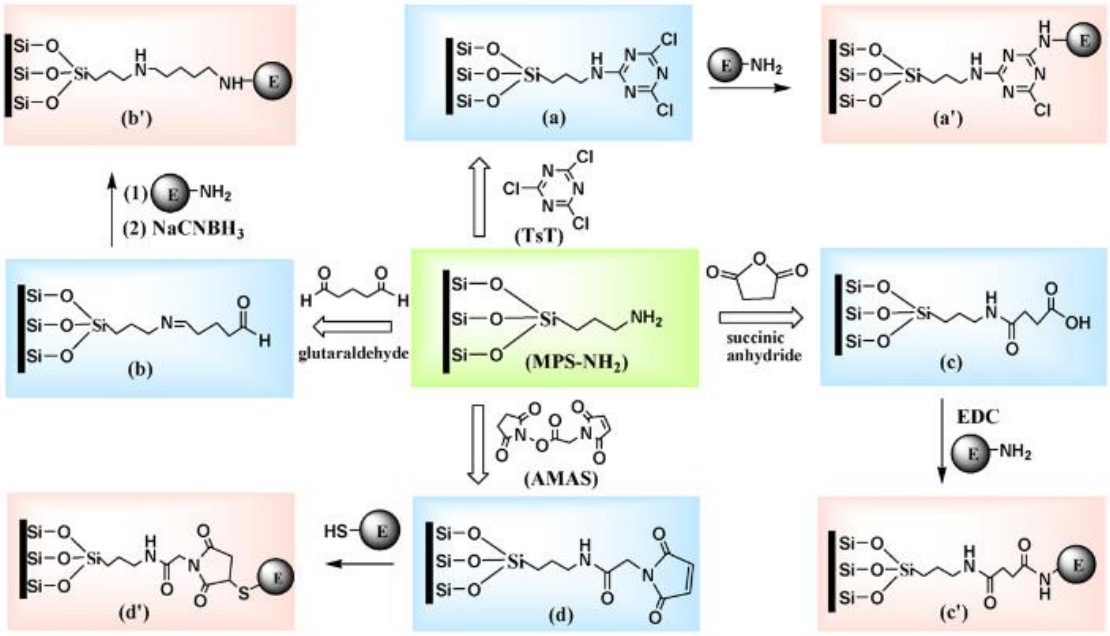

Figure 1-6: Overview of different reaction pathways to attach enzymes covalently to functionalized silica supports. E: enzyme. Reprinted from Nano Today, *4* (2), Lee, C.-H.; Lin, T.-S.; Mou, C.-Y., "Mesoporous materials for encapsulating enzymes", 165-179, Copyright 2009, with permission from Elsevier.[71]

Besides the above mentioned synthesis routes for covalently attached enzyme-host systems, there is also a very elegant way to immobilize the biomolecules covalently onto the support. An azide-alkyne click-reaction, as shown by Schlossbauer *et al.*.[74], enables very mild reaction conditions and avoids the use of toxic chemicals. It results in very high surface loading efficiencies of the enzyme and shows no blocking of the pores. This pore-blocking effect can be a disadvantage of the cross-linking method, in which the enzyme is allowed to diffuse into

the pore first and the toxic cross-linker glutaraldehyde is added in a second step to produce highly loaded and stable enzyme-host conjugates *in situ*.[75]

The click-reaction mediated immobilization was successfully employed for two different enzymes, which remained active and stable after attachment to the support as is presented in chapter 6.

1.1.5. Mesoporous silica nanoparticles as drug delivery vehicles

1.1.5.1. Stimuli-responsive drug release

Mesoporous silica nanoparticles provide many necessary requirements for an ideal drug delivery vehicle. Their large surface areas enable high loading capacities, and can therefore reduce necessary drug doses and correlated toxicity. Easy functionalization on the inside of the pores results in optimized host-guest interactions. In addition, above-mentioned capping systems attached to the outer part of the MSNs ensure tight closure of the pores and prevent premature release. This enables local delivery of the drug and avoids severe side effects induced through systemic drug distribution. Open and closure mechanisms are ‘smart’ and rely on certain stimuli. As depicted in Figure 1-7, drug release is either triggered by internal stimuli like change of pH, oxidizing or reducing environments or biomolecule induced degradation upon arrival in tumor cells or tumor microenvironment. Furthermore, the capping systems can also be opened by applying external stimuli like near infrared light (NIR), magnetic fields or ultrasound – depending on the respective capping system and target site.[20]

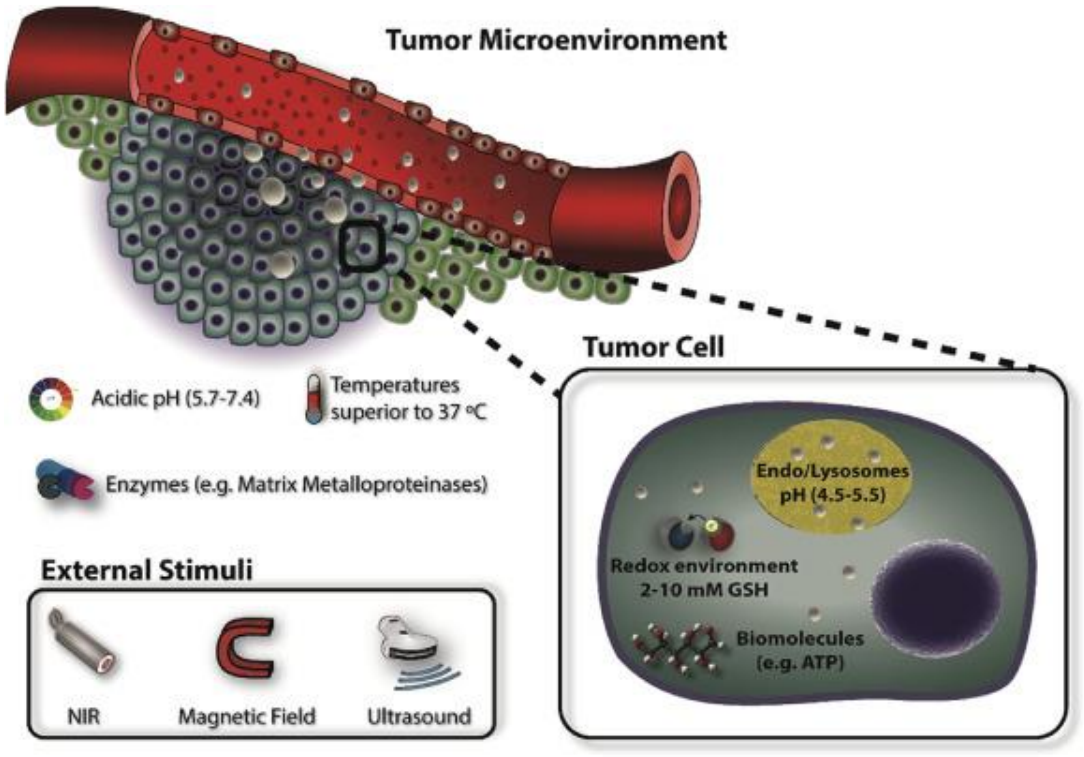

Figure 1-7: Representation of possible internal and external stimuli to trigger drug release from mesoporous silica nanoparticles in the tumor microenvironment. Reprinted from *Microporous Mesoporous Mater., 236* , Moreira, A. F.; Dias, D. R.; Correia, I. J., "Stimuli-responsive mesoporous silica nanoparticles for cancer therapy: A review", 141-157, Copyright 2016, with permission from Elsevier.[20]

A fully equipped mesoporous silica nanoparticle with stimuli-responsive capping system and optimized cargo loading and release efficiencies, conceptually represents an ideal drug delivery system.

1.1.5.2. Toxicity profile

A further crucial aspect which has to be considered for their biomedical application is the particles' biocompatibility and cytotoxicity profile. To be used as a carrier for drugs, MSNs must show a very favourable toxicity profile in the concentration range commonly used. It is known that biocompatibility can be influenced by parameters like size, surface charge, and porosity.[76-77] Several groups studied the size effect of MSNs on cellular uptake and correlated toxicity. Vallhov *et al.* compared mesoporous silica nanoparticles with sizes of 270 (± 50) nm and 2500 (± 500) nm with comparable surface areas of 520 m^2/g and 547 m^2/g respectively,

regarding their interaction with dendritic cells (DCs).[78] They could show that both particle types were taken up by human DCs *via* an energy dependent process, such as endocytosis. Nonetheless, their intracellular localization seemed to differ due to great differences in affecting the immune cells. The smaller silica particles influenced the dendritic cells only very little whereas the larger particles had a significant effect in upregulating certain immune markers. Concluding, small-sized MSNs represent ideal drug delivery vehicles, whereas larger particles could be used as immune modulators. The work of Mou *et al.* underlines the complexity of endocytosis. He compared the size-dependent particle uptake by HeLa cells with monodisperse MSNs in a size range from 30 – 280 nm.[79] With concentrations of 100 µg/mL all five differently-sized particles showed only little cytotoxicity and no constraint in cell proliferation, but a clearly size-dependent cellular uptake in the order 50 > 30 > 110 > 280 > 170 nm. These results suggest the optimal particle size of a MSN drug carrier to be 50 nm. It has to be noted that there are several contradicting studies about the size-dependent interaction between particles and cells. For example, the group of Slowing reported a relationship between smaller particles and less induced hemolysis of red blood cells, whereas Lin and Haynes determined the opposite.[80-81] Nevertheless, the general cytotoxicity of MSNs is explained with the surface silanol groups (Si-OH). They can act as hydrogen donors to form bonds with membrane parts or interact with positively charged groups of phospholipids when dissociated to SiO^-.[82] Such strong interactions can lead to membrane disruption and cell lysis, which was shown as hemolysis in red blood cells. [20, 77] A second factor leading to toxicity of MSNs are reactive oxygen species (ROS) which can be formed between radicals and water present on the surface of MSNs. ROS can stimulate certain inflammatory mediators or disrupt the cell membrane completely, leading to programmed cell death. To estimate an approximate benchmark of ROS producing activity of silica particles, the group of Zink performed comparison studies between MSNs, commonly used liposomes, SLB-covered MSNs

("protocells") and polysterene beads. As shown in Figure 1-8 , the pure MSNs (named Nanoporous Cores) generate only a very small amount of ROS in Hep3B cells. On the opposite, positively charged liposomes and MSNs covered with them show a much higher ROS production (seen in black with MitoSOX Red) and correlating % cell death (shown in grey with propidium iodide).

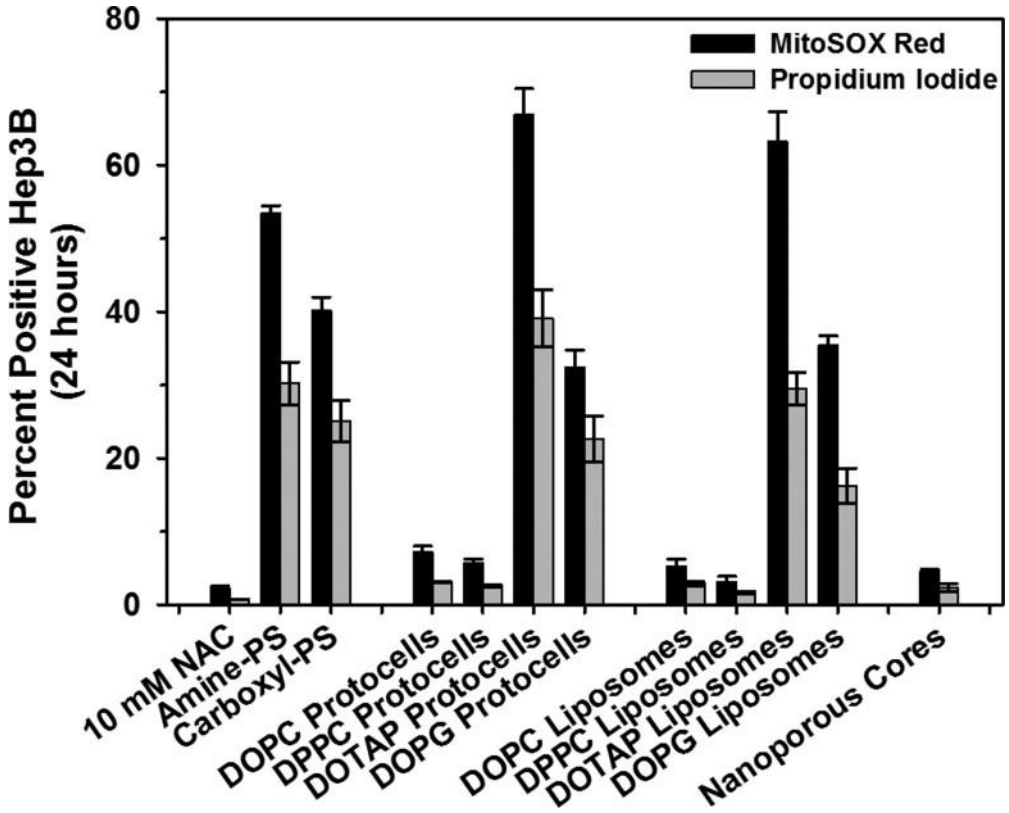

Figure 1-8: Comparison between differently charged liposomes, functionalized polystyrene beads and MSNs (unfunctionalized 'Nanoporous Cores' or SLB capped, 'Protocells') regarding their ROS production and % of induced cell death (N-acetylcysteine, NAC, an antioxidant was used as negative control). Reprinted with permission from "Mesoporous Silica Nanoparticle Nanocarriers: Biofunctionality and Biocompatibility" by Tarn, D.; Ashley, C. E.; Xue, M.; Carnes, E. C.; Zink, J. I.; Brinker, C. J., *Acc. Chem. Res.* 2013, *46* (3), 792-801. Copyright 2013 by the American Chemical Society. [77]

Additionally, to avoid hemolysis, the surface of unfunctionalized silica particles can be treated with polymers or the like.[77, 82] Besides the size, also the porosity has an impact on the particles' toxicity profile. For example, in the above mentioned hemolysis studies porous particles were also compared to nonporous Stöber silica particles. Here, it could be shown that porous MSNs have a significantly lower toxicity than dense particles. This can be attributed to

the smaller number of surface silanol groups, as well as the smaller possible MSN-cell membrane contact area.[80] Concluding, the possibility to functionalize MSNs in the chosen way, enables perfect tailoring of non-toxic porous materials for the respective biomedical application.

1.1.5.3. Passive and active delivery

In targeted drug delivery there are generally two ways for reaching the target: (i) particles can passively accumulate in the tumor tissue, or (ii) can actively target certain cells. Tumors grow rapidly in an uncontrolled manner and show certain abnormalities (also see below and Figure 1-13). In a process called angiogenesis, the tumor forms extensively new blood vessels. This leads to leaky vasculature and defect architecture of the cell membrane. Additional impaired lymphatic drainage enables accumulation of circulating nanoparticles by entering the tumor through fenestrations with sizes of approximately 400 nm.[20, 83] It is known that very small particles are rapidly cleared by renal filtration, medium sized nanoparticles by the liver and larger particles by liver and spleen.[20, 84] Concluding, the correct size and functionalization has to be chosen in a way to escape these clearing mechanisms and prolong circulation times to enable passive targeting *via* the EPR effect. As shown by He *et al.*, PEGylation of MSNs provides these effects.[84-85] Nevertheless, delivery *via* the EPR effect takes place in a passive, unspecific way and differs from tumor to tumor as well as from patient to patient.[86] Therefore, great efforts have been made towards attaching targeting ligands onto the surface of MSNs to achieve active targeting. Several successful targeting strategies have been proven *in vitro*.[1, 28, 33, 87-88] Recently, Mamaeva et al. showed active targeting *in vivo* with the well-known folate ligand, as well as the Zink group, which proved an enhanced effect of folate-functionalized MSNs regarding tumor suppression *in vivo*.[89-90] Furthermore, Gary-Bobo and co-workers

could imply mannose as successful targeting ligands *in vivo*, whereas Chen *et al.* proved active delivery with antibody-functionalized particles.[91-92]

Insights into the mechanisms of the immune system allow for the development of an indirect targeting approach. Using nanoparticles in cancer immunotherapy, the targeted sites for drug delivery are lymphoid organs. Here, the largest number of T cells can be found, augmenting the probability of a successful T cell activation. The automatic uptake of nanoparticles by cells of the innate immune system (dendritic cells, macrophages), followed by their transport *via* those cells to the lymph nodes represents, therefore, active indirect targeting. The successful implementation of this targeting approach is discussed in chapters 3 and 4.

In contrast to the large number of successfully *in vitro* used MSNs as drug delivery agents, the number of *in vivo* reports still remains scarce. Explanations for this might be the lack of complete and uniform biodistribution and cytotoxicity studies of MSNs.

To evaluate the position of MSNs in currently used nanomaterials for therapeutic treatments in clinics or clinical trials, the next section will compare MSNs with well-known organic and metallic systems.

1.1.6. Applied nanoparticle-based therapy

Nanotechnology raises high hopes and expectations for many patients in regard of better diagnostic and therapeutic treatments. Early clinical results indicate lower side effects with nanoparticle therapeutics achieved through active cellular uptake and local delivery to tumors.[93] In the following some key examples of nanotherapeutics are discussed.

1.1.6.1. Polymeric nanoparticles

Polymeric nanoparticles represent organic, soft materials, which already show great success in the clinics. They either consist of polymer-drug conjugates to increase the half-life and enhance solubility and biocompatibility of the drug, or of biodegradable polymers for controlled release upon acidification in the endosomes. Furthermore, they play a role in the synthesis of other drug carriers as described above. Besides representing a drug delivery vehicle, polymers are also employed as direct drugs. A famous example is a copolymer, randomly composed of L-glutamic acid, L-alanine, L-lysine and L-tyrosine, which is FDA-approved since 1996 under the name Copaxone. It acts as an immunomodulator to treat multiple sclerosis.[94] The most famous polymer used to enhance biological half-life as already described is polyethylene glycol short PEG. There are several FDA-approved PEGylated drug-conjugates like PEGylated granulocyte colony stimulating factor, PEGylated interferon gamma beta-1a, or Certolizumab, a PEGylated antibody fragment, and many more in clinical trials.[95] A well-established candidate of a biodegradable polymer is polylactide-co-glycolic acid (PLGA). It can incorporate several drugs and release them by slow decomposition. Loaded with the testosterone inhibiting leuprolide, it is used against symptoms of prostate cancer under the tradename Eligard.[96]

1.1.6.2. Liposomal nanoparticles

In 1965, the first and simplest form of liposomes was described as spherical vesicle consisting of a phospholipid bilayer around an aqueous cavity.[97] Accommodating drug molecules in their interior, they represent powerful and efficient nanotherapeutics of which a large number is in clinical trials or already approved. The first FDA-approved nano-drug consisted of PEGylated nano-liposomes loaded with the chemotherapeutic doxorubicin. Under the tradename Doxil its marketing approval was granted in 1995 for the treatment of ovarian cancer and AIDS-related

Kaposi's carcinoma.[98] In comparison to the free drug, Doxil delivered 4 to 16-fold higher amounts of doxorubicin to malignant cells.[99] Next to Doxil, there are several other liposomal drugs on the market like DaunoXome (loaded with Daunorobicin), Amphotec (loaded with Amphotericin B) and Mepact (loaded with Mifamurtide) to name only a few. Furthermore, they are also used in viral vaccines, the treatment of fungal diseases and photodynamic therapy.[98]

Besides these promising organic soft nanomedicines described as key representatives among others, there is also a large number of inorganic candidates for biomedical applications including metallic and metal oxide nanoparticles.

1.1.6.3. Metallic and metal oxide nanoparticles

Besides silver, hafnium oxide and others, iron oxide and gold nanoparticles represent two promising materials of metal (oxide) nanotherapeutics.[95, 100] Iron oxide nanoparticles in nanomedicine can be used in different ways: (i) in magnetic resonance imaging, (ii) in iron replacement treatments for iron-deficient anemia patients (iii) or in tumor therapy as superparamagnetic iron oxide nanoparticles (SPIONs) inducing hypothermia.[101-102] Examples of FDA-approved imaging agents in MRI are (carboxy-) dextran-coated iron oxide particles like Feridex, Sinerem or Resovist.[103] Examples of application (ii) are Venofer, Dexferrum, Feraheme and more, which are also covered with hydrophilic polymers such as dextran to treat anemia related to chronic kidney disease (CKD).[95] Another promising candidate, named Nanotherm, is applied in the treatment of glioblastoma in Germany, while the FDA approval is pending.[104] Here, particles are directly injected into the tumors and subsequent heating *via* an applied external magnetic field results in tumor cell death. Besides iron oxide particles and many others, gold nanoparticles seem to be promising materials for cancer treatment. Nevertheless, there are no FDA-approved gold-based nanoformulations until now. One of the

possible drawbacks is the high affinity of gold to DNA.[95] A promising candidate is recently waiting for its phase II clinical trial, named Aurimune. In a successful phase I, it was shown that PEGylated gold nanoparticles could deliver TNF (Tumor Necrosis Factor) to the tumor. TNF is supposed to break down the blood vessel architecture to enable succeeding chemotherapeutics to penetrate the tumor easily and eliminate it.[105]

1.1.6.4. Silica nanoparticles

Despite showing conceptually optimal features for a successful drug delivery vehicle in cancer therapy, there are no FDA approved mesoporous silica nanoparticles until now. The most promising candidates at the moment are so-called Cornell Dots. Wiesner and his group at the Cornell University developed a multimodal silica nanoparticle with a size of around 7 nm.[106] As can be seen in Figure 1-9 the particle consists of a fluorophoric Cy5 core and is covered with a PEG shell. This shell can be further functionalized, e.g., with a cyclic RGD sequence, a well-known targeting peptide for integrins, and a long-lived radiolabel. It is supposed to be used for real-time lymph node mapping during the surgery.

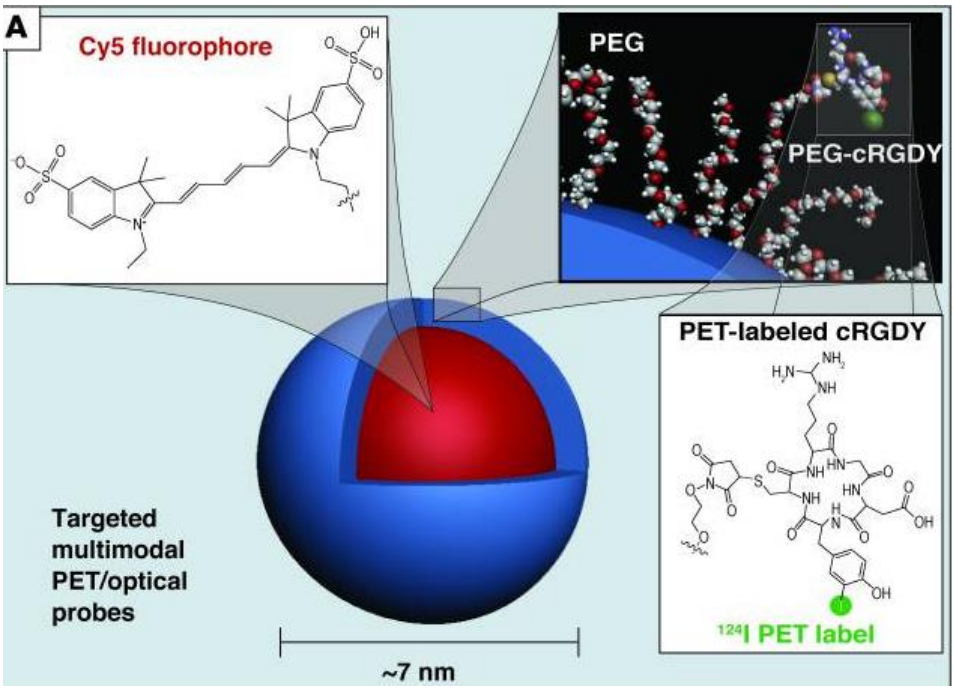

Figure 1-9: Multifunctional Cornell-Dot.[106]

This cRGDY-PEG-Cy5.5-C dot is currently waiting for the completion of its clinical trial phase 1 and 2 scheduled for April 2019.[107]

Silica itself is 'generally recognized as safe' by the FDA and is frequently taken as dietary supplement.[108] With the above mentioned outstanding characteristics it seems to be a perfect candidate for targeted drug delivery in clinical applications. However, besides the already described lack of knowledge regarding a detailed safety and biodistribution profile *in vivo*, another difficulty in the translation to clinics is the up-scaling process and reproducibility of the sometimes complex multistep syntheses.[33] Nevertheless, as soon as these hurdles are overcome, it is hoped that the first FDA approvals of silica-based nanomedicines can be expected.

A completely different approach for designing promising new drug delivery platforms is discussed in the following.

1.2 Supramolecular nanoparticles

Supramolecular nanostructures can be constructed using a cooperation of different non-covalent interactions such as hydrogen bonding, van der Waals interactions, electrostatics, metal chelation, hydrophobic and π-π stacking interaction.[109-110] The combination of many of those interactions leads to a self-assembly into defined structures. This phenomenon is well known from nature where the self-assembly of phospholipids *via* hydrophobic interactions forms cell membranes or where DNA forms a double helix *via* hydrogen bonding, as examples.[111] These materials attract great interest in the fields of biomaterials and drug delivery.[109, 111] A very interesting approach for functional drug delivery is inclusion complexation. It describes the combination of several interactions between the components 'host' and 'guest'. The binding between these two is usually enabled through hydrophobic and geometrical fitting effects.[112-113] Besides crown ethers, calixarenes, cryptands and cucurbiturils, cyclodextrins (CDs) are the most widely used hosts.[110, 112, 114-116]

There are three commonly used types of seminatural macrocyclic oligosaccharides, distinguished by the constituent numbers of glucose units. α-CDs possesses six α-D-glucopyranoside units, β-CDs seven and γ-CDs eight, which are linked by α-1,4-glycosidic bonds as shown in Figure 1-10.[112-113]

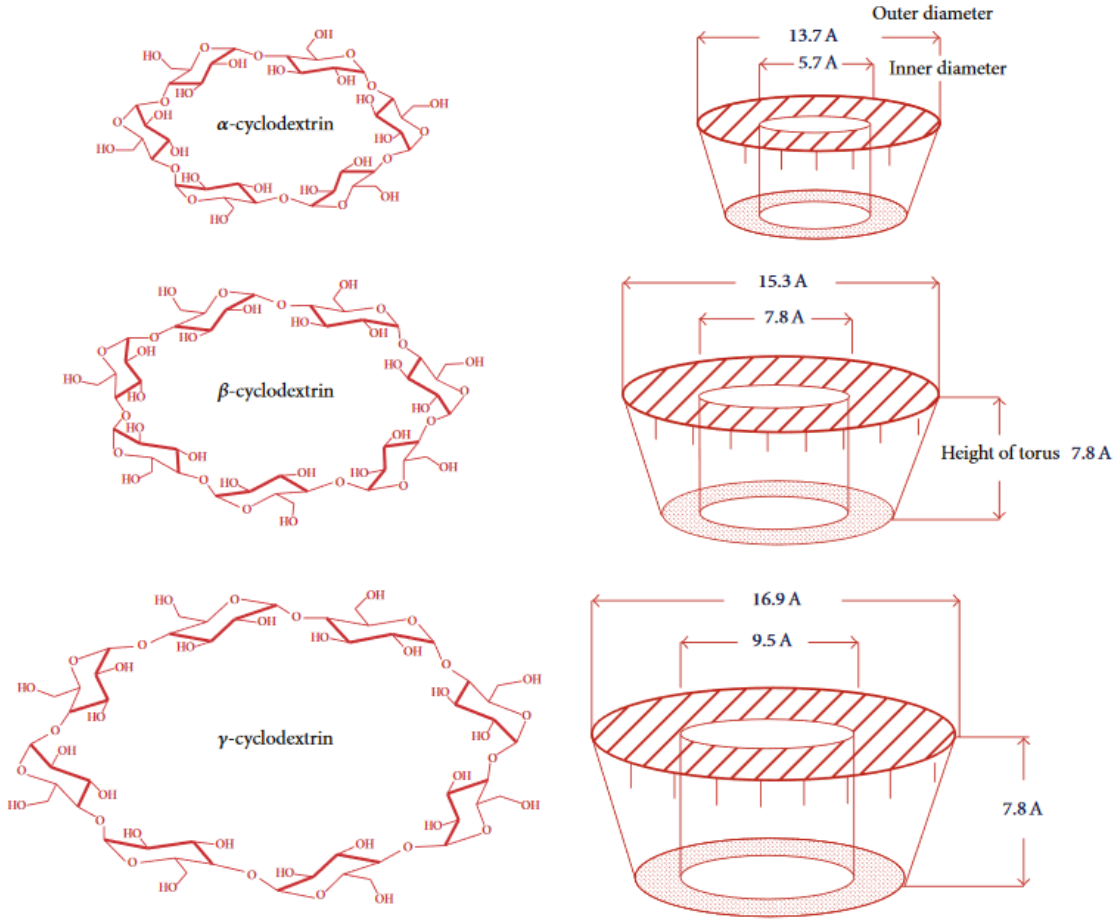

Figure 1-10: (A) Structure and dimensions of α-, β-, γ-CD.[119]

They show a conical structure with a hydrophilic external surface and a hydrophobic cavity, in which they can accommodate different guest molecules. The sizes of the respective cones are shown in Figure 1-10.[117] CDs have been extensively studied as inclusion delivery vehicles due to the increased effective drug solubility and the higher permeability in biological systems compared to the free drug as well as the control over drug release and associated smaller toxicity.[118]

Cyclodextrins can be threaded by polymers to form polyrotaxane structures, where bulky end groups keep them in place, or pseudorotaxane structures, where CD molecules can move freely along the polymer structure.[117] Liu *et al*. showed the self-assembly of polyrotaxanes made from α-CDs and cinnamic-acid-modified PEG around the chemotherapeutic drug

doxorubicin. Due to the fact that the inclusion complex offers an abundant number of hydroxyl groups, the loading efficiency was significantly higher than in a pure polymeric micelle. Furthermore, the supramolecular host-guest complex showed higher antitumor activity *in vivo* than the free drug. Another very promising example of CD-inclusion complex which made its way already into clinical trials is CRLX101.[120] It uses the potent anti-cancer drug camptothecin (CPT) which is rapidly cleared *via* the renal pathway otherwise. Conjugation to β-cyclodextrin-based polymer *via* a single glycine linker and subsequent self-assembly into 30 to 40 nm sized nanoparticles enabled sustained intratumoral CPT release (structure and formation of NPs can be seen in Figure 1-11). The results of the studies proved the drug delivery vehicle to be safe and effective, and to show favorable pharmacokinetics. Additionally, promising anti-tumor activity in non-small cell lung cancer (NSCLC) patients was observed such that further trials were encouraged.

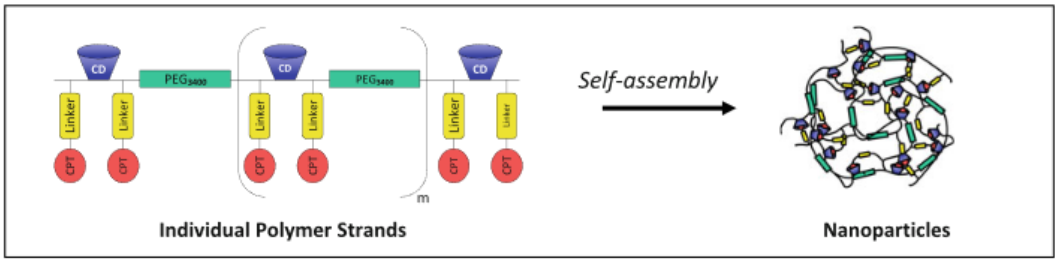

Figure 1-11: Schematic structure of CRLX101 formation. Reprinted by permission from Springer Nature Customer Service Centre GmbH: Springer Nature, *Invest. New Drugs*, "First-in-human phase 1/2a trial of CRLX101, a cyclodextrin-containing polymer-camptothecin nanopharmaceutical in patients with advanced solid tumor malignancies" by Weiss, G. J.; Chao, J.; Neidhart, J. D.; Ramanathan, R. K.; Bassett, D.; Neidhart, J. A.; Choi, C. H. J.; Chow, W.; Chung, V.; Forman, S. J.; Garmey, E.; Hwang, J.; Kalinoski, D. L.; Koczywas, M.; Longmate, J.; Melton, R. J.; Morgan, R.; Oliver, J.; Peterkin, J. J.; Ryan, J. L.; Schluep, T.; Synold, T. W.; Twardowski, P.; Davis, M. E.; Yen, Y., *31* (4), 986-1000, Copyright 2013.[120]

A second system which showed already success in clinical trials is called CALAA-01.[121] It is a four-component system and is mixed from two solutions at bedside. As shown in Figure 1-12 solution 1 contains a polyrotaxane made from cyclodextrin, PEG and adamantane end groups, as well as the human transferrin (hTf) protein targeting ligand. Upon mixing with

siRNA-containing solution 2, self-assembly into 75 nm-sized nanoparticles takes place. The intravenously injected particles represent, according to the authors, the 'first targeted, polymer-based nanoparticle carrying siRNA to be systemically administered to humans'.[121] The system was well-tolerated and could act as successful delivery vehicle of siRNA.

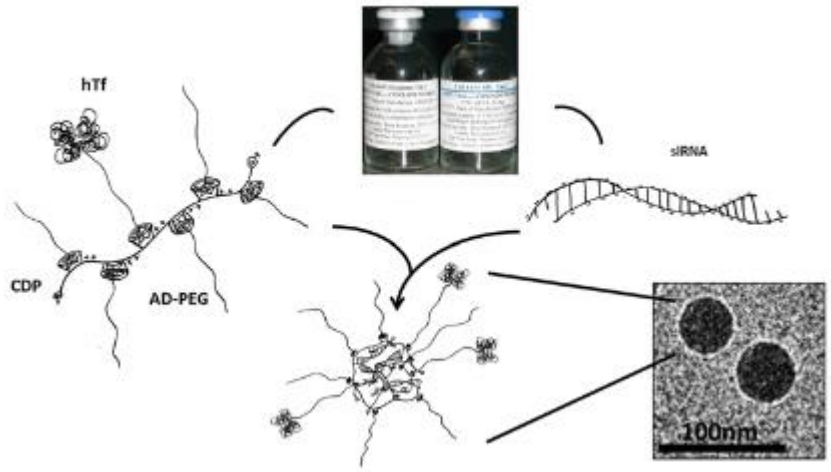

Figure 1-12: Schematic representation of self-assembly process of CALAA-01.[121]

The above mentioned systems all consist of non-covalently bound inclusion complexes which have to be orchestrated to optimally self-assemble into a defined structure. Disadvantages might be the easy reversibility of the self-arrangement process leading to decreased stability of the systems as well as a poor reaction control resulting in heterogenic products. To avoid these problems, poly(pseudo)rotaxanes can be covalently crosslinked. An example is the crosslinking of α-cyclodextrin threaded onto PEG with epichlorohydrin. Subsequent removal of the 'guest' PEG resulted in a nanosized drug delivery vehicle which was able to load new 'guests' (Cisplatin) into the cavities.[122] Gabr *et al.* presented carboxylate crosslinked β-CD nanoparticles as optimal delivery system for Rosuvastatin calcium (ROS).[123] ROS is used for the treatment of various blood lipid metabolic disorders and it is used for the prophylaxis of cardiovascular events in patients with diabetes mellitus, renal failure and the like. It is a very potent statin with poor aqueous solubility. The authors could show that inclusion complexes

with the crosslinked CD particles and ROS lead to a significantly higher oral bioavailability shown by an increased drug absorption. Comparisons to the free or marketed drug (tablet) underlined the improved results of the delivery system. Despite the promising results, it has to be mentioned that the above described crosslinked particles exhibit a broad particle size distribution indicating only moderate control over the crosslinking reactions.

In contrast, chapter 7 of this thesis describes a novel crosslinked cyclodextrin material consisting of well-defined nanoparticles which is believed to hold great promise in the field of nanotherapeutics.

1.3 Cancer

All nanoparticles mentioned above seem to be promising candidates which have the potential to enable a perfectly tailored, personalized and localized cancer therapy with increased efficacies and safety.[124] The reason for the high hopes in improved therapeutics and the immense attention, not only scientifically, is the second leading cause of death worldwide – cancer. Numbers of new cases and mortality rates are constantly rising. The current data from the World Health Organisation (WHO) predicted 9.6 million deaths worldwide for 2018, meaning that one out of six deaths results from cancer.[125] The new World Cancer Report is supposed to be released this year and will definitely not report lower numbers. Cancer develops through uncontrolled cell growth arising from genetic mutations.[126] The hallmarks of cancer proposed by Hanahan and Weinberg, shown in Figure 1-13, summarize the main abnormalities of malignant tumor development and cancer progression.[127-128]

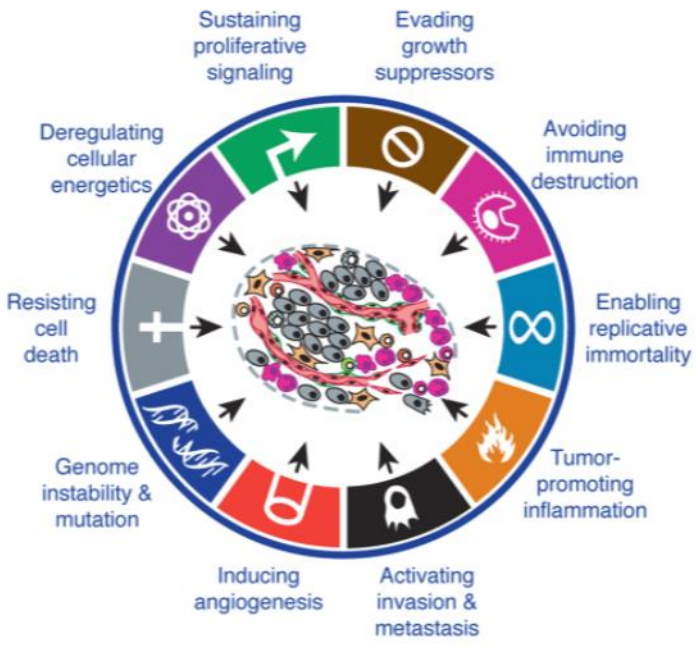

Figure 1-13: Ten hallmarks of cancer. Reprinted from Cell, *144* (5), Lee, C.-H.; Lin, T.-S.; Mou, C.-Y., "Hallmarks of Cancer: The Next Generation", 646-674, Copyright 2011, with permission from Elsevier.[128]

In 2000, the first cycle of hallmarks was published and afterwards supplemented because of newly gained knowledge. Two additional points were the tumor-promoting inflammation and the avoiding of immune-system based destruction. New insights into the complex interaction between the immune system and the cancer cells led to the conclusion that malignant cells can evade the immune system's surveillance up to the point where they harness it for their own use.[129] The body's immune system is divided into the innate and the adaptive part.[130-131] The innate immune system reacts immediately to pathogens as a first line of defense. Cells like phagocytic cells (neutrophils, macrophages), dendritic cells, natural killer (NK) and other innate lymphoid cells are present in most tissues, always on the lookout for invading microbes or aberrant cells. They play an essential role in the defense mechanism in the first hours or days, before the adaptive immune system is activated. Adaptive immunity is mediated through recognition of foreign antigens by specific lymphocytes. The two most important ones being B and T lymphocytes. Whereas B cells can recognize antigens by themselves, T cells only respond to presented antigens. This occurs through specialized antigen presenting

cells (APCs) belonging to the innate immune system. Here, dendritic cells (DCs) represent the most powerful subset of APCs: They are present in most tissues, express a variety of receptors that respond specifically to microbial molecules and are efficient at capturing, processing and presenting antigens. They are key players in modulating and initiating the innate as well as the adaptive immune system. To achieve successful killing of tumor cells, T cells have to be activated in a stepwise series of events as depicted in the cancer-immunity cycle (Figure 1-14) introduced by Chen and Mellman.[132]

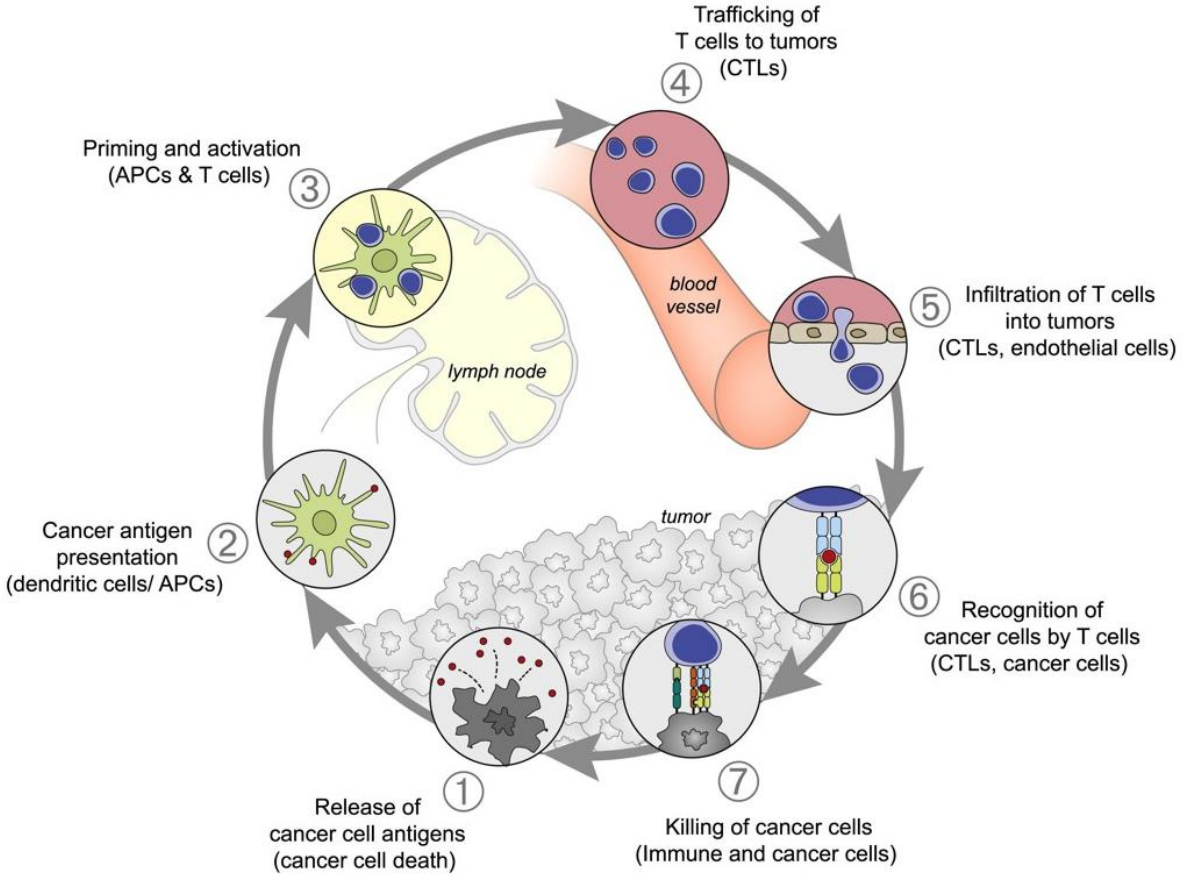

Figure 1-14: The Cancer-Immunity Cycle shows the stepwise initiation of an anticancer immune response. APCs: antigen presenting cells. CTLs: cytotoxic T lymphocytes. Reprinted from Immunity, *39* (1), Chen, Daniel S.; Mellman, I. "Oncology Meets Immunology: The Cancer-Immunity Cycle", 1-10, Copyright 2013, with permission from Elsevier.[132]

First, tumor-associated antigens (TAAs) are released from dying tumor cells. Patrolling antigen-presenting cells (like DCs) take up those TAAs. This is followed by antigen

processing, DC maturation and migration to the tumor draining lymph node. Here, presentation of the processed antigen to T cells takes place, leading to the activation of cytotoxic T lymphocytes (CTL) which can travel back to the tumor site *via* the blood circulation system. Having infiltrated the tumor tissue and recognized the cancerous cells, the CTL will kill the tumor cells, resulting in a higher number of released cancer antigens and by this amplifying the cancer-immunity cycle.

Nevertheless, cancer cells can develop strategies to block this self-propagating cycle at several steps and thus evade the immune system's surveillance. This process consists of three different phases, the so-called elimination, equilibrium and escape, as shown in Figure 1-15.[133]

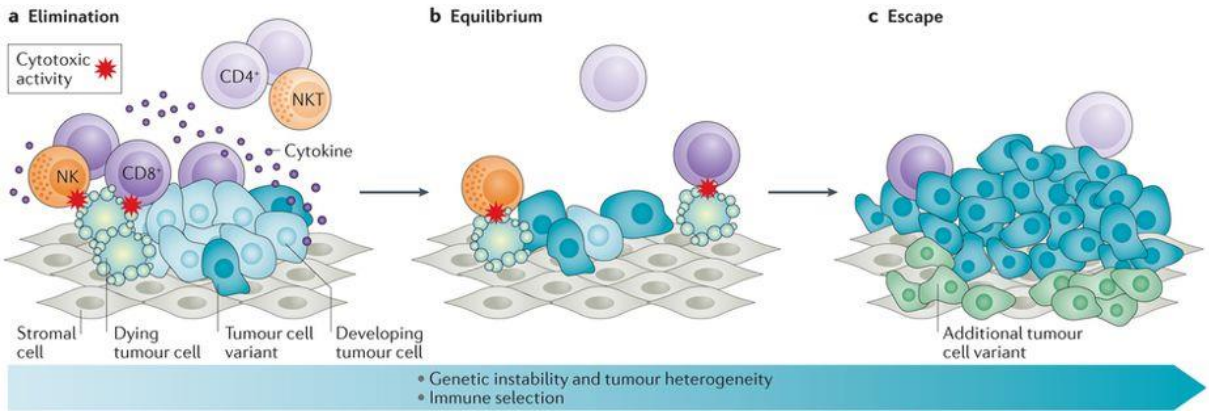

Figure 1-15: Three distinct phases of cancer progression and immunoediting. NK: natural killer cell, NKT: natural killer T cell, $CD8^+$: cytotoxic T lymphocyte, $CD4^+$: helper T cell. Reprinted by permission from Springer Nature Customer Service Centre GmbH: Springer Nature, *Nature Reviews Cancer*, "Vaccines for established cancer: overcoming the challenges posed by immune evasion" by van der Burg, S. H.; Arens, R.; Ossendorp, F.; van Hall, T.; Melief, C. J. M., *16*, 219, Copyright 2016.[133]

In the first step, called elimination, the tumor cells are killed according to the cancer-immunity cycle described above. Due to resistance arising from genetic mutations in the tumor cells, they gain the ability to survive the attacks of the immune system until an equilibrium is reached. Even more variations in the mutated cells lead to the cancer cell escape from the immune system followed by uncontrolled cancer progression.

All these fresh insights principally allow for the development of new, enhanced cancer therapies. An extremely promising and already partially applied approach is cancer immunotherapy. Here, the goal is to (re-) initiate the cancer-immunity cycle in a way that a successful, amplified cancer immune response is achieved without inducing autoimmunity. The main concept of cancer immunotherapy is discussed in the following section.

1.4 Cancer Immunotherapy

Cancer immunotherapy is seen as the upcoming fourth column in cancer therapy next to the conventional methods surgery, chemotherapy and radiation. It was called the 'breakthrough of the year' by Science[134] in 2013 and 'One of the hottest areas in cancer research' by Nature in 2018.[135] And the hype has not stopped yet about this rapidly advancing research field which has already covered a long distance. The concept of cancer immunotherapy is almost 130 years old and dates back to the year 1891 in which the young New Yorker surgeon William Coley started to treat malignant tumors partially successfully by injecting bacterial toxins. The resulting acute inflammation was supposed to activate the patient's immunity.[136-137] Coley's toxins did not find broad acceptance in clinics due to the varying results and efficacies, and the severe side effects.[138] Only time would show that it should take generations of scientists to bring cancer immunotherapy to where it is now.

In 2008, the centenary of Paul Ehrlich's Nobel Prize gave reason to commemorate the 'father of immunology and chemotherapy'. With his interdisciplinary studies in histological stainings, haematology, bacteriology, immunology and many more, he created the foundation of chemotherapy and was an outstanding scientist among his great contemporaries, such as Emil von Behring and Robert Koch.[139] His postulate "wir müssen chemisch zielen lernen" ("we have to learn how to aim chemically") combined with his idea of designing the magic bullet in the fight against cancer inspired scientists for more than a century in the field of

cancer research.[140] The magic bullet is supposed to consist of an antibody or drug that specifically targets toxins or malignant cancer cells without harming the healthy ones; and it still describes the requirements for the perfect anticancer drug nowadays.[141] Ehrlich started his search for such a magic bullet in the year 1891 by studying the effect of methylene blue on malaria patients with mediocre success.[142] Several years later he discovered an arsenic compound that effectively fought syphilis – a disease with huge impact at that time. Salvarsan - the arsenic that saves - was the first successful chemotherapeutic drug and gained Ehrlich worldwide reputation.[140, 142]

Ehrlich was not only called the father of chemotherapy, but legitimately also of immunology. His understanding of the role of the immune system and his side-chain theory became pioneer work in the world of immunology. In his theory he describes the three central aspects of an immune response of the body resulting in antibody production. First, he states that cells possess so-called 'side-chains', which bind specific toxins with high affinity. Nowadays, these 'side-chains' are termed receptors, which specifically bind antigens. Second, he postulates that this binding of a toxin to a side-chain leads to its ejection into the blood stream and the following higher production of the 'lost' side-chain on the cell's surface. This can be transferred to the clonal multiplication of a B lymphocyte upon binding the particular antigen (receptor). The third and last aspect of his theory lays in the exuberant behavior of the resulting side-chain or rather antibody production.[139] His idea that the immune system might be able to control the cancer itself should suffer several throwbacks and failures over the years until his heirs were to be able to gain hope again and experience some success.[138]

1984, Niels Kaj Jerne, Georges J. F. Köhler and César Milstein received the Nobel Prize for their theories about the specific composition and control of the immune system, as well as the discovery of the production of monoclonal antibodies (Köhler and Milstein invented the hybridoma technology) in 1975.[143-144] This method enabled the first mass production of

monoclonal antibodies and hence their first clinical applications in cancer treatment. [138, 145] The introduction of chimaeric antibodies with a mouse component of only 5-10% introduced by Greg Winter and his group paved the way for over 80 monoclonal antibodies (mAb) which have been granted marketing approval during the last 30 years, and some hundred more in current clinical studies.[146]

In 2018, two scientists were awarded with the Nobel Prize in physiology or medicine for their seminal achievements in the field of cancer immunotherapy.[147] Both scientists pursued the approach of a checkpoint blockade therapy which 'loosens the brakes' of the immune system by blocking the blocker. James P. Allison from the U.S. discovered that the cytotoxic T-lymphocyte antigen 4 (CTLA-4) regulates T cell proliferation at an early stage of an immune response. His idea was to block this checkpoint of the body, resulting in an unsuppressed reaction. 24 years after the discovery of CTLA-4, Ipilimumab - an inhibitor of CTLA-4 – was FDA-approved and became the first checkpoint inhibitor to reach patients in 2011.[134, 148] Tasuku Honjo from Japan was honored for his work on PD-1 (programmed death 1), also a negative regulator of the later T cell immune response. Antibodies that specifically block this checkpoint were FDA-approved in 2014 (Nivolumab) for melanoma and in 2015 (Pembrolizumab) for non-small-cell lung cancer (NSCLC).[149-150]

Despite those game-changing achievements, the great success of immune checkpoint inhibitors is still limited to a small percentage of patients and thus leaving a great demand for improved immunotherapies. A very promising approach to boost the antitumor T cell response is the use of tumor-specific antigens. Besides the above mentioned antibodies aiming at immune checkpoints, there is also a large number of monoclonal antibodies used to specifically target antigens expressed on cancer cells. Several of these mAbs are already FDA approved as stated above.[146, 151] For example bevacizumab is designed to block the vascular endothelial growth factor (VEGF) leading to an anti-angiogenic effect and thus limiting tumor

growth and metastatic development. It has marketing approvals under the trade name Avastin for the treatment of several cancers, especially in combination with chemotherapy. This is common for mAbs as their use in monotherapy is often not satisfactory.[152-153]

Next to mAb, engineered T cell therapies have shown recent success with the FDA approval of two CAR T cell systems.[154-155] The approach is to collect T cells from the patient's blood and modify them *ex vivo* to express so-called chimeric antigen receptors (CARs) which are specific to tumor-associated antigens. Upon re-injection to the patient, CAR T cells recognize the tumor *via* the targeted antigen and kill it. Despite the promising results, the clinical application is hampered by the complex and costly production of CAR T cells.

Another promising approach in tumor-antigen directed cancer immunotherapy are cancer vaccines which are discussed in the following section.

1.4.1 Cancer vaccines

The method of vaccination has been successfully used for more than two centuries in the form of prophylactic vaccines. In 1796, Edward Jenner was the first to develop a vaccination from cowpox to induce immunity against smallpox – a life-threatening disease at that time.[156] He named the method vaccination, deduced from the Latin word *vacca* for cow. The following great success of prophylactic vaccinations has to be attributed to the work of Louis Pasteur.[157] His principle "isolate, inactivate and inject" has been followed since to produce bacterial and viral vaccines.[158] Furthermore, he postulated that vaccination could be applied to any microbial disease, which was successfully proven in the ultimate eradication of smallpox and effective treatments of many other perilous diseases.[159] In addition, vaccines used for the prevention of cancers aetiologically induced by viruses showed also considerable success.[137] Efforts to transfer the achievements of immunoprophylaxis to immunotherapy of already

existing chronic viral infections and cancer failed for several decades. The striking difference in the target of a preventive to that of a therapeutic vaccine lies in the gained ability of cancerous cells to evade the immune system *via* different mechanisms.[160] Huge efforts are being made towards identifying new tumor-associated antigens that can effectively stimulate T cell responses without leading to a central tolerance through expressed self-antigens. Some common human cancers result from an infection with a virus like the human papillomavirus (HPV), Epstein-Barr virus or hepatitis B and C viruses and contain therefore viral antigens, which represent a great target for immunotherapy.[159, 161] Other cancer associated antigens are completely unique and have to be identified with more complex methods like SEREX, serologic identification by recombinant expression cloning, or mass spectrometry of TAAs bound to MHC I (major histocompatibility complex class I) molecules.[159, 162-163]

There are several kinds of cancer vaccines such as gene-based (mainly DNA), protein- or peptide-containing vaccines, whole cell cancer ones as well as *ex-vivo*-loaded dendritic-cell vaccines.[164-170] DNA or mRNA-based vaccines target antigen presenting cells (APCs) to be taken up, translated and thus able to induce antigen expression. They were tested in several clinical trials but due to immunogenicity and degradation problems, their success is still limited. Similar stability issues occur when applying peptide- or protein vaccines. Here, fragments which are specifically overexpressed on the tumor are used as antigens. Peptide- and protein vaccines were shown to be safe, but struggle to induce a full T cell response due to limited uptake by dendritic cells. Another source of antigens used for cancer vaccines can be derived from complete tumor cell lysates. They are deduced from the patient's isolated tumor. Whereas TAAs derived from real tumors represent an array of multiple tumor antigens and thus significantly enhancing the probability of a successful T cell response, the process to produce them from the tumor cell lysates is complex and very cost-intensive. Another

elaborate procedure is the production of *ex vivo*-loaded dendritic cell vaccines. Here, the key players for inducing a potent immune response are isolated from the patient's blood, *ex vivo* activated and loaded with TAAs before being re-injected into the patient. In 2010, the first DC-based vaccine Sipuleucel-T (Provenge) was FDA-approved for the use in prostate cancer.[171] Nevertheless, its commercialization is restricted due to the high costs and regulations for the production.

Many of the cancer vaccines described above can be improved by using a delivery system.[170, 172-173] This allows for the protection of the respective cargo as well as an enhanced uptake by DCs, thus enabling a strong local immune response while preventing autoimmunity. Furthermore, co-delivery of multiple antigens as well as of adjuvant and antigen can be accomplished. The need for the latter combination is explained in the following.

Recent insights into the functioning of antigen-presenting cells (APCs) with T cells provide useful antigenic target points for an actively attacking therapy. Especially the enhancement of antigen-presenting cell (APCs) activation, primarily dendritic cells, has been addressed to augment the priming of T cells and therefore the overall efficacy of therapeutic vaccines. Dendritic cells play a critical role in the innate immune response as they capture antigens immaturely and present them after successful maturation to T-cells *via* MHC molecules in the lymph nodes. DCs are beside B cells and macrophages (the three main subtypes of bone-marrow derived APCs) the most potent candidates to present antigens.[129, 159, 161] If the maturation of dendritic cells is successful, priming of T cells takes place in lymphoid organs *via* the presentation of processed antigens on MHC complexes on the surface of DCs. This is helped through the expression of several cytokines, such as IL-6 and IL-12, IFN-α/β, and TNF-α and costimulatory molecules, such as CD80, CD86.[129] Thus, an effective T cell response is induced resulting in activation of $CD4^+$ T cells to Th cells (T helper cells) and

$CD8^+$ cells to CTL (cytotoxic T lymphocytes), which are responsible for killing the cancer cells. This cyclic process of T cell activation is severely disturbed when the key players, the dendritic cells, are not completely activated. In this case, the maturation of the dendritic cells fails, meaning they remain in a so-called steady-state. This in turn leads to a promotion of regulatory T cells (T_{reg}), resulting in an opposed antitumor response.[137]

To avoid such effects, successful DC maturation can be achieved by adding adjuvants to the vaccine formulation which induce activation of the so-called pattern recognition receptors (PRRs). Those agonists or PRR-ligands can augment the effect of the anti-tumor immune response and are therefore fittingly called adjuvants, coming from the Latin word *adjuvare* meaning "to help".[174-175] They are responsible for the complete maturation of an APC resulting in a successful immune response. One of the most famous groups of PRRs are the transmembrane proteins named Toll-like receptors (TLRs).[129, 159, 176] They belong to the TLR-interleukin-1 (TIR) receptor superfamily.[177] There are ten different TLRs known in humans, classified by the specific pathogen-associated molecular patterns (PAMP) they respond to. TLRs trigger inflammatory responses by activating dendritic cells to coordinate a systemic defense against microbial infections.[178] If those PRR-activating agonists are left out in the vaccination formulation, one might achieve T cell tolerance instead of potent T cell activation.[129] In the following, very potent members of the TLR adjuvant family are introduced, specifically TLR-7/8 agonists.

1.4.1.1 Imiquimod/ Resiquimod

TLR-7/8 agonists represent very powerful adjuvants. Among other TLR agonists, TLR-7 and -8 are listed by the National Cancer Institute as agents belonging to the most potent anti-cancer ones.[177]

Besides TLR-3 and TLR-9, TLR-7 and -8 are present in endosomal compartments. TLR-7 is mainly found in B cells and plasmacytoid dendritic cells (pDCs), whereas TLR-8 is expressed in monocytes and myeloid dendritic cells (mDCs).[174, 179] They are specialized in viral detection and recognition of nucleic acids in late-endosomes-lysosomes, whereas other TLRs located on the cell surface mainly respond to bacterial products of extracellular pathogens (Figure 1-16). Agonists of TLR-7 and TLR-8, like single-stranded RNA coming from RNA viruses or artificial imidazoquinolines, provoke a Th1-type proinflammatory immune response resulting in the production of cytokines like IFN-γ and the activation of cytotoxic T lymphocytes (CTL).[178, 180]

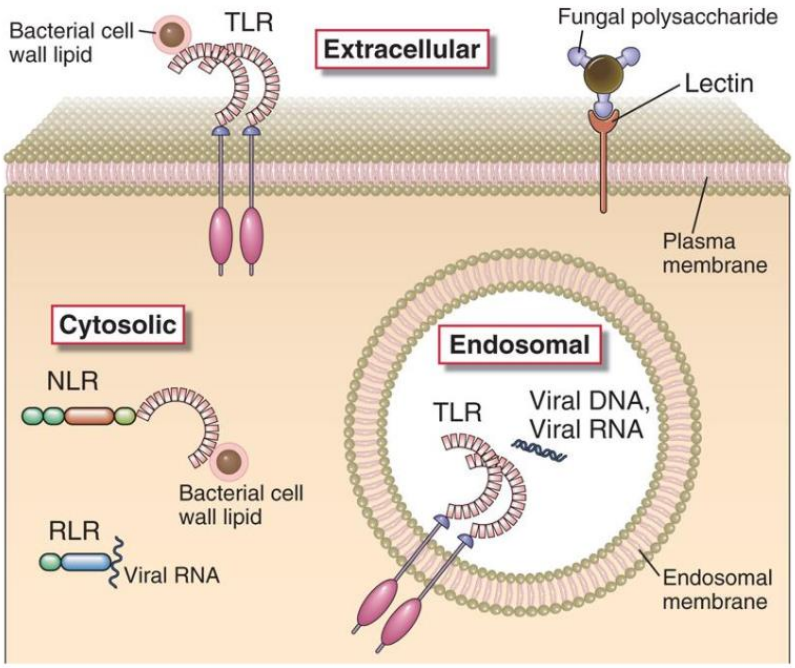

Figure 1-16: Location of the innate immune system's pattern recognition receptors (PRRs). NLR, NOD-like receptor; RLR, RIG-like receptor; TLR, Toll-like receptor [130]

The class of imidazoquinolines represents a family of small synthetic molecules, bearing a structure homologous to adenosine, which can activate TLR-7 and -8. Among others, imiquimod and resiquimod (R848) are the most prominent ones. Whereas imiquimod is already FDA approved since 2004, under the trade name Aldara, for the treatment of superficial basal cell carcinoma, resiquimod still remains in clinical trials.[181-183] Imiquimod is

100-fold less potent than resiquimod at inducing cytokine expression and is only a TLR-7 agonist, whereas resiquimod can actively stimulate TLR-7 and TLR-8.[174, 182, 184] Due to the facts mentioned above, we chose resiquimod in this work.

1.4.1.2 Nanoparticle-based TLR-7/8 vaccines

Due to its small size, resiquimod diffuses quickly away from the injection site leading to a systemic distribution. This can cause severe side effects resulting from a systemic immune response.[185] In addition, like all imidazoquinolines, resiquimod shows a poor solubility in aqueous media at physiological pH. Therefore, a formulation or encapsulation of resiquimod is needed to ensure a localized delivery of the adjuvant after administration. There are different types of delivery systems using lipidation, adsorption to alum adjuvants, conjugation to polymers or encapsulation in nanoparticles.[174] The first carrier system and adjuvant in one were aluminum salts (Alum). Despite the fact that much knowledge has been gained about the mechanisms of the immune system, this 'old system' still remains the most widely used one in clinics.[186] The biodegradable polymer PLGA (poly(D,L-lactic-co-glycolic acid)) is also intensively studied as efficient drug carrier for vaccine antigens.[177, 187] A co-delivery of adjuvant and antigen with PLGA particles was successfully shown by Ilyinskii *et al.*.[188] They compared covalently and non-covalently attached antigen/adjuvants and could show a strong and sustained local immune activation. However, this promising material shows certain drawbacks: contradictory to the stated high encapsulation efficiencies in the polymer, the actual drug loading is usually quite low. Furthermore, the system does not show a sustained release of the loaded cargo but usually presents a burst release – often prior to reaching the targeted cells. In the end, the great advantage to have a biodegradable material also presents its pitfall due to the acidic degradation products which may harm delivered proteins.[189] Mottas *et al.* applied small gold nanoparticles functionalized with 1-octanethiol and 11-

mercaptoundecane sulfonate to accommodate resiquimod in the ligand shell.[190] With this system they were able to show enhanced antitumor efficacy in comparison to the free drug. Despite the successful results, it has to be noted that the particle system with an approximate size of 5 nm is not taken up by antigen-presenting cells at the site of injection but is drained passively to the lymph node. This impairs a controlled uptake and release. A study from Lucke *et al.* uses cathepsin-responsive spider silk nanoparticles to deliver the antigen OVA.[191] The authors describe a strong activation of T cell proliferation without an additional adjuvant.

In contrast to the described organic and metallic nanoparticles, mesoporous silica nanoparticles (MSNs) represent one of the most-promising inorganic drug delivery systems. They are well-known for their large surface areas allowing high drug loading efficiencies. Furthermore, they can be perfectly tuned to accommodate the antigen and adjuvant of choice. From a variety of capping systems, the matching one can be chosen to tightly seal the pores and open them only upon action of certain stimuli. Additionally, the size and surface functionalization can be adjusted to enhance indirect active uptake by antigen-presenting cells. Studies investigating the degradation behaviour of mesoporous silica nanoparticles show its tunability and prove the decomposition into harmless silicic acid.[32-34, 192-193] Together all these facts suggest that MSNs are promising, biocompatible drug delivery vehicles.

Chapter 3 of this thesis describes the evaluation of MSNs as appropriate drug delivery vehicle for the immunostimulant cargo resiquimod and proving indeed its promising use. In addition, in chapter 4 the successful implementation of the advanced multifunctional system as optimized carrier for adjuvant R848 is shown. Enhanced uptake of the R848-loaded MSNs by DCs and the subsequent effective DC activation is reported. Furthermore, the simultaneous delivery of adjuvant and antigen is achieved, leading to an augmented T cell proliferation and thereby underlining the potential of MSNs in nanoparticle-based cancer vaccines.

1.5 References

1. Argyo, C.; Weiss, V.; Bräuchle, C.; Bein, T., Multifunctional Mesoporous Silica Nanoparticles as a Universal Platform for Drug Delivery. *Chem. Mater.* **2014,** *26* (1), 435-451.
2. Nič, M.; Jirát, J.; Košata, B.; Jenkins, A.; McNaught, A., *IUPAC Compendium of Chemical Terminology*. 2009.
3. European Commission: Definition of a nanomaterial. http://ec.europa.eu/environment/chemicals/nanotech/faq/definition_en.htm (accessed Sat. 9 March 2019).
4. Kresge, C. T.; Leonowicz, M. E.; Roth, W. J.; Vartuli, J. C.; Beck, J. S., Ordered mesoporous molecular sieves synthesized by a liquid-crystal template mechanism. *Nature* **1992,** *359* (6397), 710-712.
5. Yanagisawa, T.; Shimizu, T.; Kuroda, K.; Kato, C., The Preparation of Alkyltriinethylaininonium–Kaneinite Complexes and Their Conversion to Microporous Materials. *Bull. Chem. Soc. Jpn.* **1990,** *63* (4), 988-992.
6. Meng, X.; Nawaz, F.; Xiao, F.-S., Templating route for synthesizing mesoporous zeolites with improved catalytic properties. *Nano Today* **2009,** *4* (4), 292-301.
7. Chaudhary, V.; Sharma, S., An overview of ordered mesoporous material SBA-15: synthesis, functionalization and application in oxidation reactions. *J. Porous Mater.* **2017,** *24* (3), 741-749.
8. Möller, K.; Bein, T., Talented Mesoporous Silica Nanoparticles. *Chem. Mater.* **2016,** *29* (1), 371-388.
9. Zhao, D.; Feng, J.; Huo, Q.; Melosh, N.; Fredrickson, G. H.; Chmelka, B. F.; Stucky, G. D., Triblock copolymer syntheses of mesoporous silica with periodic 50 to 300 angstrom pores. *Science* **1998,** *279* (5350), 548-552.
10. Zhao, D.; Huo, Q.; Feng, J.; Chmelka, B. F.; Stucky, G. D., Nonionic Triblock and Star Diblock Copolymer and Oligomeric Surfactant Syntheses of Highly Ordered, Hydrothermally Stable, Mesoporous Silica Structures. *J. Am. Chem. Soc.* **1998,** *120* (24), 6024-6036.
11. Yang, P.; Gai, S.; Lin, J., Functionalized mesoporous silica materials for controlled drug delivery. *Chem. Soc. Rev.* **2012,** *41* (9), 3679-3698.
12. Zheng, H.; Tai, C.-W.; Su, J.; Zou, X.; Gao, F., Ultra-small mesoporous silica nanoparticles as efficient carriers for pH responsive releases of anti-cancer drugs. *Dalton Trans.* **2015,** *44* (46), 20186-20192.
13. Cha, B. G.; Jeong, J. H.; Kim, J., Extra-Large Pore Mesoporous Silica Nanoparticles Enabling Co-Delivery of High Amounts of Protein Antigen and Toll-like Receptor 9 Agonist for Enhanced Cancer Vaccine Efficacy. *ACS Cent. Sci.* **2018,** *4* (4), 484-492.
14. Wu, S. H.; Mou, C. Y.; Lin, H. P., Synthesis of Mesoporous Silica Nanoparticles. *Chem. Soc. Rev.* **2013,** *42* (9), 3862-3875.
15. Zhu, J.; Liao, L.; Zhu, L.; Zhang, P.; Guo, K.; Kong, J.; Ji, C.; Liu, B., Size-dependent cellular uptake efficiency, mechanism, and cytotoxicity of silica nanoparticles toward HeLa cells. *Talanta* **2013,** *107*, 408-415.
16. Shang, L.; Nienhaus, K.; Nienhaus, G. U., Engineered nanoparticles interacting with cells: size matters. *J. Nanobiotechnol.* **2014,** *12* (1), 5.
17. Vallet-Regi, M.; Rámila, A.; del Real, R. P.; Pérez-Pariente, J., A New Property of MCM-41: Drug Delivery System. *Chem. Mater.* **2000,** *13* (2), 308-311.
18. Grün, M.; Lauer, I.; Unger, K. K., The synthesis of micrometer- and submicrometer-size spheres of ordered mesoporous oxide MCM-41. *Adv. Mater.* **1997,** *9* (3), 254-257.
19. Stöber, W.; Fink, A.; Bohn, E., Controlled growth of monodisperse silica spheres in the micron size range. *J. Colloid. Interf. Sci.* **1968,** *26* (1), 62-69.
20. Moreira, A. F.; Dias, D. R.; Correia, I. J., Stimuli-responsive mesoporous silica nanoparticles for cancer therapy: A review. *Microporous Mesoporous Mater.* **2016,** *236*, 141-157.
21. Cai, Q.; Luo, Z.-S.; Pang, W.-Q.; Fan, Y.-W.; Chen, X.-H.; Cui, F.-Z., Dilute Solution Routes to Various Controllable Morphologies of MCM-41 Silica with a Basic Medium. *Chem. Mater.* **2001,** *13* (2), 258-263.
22. Nooney, R. I.; Thirunavukkarasu, D.; Chen, Y.; Josephs, R.; Ostafin, A. E., Synthesis of Nanoscale Mesoporous Silica Spheres with Controlled Particle Size. *Chem. Mater.* **2002,** *14* (11), 4721-4728.
23. Lin, H.-P.; Tsai, C.-P., Synthesis of Mesoporous Silica Nanoparticles from a Low-concentration CnTMAX–Sodium Silicate Components. *Chem. Lett.* **2003,** *32* (12), 1092-1093.
24. Fowler, C. E.; Khushalani, D.; Lebeau, B.; Mann, S., Nanoscale Materials with Mesostructured Interiors. *Adv. Mater.* **2001,** *13* (9), 649-652.
25. Möller, K.; Kobler, J.; Bein, T., Colloidal Suspensions of Nanometer-Sized Mesoporous Silica. *Adv. Funct. Mater.* **2007,** *17* (4), 605-612.

26. Frye, C. L.; Vincent, G. A.; Finzel, W. A., Pentacoordinate silicon compounds. V. Novel silatrane chemistry. *J. Am. Chem. Soc.* **1971,** *93* (25), 6805-6811.
27. Möller, K.; Bein, T., Talented Mesoporous Silica Nanoparticles. *Chem. Mater.* **2017,** *29* (1), 371-388.
28. Mackowiak, S. A.; Schmidt, A.; Weiss, V.; Argyo, C.; von Schirnding, C.; Bein, T.; Bräuchle, C., Targeted drug delivery in cancer cells with red-light photoactivated mesoporous silica nanoparticles. *Nano Lett.* **2013,** *13* (6), 2576-83.
29. Schloßbauer, A.; Sauer, A. M.; Cauda, V.; Schmidt, A.; Engelke, H.; Rothbauer, U.; Zolghadr, K.; Leonhardt, H.; Bräuchle, C.; Bein, T., Cascaded Photoinduced Drug Delivery to Cells from Multifunctional Core–Shell Mesoporous Silica. *Adv. Healthcare Mater.* **2012,** *1* (3), 316-320.
30. Argyo, C.; Cauda, V.; Engelke, H.; Rädler, J.; Bein, G.; Bein, T., Heparin-coated colloidal mesoporous silica nanoparticles efficiently bind to antithrombin as an anticoagulant drug-delivery system. *Chem. Eur. J.* **2012,** *18* (2), 428-432.
31. Datz, S.; Argyo, C.; Gattner, M.; Weiss, V.; Brunner, K.; Bretzler, J.; von Schirnding, C.; Torrano, A. A.; Spada, F.; Vrabel, M.; Engelke, H.; Bräuchle, C.; Carell, T.; Bein, T., Genetically designed biomolecular capping system for mesoporous silica nanoparticles enables receptor-mediated cell uptake and controlled drug release. *Nanoscale* **2016,** *8* (15), 8101-8110.
32. Bunker, B. C., Molecular mechanisms for corrosion of silica and silicate glasses. *J. Non-Cryst. Solids* **1994,** *179*, 300-308.
33. Vallet-Regí, M.; Colilla, M.; Izquierdo-Barba, I.; Manzano, M., Mesoporous Silica Nanoparticles for Drug Delivery: Current Insights. *Molecules* **2018**, *23* (1).
34. Möller, K.; Bein, T., Degradable Drug Carriers: Vanishing Mesoporous Silica Nanoparticles. *Chem. Mater.* **2019**, *31* (12), 4364-4378.
35. Knežević, N. Ž.; Durand, J.-O., Large pore mesoporous silica nanomaterials for application in delivery of biomolecules. N*anoscale* **2015,** *7* (6), 2199-2209.
36. Zhao, D.; Feng, J.; Huo, Q.; Melosh, N.; Fredrickson, G. H.; Chmelka, B. F.; Stucky, G. D., Triblock Copolymer Syntheses of Mesoporous Silica with Periodic 50 to 300 Angstrom Pores. *Science* **1998,** *279* (5350), 548-552.
37. Han, Y.; Ying, J. Y., Generalized Fluorocarbon-Surfactant-Mediated Synthesis of Nanoparticles with Various Mesoporous Structures. *Angew. Chem. Int. Ed.* **2005,** *44* (2), 288-292.
38. Gao, F.; Botella, P.; Corma, A.; Blesa, J.; Dong, L., Monodispersed Mesoporous Silica Nanoparticles with Very Large Pores for Enhanced Adsorption and Release of DNA. *J. Phys. Chem. B* **2009,** *113* (6), 1796-1804.
39. Lee, J. H.; Park, J.-H.; Eltohamy, M.; Perez, R.; Lee, E.-J.; Kim, H.-W., Collagen gel combined with mesoporous nanoparticles loading nerve growth factor as a feasible therapeutic three-dimensional depot for neural tissue engineering. *RSC Adv.* **2013,** *3* (46), 24202-24214.
40. Slowing, I. I.; Trewyn, B. G.; Lin, V. S. Y., Mesoporous Silica Nanoparticles for Intracellular Delivery of Membrane-Impermeable Proteins. *J. Am. Chem. Soc.* **2007,** *129* (28), 8845-8849.
41. Gu, J.; Huang, K.; Zhu, X.; Li, Y.; Wei, J.; Zhao, W.; Liu, C.; Shi, J., Sub-150nm mesoporous silica nanoparticles with tunable pore sizes and well-ordered mesostructure for protein encapsulation. *J. Colloid Interface Sci.* **2013,** *407*, 236-242.
42. Kao, K.-C.; Lin, T.-S.; Mou, C.-Y., Enhanced Activity and Stability of Lysozyme by Immobilization in the Matching Nanochannels of Mesoporous Silica Nanoparticles. *J. Phys. Chem. C* **2014,** *118* (13), 6734-6743.
43. Zhang, J.; Li, X.; Rosenholm, J. M.; Gu, H.-c., Synthesis and characterization of pore size-tunable magnetic mesoporous silica nanoparticles. *J. Colloid Interface Sci.* **2011,** *361* (1), 16-24.
44. Möller, K.; Müller, K.; Engelke, H.; Bräuchle, C.; Wagner, E.; Bein, T., Highly efficient siRNA delivery from core–shell mesoporous silica nanoparticles with multifunctional polymer caps. *Nanoscale* **2016,** *8* (7), 4007-4019.
45. Zhang, K.; Xu, L.-L.; Jiang, J.-G.; Calin, N.; Lam, K.-F.; Zhang, S.-J.; Wu, H.-H.; Wu, G.-D.; Albela, B.; Bonneviot, L.; Wu, P., Facile Large-Scale Synthesis of Monodisperse Mesoporous Silica Nanospheres with Tunable Pore Structure. *J. Am. Chem. Soc.* **2013,** *135* (7), 2427-2430.
46. Asefa, T.; MacLachlan, M. J.; Coombs, N.; Ozin, G. A., Periodic mesoporous organosilicas with organic groups inside the channel walls. *Nature* **1999,** *402*, 867.
47. Melde, B. J.; Holland, B. T.; Blanford, C. F.; Stein, A., Mesoporous Sieves with Unified Hybrid Inorganic/Organic Frameworks. *Chem. Mater.* **1999,** *11* (11), 3302-3308.
48. Inagaki, S.; Guan, S.; Fukushima, Y.; Ohsuna, T.; Terasaki, O., Novel Mesoporous Materials with a Uniform Distribution of Organic Groups and Inorganic Oxide in Their Frameworks. *J. Am. Chem. Soc.* **1999,** *121* (41), 9611-9614.
49. de Juan, F.; Ruiz-Hitzky, E., Selective Functionalization of Mesoporous Silica. *Adv. Mater.* **2000,** *12* (6), 430-432.

50. Cauda, V.; Schlossbauer, A.; Kecht, J.; Zürner, A.; Bein, T., Multiple Core−Shell Functionalized Colloidal Mesoporous Silica Nanoparticles. *J. Am. Chem. Soc.* **2009,** *131* (32), 11361-11370.
51. Kecht, J.; Schlossbauer, A.; Bein, T., Selective Functionalization of the Outer and Inner Surfaces in Mesoporous Silica Nanoparticles. *Chem. Mater.* **2008,** *20* (23), 7207-7214.
52. Lai, C.-Y.; Trewyn, B. G.; Jeftinija, D. M.; Jeftinija, K.; Xu, S.; Jeftinija, S.; Lin, V. S. Y., A Mesoporous Silica Nanosphere-Based Carrier System with Chemically Removable CdS Nanoparticle Caps for Stimuli-Responsive Controlled Release of Neurotransmitters and Drug Molecules. *J. Am. Chem. Soc.* **2003,** *125* (15), 4451-4459.
53. Schlossbauer, A.; Kecht, J.; Bein, T., Biotin-avidin as a protease-responsive cap system for controlled guest release from colloidal mesoporous silica. *Angew. Chem. Int. Ed.* **2009,** *48* (17), 3092-3095.
54. Giri, S.; Trewyn, B. G.; Stellmaker, M. P.; Lin, V. S. Y., Stimuli-Responsive Controlled-Release Delivery System Based on Mesoporous Silica Nanorods Capped with Magnetic Nanoparticles. *Angew. Chem. Int. Ed.* **2005,** *44* (32), 5038-5044.
55. Gan, Q.; Lu, X.; Yuan, Y.; Qian, J.; Zhou, H.; Shi, J.; Liu, C., A magnetic, reversible pH-responsive nanogated ensemble based on Fe3O4 nanoparticles-capped mesoporous silica. *Biomaterials* **2011,** *32* (7), 1932-1942.
56. Muhammad, F.; Guo, M.; Qi, W.; Sun, F.; Wang, A.; Guo, Y.; Zhu, G., pH-Triggered Controlled Drug Release from Mesoporous Silica Nanoparticles via Intracelluar Dissolution of ZnO Nanolids. *J. Am. Chem. Soc.* **2011,** *133* (23), 8778-8781.
57. Chen, X.; Cheng, X.; Soeriyadi, A. H.; Sagnella, S. M.; Lu, X.; Scott, J. A.; Lowe, S. B.; Kavallaris, M.; Gooding, J. J., Stimuli-responsive functionalized mesoporous silica nanoparticles for drug release in response to various biological stimuli. *Biomater. Sci.* **2014,** *2* (1), 121-130.
58. van Rijt, S. H.; Bölükbas, D. A.; Argyo, C.; Wipplinger, K.; Naureen, M.; Datz, S.; Eickelberg, O.; Meiners, S.; Bein, T.; Schmid, O.; Stoeger, T., Applicability of avidin protein coated mesoporous silica nanoparticles as drug carriers in the lung. *Nanoscale* **2016,** *8* (15), 8058-8069.
59. Park, C.; Kim, H.; Kim, S.; Kim, C., Enzyme Responsive Nanocontainers with Cyclodextrin Gatekeepers and Synergistic Effects in Release of Guests. *J. Am. Chem. Soc.* **2009,** *131* (46), 16614-16615.
60. Rühle, B.; Datz, S.; Argyo, C.; Bein, T.; Zink, J. I., A molecular nanocap activated by superparamagnetic heating for externally stimulated cargo release. *Chem. Commun.* **2016,** *52* (9), 1843-1846.
61. Cauda, V.; Engelke, H.; Sauer, A.; Arcizet, D.; Bräuchle, C.; Rädler, J.; Bein, T., Colchicine-loaded lipid bilayer-coated 50 nm mesoporous nanoparticles efficiently induce microtubule depolymerization upon cell uptake. *Nano Lett.* **2010,** *10* (7), 2484-92.
62. Popat, A.; Liu, J.; Lu, G. Q.; Qiao, S. Z., A pH-responsive drug delivery system based on chitosan coated mesoporous silica nanoparticles. *J. Mater. Chem.* **2012,** *22* (22), 11173-11178.
63. Baeza, A.; Guisasola, E.; Ruiz-Hernández, E.; Vallet-Regí, M., Magnetically Triggered Multidrug Release by Hybrid Mesoporous Silica Nanoparticles. *Chem. Mater.* **2012,** *24* (3), 517-524.
64. Niedermayer, S.; Weiss, V.; Herrmann, A.; Schmidt, A.; Datz, S.; Müller, K.; Wagner, E.; Bein, T.; Bräuchle, C., Multifunctional polymer-capped mesoporous silica nanoparticles for pH-responsive targeted drug delivery. *Nanoscale* **2015,** *7* (17), 7953-7964.
65. Moreira, A. F.; Gaspar, V. M.; Costa, E. C.; de Melo-Diogo, D.; Machado, P.; Paquete, C. M.; Correia, I. J., Preparation of end-capped pH-sensitive mesoporous silica nanocarriers for on-demand drug delivery. *Eur. J. Pharm. Biopharm.* **2014,** *88* (3), 1012-1025.
66. Zhang, Y.; Hou, Z.; Ge, Y.; Deng, K.; Liu, B.; Li, X.; Li, Q.; Cheng, Z.; Ma, P. a.; Li, C.; Lin, J., DNA-Hybrid-Gated Photothermal Mesoporous Silica Nanoparticles for NIR-Responsive and Aptamer-Targeted Drug Delivery. *ACS Appl. Mater. Interfaces* **2015,** *7* (37), 20696-20706.
67. Nordlund, G.; Sing Ng, J. B.; Bergström, L.; Brzezinski, P., A Membrane-Reconstituted Multisubunit Functional Proton Pump on Mesoporous Silica Particles. *ACS nano* **2009,** *3* (9), 2639-2646.
68. Pascual, L.; Baroja, I.; Aznar, E.; Sancenón, F.; Marcos, M. D.; Murguía, J. R.; Amorós, P.; Rurack, K.; Martínez-Máñez, R., Oligonucleotide-capped mesoporous silica nanoparticles as DNA-responsive dye delivery systems for genomic DNA detection. *Chem. Commun.* **2015,** *51* (8), 1414-1416.
69. Liu, J.; Stace-Naughton, A.; Jiang, X.; Brinker, C. J., Porous nanoparticle supported lipid bilayers (protocells) as delivery vehicles. *J. Am. Chem. Soc.* **2009,** *131* (4), 1354-1355.
70. Schlossbauer, A.; Warncke, S.; Gramlich, P. M.; Kecht, J.; Manetto, A.; Carell, T.; Bein, T., A programmable DNA-based molecular valve for colloidal mesoporous silica. *Angew. Chem. Int. Ed.* **2010,** *49* (28), 4734-4737.
71. Lee, C.-H.; Lin, T.-S.; Mou, C.-Y., Mesoporous materials for encapsulating enzymes. *Nano Today* **2009,** *4* (2), 165-179.

72. Johnson, P.; Whateley, T. L., On the use of polymerizing silica gel systems for the immobilization of trypsin. *J. Colloid Interface Sci.* **1971,** *37* (3), 557-563.
73. Lei, C.; Soares, T. A.; Shin, Y.; Liu, J.; Ackerman, E. J., Enzyme specific activity in functionalized nanoporous supports. *Nanotechnology* **2008,** *19* (12), 125102.
74. Schlossbauer, A.; Schaffert, D.; Kecht, J.; Wagner, E.; Bein, T., Click chemistry for high-density biofunctionalization of mesoporous silica. *J. Am. Chem. Soc.* **2008,** *130* (38), 12558-9.
75. Reis, P.; Witula, T.; Holmberg, K., Mesoporous materials as host for an entrapped enzyme. *Microporous Mesoporous Mater.* **2008,** *110* (2), 355-362.
76. Asefa, T.; Tao, Z., Biocompatibility of Mesoporous Silica Nanoparticles. *Chem. Res. Toxicol.* **2012,** *25* (11), 2265-2284.
77. Tarn, D.; Ashley, C. E.; Xue, M.; Carnes, E. C.; Zink, J. I.; Brinker, C. J., Mesoporous Silica Nanoparticle Nanocarriers: Biofunctionality and Biocompatibility. *Acc. Chem. Res.* **2013,** *46* (3), 792-801.
78. Vallhov, H.; Gabrielsson, S.; Strømme, M.; Scheynius, A.; Garcia-Bennett, A. E., Mesoporous Silica Particles Induce Size Dependent Effects on Human Dendritic Cells. *Nano Lett.* **2007,** *7* (12), 3576-3582.
79. Lu, F.; Wu, S.-H.; Hung, Y.; Mou, C.-Y., Size Effect on Cell Uptake in Well-Suspended, Uniform Mesoporous Silica Nanoparticles. *Small* **2009,** *5* (12), 1408-1413.
80. Slowing, I. I.; Wu, C.-W.; Vivero-Escoto, J. L.; Lin, V. S. Y., Mesoporous Silica Nanoparticles for Reducing Hemolytic Activity Towards Mammalian Red Blood Cells. *Small* **2009,** *5* (1), 57-62.
81. Lin, Y.-S.; Haynes, C. L., Impacts of Mesoporous Silica Nanoparticle Size, Pore Ordering, and Pore Integrity on Hemolytic Activity. *J. Am. Chem. Soc.* **2010,** *132* (13), 4834-4842.
82. Nash, T.; Allison, A. C.; Harington, J. S., Physico-Chemical Properties of Silica in Relation to its Toxicity. *Nature* **1966,** *210* (5033), 259-261.
83. Maeda, H.; Wu, J.; Sawa, T.; Matsumura, Y.; Hori, K., Tumor vascular permeability and the EPR effect in macromolecular therapeutics: a review. *J. Controlled Release* **2000,** *65* (1), 271-284.
84. He, Q.; Zhang, Z.; Gao, F.; Li, Y.; Shi, J., In vivo Biodistribution and Urinary Excretion of Mesoporous Silica Nanoparticles: Effects of Particle Size and PEGylation. *Small* **2011,** *7* (2), 271-280.
85. He, Q.; Zhang, J.; Shi, J.; Zhu, Z.; Zhang, L.; Bu, W.; Guo, L.; Chen, Y., The effect of PEGylation of mesoporous silica nanoparticles on nonspecific binding of serum proteins and cellular responses. *Biomaterials* **2010,** *31* (6), 1085-1092.
86. Lammers, T., Macro-nanomedicine: Targeting the big picture. *J. Controlled Release* **2019,** *294*, 372-375.
87. Ashley, C. E.; Carnes, E. C.; Phillips, G. K.; Padilla, D.; Durfee, P. N.; Brown, P. A.; Hanna, T. N.; Liu, J.; Phillips, B.; Carter, M. B.; Carroll, N. J.; Jiang, X.; Dunphy, D. R.; Willman, C. L.; Petsev, D. N.; Evans, D. G.; Parikh, A. N.; Chackerian, B.; Wharton, W.; Peabody, D. S.; Brinker, C. J., The targeted delivery of multicomponent cargos to cancer cells by nanoporous particle-supported lipid bilayers. *Nat. Mater.* **2011,** *10*, 389.
88. Mamaeva, V.; Sahlgren, C.; Lindén, M., Mesoporous silica nanoparticles in medicine—Recent advances. *Adv. Drug Deliv. Rev.* **2013,** *65* (5), 689-702.
89. Mamaeva, V.; Rosenholm, J. M.; Bate-Eya, L. T.; Bergman, L.; Peuhu, E.; Duchanoy, A.; Fortelius, L. E.; Landor, S.; Toivola, D. M.; Lindén, M.; Sahlgren, C., Mesoporous Silica Nanoparticles as Drug Delivery Systems for Targeted Inhibition of Notch Signaling in Cancer. *Mol. Ther.* **2011,** *19* (8), 1538-1546.
90. Lu, J.; Li, Z.; Zink, J. I.; Tamanoi, F., In vivo tumor suppression efficacy of mesoporous silica nanoparticles-based drug-delivery system: enhanced efficacy by folate modification. *Nanomedicine: NBM* **2012,** *8* (2), 212-220.
91. Gary-Bobo, M.; Mir, Y.; Rouxel, C.; Brevet, D.; Basile, I.; Maynadier, M.; Vaillant, O.; Mongin, O.; Blanchard-Desce, M.; Morère, A.; Garcia, M.; Durand, J.-O.; Raehm, L., Mannose-Functionalized Mesoporous Silica Nanoparticles for Efficient Two-Photon Photodynamic Therapy of Solid Tumors. *Angew. Chem.* **2011,** *123* (48), 11627-11631.
92. Chen, F.; Hong, H.; Zhang, Y.; Valdovinos, H. F.; Shi, S.; Kwon, G. S.; Theuer, C. P.; Barnhart, T. E.; Cai, W., In Vivo Tumor Targeting and Image-Guided Drug Delivery with Antibody-Conjugated, Radiolabeled Mesoporous Silica Nanoparticles. *ACS nano* **2013,** *7* (10), 9027-9039.
93. Davis, M. E.; Chen, Z.; Shin, D. M., Nanoparticle therapeutics: an emerging treatment modality for cancer. *Nat. Rev. Drug Discovery* **2008,** *7*, 771.
94. KP, J.; BR, B.; JA, C.; CC, F.; J, G.; RP, L., Extended use of glatiramer acetate (Copaxone) is well tolerated and maintains its clinical effect on multiple sclerosis relapse rate and degree of disability. *Neurology* **1998,** *50* (3), 701-708.

95. Bobo, D.; Robinson, K. J.; Islam, J.; Thurecht, K. J.; Corrie, S. R., Nanoparticle-Based Medicines: A Review of FDA-Approved Materials and Clinical Trials to Date. *Pharm. Res.* **2016,** *33* (10), 2373-87.
96. Berges, R., Eligard®: Pharmacokinetics, Effect on Testosterone and PSA Levels and Tolerability. *Eur. Urol., Suppl.* **2005,** *4* (5), 20-25.
97. Bangham, A. D.; Standish, M. M.; Watkins, J. C., Diffusion of univalent ions across the lamellae of swollen phospholipids. *J. Mol. Biol.* **1965,** *13* (1), 238-252.
98. Bulbake, U.; Doppalapudi, S.; Kommineni, N.; Khan, W., Liposomal Formulations in Clinical Use: An Updated Review. *Pharmaceutics* **2017,** *9* (2).
99. Gabizon, A.; Catane, R.; Uziely, B.; Kaufman, B.; Safra, T.; Cohen, R.; Martin, F.; Huang, A.; Barenholz, Y., Prolonged circulation time and enhanced accumulation in malignant exudates of doxorubicin encapsulated in polyethylene-glycol coated liposomes. *Cancer Res.* **1994,** *54* (4), 987-992.
100. Anselmo, A. C.; Mitragotri, S., A Review of Clinical Translation of Inorganic Nanoparticles. *AAPS J.* **2015,** *17* (5), 1041-1054.
101. Silva, A. C.; Oliveira, T. R.; Mamani, J. B.; Malheiros, S. M. F.; Malavolta, L.; Pavon, L. F.; Sibov, T. T.; Amaro, E., Jr.; Tannús, A.; Vidoto, E. L. G.; Martins, M. J.; Santos, R. S.; Gamarra, L. F., Application of hyperthermia induced by superparamagnetic iron oxide nanoparticles in glioma treatment. *Int. J. Nanomedicine* **2011,** *6*, 591-603.
102. Vallabani, N. V. S.; Singh, S., Recent advances and future prospects of iron oxide nanoparticles in biomedicine and diagnostics. *3 Biotech.* **2018,** *8* (6), 279-279.
103. Thakor, A. S.; Jokerst, J. V.; Ghanouni, P.; Campbell, J. L.; Mittra, E.; Gambhir, S. S., Clinically Approved Nanoparticle Imaging Agents. *J. Nucl. Med.* **2016,** *57* (12), 1833-1837.
104. MagForce: NanoTherm soll ein weltweiter Erfolg werden - Exklusiv-Interview. https://www.4investors.de/nachrichten/boerse.php?sektion=stock&ID=122300 (accessed Mon. 11 March 2019).
105. CytImmune Aurimune: A Nanomedicine Platform. http://www.cytimmune.com/ (accessed Mon, 11 March 2019).
106. Benezra, M.; Penate-Medina, O.; Zanzonico, P. B.; Schaer, D.; Ow, H.; Burns, A.; DeStanchina, E.; Longo, V.; Herz, E.; Iyer, S.; Wolchok, J.; Larson, S. M.; Wiesner, U.; Bradbury, M. S., Multimodal silica nanoparticles are effective cancer-targeted probes in a model of human melanoma. *J. Clin. Invest.* **2011,** *121* (7), 2768-2780.
107. Targeted Silica Nanoparticles for Real-Time Image Guided Intraoperative Mapping of Nodal Mestases. https://clinicaltrials.gov/ct2/show/record/NCT02106598?term=Cornell+Dots&rank=1 (accessed Mon. 11 March 2019).
108. Rosenholm, J. M.; Mamaeva, V.; Sahlgren, C.; Lindén, M., Nanoparticles in targeted cancer therapy: mesoporous silica nanoparticles entering preclinical development stage. *Nanomedicine* **2011,** *7* (1), 111-120.
109. Adams, D. J.; George, S. J., Supramolecular Nanostructures. *ChemNanoMat* **2018,** *4* (8), 708-709.
110. Xue, B.; Zhu, L.; Jin, X.; Zhu, X.; Yan, D., Supramolecular nanoscale drug delivery system with ordered structure. **2019**.
111. Lim, Y.-b.; Moon, K.-S.; Lee, M., Recent advances in functional supramolecular nanostructures assembled from bioactive building blocks. *Chem. Soc. Rev.* **2009,** *38* (4), 925-934.
112. Hu, Q.-D.; Tang, G.-P.; Chu, P. K., Cyclodextrin-Based Host–Guest Supramolecular Nanoparticles for Delivery: From Design to Applications. *Acc. Chem. Res.* **2014,** *47* (7), 2017-2025.
113. Chen, G.; Jiang, M., Cyclodextrin-based inclusion complexation bridging supramolecular chemistry and macromolecular self-assembly. *Chem. Soc. Rev.* **2011,** *40* (5), 2254-2266.
114. Lawrence, D. S.; Jiang, T.; Levett, M., Self-Assembling Supramolecular Complexes. *Chem. Rev.* **1995,** *95* (6), 2229-2260.
115. Nimse, S. B.; Kim, T., Biological applications of functionalized calixarenes. *Chem. Soc. Rev.* **2013,** *42* (1), 366-386.
116. Dong, S.; Luo, Y.; Yan, X.; Zheng, B.; Ding, X.; Yu, Y.; Ma, Z.; Zhao, Q.; Huang, F., A Dual-Responsive Supramolecular Polymer Gel Formed by Crown Ether Based Molecular Recognition. *Angew. Chem. Int. Ed.* **2011,** *50* (8), 1905-1909.
117. Simões, S. M. N.; Rey-Rico, A.; Concheiro, A.; Alvarez-Lorenzo, C., Supramolecular cyclodextrin-based drug nanocarriers. *Chem. Commun.* **2015,** *51* (29), 6275-6289.
118. Zheng, Y.; Wyman, W. I., Supramolecular Nanostructures Based on Cyclodextrin and Poly(ethylene oxide): Syntheses, Structural Characterizations and Applications for Drug Delivery. *Polymers* **2016,** *8* (5).
119. Gidwani, B.; Vyas, A., A Comprehensive Review on Cyclodextrin-Based Carriers for Delivery of Chemotherapeutic Cytotoxic Anticancer Drugs. *BioMed Res. Int.* **2015,** *2015*, 198268-198268.

120. Weiss, G. J.; Chao, J.; Neidhart, J. D.; Ramanathan, R. K.; Bassett, D.; Neidhart, J. A.; Choi, C. H. J.; Chow, W.; Chung, V.; Forman, S. J.; Garmey, E.; Hwang, J.; Kalinoski, D. L.; Koczywas, M.; Longmate, J.; Melton, R. J.; Morgan, R.; Oliver, J.; Peterkin, J. J.; Ryan, J. L.; Schluep, T.; Synold, T. W.; Twardowski, P.; Davis, M. E.; Yen, Y., First-in-human phase 1/2a trial of CRLX101, a cyclodextrin-containing polymer-camptothecin nanopharmaceutical in patients with advanced solid tumor malignancies. *Invest. New Drugs* **2013,** *31* (4), 986-1000.
121. Zuckerman, J. E.; Gritli, I.; Tolcher, A.; Heidel, J. D.; Lim, D.; Morgan, R.; Chmielowski, B.; Ribas, A.; Davis, M. E.; Yen, Y., Correlating animal and human phase Ia/Ib clinical data with CALAA-01, a targeted, polymer-based nanoparticle containing siRNA. *Proc. Natl. Acad. Sci.* **2014,** *111* (31), 11449.
122. Zhu, W.; Zhang, K.; Chen, Y.; Xi, F., Simple, Clean Preparation Method for Cross-Linked α-Cyclodextrin Nanoparticles via Inclusion Complexation. *Langmuir* **2013,** *29* (20), 5939-5943.
123. Gabr, M. M.; Mortada, S. M.; Sallam, M. A., Carboxylate cross-linked cyclodextrin: A nanoporous scaffold for enhancement of rosuvastatin oral bioavailability. *Eur. J. Pharm. Sci.* **2018,** *111*, 1-12.
124. Liu, R.; Lai, Y.; He, B.; Li, Y.; Wang, G.; Chang, S.; Gu, Z., Supramolecular nanoparticles generated by the self-assembly of polyrotaxanes for antitumor drug delivery. *Int. J. Nanomed.* **2012,** *7*, 5249-58.
125. Cancer. https://www.who.int/news-room/fact-sheets/detail/cancer (accessed Tue. 12 March 2019).
126 Sarkar, S.; Horn, G.; Moulton, K.; Oza, A.; Byler, S.; Kokolus, S.; Longacre, M., Cancer development, progression, and therapy: an epigenetic overview. *Int. J. Mol. Sci.* **2013,** *14* (10), 21087-21113.
127. Hanahan, D.; Weinberg, R. A., The Hallmarks of Cancer. *Cell* **2000,** *100* (1), 57-70.
128. Hanahan, D.; Weinberg, Robert A., Hallmarks of Cancer: The Next Generation. *Cell* **2011,** *144* (5), 646-674.
129. Pardoll, D., Cancer and the Immune System: Basic Concepts and Targets for Intervention. *Semin. Oncol.* **2015,** *42* (4), 523-38.
130. Abbas, A. K.; Lichtman, A. H.; Pillai, S., *Cellular and Molecular Immunology*. Ninth Edition ed.; Elsevier: Philadelphia, 2018.
131. Banchereau, J.; Steinman, R. M., Dendritic cells and the control of immunity. *Nature* **1998,** *392*, 245.
132. Chen, Daniel S.; Mellman, I., Oncology Meets Immunology: The Cancer-Immunity Cycle. *Immunity* **2013,** *39* (1), 1-10.
133. van der Burg, S. H.; Arens, R.; Ossendorp, F.; van Hall, T.; Melief, C. J. M., Vaccines for established cancer: overcoming the challenges posed by immune evasion. *Nat. Rev. Cancer* **2016,** *16*, 219.
134. Couzin-Frankel, J., Breakthrough of the year 2013. Cancer immunotherapy. *Science* **2013,** *342* (6165), 1432-3.
135. Ledford, H.; Else, H.; Warren, M., Cancer immunologists scoop medicine Nobel prize. *Nature* **2018,** *562* (7725), 20-21.
136. Nauts, H. C.; Swift, W. E.; Coley, B. L., The Treatment of Malignant Tumors by Bacterial Toxins as Developed by the Late William B. Coley, M.D., Reviewed in the Light of Modern Research. *Cancer Res.* **1946,** *6*, 205-216.
137. Mellman, I.; Coukos, G.; Dranoff, G., Cancer immunotherapy comes of age. *Nature* **2011,** *480* (7378), 480-9.
138. Dömling, A.; Holak, T. A., Programmed Death-1: therapeutischer Erfolg nach über 100 Jahren Krebsimmuntherapie. *Angew. Chem.* **2014,** *126* (9), 2318-2320.
139. Drews, J., Paul Ehrlich: Magister Mundi. *Nat. Rev. Drug Discovery* **2004,** *3*, 797.
140. Strebhardt, K.; Ullrich, A., Paul Ehrlich's magic bullet concept - 100 years of progress *Nat. Rev. Cancer* **2008,** *8*, 473-480.
141. Schwartz, R. S., Paul Ehrlich's magic bullets. *N. Engl. J. Med.* **2004,** *350* (11), 1079-80.
142. Bosch, F.; Rosich, L., The contributions of Paul Ehrlich to pharmacology: a tribute on the occasion of the centenary of his Nobel Prize. *Pharmacology* **2008,** *82* (3), 171-9.
143. Köhler, G.; Milstein, C., Continuous cultures of fused cells secreting antibody of predefined specificity. *Nature* **1975,** *256* (5517), 495–497.
144. Press Release: The Nobel Prize in Physiology or Medicine 1984. https://www.nobelprize.org/prizes/medicine/1984/press-release/ (accessed Tue. 12 Feb 2019).
145. Gura, T., Magic bullets hit the target. *Nature* **2002,** *417*, 584.
146. Kaplon, H.; Reichert, J. M., Antibodies to watch in 2019. *MAbs* **2018**.
147. Press release: The Nobel Prize in Physiology or Medicine 2018. https://www.nobelprize.org/prizes/medicine/2018/press-release/ (accessed Mon. 11 Feb 2019.).
148. Egen, J. G.; Kuhns, M. S.; Allison, J. P., CTLA-4: new insights into its biological function and use in tumor immunotherapy. *Nat. Immunol.* **2002,** *3* (7), 611-8.
149. Buchbinder, E. I.; Desai, A., CTLA-4 and PD-1 Pathways: Similarities, Differences, and Implications of Their Inhibition. *Am. J. Clin. Oncol.* **2016,** *39* (1), 98-106.

150. Iwai, Y.; Hamanishi, J.; Chamoto, K.; Honjo, T., Cancer immunotherapies targeting the PD-1 signaling pathway. *J. Biomed. Sci.* **2017,** *24* (1), 26.
151. PENTO, J. T., Monoclonal Antibodies for the Treatment of Cancer. *Anticancer Res.* **2017,** *37* (11), 5935-5939.
152. Avastin Approval History. https://www.drugs.com/history/avastin.html (accessed Wed. 20 March 2019).
153. How is Avastin designed to work? https://www.avastin.com/patient/mcrc/about/how-avastin-works.html (accessed Wed. 20 March 2019).
154. Riley, R. S.; June, C. H.; Langer, R.; Mitchell, M. J., Delivery technologies for cancer immunotherapy. *Nat. Rev. Drug Discovery* **2019,** *18* (3), 175-196.
155. Brown, C. E.; Mackall, C. L., CAR T cell therapy: inroads to response and resistance. *Nat. Rev. Immunol.* **2019,** *19* (2), 73-74.
156. Riedel, S., Edward Jenner and the history of smallpox and vaccination. *Proceedings (Baylor University. Medical Center)* **2005,** *18* (1), 21-25.
157. Smith, K., Louis Pasteur, the Father of Immunology? *Front. Immunol.* **2012,** *3* (68).
158. Rappuoli, R., Bridging the knowledge gaps in vaccine design. *Nat. Biotechnol.* **2007,** *25*, 1361.
159. Waldmann, T. A., Immunotherapy: past, present and future. *Nat. Med.* **2003,** *9*, 269.
160. Palucka, K.; Banchereau, J.; Mellman, I., Designing Vaccines Based on Biology of Human Dendritic Cell Subsets. *Immunity* **2010,** *33* (4), 464-478.
161. Pardoll, D. M., Spinning molecular immunology into successful immunotherapy. *Nat. Rev. Immunol.* **2002,** *2*, 227.
162. Krackhardt, A. M.; Witzens, M.; Harig, S.; Hodi, F. S.; Zauls, A. J.; Chessia, M.; Barrett, P.; Gribben, J. G., Identification of tumor-associated antigens in chronic lymphocytic leukemia by SEREX. *Blood* **2002,** *100* (6), 2123-31.
163. Rammensee, H.-G.; Weinschenk, T.; Gouttefangeas, C.; Stevanovi Eq, S., Towards patient-specific tumor antigen selection for vaccination. *Immunological Reviews* **2002,** *188* (1), 164-176.
164. Motl, S. E., Technology evaluation: Canvaxin, John Wayne Cancer Institute/CancerVax. *Curr. Opin. Mol. Ther.* **2004,** *6* (1), 104-11.
165. Banchereau, J.; Palucka, A. K., Dendritic cells as therapeutic vaccines against cancer. *Nat. Rev. Immunol.* **2005,** *5*, 296.
166. Ranieri, E.; Gigante, M.; Storkus, W. J.; Gesualdo, L., Translational mini-review series on vaccines: Dendritic cell-based vaccines in renal cancer. *Clin. Exp. Immunol.* **2007,** *147* (3), 395-400.
167. Huang, X.; Wang, X.; Zhang, J.; Xia, N.; Zhao, Q., Escherichia coli-derived virus-like particles in vaccine development. *NPJ Vaccines* **2017,** *2* (1), 3.
168. Hasson, S. S. A. A.; Al-Busaidi, J. K. Z.; Sallam, T. A., The past, current and future trends in DNA vaccine immunisations. *Asian Pac. J. Trop. Biomed.* **2015,** *5* (5), 344-353.
169. Schuster, M.; Nechansky, A.; Kircheis, R., Cancer immunotherapy. *Biotechnol. J.* **2006,** *1* (2), 138-147.
170. Zhang, R.; Billingsley, M. M.; Mitchell, M. J., Biomaterials for vaccine-based cancer immunotherapy. *J. Controlled Release* **2018,** *292*, 256-276.
171. Cheever, M. A.; Higano, C. S., PROVENGE (Sipuleucel-T) in Prostate Cancer: The First FDA-Approved Therapeutic Cancer Vaccine. *Clin. Cancer Res.* **2011,** *17* (11), 3520.
172. Huang, P.; Wang, X.; Liang, X.; Yang, J.; Zhang, C.; Kong, D.; Wang, W., Nano-, micro-, and macroscale drug delivery systems for cancer immunotherapy. *Acta Biomater.* **2019,** *85*, 1-26.
173. Song, W.; Musetti, S. N.; Huang, L., Nanomaterials for cancer immunotherapy. *Biomaterials* **2017,** *148*, 16-30.
174. Dowling, D. J., Recent Advances in the Discovery and Delivery of TLR7/8 Agonists as Vaccine Adjuvants. *ImmunoHorizons* **2018,** *2* (6), 185-197.
175. Pulendran, B.; Ahmed, R., Immunological mechanisms of vaccination. *Nat. Immunol.* **2011,** *12*, 509.
176. Burdette, D. L.; Vance, R. E., STING and the innate immune response to nucleic acids in the cytosol. *Nat. Immunol.* **2012,** *14*, 19.
177. Huen, A. O.; Rook, A. H., Toll receptor agonist therapy of skin cancer and cutaneous T-cell lymphoma. *Curr. Opin. Oncol.* **2014,** *26* (2), 237-44.
178. Iwasaki, A.; Medzhitov, R., Toll-like receptor control of the adaptive immune responses. *Nat. Immunol.* **2004,** *5*, 987.
179. Hornung, V.; Rothenfusser, S.; Britsch, S.; Krug, A.; Jahrsdörfer, B.; Giese, T.; Endres, S.; Hartmann, G., Quantitative Expression of Toll-Like Receptor 1–10 mRNA in Cellular Subsets of Human Peripheral Blood Mononuclear Cells and Sensitivity to CpG Oligodeoxynucleotides. *J. Immunol.* **2002,** *168* (9), 4531-4537.

180. Wang, D.; Precopio, M.; Lan, T.; Yu, D.; Tang, J. X.; Kandimalla, E. R.; Agrawal, S., Antitumor Activity and Immune Response Induction of a Dual Agonist of Toll-Like Receptors 7 and 8. *Mol. Cancer Ther.* **2010,** *9* (6), 1788-1797.
181. Institute, N. C. Cancer Treatment - Drugs - Imiquimod. https://www.cancer.gov/about-cancer/treatment/drugs/imiquimod (accessed 18 Feb 2019).
182. Rook, A. H.; Gelfand, J. M.; Wysocka, M.; Troxel, A. B.; Benoit, B.; Surber, C.; Elenitsas, R.; Buchanan, M. A.; Leahy, D. S.; Watanabe, R.; Kirsch, I. R.; Kim, E. J.; Clark, R. A., Topical resiquimod can induce disease regression and enhance T-cell effector functions in cutaneous T-cell lymphoma. *Blood* **2015,** *126* (12), 1452-1461.
183. 3M Pharmaceuticals Granted FDA Approval for Aldara -imiquimod- Cream, 5% to Treat Superficial Basal Cell Carcinoma, a Form of Nonmelanoma Skin Cancer https://news.3m.com/press-release/company/3m-pharmaceuticals-granted-fda-approval-aldara-imiquimod-cream-5-treat-superfi (accessed Wed. 20 March 2019).
184. Dockrell, D. H.; Kinghorn, G. R., Imiquimod and resiquimod as novel immunomodulators. *J. Antimicrob. Chemother.* **2001,** *48* (6), 751-755.
185. Szeimies, R. M.; Bichel, J.; Ortonne, J. P.; Stockfleth, E.; Lee, J.; Meng, T. C., A phase II dose-ranging study of topical resiquimod to treat actinic keratosis. *Br. J. Dermatol.* **2008,** *159* (1), 205-210.
186. Boraschi, D.; Italiani, P., From Antigen Delivery System to Adjuvanticy: The Board Application of Nanoparticles in Vaccinology. *Vaccines* **2015,** *3* (4).
187. Kasturi, S. P.; Skountzou, I.; Albrecht, R. A.; Koutsonanos, D.; Hua, T.; Nakaya, H. I.; Ravindran, R.; Stewart, S.; Alam, M.; Kwissa, M.; Villinger, F.; Murthy, N.; Steel, J.; Jacob, J.; Hogan, R. J.; García-Sastre, A.; Compans, R.; Pulendran, B., Programming the magnitude and persistence of antibody responses with innate immunity. *Nature* **2011,** *470*, 543.
188. Ilyinskii, P. O.; Roy, C. J.; O'Neil, C. P.; Browning, E. A.; Pittet, L. A.; Altreuter, D. H.; Alexis, F.; Tonti, E.; Shi, J.; Basto, P. A.; Iannacone, M.; Radovic-Moreno, A. F.; Langer, R. S.; Farokhzad, O. C.; von Andrian, U. H.; Johnston, L. P. M.; Kishimoto, T. K., Adjuvant-carrying synthetic vaccine particles augment the immune response to encapsulated antigen and exhibit strong local immune activation without inducing systemic cytokine release. *Vaccine* **2014,** *32* (24), 2882-2895.
189. Tabatabaei Mirakabad, F. S.; Nejati-Koshki, K.; Akbarzadeh, A.; Yamchi, M. R.; Milani, M.; Zarghami, N.; Zeighamian, V.; Rahimzadeh, A.; Alimohammadi, S.; Hanifehpour, Y.; Joo, S. W., PLGA-Based Nanoparticles as Cancer Drug Delivery Systems. *Asian Pac. J. Cancer Prev.* **2014,** *15* (2), 517-535.
190. Mottas, I.; Bekdemir, A.; Cereghetti, A.; Spagnuolo, L.; Yang, Y.-S. S.; Müller, M.; Irvine, D. J.; Stellacci, F.; Bourquin, C., Amphiphilic nanoparticle delivery enhances the anticancer efficacy of a TLR7 ligand via local immune activation. *Biomaterials* **2019,** *190-191*, 111-120.
191. Lucke, M.; Mottas, I.; Herbst, T.; Hotz, C.; Römer, L.; Schierling, M.; Herold, H. M.; Slotta, U.; Spinetti, T.; Scheibel, T.; Winter, G.; Bourquin, C.; Engert, J., Engineered hybrid spider silk particles as delivery system for peptide vaccines. *Biomaterials* **2018,** *172*, 105-115.
192. Braun, K.; Pochert, A.; Beck, M.; Fiedler, R.; Gruber, J.; Lindén, M., Dissolution kinetics of mesoporous silica nanoparticles in different simulated body fluids. *J. Sol-Gel Sci. Technol.* **2016,** *79* (2), 319-327.
193. Chen, K.; Zhang, J.; Gu, H., Dissolution from inside: a unique degradation behaviour of core–shell magnetic mesoporous silica nanoparticles and the effect of polyethyleneimine coating. *J. Mater. Chem.* **2012,** *22* (41), 22005-22012.

CHAPTER 2

Characterization

2. Characterization

For the characterization of nanoparticles, many different techniques can be applied. First, to determine the particle size, dynamic light scattering (DLS) can be applied. Furthermore, transmission electron microscopy and scanning electron microscopy can be used to estimate the sizes of the sample, as well as shape and morphology of the particles and pores. To further investigate the porous structure and large surface area of the network, N_2-sorption measurements are conducted. As indirect methods to show that silica nanoparticles possess mesopores, used for loading with different cargoes, fluorescence spectroscopy or UV-Vis measurements can be consulted – depending on the fluorescence or absorbance of the particular guest molecule. Time-based release curves are recorded with fluorescence spectroscopy to prove the tight capping and stimuli-responsive release of the (model-) drugs. UV-Vis measurements are applied to investigate the catalytic performance of LP-MSN-Enzyme constructs by means of colorimetric activity assays. Furthermore, to monitor the different steps of functionalization, Fourier-Transform Infrared (FTIR) microscopy was applied to identify the diverse functional groups. Additionally, zeta potential measurements were conducted to evaluate changes in surface charge through incorporated organic moieties. Thermogravimetric analysis (TGA) was used to determine the relative amounts of organic functionalization of core-shell MSNs. To examine the degree of hydrolysis/functionalization and gain information about the chemical bonds, magic angle solid state nuclear magnetic resonance (MAS ssNMR) was applied.

2.1. Dynamic light scattering (DLS)

Dynamic Light Scattering (DLS) is used to determine the hydrodynamic diameter or rather the Stokes diameter of the nanoparticles. This can be deduced from the obtained diffusion coefficient of the measured particles if the solvent's viscosity is known. Dynamic light scattering is also called photon correlation spectroscopy (PCS) or quasi-elastic light scattering (QELS).[1]

The principle of DLS is based on the interaction between electromagnetic radiation and particles in a comparable size range. Since the applied laser's wavelength of 633 nm is in the range of visible light, the interference with nanoparticles is very good. Samples are measured in suspension. If the refractive index of the suspended sample differs from the one of the solvent, stray light is produced. Since the sample suspensions are always prepared under dilute conditions, there is a strong Brownian molecular motion of the particles. This motion leads to fluctuations of the scattered light intensity. Due to this movement of the individual scattering centers, a frequency shift occurs due to the Doppler Effect which can be monitored through the autocorrelation function. The fluctuation and the resulting shifts are dependent on the size of the particles. Larger particles show a slower Brownian motion in comparison to smaller ones. This velocity is defined as the translational diffusion coefficient D which is related to the hydrodynamic diameter d(H) of the particles *via* the Stokes-Einstein equation (equation 2.1).

$$d(H) = \frac{kT}{3\pi\eta D} \tag{2.1}$$

Stokes-Einstein equation. d(H): hydrodynamic particle diameter, D: translational diffusion coefficient, *k*: Boltzmann's constant, *T:* temperature, *η*: the viscosity of the suspending medium.[2]

The received diameter represents the diameter of a sphere with the determined translational diffusion coefficient. This coefficient is influenced by factors like ionic strength of the medium and nature of the particles' surface which can both lead to an untrue display of the diffusion speed. It should be noted that larger particles scatter light significantly more than small particles. This means that even small amounts of large particles or agglomerates can cause high scattering intensity. As a result, the method is only suitable for relatively monodisperse and uncontaminated (e.g. by dust), non-agglomerated samples. If all those considerations are taken into account, DLS is a very powerful and commonly used method to investigate the hydrodynamic size of particles between 1 and 1000 nm.

2.2. Zeta potential

To determine the outer surface charge of nanoparticles zeta potential measurements can be applied. Furthermore, the colloidal stability of the finely dispersed solid nanoparticles in solution can be assessed. Due to dissociation of surface groups or adsorption of solvent molecules, particles are usually (slightly) charged in aqueous solution. This net charge leads to a surrounding of oppositely charged solvent molecules creating an electrostatic potential between the two phases. One distinguishes between a layer of tightly bound counter ions (Figure 2-1: positively charged, shown in red), called Stern layer, and a layer with loosely bound counter charges (Slipping plane). The ordered layers are so closely connected to the surrounded particle that they follow its Brownian movement. The rest of the very disordered surrounding ions remains at the same place in the bulk solvent. The potential at the boundary

distinguishing between those tight layers and the rest of the solvent molecules is called zeta-potential (also described with the Greek letter ζ).[3]

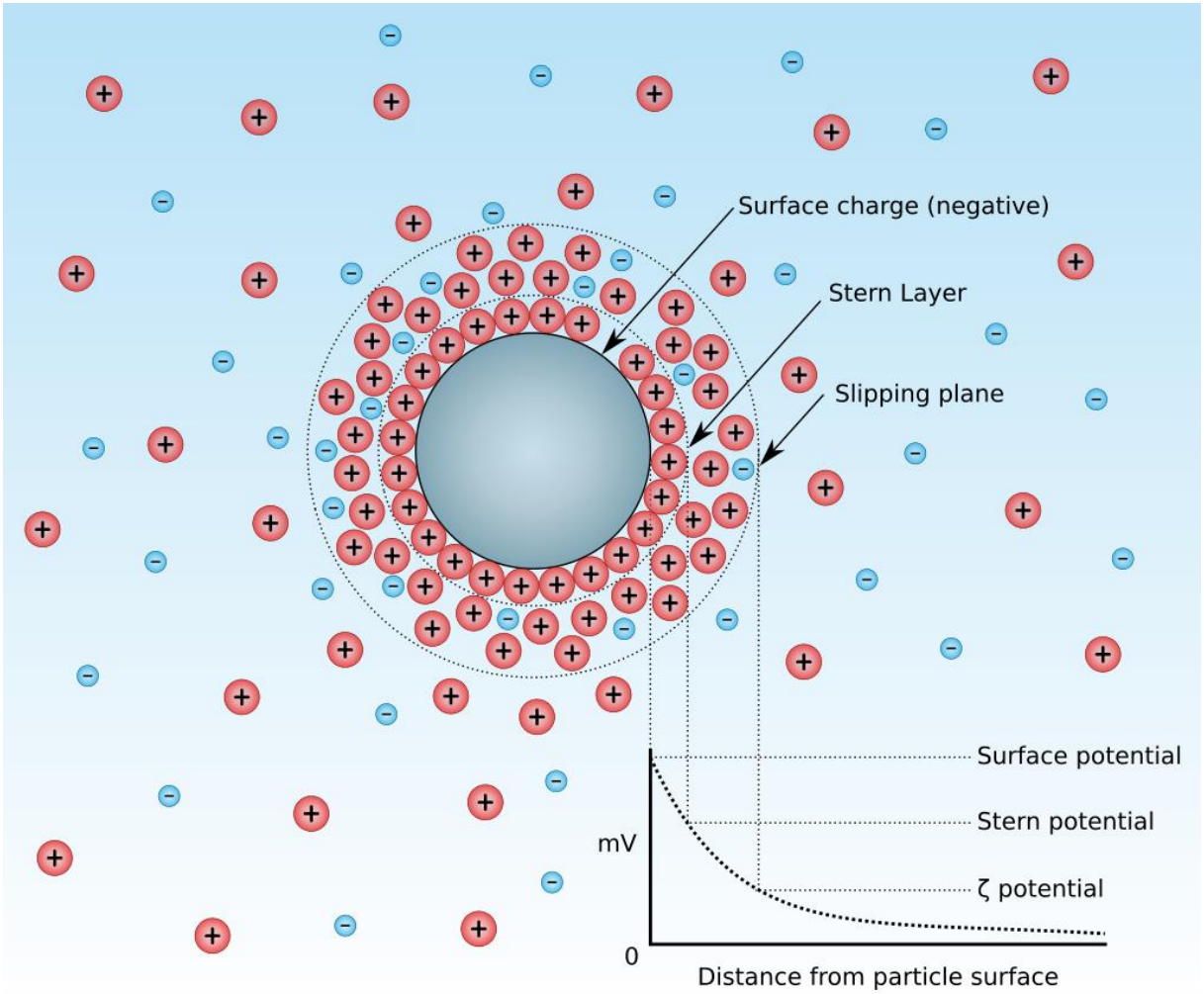

Figure 2-1: Schematic representation of a negatively charged particle surrounded by positively charged solvent ions and the description of the resulting layers.[4]

The existence of the electrical potential allows interactions with an applied external electric field. Depending on the induced direction of motion, one distinguishes four main electrokinetic effects: electrophoresis, electroosmosis, streaming potential and sedimentation potential. While the latter arises by the sedimentation of charged particles, a streaming potential is generated by letting a liquid stream by a charged surface. Electroosmosis describes the motion of a liquid induced through an applied electric field relative to a

stationary charged surface. The zeta potential can be related to the electrophoretic mobility (U_E). This is measured in electrophoresis by applying an electric field and monitoring the velocity of the charged particle to the electrode of opposite charge relative to the medium. The speed of movement depends on the dielectric constant (ε), the viscosity (η) of the medium, the strength of the applied field and the zeta potential itself. The relation between these dimensions is given by the Henry equation:

$$U_E = \frac{2\,\varepsilon\,\zeta\,f(\kappa a)}{3\,\eta} \tag{2.2}$$

Henry equation: U_E, electrophoretic mobility; ε, dielectric constant of the medium; η, viscosity of the medium; ζ, zeta potential; f (κa) Henry function with κ Debye length and a particle radius.

The Debye length κ in the Henry function describes the size of the electrical double layer. The Henry function can be approximated to 1.5 with the Smoluchowski model – suited for particles larger than 200 nm and a polar medium – or to 1.0 with the Hückel approximation for small particles in a non-polar medium.

2.3. Nitrogen sorption

Gas adsorption measurements are widely used for different porous materials to obtain their respective surface area and pore size distributions.[5] Nitrogen is commonly applied as adsorptive at 77 K and is especially recommended for mesoporous samples.[5-6] Due to the only weak *van-der-Waals* interactions between the adsorbent and adsorptive, the process is classified as physisorption. Conventionally, certain amounts of nitrogen are successively introduced into the system, which is then allowed to reach an equilibrium state. By plotting the applied nitrogen amounts (calculated in volume) versus the monitored equilibrium relative pressures, one obtains isotherms. In Figure 2-2 the extended overview of different isotherm types classified by the IUPAC is shown.[7]

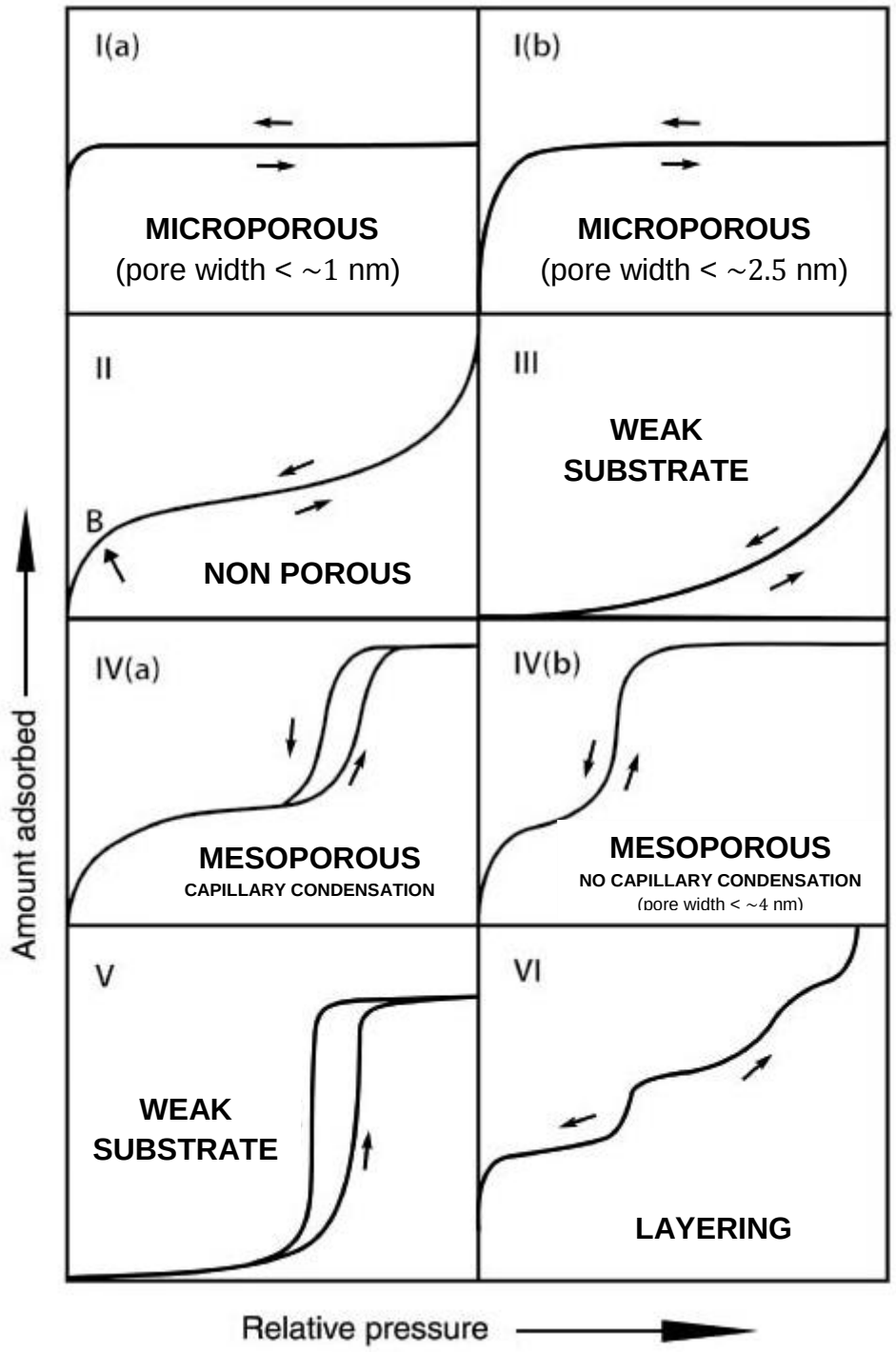

Figure 2-2: Different isotherm types classified by the IUPAC. Adapted from Thommes et al., IUPAC Technical Report, 2015, © IUPAC.[7]

The division of the isotherms is made with regard to the material's pore size and structure as well as its interactions with the adsorptive. During the desorption process hysteresis can occur. This is the case when more energy is needed to remove the gaseous adsorptive from the

solid adsorbent. It can occur due to network or pore blocking effects in pores wider than 4 nm. For the physisorption in mesoporous materials three different stages can be classified: (i) Formation of a monolayer of adsorbed nitrogen molecules which all have contact to the surface of the adsorbent, (ii) multilayer adsorption on top of monolayers, (iii) capillary condensation.[7] The most common model to describe isotherms under consideration of multilayer adsorption is the Brunauer-Emmet-Teller-, short BET-model.[8] Though it extends the Langmuir theory from monolayer to multilayer adsorption, it still remains a very simplified model. Nevertheless, it is still the most commonly one to calculate the specific surface area from the gained measurement data. For this, the monolayer capacity n_m has to be derived from a 'BET plot' following the BET equation:

$$\frac{p/p^0}{n(1-p/p^0)} = \frac{1}{n_m C} + \frac{C-1}{n_m C}(p/p^0) \tag{2.3}$$

BET equation. n: specific amount adsorbed at relative pressure p/p^0; n_m: specific monolayer capacity; C: BET constant.[7-8]

The gained value of the monolayer capacity can then be used to calculate the 'BET area'. For this, the average area of each adsorbed nitrogen molecule in a close-packed monolayer at 77 K is usually assumed to be $a_m(N_2) = 0.162$ nm^2.

$$A(BET) = n_m^a \cdot L \cdot a_m \tag{2.4}$$

Calculation of BET area with n_m^a monolayer capacity, L Avogadro constant and a_m average area occupied by adsorptive molecule.[5]

To assess mesoporosity and the pore size distribution, the phenomena capillary condensation, the third step of physisorption in mesopores, is monitored. Here, a transition from liquid to vapour phase occurs in the confined space of the capillary leading to a pore filling by immediate meniscus formation. In former days the Kelvin equation has been used to determine the pore radius. This simple model has been further developed to consider the

multilayer film formation. The modified equation is used by many models, the most used one is the mesopore size analysis of Barret, Joyner and Halenda (BJH).[9]

$$\ln(p/p^0) = -\frac{2\gamma V_m}{RT(r_p - t_c)} \tag{2.5}$$

Modified Kelvin equation for cylindrical pores. p/p^0: relative pressure , γ: surface tension, V_m: molar liquid volume, R: gas constant, T: temperature, r_p: pore radius, t_c: thickness of adsorbed multilayer film.[7]

Due to the assumptions made in the BJH model like control of meniscus curvature by rigid cylindrical pores, homogenous film formation, and no consideration of vapour-liquid and liquid-liquid interactions, medium pore sizes are often significantly underestimated. To avoid these limitations, more advanced methods like Monte Carlo and DFT simulations have evolved. They can describe the behaviour of fluids in confined pores at a molecular level with the help of statistical mechanics. Non-local density functional theory (NLDFT) based methods give reasonably realistic results for several pore shapes and different adsorptive/adsorbent pairs.

2.4. Thermogravimetric Analysis (TGA)

Thermogravimetry (TG) or Thermogravimetric Analysis (TGA) determines the mass change of a sample as a function of temperature or time.[10] These changes may be caused by thermal decomposition or combustion, as well as a chemical reactions or the like. In a thermobalance, the measurement of the mass of a sample crucible takes place simultaneously with that of a reference. This provides several signals during the heating process. In addition to the normal TGA signal, the mass change, information on temperature change (differential thermal analysis (DTA)) and heat change (differential scanning calorimetry DSC) are also obtained. This allows conclusions about the thermal stability of the sample as well as relative amounts of incorporated organic moieties.

2.5. Molecular Spectroscopy

Spectroscopy describes several analytical methods which study the interaction of electromagnetic radiation with matter.[11-12] From the resulting spectra, important information about molecular structure and chemical characteristics can be derived. Methods like ultraviolet-visible- (UV-Vis-), infrared- (IR-) and Raman, as well as fluorescence and nuclear magnetic resonance (NMR) spectroscopy all belong to the methods of molecular spectroscopy and are introduced in the following.

Electromagnetic radiation is characterized by its wavenumber λ or rather its frequency ν, which are related through the velocity of light constant c:

$$\nu \cdot \lambda = c \tag{2.6}$$

A light quantum, a photon, possesses the following energy with h representing the Planck's constant:

$$E = h \cdot \nu \tag{2.7}$$

Molecules can absorb light with appropriate frequency and are thus excited to higher energy levels. Succeeding spontaneous or stimulated emission brings the molecule back to its former (usually ground) energy level.

Interaction between electromagnetic radiation and matter leads to different energy absorption and emission processes, depending on the radiation's frequency. The complete electromagnetic spectrum is shown in Figure 2-3.

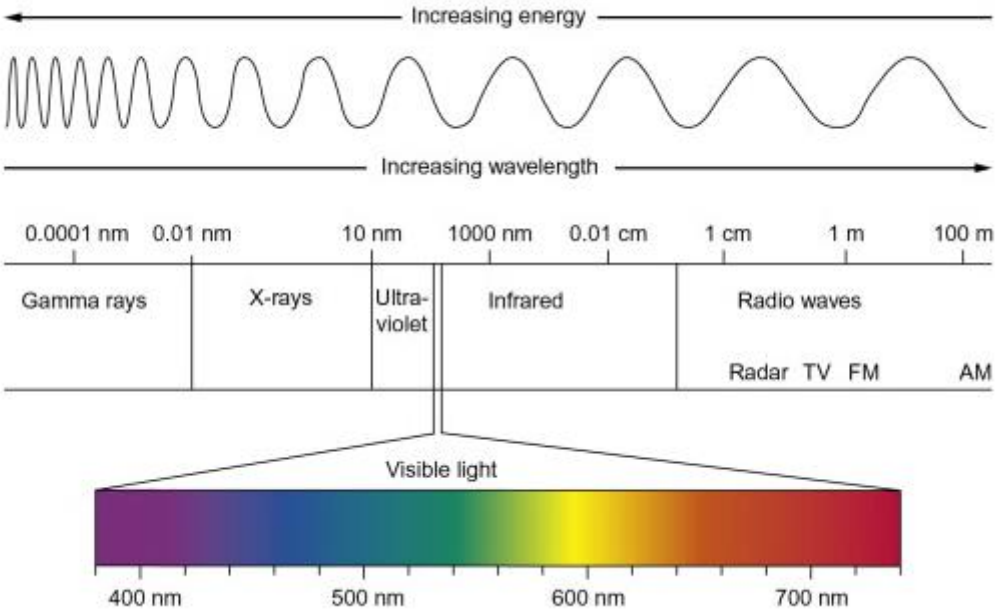

Figure 2-3: Overview of the complete electromagnetic spectrum.[13]

Methods using light in the ultra-violet, visible, infrared or radio wave region are discussed in the following.

2.5.1. UV-Vis Spectroscopy

The role of UV-Vis spectroscopy or rather spectrophotometry is important in qualitative and quantitative drug analysis, and it is commonly used in trace analysis, for example to determine the alcohol level in the blood.[14-15] Here, a sample usually in suspension is irradiated by UV or visible light. By absorption of electromagnetic radiation in this range electrons, generally valence electrons in the outer orbitals of the molecules, are excited to higher distinct energy levels. These observed absorption bands show a distinct position, intensity, from and fine structure and are associated with defined transitions. Due to the fact that they are commonly accompanied by rotational and vibrational transitions, the arising lines in the spectrum are commonly broadened and the fine structure overlayed. The measured absorption is defined by the following law, introduced by Bouguer, Lambert and Beer:

$$A = log\frac{I_0}{I} = \varepsilon \cdot c \cdot d \qquad \textbf{(2.8)}$$

Law of Bouguer, Lambert and Beer.

Here, dimensionless absorption A, also called absorbance or extinction, is defined through the ratio between intensity of incident beam I_0 and emergent one I. d describes the path length of the sample cell, c the applied concentration of the sample solutions and ε the molar absorption coefficient. The law can be applied for diluted solutions under the use of a monochromatic light source.[14]

2.5.2. IR- and Raman Spectroscopy

The complementary techniques mid-infrared (IR) and Raman spectroscopy belong both to the vibrational spectroscopy and are used to elucidate molecular structures.[16] In the field of infrared radiation, molecular vibrations and rotations are excited. These can be measured either directly as absorption in an IR spectrum or indirectly as scattered radiation in a Raman spectrum.

The IR region is differentiated between the near, middle and far infrared (NIR, MIR, FIR).[17] In the mid-infrared (MIR) region the absorption of vibrations by covalently bound molecules as well as certain group frequencies of functional, organic groups can be detected, which makes IR spectroscopy a powerful analytical method. The common range of an IR spectrum lays between 4000 and 400 cm^{-1}. A molecule vibration is IR-active if the molecule's dipole moment changes during the vibration.

To be capable to absorb the energy of incident radiation, the resonance condition has to be fulfilled. This means the energy between two distinct vibrational states, given through the quantum mechanical conditions, has to correspond to the energy of the incident photon. This energy absorption process leads to a change in vibrational energy level which results in a characteristic absorption spectrum. Successive Fourier transformation of the gained interferogram gives rise to a characteristic wavenumber-dependent spectrum with information about molecular structure and dynamics.

Whereas IR spectroscopy involves transitions between different vibrational states, Raman spectroscopy consists of a two-photon dependent scattering process.[16] Here, the sample is irradiated with monochromatic light. Subsequent, different scattering processes can be observed. The main part is comprised of elastic Rayleigh scattering and a small part shows inelastic Raman scattering. The latter can be further divided into Stokes- and Anti-Stokes

scattering, depending on the previous state of the excited molecule (if it has been in the ground state or an excited vibrational state before). The different two-photon processes are depicted in Figure 2-4. The Boltzmann distribution describes that a higher number of molecules is present in the ground state under ambient conditions. Therefore, the intensity of the Stokes lines is significantly higher than that of the Anti-Stokes Scattering.

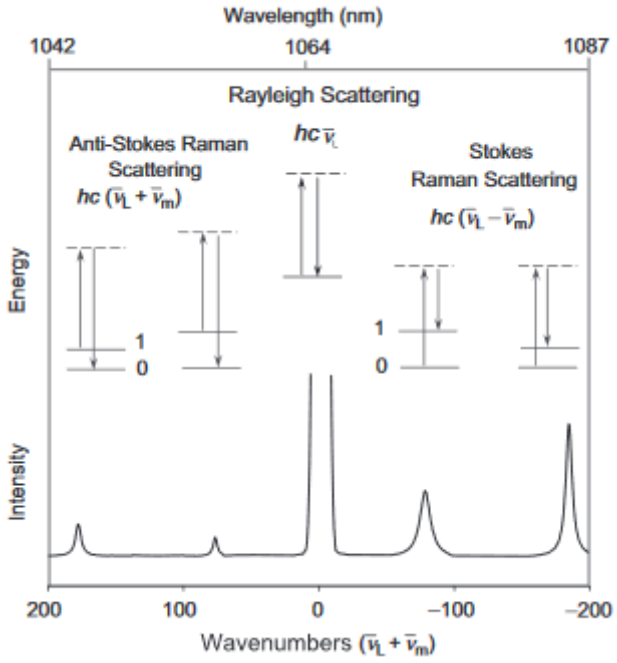

Figure 2-4: Schematic representation of elastic Rayleigh and inelastic (Anti-) Stokes Raman Scattering. The corresponding shifts in frequency relative to the laser frequency ν_L are respectively shown.[16]

A molecule is Raman active if an external electric field can deform the electron cloud surrounding the molecule, meaning to induce a change of molecular polarizability α. The respective shifts in frequency observed as Anti-Stokes or Stokes shifts are characteristic for each molecule and can give information about the molecular structure.

For molecules with a symmetry center the so-called mutual exclusion rule is valid meaning vibrations are IR-active but Raman-inactive and *vice versa*. It has to be noted that vibrations can also be inactive in both methods. If the symmetry center is missing, each vibration has to be assessed on its own whether it is IR and or Raman active.

2.5.3. Fluorescence Spectroscopy

Fluorescence spectroscopy represents a powerful and very sensitive tool in biochemical, biophysical and biomedical fields.[18] Luminescence describes the emission of light from electronically excited states of a material. It can be formally divided into two categories: fluorescence and phosphorescence. Upon light absorption, a fluorophore is excited to higher vibrational energy levels, commonly of the multiplicity S_1 or S_2. This uptake is followed by rapid vibrational relaxation to the lowest of the S_1 energy levels. From here a fast, spin-allowed emission back to the ground state *via* fluorescence can occur. Phosphorescence, on the other hand, describes the spin-forbidden and therefore slow emission of light following intersystem crossing from an excited triplet state. Here, average lifetimes of milliseconds to seconds can be observed. The distinction between fluorescence and phosphorescence can be seen in a Jablonski diagram shown in Figure 2-5.

As observed in the Jablonski diagram, the energy of emission through fluorescence is always smaller than the absorbed one. This energy loss between excitation and emission is called the Stokes shift and is caused through several effects like the mentioned vibrational relaxation as well as solvent, complexation or energy transfer effects.[14, 18]

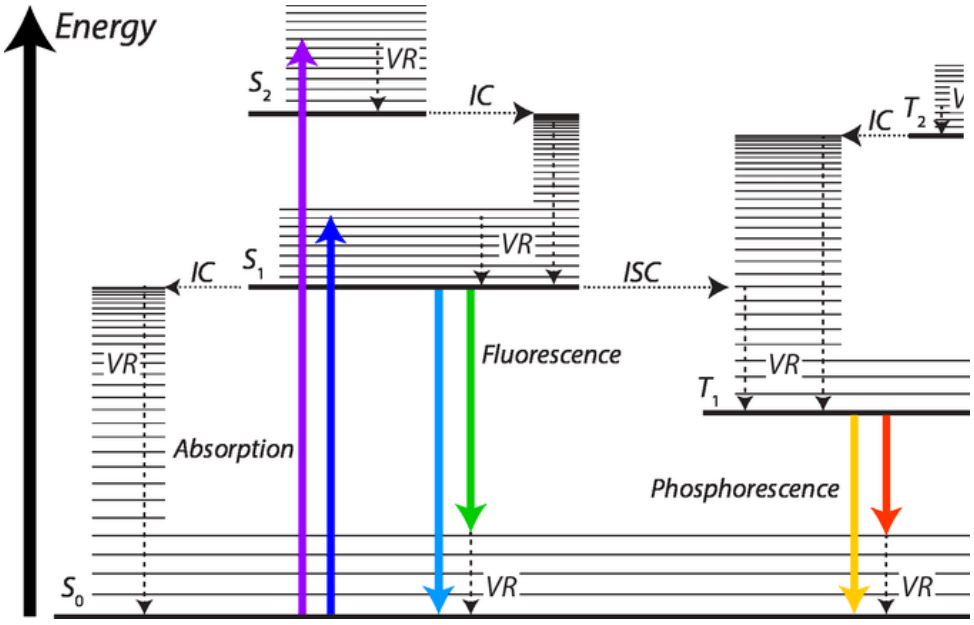

Figure 2-5: Jablonski diagram. Vertical lines represent singlet (S_n) and triplet (T_n) states. VR: vibrational relaxation, IC: internal conversion, ISC: intersystem crossing.[19]

The structure of a fluorescence spectrometer consists of a radiation source such as a xenon lamp (which has a high intensity in the wavelength range used), monochromators, the sample space and subsequent photomultiplier detectors. Finally, the data are converted into a spectrum by means of software. Besides excitation and emission spectra, time-based fluorescence measurements can be conducted.

2.5.4. Nuclear Magnetic Resonance Spectroscopy

Nuclear magnetic resonance (NMR) spectroscopy is a very sensitive method to elucidate chemical structures of organic molecules. To enable the use of NMR measurements, the respective nuclei must have a magnetic dipole moment $\mu \neq 0$.[14, 20]

This magnetic moment is defined as the product of the nuclear spin and the magnetogyric ratio γ. The latter is an empirical constant, specific for each kind of nuclei, which describes in part the isotope's sensitivity towards NMR spectroscopy.[20] By applying an external magnetic field the degenerated energy levels of the nucleus are split. Due to the thermal Boltzmann

distribution, very strong magnetic fields have to be used to generate a significant difference in spin state population. The energy difference between the states directly correlates with the strength of the magnetic field. Irradiating the sample with electromagnetic radiation in the radio wave region leads to an energy absorption connected with a successive transition to the spin state with higher energy. The following relaxation occurs either as spin-lattice or spin-spin relaxation. The first process occurs *via* energy transfer to the surrounding medium in form of heat within the longitudinal relaxation time T_1 and leads to relaxation from the high energy level to the low energy level. In addition, the transversal relaxation time T_2 describes the time period of the transversal magnetization's relaxation induced by perturbation through other spinning particles and their magnetic fields. Neighbour molecules as well as corresponding electron densities have an impact of the resonance frequency as well as the energy transfer and relaxation behaviour of the respective nuclei. Monitoring these processes allows great insight into the chemical molecular structure.

Conducting the NMR experiments with liquids allows dipole-dipole interactions and quadrupole effects to be averaged out due to the mobility of the nuclei. In the solid state they can cause severe line broadening. In addition, anisotropic effects enhance the broadening of the lines in solids as well as they lead to a more complex line structure. Additionally, spin-lattice relaxation times of nuclei like ^{13}C are extremely long. To avoid these effects in solid-state NMR, the Magic Angle Spinning (MAS) method can be applied. Here the sample is rotated with high velocity in the magic angle of 54.736° relative to the magnetic field, which avoids the above mentioned line broadening effects. To circumvent the long relaxation times cross polarization (CP) can be applied. Here, a polarisation transfer from the surrounding protons to the ^{13}C nucleus takes place, which shortens the relaxation times dramatically and enhances the ^{13}C signal.

2.6. Electron Microscopy

Electron microscopy is one of the most powerful methods to investigate and depict nanometer sized objects. By use of charged particles (electrons) one can achieve a 1000 fold higher resolution limit in comparison to standard light microscopes. Electron microscopy is a very general description and can be divided into four big subgroups. They are distinguished by their combination of the two different measurement modes, namely scanning- or static image, with the two different detection modes (reflection and transmission). The four resulting combinations are called transmission electron microscopy (TEM), reflection electron microscopy (REM), scanning electron microscopy (SEM) and scanning transmission electron microscopy (STEM). All of them except for REM are applied in practical work. The three main parts of an electron microscope are the electron source, the electromagnetic lenses (in this case especially the objective is crucial for the performance of the instrument) and a detecting and computing system for the resulting images.[21]

2.6.1. Scanning Electron Microscopy (SEM)

SEM is especially used for the investigation of (rough) surfaces and their topographies. It can depict various surfaces of massive samples immediately with depth of sharpness if the samples are stable in the high vacuum and electroconductive. The latter can be overcome for nonconductive samples by coating them. For measurements highly accelerated electrons are focussed *via* lenses onto the samples and the resulting interactions monitored. Besides backscattered electrons, which possess almost the same energy as the incident beam, secondary electrons can be recorded. These secondary electrons possess a much smaller energy than the incident ones and are recorded with a different detector. Other products of the interactions between the incident electron beam and the sample are X-rays, Bremsstrahlung and so called Auger electrons. Due to those interactions, the whole scanning electron

microscope has to be under vacuum, to enable free movement of the charged particles. As shown in Figure 2-6 the electron beam is focussed with different lenses onto the sample. Scanning coils are responsible to guide the beam to scan the sample line by line.[21-22]

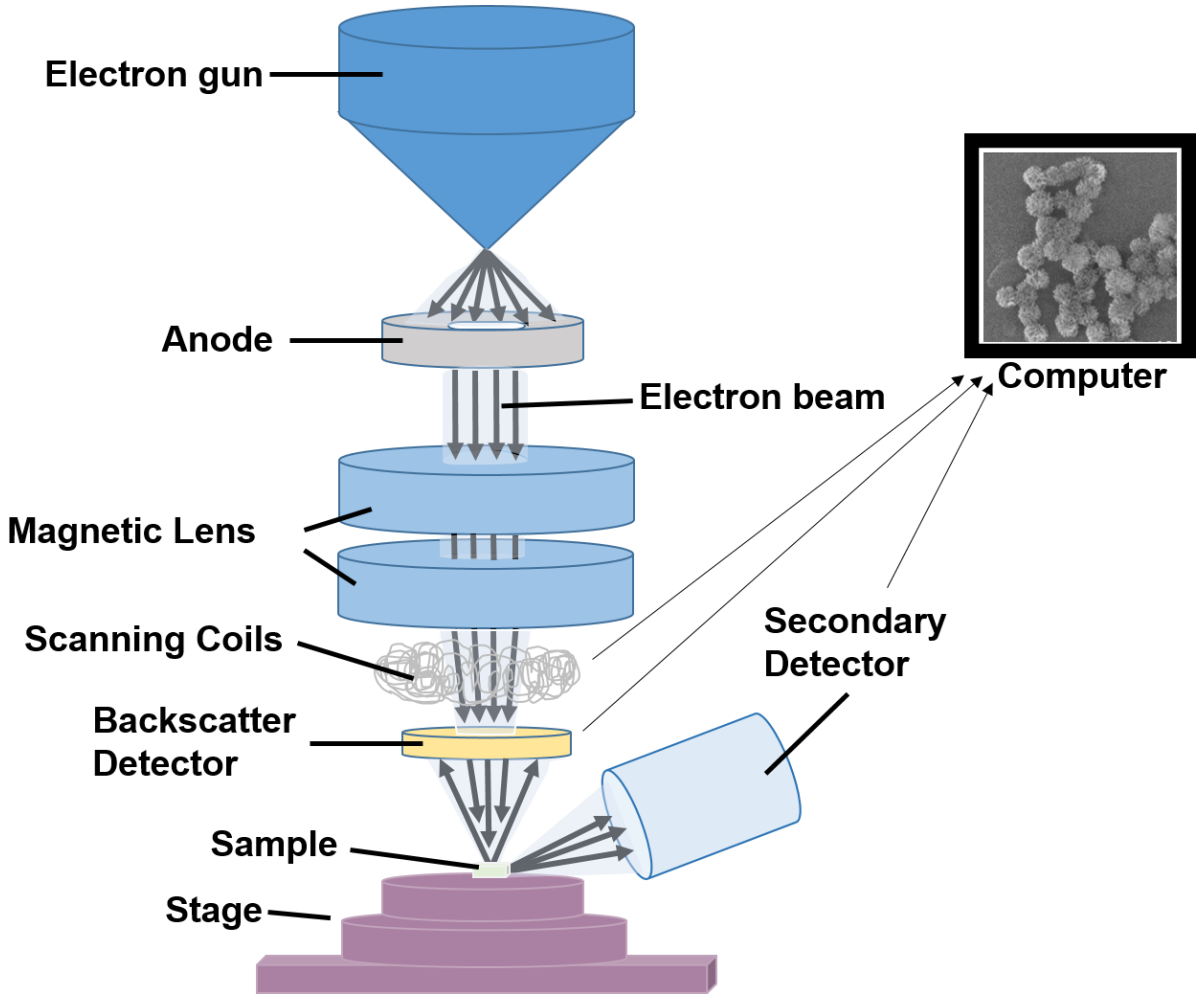

Figure 2-6: Schematic setup of a Scanning Electron Microscope.

2.6.2. Transmission Electron Microscopy (TEM)

The resolution limit of TEM is tenfold higher than the one of SEM. The main field of application is the investigation of very thin metal foils as well as biological thin sections. While SEM follows originally more the concept of a television set, TEM originates rather from a common light microscope. In comparison to SEM with its scanning mode and resulting raster image, a fixed beam is used in transmission electron microscopy leading to a

static image. Furthermore, not the reflected but the transmitted electrons are being detected. To this, a relatively big part of the sample is illuminated with the help of condenser lenses and a magnified image of the sample's refraction pattern is recorded with an optical system underneath the sample holder. In TEM measurements, acceleration voltages between 100 and 400 kV are being used, whereas in SEM only 10 to 40 kV.

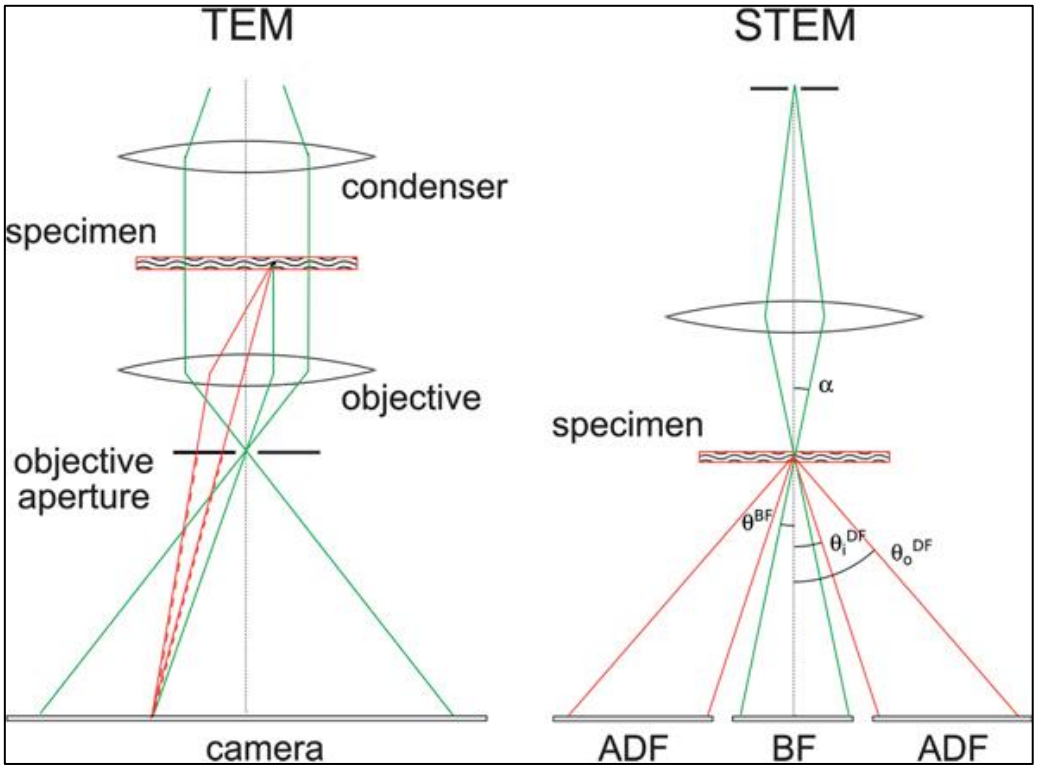

Figure 2-7: Schematic setup of TEM and STEM. Elbaum, M.; Wolf, S. G.; Houben, L., Cryo-scanning transmission electron tomography of biological cells. *MRS Bull.* **2016,** *41* (7), 542-548, reproduced with permission.[23]

2.6.3. Scanning Transmission Electron Microscopy (STEM)

This electron microscopy technique combines the scanning of a sample in a high-vacuum apparatus with the detection of transmitted electrons *via* various detectors. The array of the detectors can be seen Figure 2-7. ADF stands for annular dark field detector and collects only the scattered electrons with a ring shaped detector, whereas the bright field detector BF records not or only very little scattered electrons.[22]

2.7. References

1. Pecora, R., Dynamic light scattering measurement of nanometer particles in liquids. *J. Nanopart. Res.* **2000,** *2* (2), 123-131.
2. Malvern, Dynamic Light Scattering: An Introduction in 30 Minutes. Malvern: DLS technical note.
3. Malvern, Zeta potential: An Introduction in 30 Minutes. Malvern: Technical note.
4. Larryisgood; Mjones1984 Diagram of zeta potential and slipping plane. https://commons.wikimedia.org/wiki/File:Diagram_of_zeta_potential_and_slipping_planeV2.svg (accessed Wed. 13 March 2019).
5. Rouquerol, J.; Avnir, D.; Fairbridge, C. W.; Everett, D. H.; Haynes, J. H.; Pernicone, N.; Ramsay, J. D. F.; Sing, K. S. W.; Unger, K. K., Recommendations for the characterization of porous solids (Technical Report). *Pure Appl. Chem.* **1994,** *66* (8), 1739-1758.
6. Sing, K., The use of nitrogen adsorption for the characterisation of porous materials. *Colloids Surf., A* **2001,** *187-188*, 3-9.
7. Thommes, M.; Kaneko, K.; Neimark, A. V.; Olivier, J. P.; Rodriguez-Reinoso, F.; Rouquerol, J.; Sing, K. S. W., Physisorption of gases, with special reference to the evaluation of surface area and pore size distribution (IUPAC Technical Report). *Pure Appl. Chem.* **2015,** *87* (9-10).
8. Brunauer, S.; Emmett, P. H.; Teller, E., Adsorption of Gases in Multimolecular Layers. *J. Am. Chem. Soc.* **1938,** *60* (2), 309-319.
9. Barrett, E. P.; Joyner, L. G.; Halenda, P. P., The Determination of Pore Volume and Area Distributions in Porous Substances. I. Computations from Nitrogen Isotherms. *J. Am. Chem. Soc.* **1951,** *73* (1), 373-380.
10. Ehrenstein, G. W.; Riedel, G.; Trawiel, P., *Praxis Der Thermischen Analyse von Kunststoffen*. Carl Hanser Verlag: München, 2003.
11. Molekülspektroskopie. In *Instrumentelle Analytik und Bioanalytik*, 2008; pp 211-290.
12. Sindhu, P. S., *Fundamentals of Molecular Spectroscopy*. New Age International (P) Limited, Publishers: Delhi, 2006.
13. Vallero, D. A.; Letcher, T. M., Chapter 12 - Radiation. In *Unraveling Environmental Disasters*, Vallero, D. A.; Letcher, T. M., Eds. Elsevier: Boston, 2013; pp 299-320.
14. Hesse, M.; Meier, H.; Zeeh, B., *Spektroskopische Methoden in der organischen Chemie*. Seventh ed.; Thieme: Stuttgart, 2005.
15. Gorog, S., *Ultraviolet-Visible Spectrophotometry in Pharmaceutical Analysis*. CRC Press: 2017.
16. Larkin, P., *Infrared and Raman Spectroscopy - Principles and Spectral Interpretation*. Elsevier: San Diego, 2011.
17. Colthup, N. B.; Wiberley, S. E.; Daly, L. H., *Introduction to Infrared and Raman Spectroscopy*. Second ed.; Academic Press: New York, 1975.
18. *Principles of Fluorescence Spectroscopy*. Springer: Boston, 2006.
19. Dzebo, D. Photon Upconversion through Triplet-Triplet Annihilation: Towards Higher Efficiency and Solid State Applications. 2016.
20. Cavanagh, J.; Fairbrother, W. J.; Arthur G. Palmer, I.; Rance, M.; Skelton, N. J., *Protein NMR Spectroscopy - Principles and Practice*. Elsevier: Burlington San Diego, 2007.
21. Colliex, C.; Kohl, H., *Elektronenmikroskopie: eine anwendungsbezogene Einführung*. Wiss. Verlag-Ges.: Stuttgart, 2008.
22. Reimer, L.; Pfefferkorn, G., *Raster-Elektronenmikroskopie*. Second ed.; Berlin Heidelberg 1977.
23. Elbaum, M.; Wolf, S. G.; Houben, L., Cryo-scanning transmission electron tomography of biological cells. *MRS Bull.* **2016,** *41* (7), 542-548.

CHAPTER 3

Immune response to functionalized mesoporous silica nanoparticles for targeted drug delivery

The following results have been achieved in a cooperation: Simon Heidegger, Alexandra Schmidt, Thomas Bein and Carole Bourquin designed the concept of the project and interpreted the results. Dorothée Gößl and Stefan Niedermayer designed, synthesized and characterized the mesoporous silica nanoparticles. Simon Heidegger performed and analyzed the *in vitro* experiments with primary cells. Stefan Endres and Christian Argyo gave methodological support and advice. The study was guided by Thomas Bein and Carole Bourquin and is the groundwork for the experiments described in Chapter 4.

3. Immune response to functionalized mesoporous silica nanoparticles for targeted drug delivery

This chapter was published as:

Simon Heidegger, Dorothée Gößl, Alexandra Schmidt, Stefan Niedermayer, Christian Argyo, Stefan Endres, Thomas Bein, Carole Bourquin, *Nanoscale* **2016**, *8*, 938–948. Reproduced with permission from The Royal Society of Chemistry.

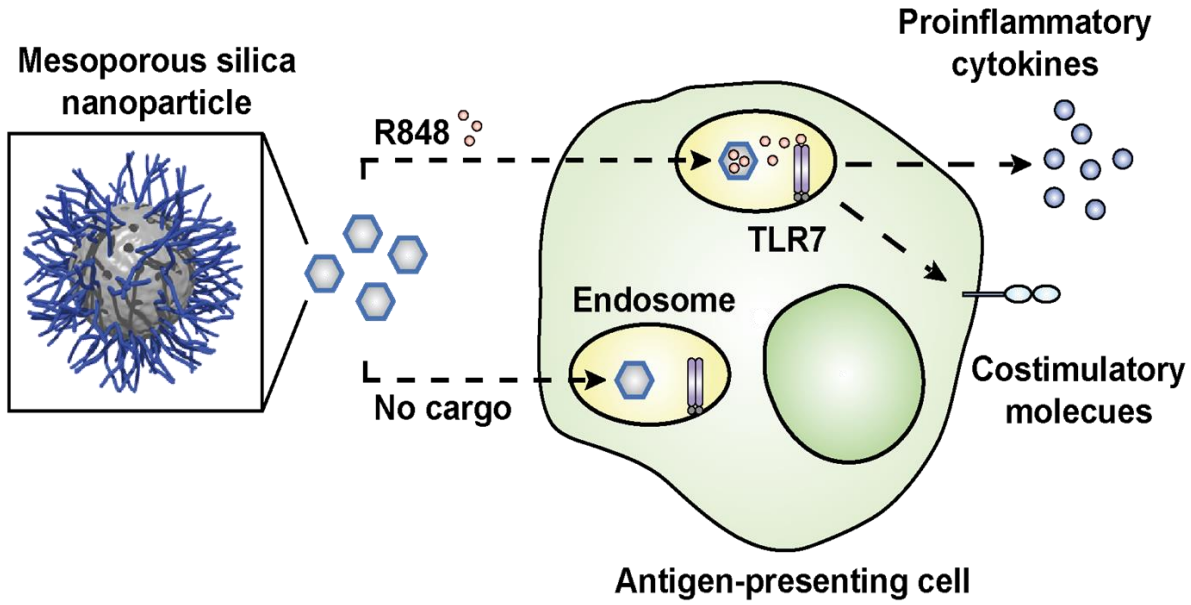

Abstract

Multifunctional mesoporous silica nanoparticles (MSN) have attracted substantial attention with regard to their high potential for targeted drug delivery. For future clinical applications it is crucial to address safety concerns and understand the potential immunotoxicity of these nanoparticles. In this study, we assess the biocompatibility and functionality of multifunctional MSN in freshly isolated, primary murine immune cells. We show that the functionalized silica nanoparticles are rapidly and efficiently taken up into the endosomal compartment by specialized antigen-presenting cells such as dendritic cells. The silica nanoparticles showed a favorable toxicity profile and did not affect the viability of primary immune cells from the spleen in relevant concentrations. Cargo-free MSN induced only very low immune responses in primary cells as determined by surface expression of activation markers and release of pro-inflammatory cytokines such as Interleukin-6, -12 and -1β. In contrast, when surface-functionalized MSN with a pH-responsive polymer capping were loaded with an immune-activating drug, the synthetic Toll-like receptor 7 agonist R848, a strong immune response was provoked. We thus demonstrate that MSN represent an efficient drug delivery vehicle to primary immune cells that is both non-toxic and non-inflammagenic, which is a prerequisite for the use of these particles in biomedical applications.

3.1. Introduction

In biomedical research applications, rationally designed nanoparticles are engineered for targeted delivery of various drugs or vaccines.[1] With spatio-temporally controlled release of their therapeutic cargo, such nanoparticles have the potential to increase drug efficacy while minimizing undesired off-target effects. However, due to their nanoscale size, chemical composition and surface reactivity, nanoparticles can be potentially detected by and interact with the host immune response.[2] While in certain applications (e.g. vaccine delivery) an immunostimulatory function may be desirable,[3] uncontrolled systemic immune activation will limit their therapeutic use. Thus, the profound understanding of a nanomaterial's interaction with the immune system and its possible stimulatory and suppressive actions are a critical prerequisite for any clinical application.

Specialized antigen-presenting cells (APC) of the innate immune system, such as dendritic cells (DC), constantly sample their surroundings, taking up cell debris and foreign materials. These cells are equipped with a variety of pattern-recognition receptors that allow for the detection of invading pathogens or signs of cell stress and damage. Ligation of these receptors results in maturation of APCs associated with expression of costimulatory molecules (such as CD80 and CD86), the release of proinflammatory cytokines and eventually the initiation of a subsequent adaptive immune response.[4] DCs have been shown to efficiently engulf various kinds of nanoparticles both in vitro and in vivo,[5, 6] but the consequences with regard to subsequent immune responses remain poorly understood.

Previous work of some of us has been focused on the development of core-shell colloidal mesoporous silica nanoparticles.[7, 8] Due to their different molecular functionalization in the core and the shell, the MSN can be equipped with internal functionality for controlled host-

guest interactions, a system for accurate cargo release upon external stimuli, as well as targeting ligands towards the required type of cell. A broad variety of different triggered-release capping systems were presented in the past years, based on external stimuli,[9-11] or triggered by intracellular events.[12-14] We recently reported a multifunctional system based on a pH-responsive polymer (poly(2-vinylpyridine), MSN-PVP) that allows for the facile delivery of membrane-permeable cargos into cancer cells.[15] With the possibility to integrate almost any functionality of interest, as well as the efficient synthesis, this system holds promise for wide-ranging biological and medical applications. In general, the special properties of MSN have been successfully implemented for experimental targeted anti-cancer therapies and vaccines.[16, 17] Thereby, MSN-based adjuvants have been shown to elicit potent anti-tumor and anti-microbial immune responses.[18, 19] A recent report demonstrated that injectable mesoporous silica rods can form macroporous structures that provide a cellular microenvironment for host immune cells *in vivo*, thus modulating their function and increasing vaccine efficacy.[20]

In this study, we investigate the immune-modulatory properties of MSN in primary murine splenocytes. We show that MSN themselves provoke only a marginal immune response but when loaded with a synthetic immune activator can function as an efficient delivery tool for potent immune activation.

3.2. Results

MSN particle characteristics

As reported previously,[15] the template-free MSN-NH_2 show a wormlike pore structure with an average pore size of 3.8 nm and feature a large surface area (1097 m^2/g) which is typical for MSN (Figure 3-1and Table 3-1).

Table 3-1 Key features of pH-responsive MSN-PVP

Sample	Particle size[a] [nm]	BET surface area [m^2/g]	Pore size[b] [nm]	Relative mass loss[c] [%]
MSN-NH_2	160	1097	3.8	15
MSN-PVP	550	617	3.4	62

[a] Particle size refers to the peak value derived from dynamic light scattering (DLS). [b] Non-linear density functional theory (NLDFT) pore size refers to the peak value of the pore size distribution. [c] Relative mass loss obtained by thermogravimetric analysis (TGA). All curves were normalized to 150 °C.[15]

The covalent modification of MSN-NH_2 with a boc-protected poly(2-vinylpyridine) and the following de-protection was monitored with several characterization methods; the accessible pore size as determined by nitrogen sorption measurements is barely affected by the surface modification with the pH-responsive polymer, whereas the decrease of the specific surface area is relatively large. This can be explained by the addition of non-porous polymer to the outer surface and the blocking of some pores by frozen polymer on the surface layer of the MSN. Dynamic light scattering (DLS) measurements in aqueous media revealed an average particle size of 160 nm for MSN-NH_2 and 550 nm for MSN-PVP. The polymer-modified sample shows some aggregation behaviour in water due to the hydrophobicity at pH 7, indicated by the apparent size increase to 550 nm. However, transmission electron

microscopy (TEM) revealed that the polymer-functionalized sample MSN-PVP still features a narrow particle size distribution, which makes them excellent candidates as drug delivery vehicles.

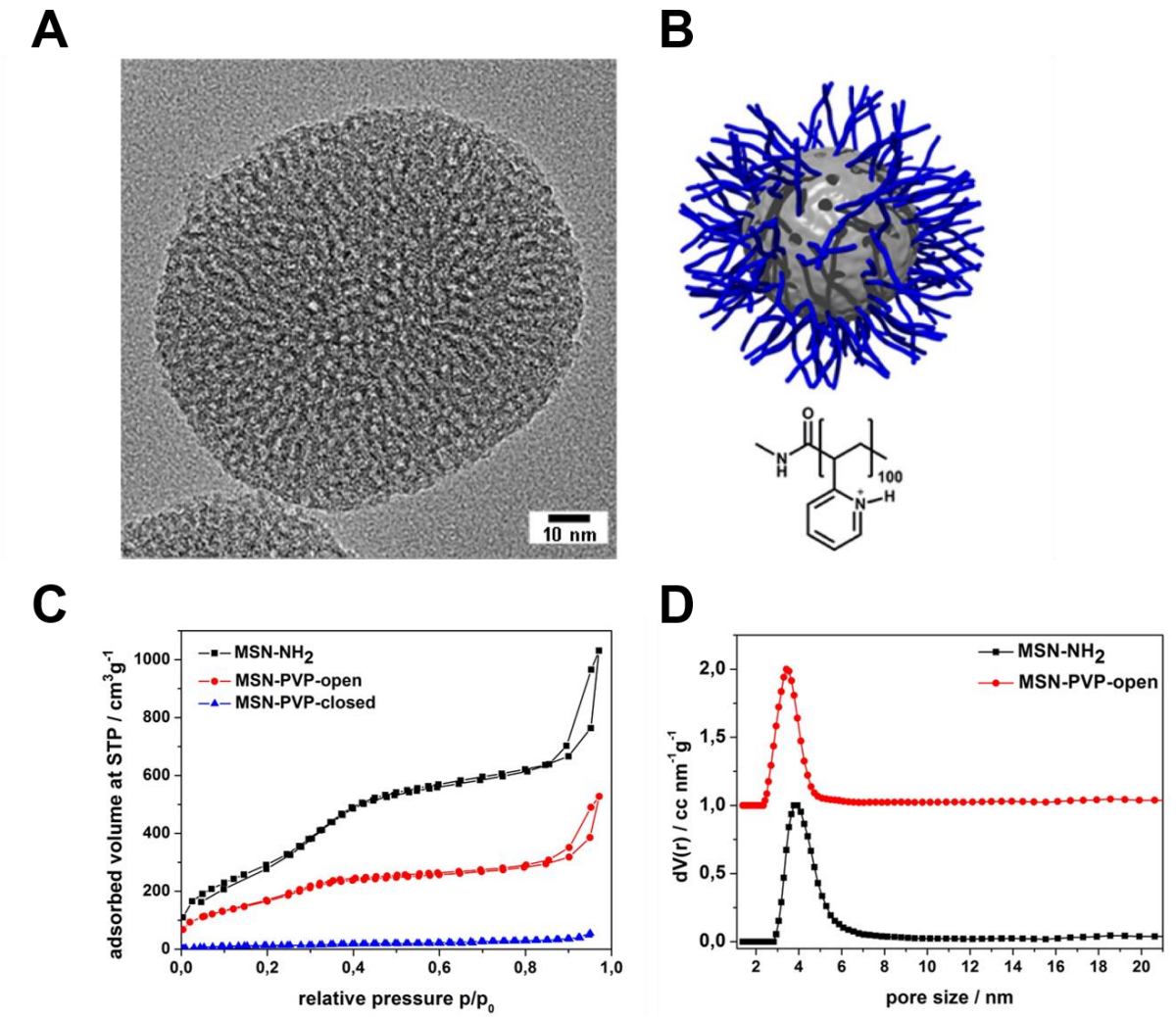

Figure 3-1 Characteristics and structure of mesoporous silica nanoparticles. (A) Transmission electron micrograph of a template-extracted MSN-NH_2, exhibiting a worm-like structure. (B) Schematic illustration of the pH-responsive nanocarrier system (MSN-PVP) employed in this work at a pH value of 5 (open state). The inorganic-organic hybrid material consists of a mesoporous silica core (grey) and a covalently attached pH-responsive polymer (poly(2-vinylpyridine), blue). (C) Nitrogen sorption isotherms of the samples MSN-NH_2 (black), MSN-PVP-open (red) and MSN-PVP-closed (blue). These data have already been presented in ref. 15. (D) Calculated NLDFT pore size distributions for the samples MSN-NH_2 (black) and MSN-PVP-open (red); data of the red curve are shifted by a value of 1.0 along the *y*-axis for clarity.

Efficient uptake of mesoporous silica nanoparticles by specialized antigen-presenting cells

To test whether MSN-NH_2 can serve as a delivery tool in primary immune cells, freshly isolated mouse splenocytes that harbor a variety of different immune cells were cultured in the presence of fluorescently-labeled MSN (MSN-FITC) overnight. The uptake of labeled MSN-FITC by different cell types was analyzed by flow cytometry. Cells of the innate immune system, that includes macrophages and dendritic cells, showed high uptake of MSN-FITC, as measured by fluorescence signal-positive cells (Figure 3-2A). As such, dendritic cells, which are highly specialized in antigen uptake, processing and presentation, were more efficient in uptake than macrophages. In contrast, T and B cells, which are the effector cells of the adaptive immune system, showed only trace fluorescence signal positivity. The intracellular uptake of MSN-FITC was clearly concentration-dependent (Figure 3-2B). Fluorescent microscopy showed a speckled distribution pattern of fluorescent signals within dendritic cells, suggesting uptake of labeled MSN into distinct intracellular compartments but not into the cytosol or nucleus (Figure 3-2C). Indeed, counter-staining with a fluorescent marker for lyso-/endosomes showed co-localization with the fluorescein-labeled MSN. In summary, MSN show rapid and efficient uptake into the endosomal compartment of specialized antigen-presenting cells such as dendritic cells but not into adaptive immune cells.

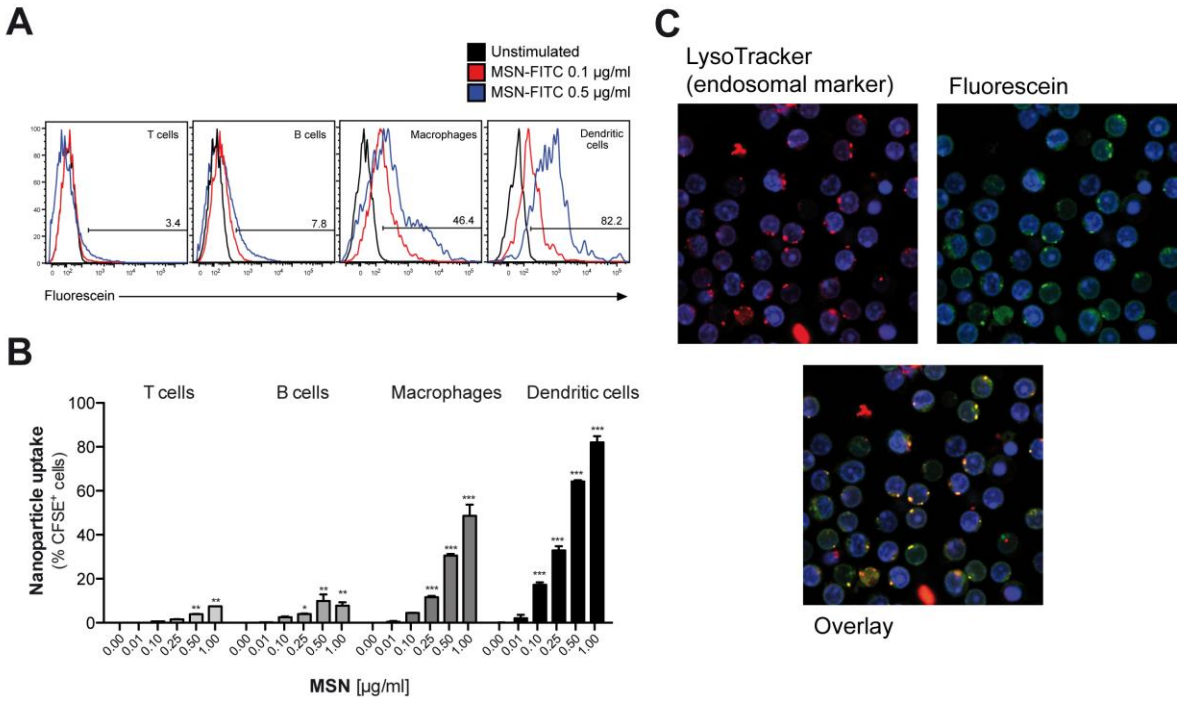

Figure 3-2 Mesoporous silica nanoparticles are efficiently taken up by antigen-presenting cells. (A, B) Freshly isolated, total splenocytes were incubated for 18 h with different concentrations of fluorescein-labeled MSN (MSN-FITC). The uptake of fluorescence signals by different cell populations was determined by flow cytometry. (A) Representative histograms are gated on the indicated cell subset. The numbers give the percentage of fluorescein highly positive-stained cells. (B) Diagrams show the mean percentage of fluorescein-positive cells of triplicate samples ± s.e.m. An asterisk indicates comparison with unstimulated cells. (C) Complete splenocytes were incubated for 3 h with 0.1 µg mL^{-1} MSN-FITC. Cell endosomes were stained with LysoTracker™ and intracellular MSN localization was determined by fluorescence microscopy. All results are representative of at least two independent experiments. No stim., no stimulation.

MSN-NH_2 are non-toxic and do not affect the viability of splenocytes, unless used in very high concentrations

We next sought to determine the cytotoxicity of MSN for primary cells. For this purpose, freshly isolated splenocytes were cultured in the presence of increasing concentrations of MSN-NH_2 and 18 hours later, we performed Annexin V / propidium iodide (PI) analysis by flow cytometry. Annexin V binds to phosphatidylserins, which in apoptotic cells are translocated from the inner to the outer leaflet of the plasma membrane, and are thus exposed to the external cellular environment.[23] PI is a small molecule that intercalates into double-stranded DNA and becomes fluorescent upon intercalation. PI can only reach nuclear DNA

when the cell's integrity is severely compromised during late apoptosis and cell death. The gating strategy for early and late apoptotic cells is depicted in the representative dot blot (Figure 3-3A). MSN-NH_2 showed a favorable (low) toxicity profile in primary cells and induced marked apoptosis only when used in very high concentrations of 200 µg mL^{-1}. The common cytotoxic chemotherapeutic drug oxaliplatin was used as a positive control.

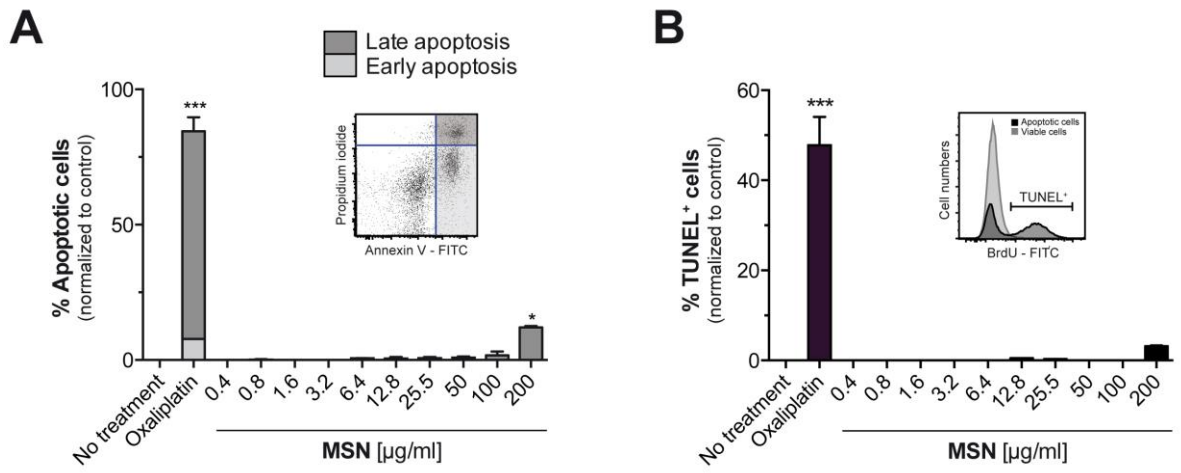

Figure 3-3 MSN-NH_2 are non-toxic and do not affect the viability of splenocytes, unless used in very high concentrations. Complete splenocytes were incubated for 18 h with different concentrations of MSN-NH_2. (A) Cell integrity and viability of splenocytes as determined by propidium iodide (PI) exclusion and Annexin V staining was analyzed by flow cytometry. The dot blot shows the gating strategy of viable (PI^- Annexin V^-), early (PI^-, Annexin V^+) and late apoptotic (PI^+, Annexin V^+) cells. (B) DNA fragmentation was assessed by TUNEL assay. The histogram shows the gating strategy for $TUNEL^+$ cells. All data give the mean percentage of apoptotic cells of triplicate samples ± s.e.m. The mean base-line level of apoptosis in the untreated control group was set as zero %. An asterisk indicates comparison to untreated cells. Results are representative of at least two independent experiments.

To confirm these data, we also performed terminal deoxynucleotidyltransferase dUTP nick end labeling (TUNEL). During the late phase of apoptosis endonucleases degrade the higher order chromatin structure into small DNA pieces. With the TUNEL assay these DNA fragments can be identified through addition of bromolated deoxyuridine triphosphates (Br-dUTP) to the 3'-hydroxyl (OH) termini of double- and single-stranded DNA by the endogenous enzyme terminal deoxynucleotidyl transferase (TdT) and subsequent staining with an FITC-labeled anti-BrdU antibody. The TUNEL analysis confirmed that MSN-NH_2 are non-toxic to primary murine splenocytes over a wide concentration range (Figure 3-3B).

Mesoporous silica nanoparticles induce only very low immunological responses in primary myeloid immune cells

As a next step, we focused on the immunological response of mammalian primary immune cells to cargo-free MSN. For the implementation of any nanoparticle constructs as molecular delivery system, it is essential to fully understand their immune-modulatory potential in order to tightly control the initiation of immune responses according to the therapeutic goal. Thus, freshly isolated splenocytes were cultured in the presence of MSN-NH_2. After 24 hours, surface expression of the B7 family member CD80, a co-stimulatory molecule and activation marker, was examined on different antigen-presenting cells by flow cytometry with specific fluorochrome-coupled antibodies. Additionally, the concentration of the secreted pro-inflammatory cytokines IL-6 and IL-12p70 in the culture supernatant of stimulated cells was quantified by enzyme-linked immunosorbent assay (ELISA). Synthetic unmethylated CpG sequence-containing oligonucleotides (CpG-ODN) that resemble bacterial DNA were used as a positive control. CpG-ODN bind to the endosomal Toll-like receptor (TLR) 9, thereby initiating a full-blown immune response.[24] In comparison to CpG-ODN, MSN-NH_2 induced only low levels of CD80 expression on monocytes and dendritic cells, indicating that the cargo-free nanoparticles barely activate immune responses (Figure 3-4A). The secretion profile of pro-inflammatory cytokines confirmed these findings, as cells cultured with MSN-NH_2 released only low amounts of IL-6 and IL-12p70 (Figure 3-4B). Crystalline silica (found in nature as sand or quartz) have been shown to activate a cytosolic multi-protein complex called the NALP3 inflammasome resulting in the release of bioactive IL-1β, a very potent pro-inflammatory cytokine.[25] In contrast, MSN-NH_2 only induced trace levels of IL-1β (Figure 3-4C).

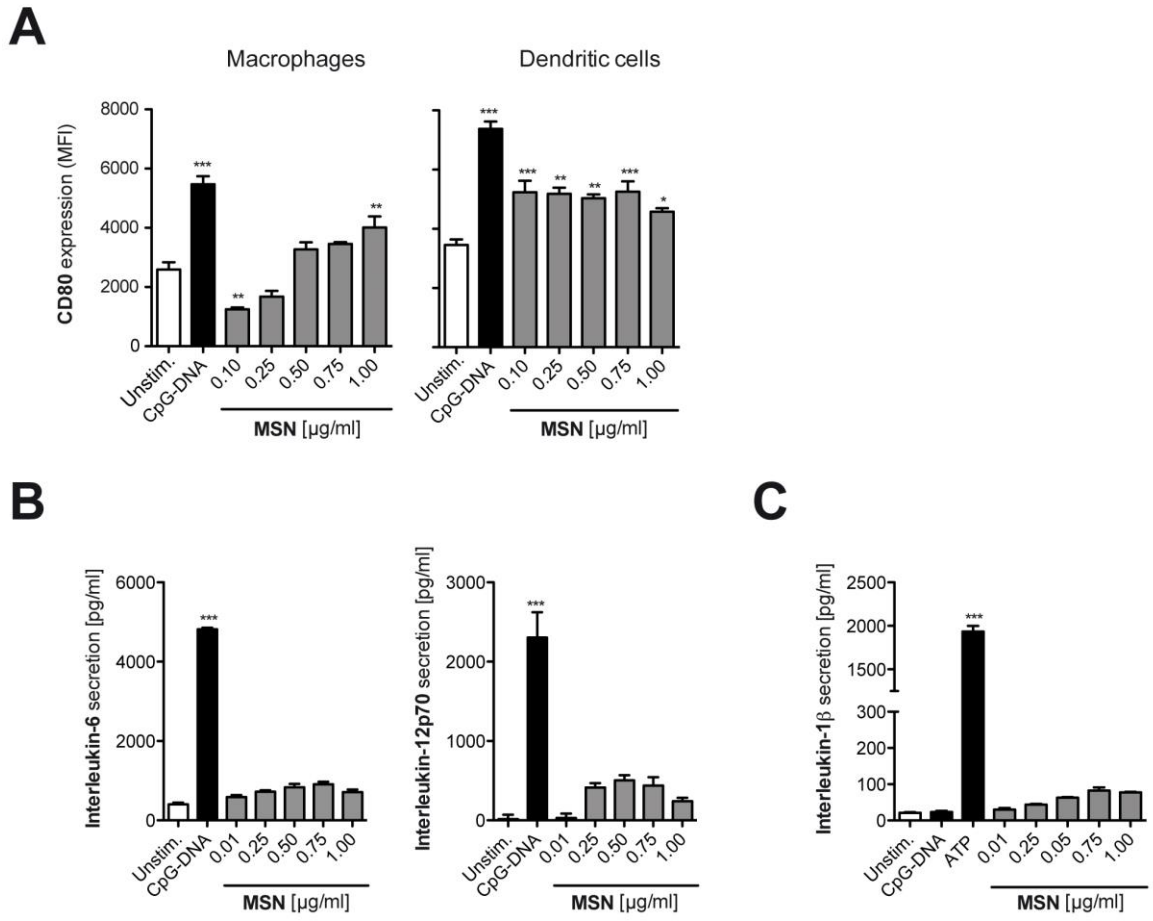

Figure 3-4 Mesoporous silica nanoparticles induce only very low immunological responses in primary myeloid immune cells. Complete splenocytes were incubated for 18 h with different concentrations of MSN-NH2. (A) The surface expression of the co-stimulatory molecule CD80 on myeloid antigen-presenting cells was analyzed by flow cytometry. Data give the mean fluorescence intensity (MFI) of the indicated marker on triplicate samples ± s.e.m. The amounts of the pro-inflammatory cytokines (B) IL-6, IL-12p70 and (C) IL-1β in the cell culture supernatant were determined by ELISA. Data give the mean values of triplicate samples ± s.e.m. An asterisk indicates comparison to unstimulated cells. All results are representative of at least two independent experiments.

To exclude that adsorption of the analyzed cytokines to the cationic surface of MSN-NH_2, could influence the cytokine measurements, we incubated defined concentrations of recombinant cytokines with either non-functionalized (bare) MSN or MSN-NH_2 for 18h in cell culture medium. The presence of MSN did not alter the concentration of any of the cytokines tested (Figure S 3-1A). In line with these findings, we found that MSN without surface functionalization did not induce the release of proinflammatory cytokines when

incubated with primary murine splenocytes (Figure S 3-1B). In summary, these data demonstrate that MSN-NH_2 only mildly activate primary murine APCs.

Bystander lymphoid cells are not stimulated by mesoporous silica nanoparticles

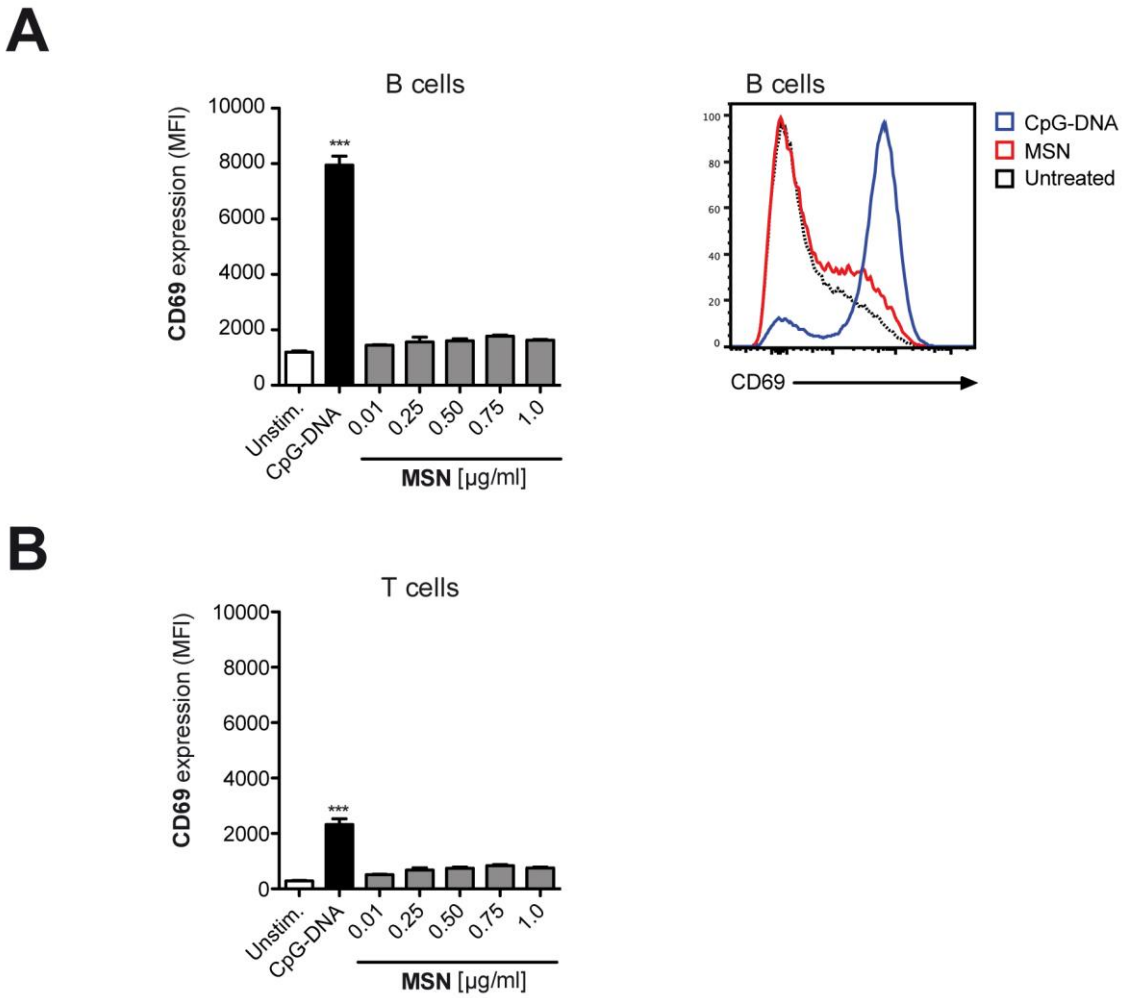

Figure 3-5 Mesoporous silica nanoparticles do not result in activation of bystander lymphoid cells. Complete splenocytes were incubated for 18 h with different concentrations of MSN-NH_2. Expression of the activation marker CD69 on effector (A) B lymphocytes and (B) T lymphocytes was analyzed by flow cytometry. The representative histogram is gated on $B220^+$ B cells and illustrates CD69 expression (black dotted line, unstimulated cells; red line, 1 µg mL−1 MSN; blue line, CpG-DNA). Data in the graphs give the mean values of triplicate samples ± s.e.m. An asterisk indicates comparison to unstimulated cells. All results are representative of at least two independent experiments.

T and B lymphocytes are the effector cells of the adaptive immune system. We have shown that these cell types do not efficiently take up MSN-FITC and are thus unlikely to directly recognize these nanoparticles (Figure 3-2A,B). However, T and B cells may react to low

levels of pro-inflammatory cytokines released by antigen-presenting cells in response to MSN. In order to investigate the immunostimulatory effect of MSN on such bystander lymphocytes, complete splenocytes (containing both antigen-presenting cells and lymphocytes) were cultured in the presence of MSN-NH_2 and expression of the transmembrane C-type lectin CD69, an early activation marker on B and T cells, was analyzed by flow cytometry. We found that neither B nor T cells showed upregulation of the activation marker CD69 (Figure 3-5), indicating that the low-level cytokine release by antigen-presenting cells in response to MSN-NH_2 is not sufficient for activation of bystander lymphocytes.

In summary, our findings show that MSN-NH_2 are rapidly taken up into specialized antigen-presenting cells but are non-toxic and only weakly immunostimulatory to primary murine immune cells.

Functionalized mesoporous silica nanoparticles are an efficient delivery tool for the synthetic immunostimulatory TLR7 ligand R848

To test whether MSN can principally function as delivery tool in primary immune cells, MSN coated with a pH-responsive polymer (MSN-PVP) were loaded with R848. A defined amount of the drug was adsorbed at low pH values into the mesopores of MSN-PVP, followed by the subsequent closure of the polymer coat on the mesoporous nanoparticles at pH 7. Following internalization and shuttling into the endosome, the local acidic environment allows for re-opening of the mesopores and release of the cargo. The low molecular weight, synthetic imidazoquinoline compound R848 (also called resiquimod) induces potent immune responses upon uptake and ligation to endosomal TLR7.[26] Indeed, we found that both unbound (molecules suspended in liquid) as well as MSN-PVP-encapsulated R848 induced activation

of dendritic cells with potent upregulation of CD80 and release of pro-inflammatory IL-6 (Figure 3-6A and B).

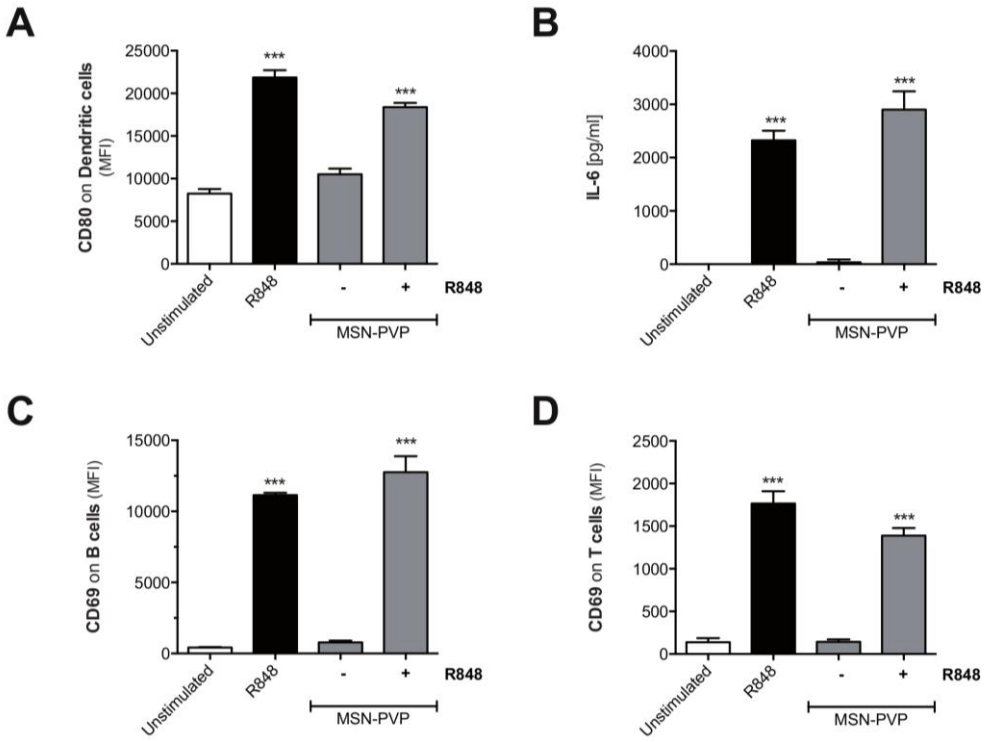

Figure 3-6 Mesoporous Mesoporous silica nanoparticles are an efficient delivery tool for the synthetic immunostimulatory TLR7 ligand R848. Complete splenocytes were incubated for 18 h either with the small molecule immunostimulant R848, cargo-free, or R848-loaded MSN-PVP, respectively. (A) The surface expression of the co-stimulatory molecule CD80 on dendritic cells was analyzed by flow cytometry. (B) The level of Interleukin-6 in the cell culture supernatant was determined by ELISA. Expression of the activation marker CD69 on effector (C) B lymphocytes and (D) T lymphocytes was analyzed by flow cytometry. Data give the mean values of triplicate samples ± s.e.m. An asterisk indicates comparison to unstimulated cells. All results are representative of two independent experiments

Such R848-mediated dendritic cell activation was associated with strong upregulation of the activation marker CD69 on co-cultured lymphocytes (Figure 3-6C and D). This activation affected both B cells and bystander T cells that do not express functional TLR7. These data show that MSN-PVP can be used as a drug delivery tool in primary immune cells. A therapeutic approach to use the targeted release of MSN cargo in the endosome of immune cells in order to target endosomal receptors such as TLR7 with stimuli-responsive capping mechanisms in cancer immunotherapy will be the subject of future studies.

3.3. Discussion

Despite intense research in the field of nanomedicine, fundamental knowledge about the interaction of nanomaterials with the cellular components of the host immune system remains scarce. We demonstrate in this work that MSN-NH_2 particles are rapidly and efficiently taken up by specialized antigen-presenting cells (APCs) such as dendritic cells and macrophages and are delivered into endo-/lysosomes. Efficient uptake of MSN via endocytosis into non-immune cells, in particular different types of tumor cell lines, has been observed previously.[27-29] For example, for HeLa cervical adenocarcinoma cells, Mou and co-workers reported a size-dependent endosomal uptake of MSN, favouring a size range of 50 - 120 nm.[30] In contrast to tumor cells, APCs are specialized to scavenge their environment by taking up and sampling cell debris and foreign material, and are also equipped with a variety of germ-line encoded immune receptors to identify invading microorganisms. Many of these receptors, especially several members of the family of Toll-like receptors (TLR), are localized in the endosome and upon ligation of pathogenic material lead to innate immune stimulation. However, our results demonstrate that the uptake of cargo-free MSN-NH_2 into APCs did not result in immune activation, as dendritic cells and macrophages showed only mild upregulation of the co-stimulatory molecule CD80 and released only low levels of pro-inflammatory cytokines. Similarly, Lee *et al.* showed that incubation of a macrophage cell line or peritoneal macrophages with MSN resulted in only trace release of cytokines and that short-term *in vivo* application of MSN in mice did not lead to contact hypersensitivity.[31] However, treatment of mice with MSN over a time course of several weeks resulted in histological changes in liver and spleen.[32] We note that such findings are expected to be very dependent on the size, surface functionalization and zeta potential of the particles and thus cannot be generalized for different types of MSN. Generally, the impact of repetitive treatments with MSN must be carefully evaluated before long-term clinical applications are conducted.

Crystalline silica have been shown to potently activate the NLRP3 inflammasome, a cytosolic multiprotein complex, triggering the release of the bioactive form of the potent pro-inflammatory cytokine IL-1β.[33] Similar to crystalline silica, non-functionalized, amorphous silica nanoparticles can activate the inflammasome, leading to significant IL-1β secretion.[34] In contrast, here we demonstrate that the molecularly functionalized MSN-NH_2 particles do not induce relevant levels of IL-1β release from primary murine splenocytes. Initial reports suggested that phagocytosis of crystalline silica with a median particle size of 5 µm results in presumably osmotic swelling and damage of the lysosome, leading to activation of the NALP3 inflammasome, which is triggered by lysosomal rupture and content release, not the crystal structure itself.[33] While others linked the formation of reactive oxygen species during an oxidative stress situation to NLRP3 activation,[35] the exact molecular mechanism and prerequisite for inflammasome activation remains to be determined. We propose that due to their size and molecularly functionalized surface structure, spherical MSN-NH_2 in comparison to silica crystals do not induce lysosomal damage and subsequent inflammasome-mediated IL-1β release. Generally, besides the physicochemical properties of particle size and surface chemistry, the biological activity of MSN has also been attributed to shape features such as aspect ratio and morphology.[36]

MSN have attracted much interest for their potential as drug delivery vehicles to control various cell functions by the stimuli-responsive delivery of bioactive cargos.[37-39] An ideal drug delivery vehicle based on MSN may be composed of a multifunctional silica core able to specifically control the interaction with diverse active cargo components. The cargo molecules (e.g. pharmaceutically active drugs) are adsorbed in the mesopores of the nanoparticles, yielding an effective shielding from external degradation in biological fluids.[40, 41] Such multi-functional MSN have been successfully evaluated as antigen carriers and

adjuvants for vaccine delivery.[17] Thereby, MSN have shown intrinsic adjuvant activity under certain conditions, thus potentiating antigen-specific T-cell immune responses.[42, 43] Interestingly, MSN have been described to enhance MHC class I-restricted presentation of antigens by human dendritic cells.[44] This process called cross-presentation is a vital prerequisite for the induction of adaptive T-cell immunity against exogenous antigens such as tumor proteins. We found that the functionalized MSN-NH_2 without protein or adjuvant cargo do not interact with or activate T- and B-lymphocytes *in vitro*. These findings underline the important role of dendritic cells at the interface of innate and adaptive immunity. Importantly, the lack of unspecific lymphocyte priming by the MSN carrier system is a promising requisite for future *in vivo* applications in order to use the high specificity of molecular immunostimulants either on the surface of the MSN or delivered as cargo from its pore system.

Generally, the application of immunostimulatory adjuvants or vaccines via MSN harbors the risk of undesired systemic inflammatory responses upon the uptake of cargo-loaded MSN and subsequent cargo release. These dangerous adverse events can possibly be circumvented by context-dependent, spatiotemporally controlled cargo release. We and other groups pursue a promising approach that takes advantage of internal triggers such as an intracellular change in pH[45, 46] The efficient pH-responsive closing and opening mechanism of a reversible polymer cap system has been previously demonstrated by time-based fluorescence release experiments; fluorescent dyes were used in these studies.[15, 47] In this work, the synthetic TLR7 agonist R848 (resiquimod) was used as active cargo. R848-loaded MSN-PVP particles induced strong stimulation of dendritic cells with potent release of pro-inflammatory cytokines as well as activation of bystander lymphocytes. As a defined ligand for endosomal TLR7/8, R848 was presumably released after pH-dependent reopening of the mesopores in the endosome. Whether such spatially controlled release can augment the efficacy and

regulation of the subsequent immune response is the focus of ongoing research. Similarly, temporally defined release of the MSN-PVP cargo also appears attractive, as the kinetics of receptor sensitivity strongly influence the outcome of R848-based cancer immunotherapy.[48]

3.4. Conclusion

In summary, we demonstrate in this study that MSN-NH_2 nanoparticles are non-toxic to primary murine leukocytes and provoke only trace immune activation. In addition, surface functionalized MSN-PVP can serve as a pH-triggered drug delivery tool for the synthetic TLR7/8 ligand R848 to induce potent immune activation in responder cells. The controlled release of their immunomodulatory cargo by otherwise non-immunogenic MSN is a promising tool in future therapies in order to achieve localized immune activation (e.g. in the tumor microenvironment) while preventing undesired, systemic adverse effects.

3.5. Experimental Part

Materials. All reagents were purchased from commercial suppliers. Tetraethyl orthosilicate (TEOS, Sigma-Aldrich, >98%), cetyltrimethylammonium chloride (CTAC, Fluka, 25wt% in H_2O), triethanolamine (TEA, Sigma-Aldrich, 98%), (3-aminopropyl)-triethoxysilane (APTES, Fluka, 95%), N-(3-dimethylaminopropyl)-N-ethylcarbodiimide hydrochloride (EDC, Sigma-Aldrich, 97%), ammonium nitrate (Sigma-Aldrich, 99%), conc. hydrochloric acid (Sigma-Aldrich, >95%, 37 wt%), α-amino-ω-carboxy terminated poly(2-vinylpyridine) (NH_2-PVP-COOH, Polymer Source, M_n = 10.000, PDI = 1.08), Boc anhydride (Aldrich, 95%), N-hydroxysulfosuccinimide sodium salt (*sulfo*-NHS, Sigma-Aldrich, 98%), ethanol (EtOH, Sigma-Aldrich, >99.5%), tetrahydrofuran (THF, anhydrous, Sigma-Aldrich, ≥99.9%), trifluoroacetic acid (TFA, Acros Organics, 99%), magnesium sulfate ($MgSO_4$, anhydrous, Sigma-Aldrich, ≥99.5%), triethylamine (Sigma-Aldrich, ≥99%), fluorescein isothiocyanate (FITC, Fluka, >90%), saline-sodium citrate buffer concentrate (SSC-buffer (20x), Sigma-Aldrich), citric acid buffer solution (citric acid/HCl/NaCl buffer, pH 2, Sigma-Aldrich), TLR7 agonist R848 (Invivogen, Toulouse). All chemicals were used as received without further purification. Doubly distilled water from a Millipore system (Milli-Q Academic A10) was used for all synthesis and purification steps.

Preparation of colloidal mesoporous silica nanoparticles without functionalization. Unfunctionalized (bare) MSN were prepared as previously reported.[21] Briefly, a mixture of triethanolamine (TEA) and tetraethyl orthosilicate (TEOS) was heated at 90 °C under static conditions, resulting in solution A. In the meantime, a second solution consisting of cetyltrimethylammonium chloride (CTAC) and bi-distilled water was prepared and heated to 60 °C, before it was added to solution A. The resulting mixture was stirred (500 rpm) at

ambient temperature overnight yielding MSN without functionalization. Afterwards, the organic template was removed via a two-step extraction.

Preparation of shell-functionalized colloidal mesoporous silica nanoparticles. Polymer-capped mesoporous silica nanoparticles (MSN-PVP) were synthesized as described previously.[7, 15] In brief, colloidal MSN with an amino-functionality (MSN-NH_2) were prepared by a delayed co-condensation approach with cetyltrimethylammonium chloride (CTAC) as structure directing agent and tetraethylorthosilicate (TEOS) as primary silica source.[7] In order to introduce the outer shell functionalization, 3-aminotriethoxysilane (APTES) was added during the condensation process. The synthesis was followed by a facile extraction of the organic template from the mesopores. Then, 50 mg of the template-extracted MSN-NH_2 were subsequently reacted with a boc-protected bi-functional polymer (COOH-PVP-NHboc) dissolved in THF in an EDC-assisted amidation reaction. The reaction was followed by the deprotection of the polymer with trifluoroacetic acid, yielding the sample MSN-PVP.[15]

Fluorescein labeling of the MSN. Fluorescein isothiocyanate (FITC)-labeling of MSN-NH_2 was performed following a described procedure.[22] In brief, 50 mg of MSN-NH_2 dispersed in ethanol (25 mL) were added to an ethanolic solution of FITC (25 mL, containing 7.4 mg FITC, 0.19 mmol). The suspension was stirred at ambient temperature in the dark for 24 h. The resulting sample MSN-FITC was collected by centrifugation (19.000 rpm, 43.146 RCF, 20 min) and washed three times with ethanol (25 mL each) by subsequent centrifugation and redispersion. After the final centrifugation step the particles were resuspended in absolute ethanol. For cell experiments, 1 mg of the labeled MSN were centrifuged and resuspended in 1 mL phosphate-buffered saline (PBS).

MSN loading with the synthetic TLR7 agonist R848. 1 mg MSN-PVP were dispersed in 240 µL of sterile water. To open the pores and enable the uptake of the respective drug molecule, 50 µL of citrate buffer (pH 2) was added, followed by the addition of 10 µL R848 of the stock solution (1 mg/mL), yielding an overall drug concentration of 10 µg/300 µL in the solution. The particles were stirred overnight, centrifuged, and re-dispersed in 700 µL SSC buffer (pH 7) to enable the closure mechanism of the pH-responsible polymer. The resulting particles were washed extensively with SSC buffer (pH 7) and finally redispersed in 1 mL SSC. For incubation with primary cells, MSN were centrifuged and redissolved in complete RPMI medium (see below).

Characterization of MSN. Centrifugation was performed using a Sorvall Evolution RC equipped with a SS-34 rotor or an Eppendorf centrifuge 5418 for small volumes. All samples were investigated with an FEI Titan 80-300 transmission electron microscope operating at 300 kV with a high-angle annular dark field detector. A droplet of the diluted MSN solution in absolute ethanol was dried on a carbon-coated copper grid. Nitrogen sorption measurements were performed on a Quantachrome Instruments NOVA 4000e. All samples (15 mg each) were heated to 60 °C for 12 h in vacuum (10 mTorr) to outgas the samples before nitrogen sorption was measured at 77 K. Pore size and pore volume were calculated by a NLDFT equilibrium model of N_2 on silica, based on the desorption branch of the isotherms. In order to remove the contribution of the interparticle textural porosity, pore volumes were calculated only up to a pore size of 8 nm. A BET model was applied in the range of 0.05 – 0.20 p/p_0 to evaluate the specific surface area of the samples. Dynamic light scattering (DLS) measurements were performed on a Malvern Zetasizer-Nano instrument equipped with a 4 mW He-Ne laser (633 nm) and an avalanche photodiode. The hydrodynamic radius of the particles was determined by dynamic light scattering in ethanolic or aqueous suspension. For this purpose, 100 µL of an ethanolic suspension of MSN particles (ca. 10 mg/mL) was diluted

with 3 mL of ethanol or water prior to the measurement. Zeta potential measurements of the samples were performed on a Malvern Zetasizer-Nano instrument equipped with a 4 mW He-Ne laser (633 nm) and an avalanche photodiode. Zeta potential measurements were performed using the add-on Zetasizer titration system (MPT-2) based on diluted NaOH and HCl as titrants. For this purpose, 1 mg of the particles was diluted in 10 mL bi-distilled water. Thermogravimetric analysis was performed on a Netzsch STA 440 C TG/DSC with a heating rate of 10 K / min in a stream of synthetic air of about 25 mL/min. The mass was normalized to 100% at 150 °C for all samples to take into account solvent desorption.

Mice. Female C57Bl/6 mice were purchased from Harlan-Winkelmann. Mice were at 6-8 weeks of age at the time of the experiment. Animal studies were approved by the local regulatory agency (Regierung von Oberbayern, Munich, Germany).

Media, reagents and cell culture. Single cell suspensions from spleens were obtained as follows: Spleens were mechanically disrupted and the tissue was subsequently filtered through a 100 µm cell strainer (BD Biosciences, Heidelberg, Germany). Erythrocytes were lysed with ammonium chloride buffer (BD Biosciences). Cell yield and viability were assessed by trypan blue exclusion and a Neubauer counting chamber. Splenocytes were then cultured in complete RPMI (Roswell Park Memorial Institute) 1640 medium (10% fetal calf serum (FCS), 2 mM L-glutamine, 100 µg/mL streptomycin and 1 IU/mL penicillin) at 37 °C in 10% CO_2. In some conditions, CpG 1826 (unmethylated CpG sequence-containing oligonucleotides, a TLR9 agonist, 3 µg/mL, from Invivogen, Toulouse, France) was added to the culture. For maximal IL-1β release, DCs were primed with lipopolysaccharide (LPS, a TLR4 agonist, 20 ng/ml, from Invivogen) overnight and ATP (5 mM, from Sigma-Aldrich) was added to the culture 2 hours prior to the analysis. For exposure to nanoparticles, splenocytes were seeded in complete RMPI at a density of 1.0 x 10^6 / mL in 96-well tissue

culture plates. Silica nanoparticles were added in complete RPMI medium at the indicated concentration. After 18 - 24 hours, cells and culture supernatant were analyzed.

Quantification of cytokines. Cell supernatants were analyzed for cytokine secretion by ELISA (R&D Systems or eBioscience) according to the manufacturers' protocol.

Flow cytometry and apoptosis assay. Cell suspensions were stained in PBS with 1% FCS. Fluorochrome-coupled antibodies against the surface antigens B220, CD3, CD4, CD8, CD11b, CD11c, CD69, CD80, F4/80 and appropriate isotype controls were purchased from BioLegend. Data were acquired on a FACSCanto II (BD Biosciences) and analyzed using FlowJo software (Tree Star, Ashland, OR). The Annexin V-FITC Apoptosis Detection KIT 1 (BD Biosciences) was used for detection of apoptotic cells. Following surface staining and 2 washing steps, single-cell suspensions were resuspended in the provided buffer, incubated with Annexin V - FITC and propidium iodide (PI) and subsequently analyzed by flow cytometry. Terminal deoxynucleotidyltransferase dUTP nick end labeling (TUNEL staining) was done with the APO-BRDU™ Kit (BD Pharmingen) according to the manufacturer's protocol. The chemotherapeutic drug oxaliplatin (30 µg/ml) was used as a positive control for cell death induction.

Confocal Microscopy. Splenocytes were incubated for 4 hours with fluorescein-tagged NPs, washed and re-suspended in culture medium. 75 nM LysoTracker® (Invitrogen) and 3 µg/mL Hoechst dye (Invitrogen) were used for lysosomal and nuclear staining. Stained cells were visualized using a confocal laser scanning microscope (TCS SP5II, Leica).

Statistics. All data are presented as mean ± S.E.M. Statistical significance of single experimental findings was assessed with the independent two-tailed Student's t-test. For multiple statistical comparison of a data set the one-way ANOVA test with Bonferroni

post-test was used. Significance was set at *p*-values $p < 0.05$, $p < 0.01$ and $p < 0.001$ and was then indicated with an asterisk (*, ** and ***). All statistical calculations were performed using Graphpad Prism (GraphPad Software).

3.6. References

1. M. A. Shah, N. He, Z. Li, Z. Ali and L. Zhang, *J. Biomed. Nanotechnol.*, 2014, **10**, 2332-2349.
2. M. J. Smith, J. M. Brown, W. C. Zamboni and N. J. Walker, *Toxicol. Sci.*, 2014, **138**, 249-255.
3. C. K. Prashant, M. Kumar and A. K. Dinda, *J. Biomed. Nanotechnol.*, 2014, **10**, 2317-2331.
4. A. Iwasaki and R. Medzhitov, *Nat. Immunol.*, 2015, **16**, 343-353.
5. G. F. Goya, I. Marcos-Campos, R. Fernandez-Pacheco, B. Saez, J. Godino, L. Asin, J. Lambea, P. Tabuenca, J. I. Mayordomo, L. Larrad, M. R. Ibarra and A. Tres, *Cell Biol. Int.*, 2008, **32**, 1001-1005.
6. V. Manolova, A. Flace, M. Bauer, K. Schwarz, P. Saudan and M. F. Bachmann, *Eur. J. Immunol.*, 2008, **38**, 1404-1413.
7. V. Cauda, A. Schlossbauer, J. Kecht, A. Zurner and T. Bein, *J. Am. Chem. Soc.*, 2009, **131**, 11361-11370.
8. J. Kobler, K. Moller and T. Bein, *ACS Nano*, 2008, **2**, 791-799.
9. K.-J. Chen, E.-Y. Chaung, S.-P. Wey, K.-J. Lin, F. Cheng, C.-C. Lin, H.-L. Liu, H.-W. Tseng, C.-P. Liu, M.-C. Wei, C.-M. Liu and H.-W. Sung, *ACS Nano*, 2014, **8**, 5105-5115.
10. A. Schloßbauer, A. M. Sauer, V. Cauda, A. Schmidt, H. Engelke, U. Rothbauer, K. Zolghadr, H. Leonhardt, C. Bräuchle and T. Bein, *Adv. Healthcare Mater.*, 2012, **1**, 316-320.
11. C. R. Thomas, D. P. Ferris, J.-H. Lee, E. Choi, M. H. Cho, E. S. Kim, J. F. Stoddart, J.-S. Shin, J. Cheon and J. I. Zink, *J. Am. Chem. Soc.*, 2010, **132**, 10623-10625.
12. C. Coll, L. Mondragón, R. Martínez-Máñez, F. Sancenón, M. D. Marcos, J. Soto, P. Amorós and E. Pérez-Payá, *Angew. Chem. Int. Ed. Engl.*, 2011, **50**, 2138-2140.
13. C.-Y. Lai, B. G. Trewyn, D. M. Jeftinija, K. Jeftinija, S. Xu, S. Jeftinija and V. S. Y. Lin, *J. Am. Chem. Soc.*, 2003, **125**, 4451-4459.
14. A. Schlossbauer, C. Dohmen, D. Schaffert, E. Wagner and T. Bein, *Angew. Chem. Int. Ed. Engl.*, 2011, **50**, 6828-6830.
15. S. Niedermayer, V. Weiss, A. Herrmann, A. Schmidt, S. Datz, K. Müller, E. Wagner, T. Bein and C. Bräuchle, *Nanoscale*, 2015, **7**, 7953-7964.
16. N. Ž. Knežević and J.-O. Durand, *ChemPlusChem*, 2015, **80**, 26-36.
17. K. T. Mody, A. Popat, D. Mahony, A. S. Cavallaro, C. Yu and N. Mitter, *Nanoscale*, 2013, **5**, 5167-5179.
18. K. T. Mody, D. Mahony, J. Zhang, A. S. Cavallaro, B. Zhang, A. Popat, T. J. Mahony, C. Yu and N. Mitter, *Biomaterials*, 2014, **35**, 9972-9983.
19. X. Wang, X. Li, A. Ito, Y. Sogo and T. Ohno, *Acta Biomater.*, 2013, **9**, 7480-7489.
20. J. Kim, W. A. Li, Y. Choi, S. A. Lewin, C. S. Verbeke, G. Dranoff and D. J. Mooney, *Nat. Biotech.*, 2015, **33**, 64-72.
21. K. Möller, J. Kobler and T. Bein, *Adv. Funct. Mater.*, 2007, **17**, 605-612.
22. H. Salmio and D. Brühwiler, *J. Phys. Chem. C*, 2007, **111**, 923-929.
23. G. Koopman, C. P. Reutelingsperger, G. A. Kuijten, R. M. Keehnen, S. T. Pals and M. H. van Oers, *Blood*, 1994, **84**, 1415-1420.
24. H. Hemmi, O. Takeuchi, T. Kawai, T. Kaisho, S. Sato, H. Sanjo, M. Matsumoto, K. Hoshino, H. Wagner, K. Takeda and S. Akira, *Nature*, 2000, **408**, 740-745.
25. C. Dostert, V. Petrilli, R. Van Bruggen, C. Steele, B. T. Mossman and J. Tschopp, *Science*, 2008, **320**, 674-677.
26. H. Hemmi, T. Kaisho, O. Takeuchi, S. Sato, H. Sanjo, K. Hoshino, T. Horiuchi, H. Tomizawa, K. Takeda and S. Akira, *Nat. Immunol.*, 2002, **3**, 196-200.
27. Z. Tao, B. B. Toms, J. Goodisman and T. Asefa, *Chem. Res. Toxicol.*, 2009, **22**, 1869-1880.
28. J. Zhu, J. Tang, L. Zhao, X. Zhou, Y. Wang and C. Yu, *Small*, 2010, **6**, 276-282.
29. A. M. Sauer, A. Schlossbauer, N. Ruthardt, V. Cauda, T. Bein and C. Bräuchle, *Nano Lett.*, 2010, **10**, 3684-3691.
30. F. Lu, S.-H. Wu, Y. Hung and C.-Y. Mou, *Small*, 2009, **5**, 1408-1413.
31. S. Lee, H.-S. Yun and S.-H. Kim, *Biomaterials*, 2011, **32**, 9434-9443.
32. S. Lee, M.-S. Kim, D. Lee, T. K. Kwon, D. Khang, H.-S. Yun and S.-H. Kim, *Int. J. Nanomedicine*, 2013, **8**, 147-158.
33. V. Hornung, F. Bauernfeind, A. Halle, E. O. Samstad, H. Kono, K. L. Rock, K. A. Fitzgerald and E. Latz, *Nat. Immunol.*, 2008, **9**, 847-856.
34. M. Winter, H.-D. Beer, V. Hornung, U. Krämer, R. P. F. Schins and I. Förster, *Nanotoxicology*, 2011, **5**, 326-340.
35. R. Zhou, A. Tardivel, B. Thorens, I. Choi and J. Tschopp, *Nat. Immunol.*, 2010, **11**, 136-140.
36. N. Hao, L. Li and F. Tang, *J. Biomed. Nanotechnol.*, 2014, **10**, 2508-2538.

37. J. L. Vivero-Escoto, I. I. Slowing, B. G. Trewyn and V. S. Y. Lin, *Small*, 2010, **6**, 1952-1967.
38. J. M. Rosenholm, C. Sahlgren and M. Linden, *Nanoscale*, 2010, **2**, 1870-1883.
39. C. Argyo, V. Weiss, C. Bräuchle and T. Bein, *Chem. Mater.*, 2013, **26**, 435-451.
40. V. Cauda, C. Argyo and T. Bein, *J. Mater. Chem.*, 2010, **20**, 8693-8699.
41. Y. S. Lin, N. Abadeer and C. L. Haynes, *Chem. Commun.*, 2011, **47**, 532-534.
42. N. Kupferschmidt, K. R. Qazi, C. Kemi, H. Vallhov, A. E. Garcia-Bennett, S. Gabrielsson and A. Scheynius, *Nanomedicine (London, U. K.)*, 2014, **9**, 1835-1846.
43. D. Mahony, A. S. Cavallaro, F. Stahr, T. J. Mahony, S. Z. Qiao and N. Mitter, *Small*, 2013, **9**, 3138-3146.
44. A. Jimenez-Perianez, B. Abos Gracia, J. Lopez Relano, C. M. Diez-Rivero, P. A. Reche, E. Martinez-Naves, E. Matveyeva and M. Gomez del Moral, *Clin. Dev. Immunol.*, 2013, **2013**, 362163.
45. C. H. Lee, S. H. Cheng, I. P. Huang, J. S. Souris, C. S. Yang, C. Y. Mou and L. W. Lo, *Angew. Chem. Int. Ed. Engl.*, 2010, **49**, 8214-8219.
46. A. Schlossbauer, C. Dohmen, D. Schaffert, E. Wagner and T. Bein, *Angew. Chem. Int. Ed.*, 2011, **50**, 6828-6830.
47. A. Schlossbauer, J. Kecht and T. Bein, *Angew. Chem. Int. Ed. Engl.*, 2009, **48**, 3092-3095.
48. C. Bourquin, C. Hotz, D. Noerenberg, A. Voelkl, S. Heidegger, L. C. Roetzer, B. Storch, N. Sandholzer, C. Wurzenberger, D. Anz and S. Endres, *Cancer Res.*, 2011, **71**, 5123-5133.

3.7. Appendix

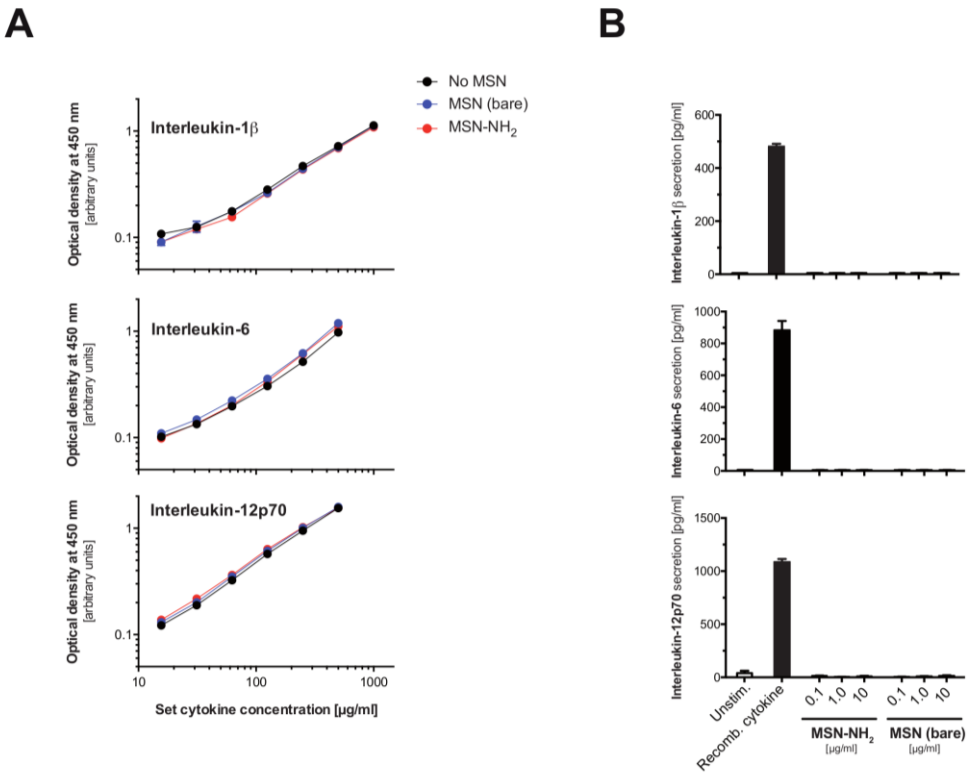

Figure S 3-1 Cytokines are not adsorbed to the cationic surface of MSN-NH_2. (A) MSN-NH_2 and unfunctionalized (bare) MSN were incubated with defined concentrations of recombinant cytokines. After 18 h, the concentration of the indicated cytokines in the culture medium was analyzed by ELISA. (B) Complete splenocytes were incubated for 18 h with different concentrations of MSN-NH_2 or bare MSN. The amounts of the pro-inflammatory cytokines IL-1β, IL6 and IL12p70 in the cell culture supernatant were determined by ELISA. Data give the mean value of triplicate samples ± s.e.m. All results are representative of two independent experimenta.

CHAPTER 4

Mesoporous silica nanoparticles as pH-responsive drug carrier for R848

The following chapter is a joint project: The nanoparticle synthesis was performed and optimized by Dorothée Dollenmayer, Natasha Ustyanovska, Stefan Datz and Olga Zhuzhgova. Characterization and optimization of the carrier system as well as *in cuvette* stability, loading and release and quantification measurements were performed and interpreted by Dorothée Dollenmayer. Thomas Bein and Hanna Engelke guided the studies. The live cell imaging experiment was performed by Daniel Hauser. The *in vivo* biodistribution and toxicity studies as well as the *in vitro* toxicity, uptake, immune activation and T cell proliferation studies were performed and interpreted by Julia Wagner. Carole Bourquin guided the studies. This project will also be part of the doctoral thesis of Julia Wagner.

4. Mesoporous silica nanoparticles as pH-responsive drug carrier for R848

This chapter consists of the following manuscript:

Dorothée Gößl[§], Julia Wagner[§], Daniel Hauser, Natasha Ustyanovska, Stefan Datz, Olga Zhuzhgova, Hanna Engelke, Thomas Bein[*], Carole Bourquin[*], *to be submitted* **2019**.

[§,*]These authors contributed equally.

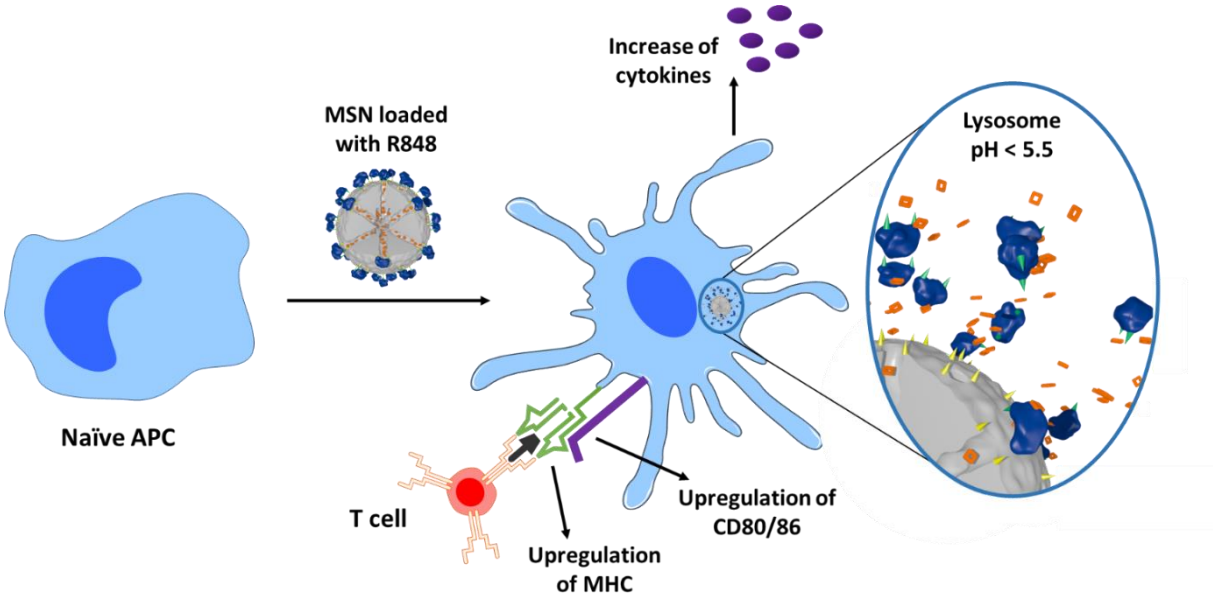

Abstract

Nanoparticle-based cancer immunotherapies aim to improve the safety and efficacy of small-molecule immune-stimulants through targeted and local delivery to specialized antigen-presenting cells (APCs). Multifunctional mesoporous silica nanoparticles (MSNs), with their large surface areas, their tunable particle and pore sizes and their spatially-controlled functionalization, represent a safe and non-inflammagenic carrier system for these immune-modulatory molecules. In this study, we demonstrated the potential of MSNs as a pH-responsive drug carrier system for the immune-stimulant R848 (resiquimod), a synthetic Toll-like receptor 7 and 8 agonist. Equipped with a unique biotin-avidin-cap, the tailor-made nanoparticles showed efficient stimuli-response release of their R848 cargo if the environmental pH dropped to 5.5 or below. We showed that the MSNs were rapidly taken up by APCs into the acidic environment of the lysosome and, upon subcutaneous injection into mice, mainly accumulated in migratory dendritic cells (DCs) in the draining lymph node. Particles loaded with R848 potently activated DCs as observed by the upregulation of co-stimulatory molecules and the release of pro-inflammatory cytokines. Furthermore, simultaneous delivery of the model antigen OVA and the adjuvant R848 resulted in an augmented antigen-specific T cell response. In sum, we were able to demonstrate that MSNs represent an optimal tool for targeted delivery of the immune-modulator R848 to antigen-presenting cells and hold considerable promise as a cancer vaccine carrier in future therapies.

4.1. Introduction

In recent years, cancer immunotherapies have revolutionized the field of cancer research.[1] The novel idea behind immunotherapies is to harness the power of the immune system to fight the cancerous cells instead of targeting the tumor directly. For a successful anti-tumor response, antigen-presenting cells (APC) such as dendritic cells (DCs) need to take up tumor antigens, undergo maturation and migrate to the tumor-draining lymph node. Upon recognizing the antigen presented by the APCs, cytotoxic T cells are activated and proliferate before traveling back to the tumor site to kill the cancerous cells.[2] However, tumor cells can evade their immune destruction by suppressing and controlling immune cells. Thus, a major success in cancer immunotherapy was the development of immune checkpoint inhibitors such as ipilimumab and nivolumab – antibodies which block the inhibitory interaction between tumor and T cells and thus unleash the killing ability of cytotoxic T cells.[3] These antibodies help just a small percentage of patients, however, and the demand for different cancer immunotherapy strategies still remains high. One such strategy involves boosting the antigen-presenting cells in order to increase the activation of cytotoxic T cells by targeting the pattern recognition receptors (PRRs) of APCs. These receptors normally sense pathogen-associated molecular patterns (PAMPs) upon infection and promote the maturation of the APCs. Among the most studied receptors is the family of the Toll-like receptors (TLR), and several TLR agonists are being investigated for their use in cancer immunotherapy.[4] The TLR-7/8 agonist imiquimod has already been successfully used for the topical treatment of basal cell carcinoma after its FDA-approval in 2004.[5] Besides imiquimod, resiquimod or R848 also belongs to the group of imidazoquinolines and was shown to be one hundred times more potent.[6-7] However, systemic applications of TLR7/8 agonists remain clinically problematic due to their toxicity at the dose required for them to be effective.[8-10]

Therefore, improved delivery systems are urgently needed to achieve a more localized and targeted immune response and thus to enhance the safety and efficacy of these immune-activating drugs. The use of nanoparticles as delivery systems has already shown great promise in pre-clinical and clinical studies. By using DC-targeted nanoparticles that carry adjuvants, several studies were able to demonstrate an increase in $CD8^+$ cytotoxic T cells in the tumor microenvironment as well as subsequent tumor shrinkage.[11-14] Several of these studies used the nanoparticles as a platform for cancer vaccination, meaning that they delivered not only an immune-activator such as TLR7/8 ligands to the cells, but also a tumor-specific antigen.

The most promising nanoparticulate delivery platforms to date include liposomes, polymers, gold nanoparticles and mesoporous silica nanoparticles. Liposomes represent a well-studied delivery system with several FDA-approved formulations for chemotherapeutic delivery. They are thus also well-studied for cancer vaccination.[15-16] However, liposomal formulations show a poor control of drug release kinetics. This may lead either to a burst release, often prior to reaching the target, or an impaired release, depending on the hydrophobicity or hydrophilicity of the drug.[17] Another intensively studied material is poly(D,L-lactic-co-glycolic acid) (PLGA) nanoparticles.[18-21] For example, Ilyinskii *et al.* could show that polymeric PLGA nanoparticles loaded with the immune-stimulant resiquimod and the antigen OVA could induce a strong and sustained local immune activation.[22] Although PLGA are FDA-approved, it is known that their biodegradation leads to acidic products, like glycolic and lactic acid, which may degrade peptides and proteins and thus may limit their delivery. This limitation is amplified by the fact that the polymeric particles can only accommodate hydrophobic or lipophilic drugs, whereas many potent antigens and adjuvants are hydrophilic.[17] In addition, the clinical efficiency of these particles shows poor results, probably due to the formation of a protein corona *in vivo* which decreases colloidal stability of

the particles and accelerates their clearance by macrophages.[23] Besides these organic platforms, metallic ones such as gold nanoparticles (AuNPs) are also being investigated for their use in cancer immunotherapy. AuNPs exhibit a versatile surface chemistry and a high affinity with dendritic cells. In a previous study, we could show that small functionalized gold nanoparticles could successfully load the TLR7/8 ligand resiquimod in their ligand shell, and we observed enhanced antitumor efficacy with the loaded particles compared to the free drug.[24] Despite those encouraging results, the clinical application of gold nanoparticles is hampered by their high affinity to nucleic acids and related toxicity issues.[25-26] The long-term accumulation of AuNPs in the body also raises additional safety concerns.[27]

Mesoporous silica nanoparticles (MSNs) represent one of the most promising inorganic drug delivery systems. Their size and pore structure can easily be tuned, yielding colloidally stable MSNs with narrow pore size distributions. Moreover, they possess very large surface areas and pore volumes and thus show high cargo loading efficiencies. They can be functionalized with spatial control, thus enabling perfectly tailored host-guest relations inside the pores as well as a matching external surface allowing for optimized particle-cell interactions.[28] With respect to the above-mentioned safety concerns, MSNs show a tuneable degradation behaviour resulting in harmless silicic acid and related molecules.[29-31] Furthermore, we were able to show in a previous study that these MSNs hold promise as an ideal drug vehicle for immune-modulatory cargo.[32]

In this project, we present spatially segregated core-shell mesoporous silica nanoparticles (MSNs) as a tight pH-responsive drug carrier system for the immune-stimulant resiquimod. We show that loaded R848 is successfully delivered to antigen-presenting cells, resulting in potent APC maturation. We also show that co-loading R848 and the antigen OVA on the

particles results in augmented T cell activation. This suggests that MSNs hold great potential as a cancer vaccine carrier.

4.2. Results

Synthesis and characterization of MSN-Avidin particles

Core-shell functionalized MSNs were prepared *via* a modified site-specific co-condensation approach with cetyltrimethylammonium chloride (CTAC) as organic template and tetraethylorthosilicate as primary silica source.[35]

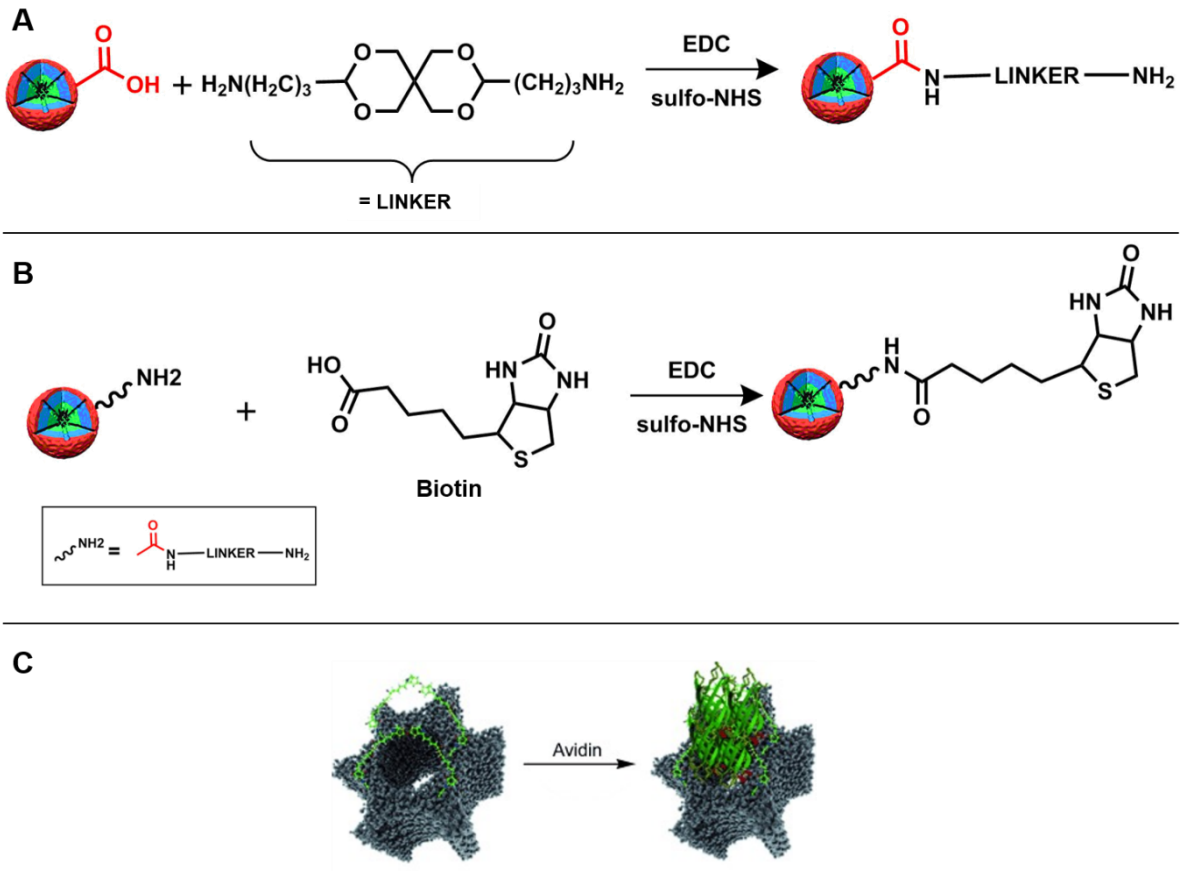

Figure 4-1. Synthesis schemes of different functionalization steps to construct avidin-capped MSNs. Particle represents co-condensed core-shell MSNs. Green core: phenyl functionality. Blue intermediate layer: Pure TEOS. Red external surface: Carboxylic moieties. (A) EDC coupling reaction of acetal linker to carboxylic functionalized MSNs. (B) Covalent attachment of biotin to residual amine groups of acetal linker *via* EDC-assisted amidation reaction. (C) Avidin (green) capping of pores (grey) *via* formation of strong avidin-biotin complex (scheme from Schlossbauer *et al.*[37]).

The core of the particles was functionalized with phenyl groups to accommodate hydrophobic R848 and the external surface was functionalized with carboxylic groups, allowing for successive modifications to attach a stimuli-dependent capping system, consisting of a pH-responsive acetal linker and a biotin-avidin complex as bulky gatekeeper.

In the first step of subsequent core-shell MSN modification, shown in Figure 4-1 A, the pH-responsive acetal linker (AK) is covalently bound to the carboxylic-functionalized periphery of the particles *via* an EDC-assisted amidation reaction. This step is followed by a second EDC-coupling between the residual amine-group of the attached acetal linker and the COOH-group of biotin (Figure 4-1 B). Capping of the pores is achieved through non-covalent attachment of avidin through formation of the biotin-avidin complex. This interaction is the strongest known non-covalent link between a protein and its ligand and shows a dissociation constant of $K_d = 10^{-15}$ M.[38] Avidin possesses four binding sites for biotin, therefore, it is added in great excess to avoid any cross-coupling reaction between two or more different particles. With its dimensions of 5 x 5 x 4 nm^3, avidin is big enough to completely block the 3.2 nm pore.[39] The concept is shown in Figure 4-1 C.[37]

The transmission electron microscope (TEM) image of the template-free core-shell MSNs shows spherical particles with sizes of around 70 nm and a wormlike pore structure (Figure 4-2A). Dynamic light scattering measurements (DLS) reveal colloidally stable particles with a narrow particle size distribution (Figure 4-2 B). Particle sizes obtained with this method show a mean value of 146 nm (hydrodynamic diameter) for the core-shell MSNs MSN-Ph_{in}-$COOH_{out}$. Functionalization with acetal linker and biotin shows only a moderate increase in size up to a mean value of 183 nm. DLS measurements of avidin-capped particles in aqueous solutions demonstrate a shift to higher sizes of around 280 nm. This can be explained by the attachment of the bulky protein as well as a small agglomeration effect. The difference in the sizes measured by TEM and DLS can be partially attributed to the larger hydrodynamic radius of the particles measured in solution and determined with DLS. Some additional agglomeration effect may also contribute to the increased size in DLS. Additionally, in a former paper by Cauda *et al.* it was shown that DLS leads to a systematic overestimation of size compared to techniques like TEM, SEM and FCS.[40] Sorption measurements reveal an

average pore size of around 3.2 nm and large surface areas (1006 m^2/g for MSN-Ph_{in}-$COOH_{out}$) which are typical for MSNs **(**Figure 4-2 C**)**. The respective values for the functionalized samples are shown in Figure 4-2 D.

All samples, except MSN-Ph_{in}-$Avidin_{out}$, exhibit a type IV isotherm which is typical for mesoporous materials. The avidin capped sample shows a type II isotherm which is assigned to non-porous materials and proves the successful pore closure mechanism. The Brunauer-Emmet-Teller (BET) surface areas were calculated from the respective isotherms in the range p/p_0 = 0.05-0.2 and are summarized in the table shown in Figure 4-2 D. The samples MSN-Ph_{in}-$COOH_{out}$, AK_{out}, $Biotin_{out}$ all feature a very large specific surface area which is characteristic for MSNs. The decrease of BET surface area in the sample MSN-Ph_{in}-AK_{out} to 824 m^2/g may be attributed to some crosslinking events through the bifunctional acetal linker. Additionally, electrostatic interactions between the residual amine-group of the attached linker and unfunctionalized carboxyl groups of the MSNs might occur. This may lead to minor pore blocking, apparent in the smaller BET surface area. To minimize those effects, the acetal linker was used in great excess in the amidation reaction. In contrast, the specific surface area of the sample MSN-Ph_{in}-$Biotin_{out}$ is with 1025 m^2/g even higher than the BET area of MSN-Ph_{in}-$COOH_{out}$. This effect comes supposedly from the attachment of additional biotin molecules to the free amine group of the linker which enlarges the overall surface area slightly. On the other hand, the very low specific surface area of MSN-Ph_{in}-$Avidin_{out}$ with 32 m^2/g proves the efficient pore sealing upon addition of the bulky gatekeeper avidin. The mean pore size of the samples MSN-Ph_{in}-$COOH_{out}$ was calculated to be 3.2 nm which is significantly smaller than the 4 nm pores which are commonly achieved with this synthesis route under use of smaller organosilane amounts.[35] It is stated in literature that in contrast to hydrophilic organic moieties, hydrophobic organosilanes are capable of aligning with the organic tails of the template instead of disturbing the micelle structure.[41] This results in

smaller particle sizes and also shows a pore shrinking effect in comparison to incorporation of other organosilanes.[35, 42-43]

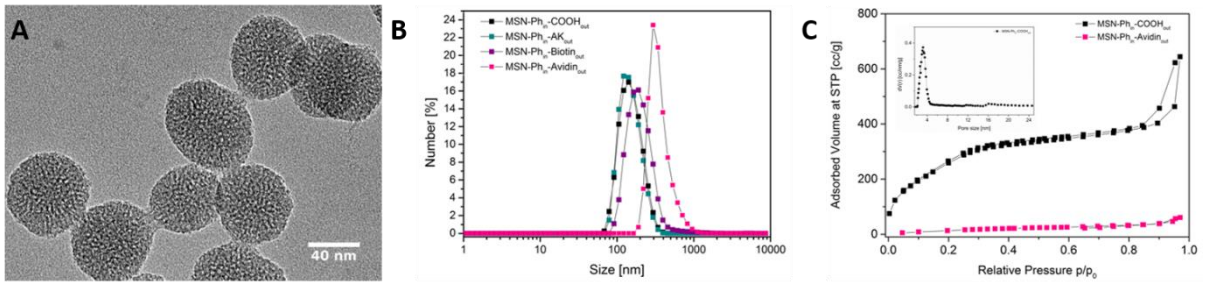

Sample	Surface Area [m^2/g]	Pore Volume [cm^3/g]	Pore Size [nm]	IEP
MSN-Ph_{in}-$COOH_{out}$	1006	0.92	3.2	3.44
MSN-Ph_{in}-AK_{out}	824	0.73	3.2	4.98
MSN-Ph_{in}-$Biotin_{out}$	1025	0.79	3.2	5.53
MSN-Ph_{in}-$Avidin_{out}$	32	-	-	9.01

Figure 4-2. Characterization of functionalized MSNs. (A) TEM image of core-shell MSN-Ph_{in}-$COOH_{out}$. (B) DLS measurements of samples MSN-Ph_{in}-$COOH_{out}$ (black) MSN-Ph_{in}-AK_{out} (cyan), MSN-Ph_{in}-$Biotin_{out}$ (purple), MSN-Ph_{in}-$Avidin_{out}$ (pink). (C) BET isotherm and pore size distribution (inset) for clarity reasons only shown for sample MSN-Ph_{in}-$COOH_{out}$ (black) and MSN-Ph_{in}-$Avidin_{out}$ (pink). (D) Table summarizing results of N_2-sorption measurements and isoelectric points (IEPs) of corresponding zetal potential measurements shown in (E). (E) Titration curves of zeta potential measurements of all four samples. (F) IR spectra of all four samples (for clarity reasons respectively shifted by a factor of 0.25).

Concluding, the successful incorporation of a large phenyl-content is indicated by the calculated smaller pore sizes. Modifications of the particle's external surface with acetal linker and biotin have no impact on the pore size. Therefore, the pore size distributions derived from NLDFT calculations for the samples MSN-Ph_{in}-AK_{out} and MSN-Ph_{in}-$Biotin_{out}$ also show a mean pore size of 3.2 nm. This proves the spatial control over the selective functionalization of the external surface with little or no effect on the pore accessibility. The corresponding pore volumes show a slight decrease after functionalization with the acetal linker and biotin, respectively. This further proves the assumption of minor pore blocking events through crosslinking reactions as described above. All results from nitrogen sorption measurements are summarized in Figure 4-2 D.

Zeta potential measurements can be applied to monitor the different functionalization steps (Figure 4-2 E). MSN-Ph_{in}-$COOH_{out}$ shows an isoelectric point of 3.4 and a zeta potential of almost – 50 mV. This negative zeta potential confirms the successful implementation of TEPSA, including the ring opening of the succinic anhydride of the organosilane and the resulting two adjacent carboxyl groups. After attachment of the acetal linker, the IEP is shifted by almost 1.5 because of the residual amine end groups of the linker which are positively charged at acidic pH. MSN-Ph_{in}-$Biotin_{out}$ possesses an IEP of pH 5.5. This can be explained with the urea containing motif in biotin. Through the possible resonance forms at least one of the two nitrogen atoms is protonated at slightly acidic pH. Adding avidin to the particles results in a zeta potential of around + 20 mV and a tremendous shift in isoelectric point to a pH value of 9.01. This can be attributed to the large number of N-termini present in the protein cap.

The different surface functionalization steps, including the capping with avidin protein, are also apparent in IR spectra, as shown in Figure 4-2 F. The silica framework vibrations are visible in all spectra in the region between 1240 and 1000 cm^{-1}. Furthermore, the phenyl core of the MSNs is indicated in all samples by a peak at 1431 cm^{-1} (C=C stretching vibrations) and at 3077 cm^{-1} and 3059 cm^{-1}, respectively, which indicate the aromatic C-H stretching vibrations of the phenyl ring. Sample MSN-Ph_{in}-$COOH_{out}$ shows additional peaks at 1740 and 1720 cm^{-1} belonging to the COOH stretching vibrations of saturated dicarboxylic acids. This proves the successful *in situ* ring opening of the succinic anhydride silane TEPSA. Addition of acetal linker *via* amidation reaction results in a new vibration band at 1599 cm^{-1}, which can be attributed to the deformation vibration of free amines, present at the unbound site of the difunctional linker. After biotinylation *via* EDC amidation, a new C=O stretching vibration band arises at 1658 cm^{-1} belonging to the biotin group. This peak is obscured upon avidin addition by the Amide I and II stretching vibrations, occurring at 1660 cm^{-1} (Amide I: C=O

stretching vibration) and 1640 cm^{-1} (Amide II: N-H deformation stretching vibration and C-N stretching vibration).

Besides the already mentioned characterization methods, thermogravimetric analysis (TGA) can be used to investigate the successful functionalizations and the avidin capping step. To exclude the effect of physisorbed water in the samples, all TGA/DSC curves were normalized to 100% at 130 °C. Incorporation of a large phenyl content can be observed with a mass loss of 28% in the sample MSN-Ph_{in}-$COOH_{out}$ (Figure 4-3 A). 13% thereof can be attributed to the decomposition of ethoxy groups as well as to silanol condensation which can be seen in the comparison to unfunctionalized particles (Figure S 4-1, Equation S 1). Most aliphatic groups decompose in the temperature range between 130-300 °C. This is shown in Figure 4-3 B in the first endothermic signal at around 300 °C which can be attributed to the decomposition of external carboxylic groups in sample MSN-Ph_{in}-$COOH_{out}$ (black DSC curve).

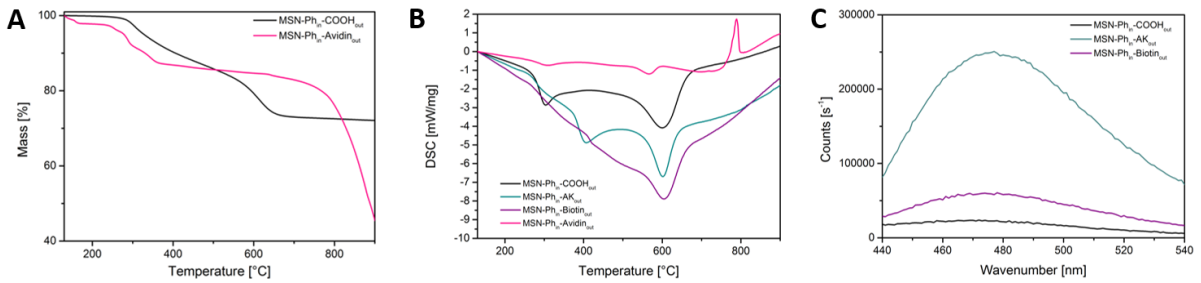

Figure 4-3. Additional characterization of successful functionalization process. (A) TGA measurement for sample MSN-Ph_{in}-$COOH_{out}$ (black) and MSN-Ph_{in}-$Avidin_{out}$ (pink) (heating rate: 10 K / min, flow rate of synthetic air: 25 mL/min). Spectra are normalized to 100% at 130 °C (B) Corresponding DSC curves of MSN-Ph_{in}-$COOH_{out}$ (black) MSN-Ph_{in}-AK_{out} (cyan), MSN-Ph_{in}-$Biotin_{out}$ (purple), MSN-Ph_{in}-$Avidin_{out}$ (pink). (C) Emission spectra after fluram assay of the samples MSN-Ph_{in}-$COOH_{out}$, -AK_{out}, -$Biotin_{out}$.

Furthermore, the decomposition of the AK linker can be observed in the cyan curve at 400 °C. The high thermal stability of the phenyl ring can be detected in all samples with a combustion temperature at 600 °C. This enhanced thermal stability is also observed in the biotinylated sample. Addition of the enzyme avidin to the MSNs leads to an even higher thermal stability, initiating the weight loss only at 800 °C. This may be attributed to a carbonization effect

which can occur during the measurement. Here, a relatively fast heating ramp is applied which can lead to the mentioned carbonization effect of the highly organic protein due to a lack of sufficient oxygen. The 'delayed' decomposition then results in an exothermic signal as can be seen in Figure 4-3 B.

Finally, we confirmed successful functionalization by monitoring the presence of free amine groups in a fluram assay. Here, the dye fluorescamine, short fluram, reacts with primary amines to form pyrrolinone type moieties, resulting in fluorescence activity of the molecule.[44] As can be seen in Figure 4-3 C, fluram does not show any fluorescence when added to a solution of MSN-Ph_{in}-$COOH_{out}$ (black curve), whereas a tremendous increase in fluorescent counts can be seen after successful addition of the acetal linker (MSN-Ph_{in}-AK_{out}, cyan curve). This can be explained with the free residual primary amine groups of the AK linker and proves its successful one-sided attachment to the particles. Subsequent biotinylation shows again a very low fluorescence of the dye. Amine groups present in the biotin structure cannot react with fluram as they are secondary instead of primary amines. The slightly higher amount of detected fluorescence in comparison to the carboxylated MSNs indicates a minor deviation from a complete biotin addition to all available acetal linker molecules.

All in all, we could show that core-shell MSNs were successfully modified with a pH-responsive acetal linker, followed by biotinylation and thus enabling pore closing *via* formation of a strong biotin-avidin complex.

Comparison of two capping systems – PVP versus Avidin

Previous work in our laboratory described a pH-sensitive MSN architecture with a PVP capping system.[45] In a further study, we investigated the properties of amine- and PVP-functionalized MSNs regarding their toxicity and immune-modulatory profile.[32] It was demonstrated that MSNs represent a safe, non-toxic carrier system which activates the

immune system only to a very small extent. Furthermore, it was shown that functionalization with the pH-responsive PVP polymer as gatekeeper and successive loading and release with immune-stimulating resiquimod could represent a promising platform for future immune therapies.

Due to the fact that the PVP system showed a slightly impaired release of the cargo at lower pH due to pore blocking by polymer, the PVP cap was compared to a biotin-avidin system. Here, the bulky gatekeeper is attached to the MSN periphery *via* a pH-responsive cleavable acteal linker. Upon acidification of the environment, the linker is hydrolyzed and the complete cap irreversibly detached.

First, time-based fluorescence measurements *in cuvette* were performed to compare the (loading and) release efficiencies of both systems. For this purpose the loaded samples were put into a special teflon cap, which was successively sealed with a dialysis membrane and put on top of a cuvette filled with the respective buffer. Both samples open up with different pH-dependent mechanisms in MES buffer (pH 5.5). This enables released R848 to diffuse through the membrane and to be detected in the cuvette by measuring its fluorescence. The time-based release of both samples is shown in Figure 4-4 B. Both systems show a tight capping with very little premature release. At pH 5.5 the MSN-Avidin system exhibits a strong release of R848, whereas MSN-PVP releases only a minor amount in comparison.

For a more functional, physiological comparison of the two capping systems, a cell-based assay was performed. To this end, the different R848-loaded nanocarriers were investigated in their ability to activate antigen-presenting cells (APCs). APCs such as dendritic cells represent key players of the innate immune system and are potent inducers of an adaptive immune response when activated. Therefore, bone marrow derived dendritic cells (BMDCs) were incubated with the two different R848-loaded MSN particles. It is known that R848 is an

efficient activator of dendritic cells and leads to upregulation of co-stimulatory molecules on their surface as well as to production of pro-inflammatory cytokines.[46] As shown in Figure 4-4, BMDCs produced the pro-inflammatory cytokine interleukin-6 (IL-6) and upregulated the co-stimulatory molecule CD80 upon incubation with MSN-R848-Avidin. However, MSN-R848-PVP failed to properly induce dendritic cell activation as seen by barely detectable IL-6 production and absence of CD80 upregulation with the concentrations used.

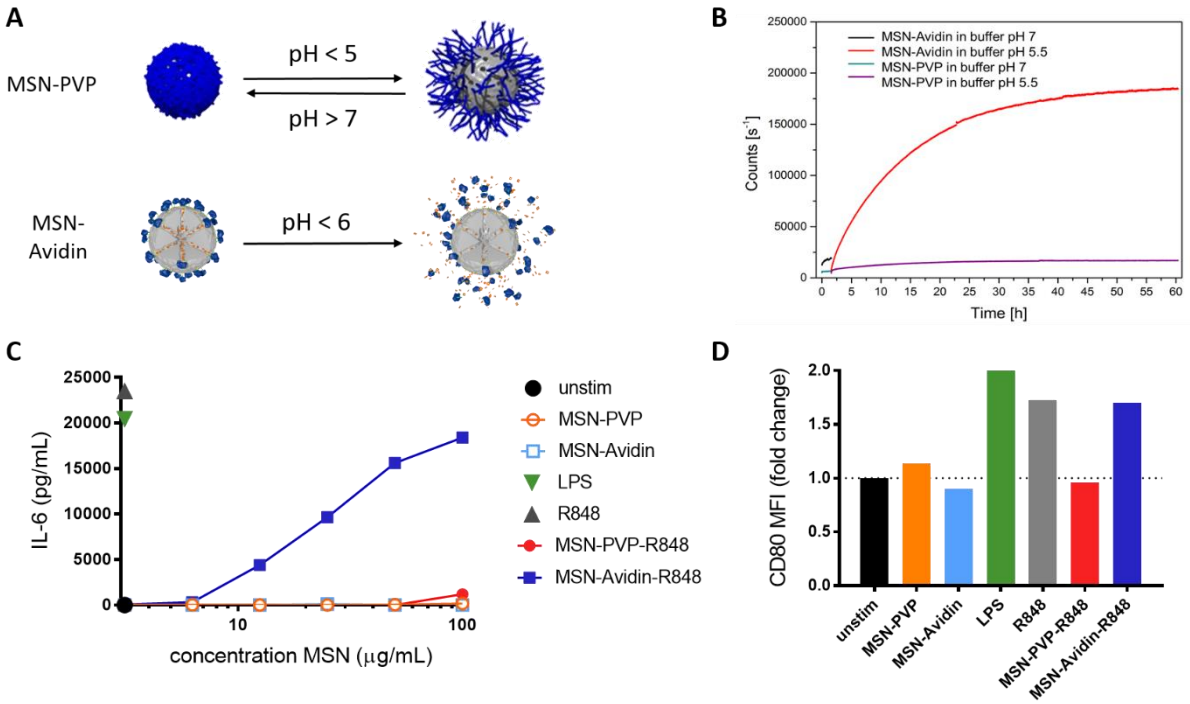

Figure 4-4. MSN-Avidin is superior to MSN-PVP as R848 carrier. Two different capping systems, PVP and Avidin (A), were compared in their ability to release R848 from the mesopores and thus activate dendritic cells. (B) The *in cuvette* time-based fluorescent release of R848 from MSN-Avidin or MSN-PVP was measured at pH 7 (DPBS buffer) and pH 5.5 (MES buffer). (C) BMDCs were incubated with increasing concentrations of the indicated MSN particles. Lipopolysaccharide (LPS, 100 ng/mL) and R848 (200 ng/mL) were included as positive controls. The secretion of the cytokine IL-6 was assessed by ELISA. (D) The cell surface expression of the co-stimulatory molecule CD80 was determined by flow cytometry. In the graph shown the MSN concentration is 50 µg/mL. The mean fluorescence intensity (MFI) in live cells is expressed relative to the unstimulated control.

In conclusion, the Avidin cap is far superior to the PVP cap as R848 release is significantly increased.

Optimization of the carrier system MSN-Avidin

Choosing the matching functionalization of the nanocarrier

Having found the optimal capping system on the outside of the particles, we next optimized the interior of the particles in regard of the drug's hydrophobicity. To enable hydrophobic interactions between the cargo and the pores, we chose hydrophobic phenyl moieties for the inside. We could show that an exchange of phenyl groups to amine groups inside the pore almost completely prevented loading of the drug due to electrostatic repulsion. This underlines that the interior of the particles has a pronounced effect on drug loading efficiency (Figure 4-5). A second step was to identify the best buffer for the loading process of resiquimod (R848). R848 is mainly uncharged at physiological pH due to a pK_a of about 6.7 of its imidiazo group. The protonation of the group at lower pH leads to a better solubility in aqueous solution and therefore a better loading performance. Nevertheless, buffers below pH 6.0 cannot be used with the chosen capping system due to the beginning hydrolysis of the acetal linker.[47] To enable hydrophobic interaction between R848 and the phenyl moieties inside the pores, a buffer with antichaotropic or rather kosmotropic ions was chosen. According to the Hofmeister series ions are divided into kosmotropic or chaotropic depending on their ability to (de-) stabilize biopolymers. Kosmotropic ions are commonly being used to either precipitate biomolecules or enhance their adsorption onto hydrophobic chromatography matrices.[48-51] The hydrophobic effect is described as the repulsion between a nonpolar compound and a polar environment such as water.[52] If a hydrophobic compound is dissolved in aqueous solution, a forced hydration shell of highly ordered water molecules is built around it which is combined with a loss of entropy. If there are more hydrophobic molecules present, they will agglomerate quickly due to an increase of entropy. By adding salts to water, one changes the conditions to either favor hydrophobic interactions or to disrupt the structure of the surrounding water molecules and therefore decrease the hydrophobic interactions.[53]

Sodium citrate is a kosmotropic salt which, at high concentrations, enhances the hydrophobic interactions. Sodium chloride is quite in the middle of the Hofmeister series, showing neither a strong salting in nor a salting out effect. The combination of both salts can be found in the highly concentrated Saline Sodium Citrate (SSC) 20x buffer. As can be seen in Figure 4-5, SSC buffer leads to the best loading result of the phenyl functionalized MSNs.

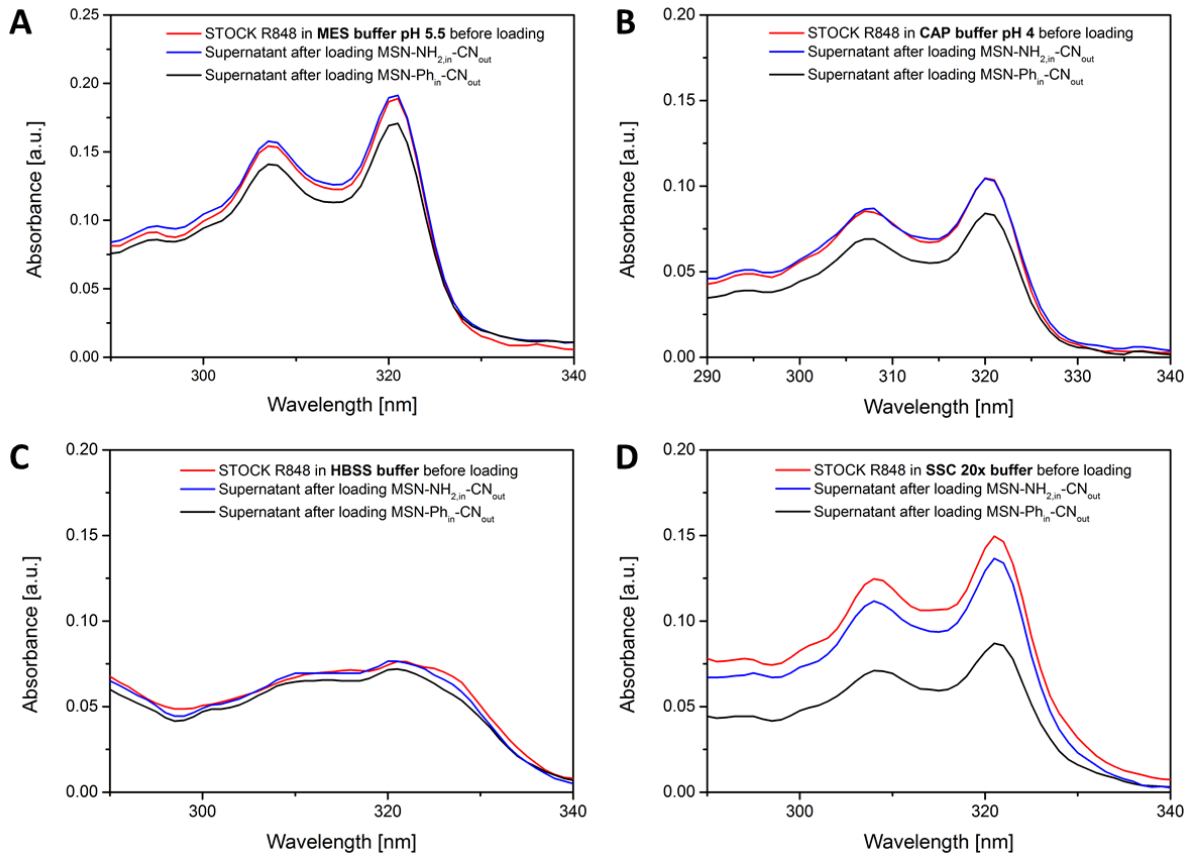

Figure 4-5. Loading in SSC20x buffer (pH 7.0) with phenyl functionalized MSNs shows the highest R848 uptake in pores. (A) Absorption spectrum of supernatants after R848 loading in 1 M MES buffer (pH 5.5). Red curve shows resiquimod stock solution in MES buffer; blue curve shows supernatant after loading of resiquimod into MSN-$NH_{2,in}$–CN_{out}, black curve shows supernatant for MSN-Ph_{in}–CN_{out}. Corresponding spectrum of supernatants after R848 loading in 0.1 M Citric Acid Phosphate Buffer (pH 4) (B), after R848 loading in HBSS buffer (pH 7.8) (C), after R848 loading in SSC20x (pH 7) (D).

Experimentally the loading efficiency in each buffer was assessed by washing the particles once with the respective buffer and then incubating them with the same amount of the R848 stock solution, prepared in the respective buffer. After 24 h at room temperature the particles were centrifuged and the supernatant measured with UV-Vis (nanodrop). To only focus on the

inside of the particles, the outside was functionalized with a neutral nitrile group, which should not interact with the cargo during the loading. As mentioned above, buffers with lower pH show a moderate loading behavior (Figure 4-5 A: MES buffer pH 5.5, 1 M), even at smaller concentrations (Figure 4-5 B: Citric Acid Phosphate (CAP) buffer pH 4, 0.1 M) due to the protonation of the imidazo group, whereas HBSS (Hank's Balanced Salt Solution) buffer with a pH of 7.8 (Figure 4-5 C) shows no loading of R848 into the pores of both samples. All in all, SSC buffer with salt concentrations of 3.0 M NaCl und 0.3 M sodium citrate and a pH value of 7.0 showed the highest loading efficiency for both samples, and especially for the MSN-Ph_{in}–CN_{out} (Figure 4-5 D).

In conclusion, the optimized R848 delivery vehicle consists of phenyl functionalized MSNs with a pH-responsive acetal linker in combination with a biotin-avidin complex as capping system.

Testing the optimized nanocarrier in long-term cuvette experiments

To avoid prematurely released R848 that leads to systemic distribution, the particles must be tightly sealed at physiological pH and show long-term stability. To test this, we performed a time-based release study in two different buffers at pH 7.0 and pH 5.5, respectively. Subsequently, we measured both samples in parallel with a multi-cuvette holder at 37 °C for 60 hours. To prove that the sample at pH 7.0 (blue curve Figure 4-6) was tightly sealed and did not lose its ability to open up at lower pH, we performed a buffer change experiment. For this, the membrane sealed cap with R848-loaded MSNs re-dispersed in SSC20x buffer was transferred after measuring for 60 hours at 37 °C to a cuvette with fresh MES buffer (pH 5.5). After two to three hours, the SSC buffer in the cap was completely exchanged with MES buffer. The resulting hydrolysis of the acetal linker could be measured with increasing amounts of detected R848 (dark pink curve).

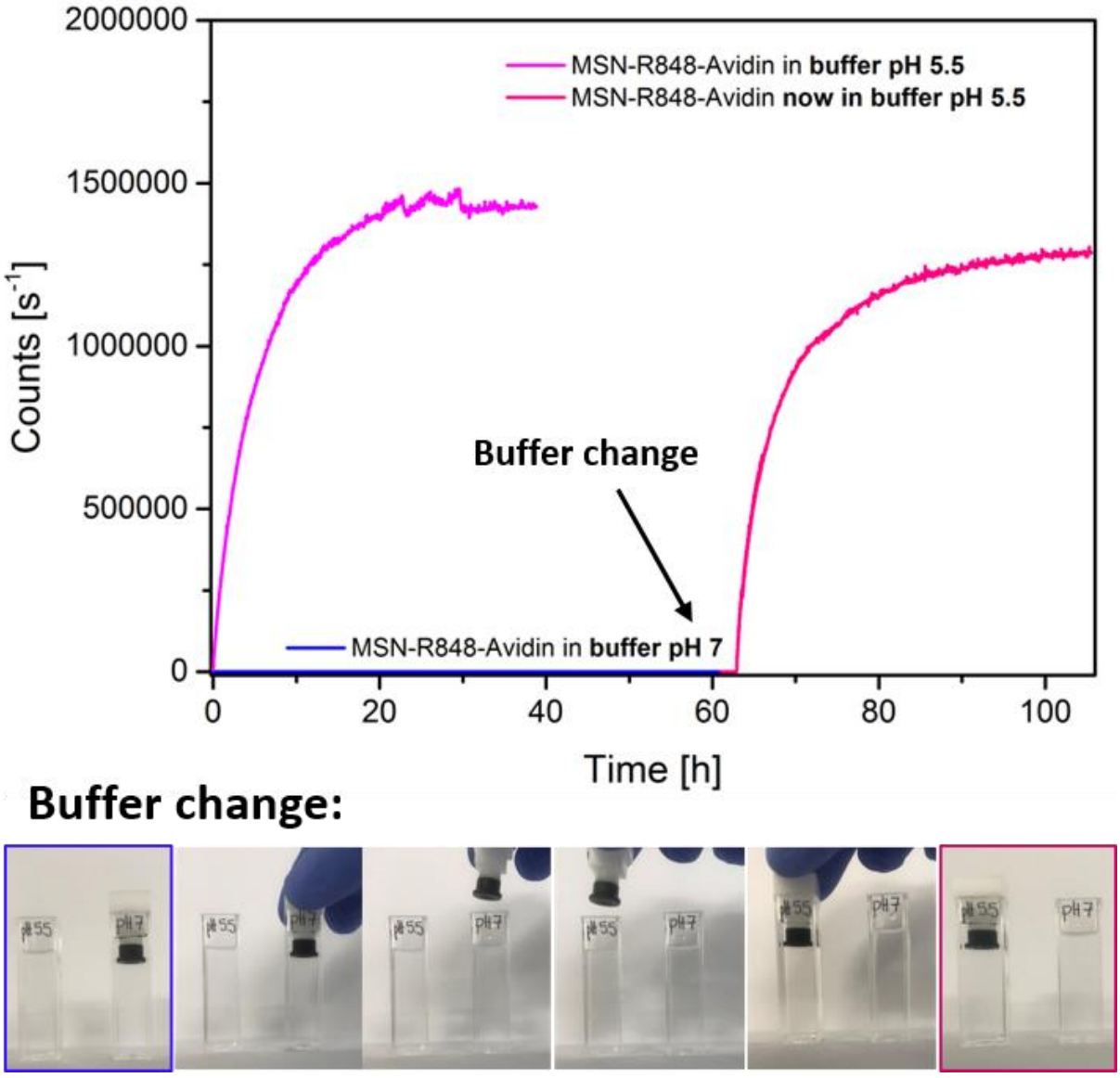

Figure 4-6. Buffer change experiment proves long-term stability of MSN-R848-Avidin at physiological pH. Time-based fluorescent release of resiquimod is measured simultaneously at pH 5.5 (MES buffer, pink curve) and pH 7.0 (SSC buffer, blue curve) and 37 °C. After 60 h a buffer change experiment takes place, as shown in the pictures: Starting from the left blue box, the cap containing tightly closed MSNs at pH 7.0 is moved to a cuvette filled with fresh MES buffer (pH 5.5). This cuvette shown in the dark pink box on the right is put back to measure the time-based release at pH 5.5 (MES buffer, dark pink curve).

Concluding, the MSN-R848-Avidin system proved long-term stability and efficient release.

Uptake of MSN into lysosomes of antigen-presenting cells

For the success of our pH-responsive drug-carrier system, it is important that the particles are efficiently taken up by antigen-presenting cells and accumulate in the acidic environment of the lysosome to ensure targeted drug-release. To investigate if our MSN-Avidin particles indeed end up in the lysosome of antigen-presenting cells, fluorescently labeled MSNs were added to a macrophage cell line (J774A.1) and analyzed by live cell imaging. To be able to see co-localization, we stained the lysosomes with LysoTracker. Uptake of MSNs into the cells was already visible 20 min after addition of the nanoparticles. After 30-40 min, a clear co-localization between the blue-stained lysosomes and the red-labelled MSNs was apparent, recognizable by the pinkish color where lysosomes and MSNs overlap (Figure 4-7 A).

In order to examine the uptake of MSNs in primary cells, freshly isolated lymph node cells and splenocytes were incubated with different concentrations of Atto633-labelled MSNs. As shown in Figure 4-7 B (and Suppl. Figure S 4-3), the particles were readily taken up by DCs (characterized as $CD19^{-}CD3^{-}CD11c^{+}$ cells) in a concentration-dependent manner. This uptake was so efficient that at higher MSN concentrations a total of 80% of all dendritic cells were MSN^{+}.

Besides the uptake, it is also important to assess whether the pH-responsive MSNs are safe to use as drug-carrier systems. Therefore, their cytotoxicity was examined on freshly isolated lymph node cells and splenocytes *in vitro* with the help of a Zombie dye. Zombie dyes react with primary amine groups on proteins. Therefore, the staining appears brighter in dead cells as the dye can enter through the disrupted cell membrane and label cytoplasmic proteins. For up to 100 µg/mL of our MSNs, we could not observe any toxic effect on these cells (Figure 4-7 C and Suppl. Figure S 4-3), and this was also true for J774A.1 macrophages and BMDCs (data not shown).

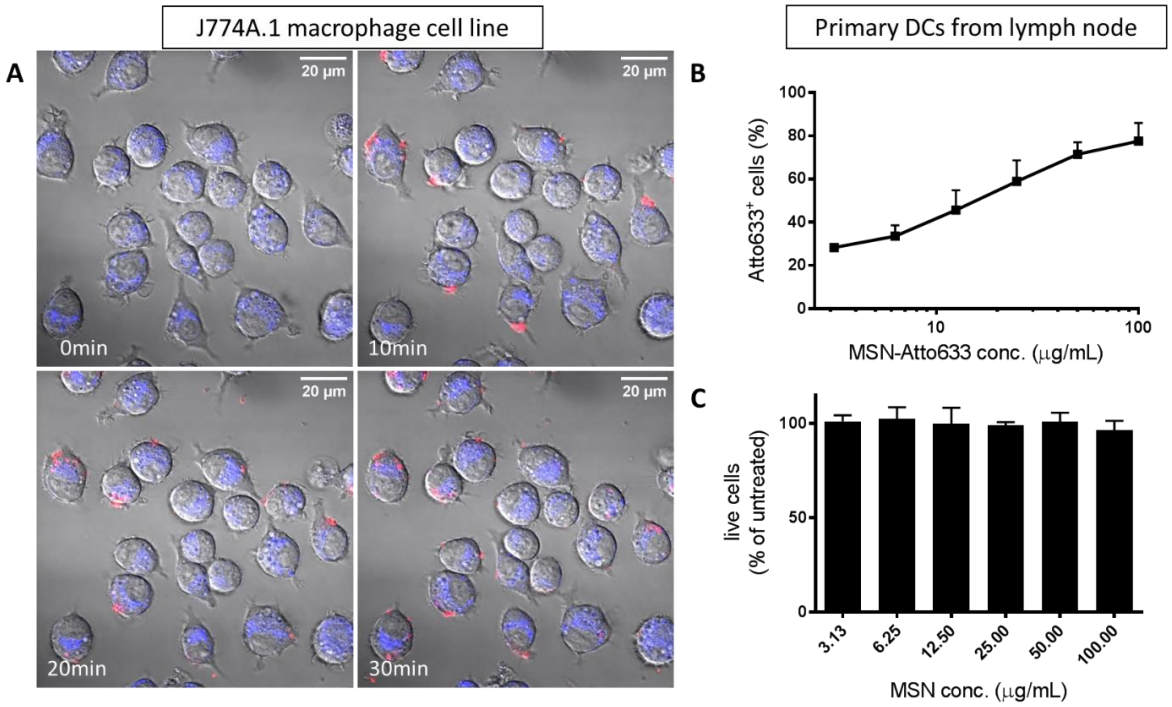

Figure 4-7. MSNs are taken up into the lysosome of antigen-presenting cells. (A) J774A.1 macrophages were stained with LysoTracker (blue) and MSN-Atto633 (red) were added to the cells at time point 0 min. Images were taken every 10 min. (B, C) Mouse lymph node cells were incubated with increasing concentrations of MSN-Atto633 for 24 h and analyzed by flow cytometry. Dead cells were excluded with the help of a Zombie dye and the dendritic cell population was characterized by $CD19^{-}CD3^{-}CD11c^{+}$ cells. The graphs show the mean and SD of minimum three independent experiments.

All in all, our MSNs did not show any cytotoxicity in the concentration range used and were readily taken up by antigen-presenting cells of the immune system.[32] Therefore, our system fulfills all the basic requirements for a promising drug delivery vehicle.

Successful activation of dendritic cells with MSN-R848

Dendritic cells are among the most potent antigen-presenting cells and patrol the body in search for pathogens or aberrant cells. Upon encounter with one of these, DCs will mature and become activated. This will result in the expression of high levels of MHC-peptide complex and co-stimulatory molecules as well as secretion of pro-inflammatory cytokines, all of which are pre-requisites for a successful induction of adaptive immune responses.

To evaluate the optimized R848 loading and release efficiencies of our avidin-system, we investigated their effect on the activation of APCs. To this end, we incubated BMDCs with

different concentrations of R848-loaded MSN and compared their response to the effect of a corresponding amount of free R848 and unloaded MSN. MSN-R848 induced secretion of high amounts of IL-6 and IL-12p40 (Figure 4-8 A) and led to upregulation of the co-stimulatory molecules CD80 and CD86 and of the MHC I complex (Figure 4-8 B). The unloaded MSN did not show any cell activating properties. Importantly, the supernatant coming from the spun down MSN-R848 induced only very low levels of IL-6 production in BMDCs. This indicates that the particles were quite stable even in cell culture conditions and only released vanishingly small amounts of R848 pre-maturely.

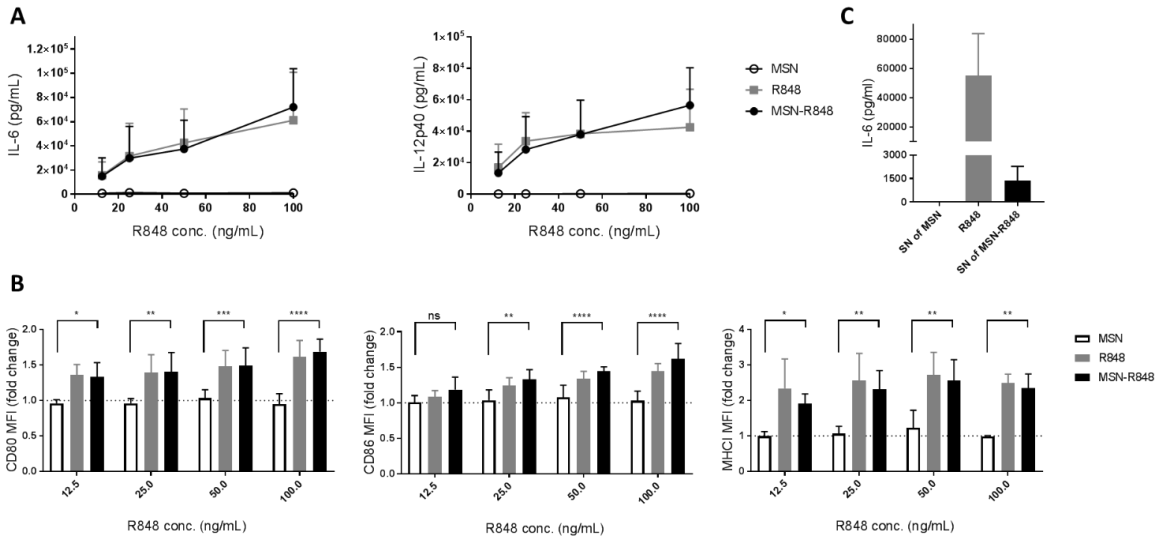

Figure 4-8. R848-loaded MSN successfully activate dendritic cells. BMDCs were incubated with increasing concentrations of MSN-R848. The amount of MSN-R848 was calculated with the help of R848-release measurements and an equimolar amount of loaded or free R848 was used. (A) The secretion of the cytokines IL-6 and IL-12p40 was measured in the cell culture supernatants by ELISA. (B) The cell surface expression of the MHC I complex and of the co-stimulatory molecules CD80 and CD86 was assessed by flow cytometry. The mean fluorescence intensity (MFI) in live cells is expressed relative to the unstimulated control. (C) BMDCs were incubated with supernatants (SN) coming from different MSN batches for 24 h. The amount of SN corresponded to the same amount of MSN that would be necessary to reach 50 ng/mL R848. The IL-6 production was measured in the cell culture supernatants by ELISA. The graphs show the mean and SD of minimum four independent experiments.

In conclusion, we developed a system that can efficiently deliver the immune-stimulant R848 to antigen-presenting cells and induce a robust immune response – measured by the upregulation of cytokine production, expression of costimulatory molecules and MHC I complex in dendritic cells.

Co-loaded MSN-R848-OVA particles enhance T cell proliferation

Potent activation of dendritic cells is important to induce a powerful cytotoxic T cell response. T cells are part of the adaptive immune system and can directly kill infected or cancerous cells when activated. Activation of T cells happens when they recognize a specific antigen presented by the MHC complex on APCs with proper co-stimulation. These antigen-specific T cells will then proliferate to fight the cells that express the recognized antigen. Cancer vaccines take advantage of this phenomenon by using a tumor-specific antigen in combination with an adjuvant to induce a strong T cell response. In order to improve our delivery system and induce a more directed, specific immune response, we attached the model antigen ovalbumin to the capping system avidin. Here, we used the peptide SIINFEKL (OVA peptide) instead of the whole protein, because the peptide usually results in a higher selectivity due to a limited number of possible epitopes. From now on, the short-form "OVA" stands for the OVA peptide.

To study how our new MSN-R848-OVA system performs in inducing activation and proliferation of T cells, we co-cultured BMDCs, stimulated with R848- and/or OVA-loaded particles, with OVA-specific T cells. To follow proliferation, T cells were labelled with the fluorescent dye CFSE (5-(and 6)-carboxyfluorescein diacetate succinimidyl ester). CFSE passively diffuses into cells and covalently links to intracellular molecules which leads to its dilution with each cell division. Therefore, lower presence of CFSE means that the T cells proliferated. As shown in Figure 4-9 A, over 80% of the T cells proliferated when incubated with MSN-R848-OVA-stimulated BMDCs. Importantly, this was considerably more than with "MSN-R848 plus free OVA" or with "free R848 and free OVA". Furthermore, activation of T cells - measured by the upregulation of CD25 – was also most pronounced when incubated with MSN-R848-OVA stimulated BMDCs.

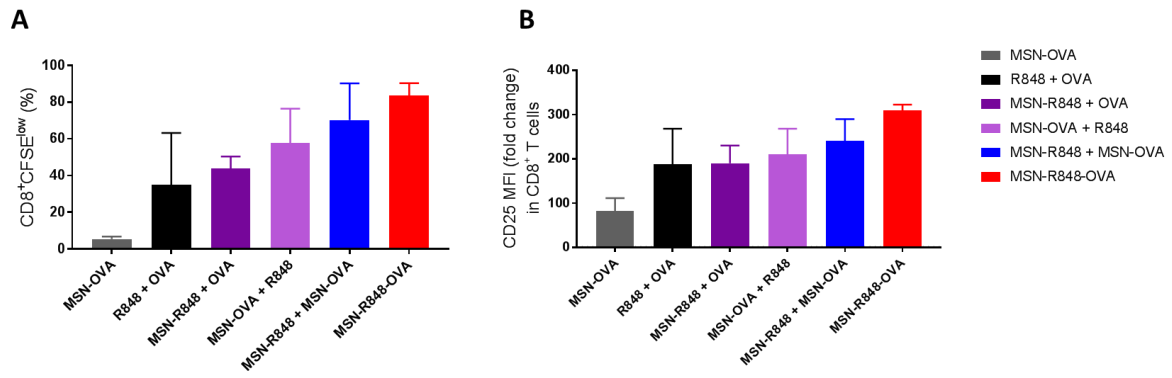

Figure 4-9. MSN-R848-OVA particles induce T cell proliferation and activation in vitro. BMDCs were exposed to different combinations of R848- and/or OVA peptide-loaded MSN. The amount of MSN-R848 used was equimolar to 50 ng/mL R848; free OVA peptide was used at a concentration of 10 ng/mL. After 24 h, OVA-specific, CFSE-labeled CD8+ T cells were added to the BMDCs and co-cultured for another 2-3 days. (A) Proliferation of T cells was determined by analysis of CFSE expression (CFSElow) with flow cytometry. (B) Activation of T cells was assessed by the surface expression of CD25. The MFI in live CD8+ T cells is expressed relative to the unstimulated control. The graphs show the mean and SD of two independent experiments.

In conclusion, MSN-R848-OVA stimulated dendritic cells induced a potent cytotoxic T cell response and seem to be promising vaccine carriers.

Biodistribution of MSN-Avidin in mice

After proving the potential of pH-responsive MSN in vitro, we investigated their safety and biodistribution in vivo. C57BL/6 mice were injected sc. with fluorescent Atto633-labelled MSN or PBS and left for 14 days with daily assessment of weight and behaviour. In this time period, the mice did not show any toxicity signs and gained weight comparable to the control group (Suppl. Figure S 4 4).

For the biodistribution evaluation, mice were analyzed one day after MSN-Atto633 injection (Figure 4 10 A). The ipsilateral inguinal and axillary as well as the contralateral inguinal lymph nodes (LNs) and the spleen were investigated for MSN-Atto633+ cells by flow cytometry (Figure 4 10 B). Unsurprisingly, we found the highest amount of MSN+ cells in the ipsilateral inguinal lymph node (iLN), which is the draining lymph node for the injection site (Figure 4 10 C). Few mice also showed MSN+ cells in the ipsilateral axillary LN. However,

these mice had less MSN+ cells in the iLN, which led us to the conclusion that a slight variation in the injection site could have turned the axillary LN to the first draining LN

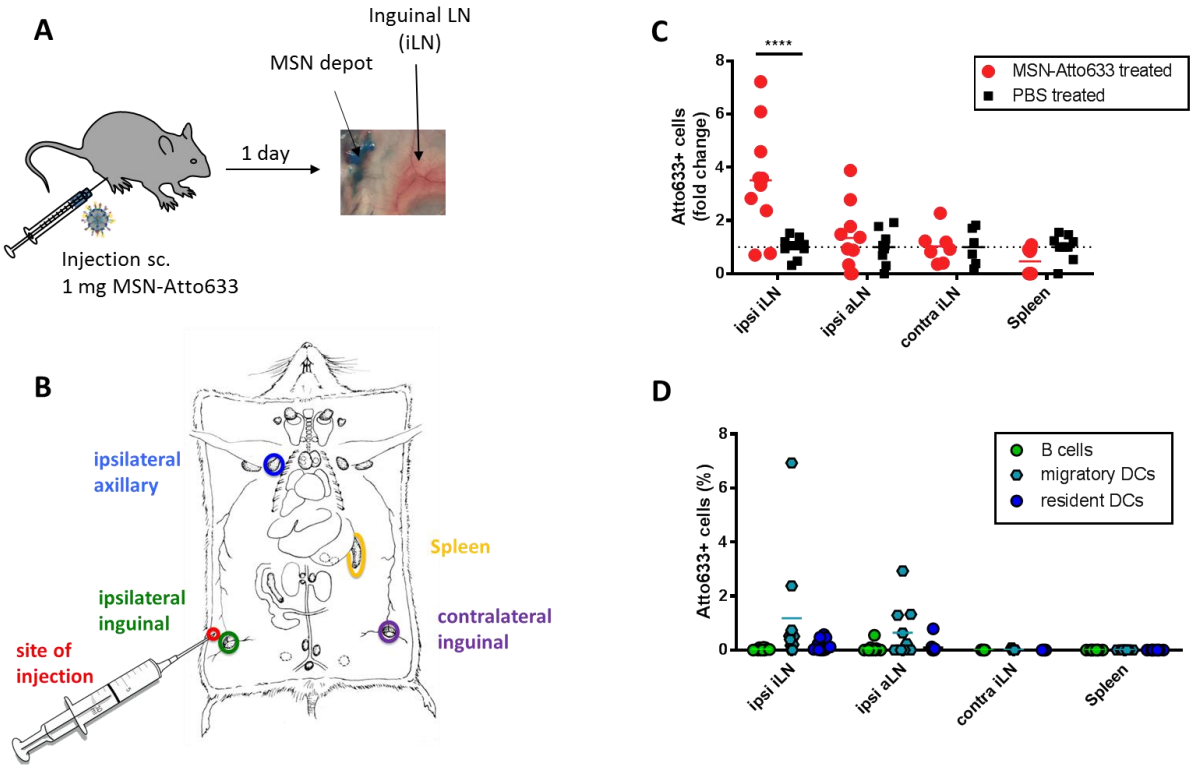

Figure 4-10. MSNs are mainly found in the draining lymph node in migratory DCs. (A) 1 mg of Atto633-labeled MSNs were subcutaneously injected into the right hind limb of mice and analyzed after 24 h. (B) Ipsilateral and contralateral lymph nodes and spleens were analyzed by flow cytometry (the scheme was adapted from Dunn, T.B. 1954).[54] (C) The amount of MSN-Atto633^{+} cells in the different organs was compared to the control group (PBS). (D) The uptake of MSN-Atto633 was analysed in different cell populations: B cells (CD45^{+}CD3^{-}CD19^{+}), resident DCs (CD45^{+}CD3^{-}CD19^{-}CD11c^{+}MHCII^{low}), migratory DCs (CD45^{+}CD3^{-}CD19^{-}CD11c^{+}MHCII^{high}). The graphs show the results of three independent experiments.

In all mice, we consistently found that the contralateral lymph node and the spleen did not show any MSN-Atto633+ cells after 24 h. Further analyzing the different cell populations in these organs, we could see that mainly migratory DCs (CD19-CD3-CD11c+MHCIIhigh) in the ipsilateral iLN took up the MSNs (Figure 4 10 D). As the avidin-capped MSNs with a particle size of around 280 nm are too large to be drained with the interstitial flow to lymphoid organs from the injection site, it came as no surprise to find them predominantly in migratory dendritic cells. Thus, MSNs are taken up by patrolling dendritic cells and brought to the next draining lymphoid organ, in our case mostly the ipsilateral inguinal lymph node.

4.3. Discussion and Conclusion

In this study, we developed a tight pH-responsive drug delivery system for the TLR7/8 ligand R848 that induced potent immune activation. By comparing a reversibly working polymer capping system that opens and closes upon pH-dependent (de-) protonation of the PVP group with an avidin closure mechanism triggered by the hydrolysis of the acetal linker at lower pH, we were able to show that irreversible detachment of the bulky protein gatekeeper leads to enhanced drug release. Furthermore, we demonstrated that correctly tailoring the multifunctional MSNs enables augmented loading of the hydrophobic drug R848. For this purpose, we performed a delayed co-condensation approach, developed in our group, to introduce phenyl groups solely into the pores.[42] It was proven before that this synthesis procedure allows spatial control over incorporated organic moieties.[35] Delayed functionalization of the exterior surface in the same synthesis procedure with carboxylic groups allowed for further modification with a pH-responsive acetal linker and the respective biotin-avidin capping system. The pH-dependent hydrolysis of the linker, already shown in literature, enables stimuli-responsive opening of the pores.[47] This stimulus is of particular interest in the project described here due to the fact that MSN are taken up into dendritic cells. This uptake occurs as energy-dependent endocytosis because of the nanoparticles' size of 280 nm as also shown by Vallhov *et al.*.[55] The pH in the endosome drops to a value of pH 5.5 when it fuses with the lysosome. It thereby triggers the cleavage of the applied acetal linker, inducing the pore opening and therefore also drug release through complete detachment of the bulky biotin-avidin complex.[56] Besides closing the drug loaded pores tightly, capping of the MSNs with the protein avidin also leads to improved particle-cell interactions. As shown by van Rijt *et al.,* avidin coating of the MSNs leads to enhanced biocompatibility.[57] Compared to amine-functionalized MSNs which were shown to exhibit a strong protein corona formation, avidin coating of the particles minimizes this effect and the subsequent clearance by

macrophages.[58] Furthermore, Zhang *et al.* reported that anionic vaccines were not taken up by APCs due to the repulsion of negatively charged particles and negatively charged phospholipid bilayers of the cell membranes.[59] The dramatic change in surface charge after addition of avidin to the MSNs, as seen by a shift in zeta potential from – 50 mV (MSN-Ph_{in}–$COOH_{out}$) to + 20 mV (MSN-Ph_{in}–$Avidin_{out}$), enables an attractive and not repulsive particle-dendritic cell interaction and thus facilitates the uptake by APCs. Successful uptake of avidin-coated MSNs in antigen-presenting cells *in vitro* was already observed within 30 min, proving the positive influence of the protein capping system. Furthermore, we could show that our MSN system was also preferably taken up by APCs *in vivo*. After subcutaneous injection of the particles into mice, they were mainly found in migratory dendritic cells in the draining LN. As the size of the MSNs prevents them from draining freely to the closest lymphoid organs, an entrapment of MSNs, consisting of all MSNs that were not yet taken up by cells under the skin could still be observed after 24 h. This depot effect could be beneficial in a clinical setting with loaded particles. It would ensure the continuous uptake of the particles by migratory dendritic cells, which would lead to a prolonged immune cell activation in the lymph node beyond 24 h. Yet the balance between a stronger, continuous immune response and the induction of immune tolerance will have to be closely investigated in future experiments.

When OVA peptide and R848 were co-loaded into the MSNs, we could demonstrate that potent T cell activation and proliferation was induced. As previously shown, simultaneous delivery of both adjuvant and antigen to the same cell increases the potency of a vaccine.[60] This phenomenon is also apparent with our MSN-R848-OVA particles and underlines the great potential of MSNs as combined carrier system for both adjuvant and antigen. In this work, we used only the OVA peptide as a model antigen. However, the system is easily adaptable and other antigens could be attached to avidin. This means that even several

different tumor-specific antigens could be loaded onto the MSNs to achieve a stronger anti-tumor effect.[61-65] Furthermore, the MSNs could also accommodate patient-specific tumor-antigens to generate a "personalized" MSN vaccine carrier system. The adjustability of the pore size of mesoporous silica particles also enables loading of larger antigen proteins. This was shown by Cha *et al.,* who successfully delivered the complete OVA protein in combination with a TLR-9 adjuvant in extra-large pore MSNs.[66] It has to be noted that antigen and adjuvant were both loaded *via* electrostatic interactions into randomly amine-functionalized particles without additional capping system. This may cause premature release and therefore systemic activation or enhanced protein corona formation and thus rapid clearance of the particles before they reach dendritic cells. Our spatially controlled synthesis of core-shell MSN with a multifunctional capping system can overcome these problems.

In sum, we were able to demonstrate that MSNs hold considerable promise as a carrier system for the immune-stimulant R848. They display significant adjustability and flexibility which allows for simultaneous delivery of adjuvant and antigen and the specific generation of an enhanced T cell response. Our tight pH-responsive system thus shows great potential as a successful cancer vaccine in future therapies, enabling advantageous local immune activation while preventing adverse systemic events.

4.4. Experimental Part

Materials. All reagents were purchased from commercial suppliers. Tetraethyl orthosilicate (TEOS, Sigma-Aldrich, >98%), cetyltrimethylammonium chloride (CTAC, Fluka, 25wt% in H_2O), triethanolamine (TEA, Sigma-Aldrich, 98%), triethoxyphenylsilane (PhTES, Sigma-Aldrich, 98%), 3-(triethoxysilyl)propylsuccinic anhydride (TEPSA, ABCR, 60-70%), 3,9-bis(3-aminopropyl)-2,4,8,10-tetraoxaspiro[5.5]undecane (AK linker, TCI, ≥ 98%), biotin (Sigma-Aldrich, ≥99%), avidin, egg white (Merck Millipore, ≥10 units/mg protein), (3-aminopropyl)-triethoxysilane (APTES, Fluka, 95%), N-(3-dimethylaminopropyl)-N-ethylcarbodiimide hydrochloride (EDC, Sigma-Aldrich, 97%), ammonium nitrate (Sigma-Aldrich, 99%), conc. hydrochloric acid (Sigma-Aldrich, >95%, 37 wt%), α-amino-ω-carboxy terminated poly(2-vinylpyridine) (NH_2-PVP-COOH, Polymer Source, M_n = 10.000, PDI = 1.08), Boc anhydride (Aldrich, 95%), N-hydroxysulfosuccinimide sodium salt (*sulfo*-NHS, Sigma-Aldrich, 98%), ethanol (EtOH, Sigma-Aldrich, >99.5%), tetrahydrofuran (THF, anhydrous, Sigma-Aldrich, ≥99.9%), trifluoroacetic acid (TFA, Acros Organics, 99%), magnesium sulfate ($MgSO_4$, anhydrous, Sigma-Aldrich, ≥99.5%), triethylamine (Sigma-Aldrich, ≥99%), saline-sodium citrate buffer concentrate (SSC-buffer (20x), Sigma-Aldrich), 2-morpholinoethanesulfonic acid hydrate (MES hydrate, Sigma-Aldrich, ≥99,5%), fluorescamine (Fluram, Sigma-Aldrich, ≥99%), TLR-7/8 agonist resiquimod (R848, Enzo, ≥98%), OVA 257-264 peptide (chicken egg albumin, Invivogen, ≥95%), 2-iminothiolane hydrochloride (Sigma-Aldrich, ≥98%), alpha-maleimido-24(ethylene glycol)-omega-propionic acid succinimidyl ester (mal-dPEG(24)-NHS, Iris Biotech GmbH). All chemicals were used as received without further purification. Doubly distilled water from a Millipore system (Milli-Q Academic A10) was used for all synthesis and purification steps.

Preparation of MES buffer (0.1 M, pH 5.5). 2-(N-Morpholino)ethanesulfonic acid (MES, 9.76 g) was dissolved in 500 mL water. The pH was adjusted to 5.5 using sodium hydroxide (1 M).

Synthesis procedures.

Polymer-capped MSNs (MSN-PVP) were synthesized and loaded with R848 as previously described.[33, 32, 34]

Preparation of core-shell-functionalized colloidal mesoporous silica nanoparticles (MSN-Ph_{in}-$COOH_{out}$). Core-shell functionalized MSNs were synthesized according to a slightly modified synthesis approach as previously reported.[35] In detail, a mixture of tetraethyl orthosilicate (TEOS, 1.62 g, 7.79 mmol) and triethoxyphenylsilane (PhTES, 0.45 g, 1.86 mmol) was added as a layer on top of triethanolamine (TEA, 14.3 g, 95.6 mmol) and heated without stirring at 90 °C for 20 min in a polypropylene reactor. Subsequently, a solution of cetyltrimethylammonium chloride (CTAC, 2.41 mL, 1.83 mmol, 25 wt% in H_2O) and ammonium fluoride (NH_4F, 100 mg, 2.7 mmol) in water (21.7 g, 1.21 mmol) preheated to 60 °C was quickly added and the reaction mixture vigorously stirred (700 rpm, 20 min) while cooling down to room temperature. Afterwards, four equal portions of TEOS (192.2 mg in total, 0.922 mmol) were added every 3 min and the reaction mixture was allowed to stir for another 30 min at room temperature. In the end, TEOS (38.3 mg, 184 µmol) and 3-(triethoxysilyl)propylsuccinic anhydride (TEPSA, 56.2 mg, 184 µmol) were added and the resulting mixture allowed to stir overnight at room temperature. In the following, MSNs were collected by centrifugation (43,146 rcf, 20 min) and re-dispersed in absolute ethanol. Subsequent template extraction of the MSNs was performed in 100 mL ethanolic solution, containing ammonium nitrate (NH_4NO_3, 2 g), under reflux heating at 90 °C for 45 min. After centrifugation (7179 rcf, 15 min) and re-dispersion in ethanol, the described extraction was

performed a second time. Finally, the MSNs were collected by centrifugation (7179 rcf, 15 min) and washed with 100 mL absolute ethanol, resulting in the sample MSN-Ph_{in}–$COOH_{out}$.

AK linker attachment (MSN-Ph_{in}–AK_{out}). 50 mg MSN-Ph_{in}–$COOH_{out}$ were collected by centrifugation (7179 rcf, 15 min) and re-dispersed in 70 mL of a 1:1 = EtOH:HBSS buffer solution. Subsequently, N-(3-dimethylaminopropyl)-N-ethylcarbodiimide hydrochloride (EDC, 20 µL, 114.4 µmol) was added under vigorous stirring of the particle solution. 10 minutes later, N-hydroxysulfosuccinimide sodium salt (sulfo-NHS, 2.6 mg, 12 µmol) was added and the reaction mixture allowed to stir five more minutes at room temperature. Afterwards, the acetal linker 3,9-bis(3-aminopropyl)-2,4,8,10-tetraoxaspiro[5.5]undecane (AK linker, 917 µL (55 mg, 0.20 mmol) from stock solution with c = 60 mg/mL in 1:1-EtOH:HBSS-mixture) was added dropwise to the solution and the resulting mixture was allowed to stir overnight (700 rpm, room temperature). Particles were collected by centrifugation (7179 rcf, 15 min) and washed twice with absolute ethanol (50 mL).

Biotin functionalization (MSN-Ph_{in}–$Biotin_{out}$). Biotin (6 mg, 24.6 µmol) was dissolved in a DMSO/EtOH mixture (500 µL DMSO, 2.5 mL EtOH). Subsequently, EDC (6 µL, 34.3 µmol) was added under vigorous stirring, followed by sulfo-NHS (0.78 mg, 3.6 µmol). Then, 30 mg of MSN-Ph_{in}–AK_{out}, re-dispersed in 40 mL ethanol, was added dropwise to the solution. The reaction mixture was allowed to react overnight (700 rpm, room temperature). Particles were collected by centrifugation (7179 rcf, 15 min) and washed likewise twice with absolute ethanol (50 mL).

Avidin coating (MSN-Ph_{in}-$Avidin_{out}$). 2 mg MSN-R848-Biotin was centrifuged (5500 rcf, 4 min, 15 °C) and re-dispersed in 400 µL avidin solution (c=10 mg/mL). The reaction mixture was allowed to react under dark and static conditions at room temperature overnight. The

resulting particles (MSN-Ph_{in}-$Avidin_{out}$) were extensively washed with SSC20x buffer (pH 7.0) and centrifuged (5500 rcf, 4 min., 15 °C) until no absorption was detected in the supernatant.

Attachment of OVA peptide to avidin cap (MSN-Ph_{in}-OVA_{out}). A solution with 1 mg of the R848-loaded MSN-Avidin was centrifuged (5500 rcf, 4 min., 15 °C) and the solid was redispersed in 500 µL DPBS buffer. In the meantime, 2-iminothiolane hydrochloride (0.4 mg, 2.9 µmol) was added to a solution of 50 µL of OVA peptide (c = (OVA-Stock) = 1 mg/mL in bi-distilled water) in 450 µL DPBS buffer. The mixture was allowed to react for 1 h at room temperature under static conditions. Afterwards, the hetero-bifunctional PEG-linker mal-PEG(24)-NHS (0.6 mg, 430 µmol) was added and the reaction mixture allowed to react another hour at room temperature without stirring. The activated OVA-PEG-linker was successively added to the MSN solution and the mixture was allowed to react one more hour (static conditions). Subsequently, the OVA-functionalized particles were washed three times with DPBS buffer (5500 rcf, 4 min., 15 °C).

Labeling of MSNs with covalently attached Atto-dyes. 1 mg of MSN-SH_{in}-$Biotin_{out}$ was redispersed in 1 mL ethanol and 5 µL Atto633-maleimide (or alternatively Atto488-mal) was added. The reaction mixture was allowed to react overnight at room temperature in the dark under static conditions. Subsequently, the labeled particles were washed three times with ethanol (1 mL EtOH, 14000 rpm, 5 min, RT) and one time with SSC20x buffer before avidin was added to the solution (as described above). Labeled particles were used for uptake and biodistribution studies.

Characterization of MSNs. Centrifugation was performed using a Sigma 3-30KS equipped with a fixed-angle rotor 12310 or an Eppendorf centrifuge (5430 for volumes up to 50 mL or 5418 for small volumes). Samples were investigated with a Tecnai G2 20 S-Twin

transmission electron microscope operated at 200 kV with a bright field detector. A droplet of the diluted MSN solution in absolute ethanol was dried on a carbon-coated copper grid at room temperature for several hours. Nitrogen sorption measurements were performed on a Quantachrome Instruments NOVA 4000e. In general, samples (15 mg each) were heated to 60 °C for 12 h in vacuum (10 mTorr) to outgas them before nitrogen sorption measurements. MSN-Ph_{in}–$Avidin_{out}$ was the only sample which was outgassed at room temperature for 12 h in vacuum (10 mTorr). Subsequent nitrogen sorption measurments were performed at 77 K. Pore size and pore volume were calculated by a NLDFT equilibrium model of N_2 on silica, based on the adsorption branch of the isotherms. Pore volumes were calculated only up to a pore size of 8 nm to avoid contributions of interparticle textural porosity. The specific surface area of the samples was determined with a BET model applied in the range of 0.05 – 0.20 p/p_0. Dynamic light scattering (DLS) measurements were performed on a Malvern Zetasizer-Nano instrument equipped with a 4 mW He-Ne laser (633 nm) and an avalanche photodiode. To determine the hydrodynamic radius of the particles, 100 µL of an ethanolic MSNs suspension (ca. 10 mg/mL) was diluted with 3 mL of ethanol prior to the DLS measurement. The sample MSN-Ph_{in}–$Avidin_{out}$ was respectively measured in water. Zeta potential measurements of the samples were performed on a Malvern Zetasizer-Nano instrument equipped with a 4 mW He-Ne laser (633 nm) and an avalanche photodiode using the add-on Zetasizer titration system (MPT-2) (based on diluted NaOH and HCl as titrants). For this purpose, particles were diluted in 10 mL bi-distilled water to achieve a final MSN concentration of 0.1 mg/mL. Thermogravimetric analysis was performed on a Netzsch STA 440 C TG/DSC with a heating rate of 10 K / min in a stream of synthetic air of about 25 mL/min. The mass was normalized to 100% at 130 °C for all samples to exclude the influence of solvent desorption. A Thermo Scientific Nicolet iN10 IR-microscope was used to record infrared spectra of dried sample powders in reflection-absorption mode with a liquid-N_2

cooled MCT-A detector. UV-Vis measurements with 2 µl of the samples were performed on a NanoDrop 2000c spectrometer from Thermo Scientific Fisher. Time-based fluorescence release experiments were performed at 37 °C on a PTI spectrofluorometer equipped with a xenon short arc lamp (UXL-75XE USHIO) and a photomultiplier detection system (Model 810/814) with λ_{ex} = 323 nm and λ_{em} = 342 nm. Emission scans of fluorescent samples and corresponding calibration curves were measured at room temperature with λ_{ex} = 323 nm and λ_{em} = 335-355 nm.

Fluram assay. 2.5 mg particles from ethanolic solution were washed one time with MeOH and subsequently redispersed in 2 mL MeOH. Subsequently, 1 mL of a freshly prepared Fluram solution (6.957 mg in 5 mL MeOH, 5 mM) was added and the mixture vigorously shaken and vortexed for 2 minutes. Immediately afterwards, samples were measured with fluorescence spectroscopy (λ_{ex} = 420 nm, λ_{em} = 440-540 nm).

Release experiments.

Drug loading. 2 mg MSN-Ph_{in}–$Biotin_{out}$ was washed once with SSC20x buffer, followed by re-dispersion in 500 µL R848 stock solution (consisting of 50 µL resiquimod (c=10 mg/mL) in 450 µL SSC20x buffer (pH 7.0)), yielding an overall drug concentration of 1 mg/mL in the loading solution. The particles were shaken for 1 h (thermoshaker, 600 rpm, room temperature), centrifuged, washed 5 times with SSC20x buffer and re-dispersed in 400 µL avidin solution (c = 10 mg/mL in SSC20x buffer) to trigger closure of the pores by biotin-avidin complex formation. The resulting particles (MSN-Ph_{in}-$Avidin_{out}$) were extensively washed with SSC20x buffer (pH 7.0) until no absorption was detected in the supernatant. For *in vivo* experiments, MSNs were re-dispersed in SSC20x buffer at a concentration of 10 mg/mL.

Time-based fluorescence release experiments *in cuvette*. A sample of 1 mg R848-loaded MSNs re-dispersed in 1 mL SSC20x buffer was split into two and centrifuged (5500 rcf, 4 min., 15 °C). One half (0.5 mg MSNs) was re-dispersed again in 200 µL SSC20x buffer (pH 7.0), the other half in 200 µL MES buffer (pH 5.5). Afterwards, the MSNs (200 µL each) were transferred to custom-made caps which were sealed with a dialysis membrane (ROTH Visking type 8/32, MWCO 14,000 g/mol) and put on top of a disposable PMMA cuvette (UV grade). The cutoff molecular weight of the dialysis membrane is too low for MSNs and the detached biotin-avidin complex, meaning only released resiquimod can diffuse through the membrane to be measured in the cuvette. The cuvette setup can be seen in Figure 4-6 (buffer change experiment). The pH-dependent cargo release was measured at 37 °C for 60 h (λ_{ex} = 323 nm, λ_{em} = 342 nm).

Quantification of released resiquimod. To determine the amount of released resiquimod, samples were allowed to cool down to room temperature after the time-based release. Subsequently, emission scans were performed at 22 °C (λ_{ex} = 323 nm, λ_{em} = 335-355 nm). To enable quantification (calibration), emission scans of concentration ranges of resiquimod in the respective buffers were measured under the same condition as mentioned above. Results were plotted and linearly fitted with Origin Pro 9.0, to be able to calculate the released resiquimod amounts.

Supernatant/Loading control with UV-Vis (Nanodrop). To follow the time-dependent loading of resiquimod, supernatants during the loading process were measured with Nanodrop (2 µL sample, blank: corresponding buffer). Furthermore, the successful washing procedure was monitored by measuring the decreasing absorption of the washing supernatants.

Biological assays.

Uptake of MSN by antigen-presenting cells. J774A.1 macrophages (ATCC, TIB-67) were plated at a concentration of $5*10^4$ cells/well on a Lab-Tek chamber plate (Nunc) in high glucose (4.5 g/L) DMEM (Biowest) supplemented with 10% FBS (MP Biomedicals), 2 mM L-Glutamine (Corning, Fisher Scientific), 1 mM Sodium pyruvate (Gibco) and 0.5% Ciprofloxacin (Bayer). After overnight incubation at 37 °C, the cells were stained with LysoTracker™ (Blue DND-22, life technologies) for 1 h at a final concentration of 50 nM. Atto633-labeled MSNs (20 µg/mL) were then added directly onto the cells. Live cell imaging was performed using a confocal microscope (Zeiss LSM 710 Meta) with 63x magnification.

To assess uptake into primary cells, single cell suspensions from total spleen and lymph nodes were used. To obtain single cell suspensions from spleens, the tissue was mechanically disrupted and filtered through a 40 µm cell strainer (Corning). Erythrocytes were lysed using Pharm Lyse™ buffer (BD Biosciences). To attain single cell suspensions from lymph nodes, the tissue was cut and digested in RPMI-1640 (Gibco) supplemented with 2% FBS (MP Biomedicals), 1x Penicillin/Streptomycin (Gibco), 10 mM HEPES (Gibco), 2 mM calcium chloride (Acros Organics), 3 mg/mL Collagenase IV (Worthington) and 200 U/mL DNAse I (Worthington) at 37 °C for 20-30 min on a shaker. After digestion, the suspension was filtered through a 40 µm cell strainer (Corning). Splenocytes or lymph node cells were cultured in RPMI-1640 (Gibco), 10% FBS (MP Biomedicals), 2 mM L-Glutamine (Gibco), 1x Penicillin/Streptomycin (Gibco), 1 mM Sodium pyruvate (Gibco), 1x Non-essential amino acids (Gibco), 50 µM 2-mercaptoethanol (Gibco) on a 96-well flat bottom plate (Greiner) at a density of $5*10^5$ cells/well. MSN were added at concentrations between 3-200 µg/mL to the cells and incubated overnight before analysis by flow cytometry.

Dendritic cell activation assay. Bone marrow derived dendritic cells (BMDCs) were generated as previously described[36] with the only difference that cells were split 1 to 2 at day 3. On day 6 BMDCs were seeded on a 96-well flat bottom plate (Greiner) at a density of $1*10^5$ cells/well and stimulated with different concentrations of R848-loaded MSN, free R848 (Enzolive), LPS (Lipopolysaccharide, Invivogen) or supernatants coming from the spun down MSN formulations. The amount of MSN-R848 was calculated with the help of R848-release measurements and an equimolar amount of loaded or free R848 was used. After 18-24 h, cells and culture supernatants were collected and analyzed by flow cytometry and ELISA, respectively.

T cell proliferation assay *in vitro*. BMDCs were generated as described in the previous section and seeded at a density of $1*10^5$ cells/well on a 96-well flat bottom plate. Cells were then stimulated with different concentrations of R848- and/or SIINFEKL-loaded MSN for 24h. SIINFEKL-specific $CD8^+$ T cells were isolated from spleens coming from OT-I transgenic mice. For purification of $CD8^+$ T cells, magnetic-associated cell sorting (MACS) with the $CD8a^+$ T cell isolation kit (Miltenyi) was performed according to manufacturer's protocol. T cells were stained with 0.5 µM CFSE (5-(and 6)-carboxyfluorescein diacetate succinimidyl ester, Biolegend) for 10 min at 37 °C before adding them onto the stimulated BMDCs at a density of $1*10^5$ cells/well in very-low endotoxin RPMI-1640 (Biochrom), 10% FBS (MP Biomedicals), 2 mM L-Glutamine (Gibco), 1x Penicillin/Streptomycin (Gibco), 1 mM Sodium pyruvate (Gibco), 1x Non-essential amino acids (Gibco), 50 µM 2-mercaptoethanol (Gibco). T cell proliferation and activation was analyzed by flow cytometry and ELISA after 2-3 days.

Quantification of cytokines. Cell supernatants were collected and analyzed for cytokine secretion by enzyme-linked immunosorbent assay (IL-6, IL-12p40 ELISA kits, Biolegend) according to the manufacturer's protocol.

Flow cytometry. Cell suspensions were stained in PBS (Gibco) with 0.5% BSA (Pan Biotech), 0.5 mM EDTA (Promega). Fc receptor block (TruStain FCX anti-mouse CD16/32), fluorochrome-coupled antibodies against the surface antigens CD3, CD4, CD8, CD11b, CD11c, CD19, CD25, CD45, CD80, CD86, MHCI, MHCII and appropriate isotype controls were all purchased from Biolegend. To assess cell death, a Zombie dye (Biolegend) was used according to manufacturer's protocol. Cells were acquired on the flow cytometer Novocyte (Acea Biosciences) and analyzed using the software FlowJo V10.

MSN biodistribution in mice. To assess the biodistribution of the particles in different organs, mice were injected subcutaneously (sc.) in the right hind limb with 1 mg of Atto633-labeled MSN in a volume of 100 µl. For the control group 100 µl of PBS was injected. After 24 h, lymph nodes and spleens were collected and organs were processed as described in previous sections to obtain single cell suspensions. The cells were then analyzed by flow cytometry.

Mice. Female C57Bl/6 and OT-I mice (purchased from Charles River, France) were housed under specific pathogen-free conditions and were 6-16 weeks of age at the time of the experiment. All animal studies were conducted in accordance with local regulations.

Statistics. All data sets are presented as mean + SD (standard deviation). For multiple statistical comparison of a data set the two-way ANOVA test with either Turkey or Sidak post-test was used. Significance was set at *p*-values $p < 0.05$, $p < 0.01$, $p < 0.001$, $p < 0.0001$ and was then indicated with an asterisk (*, **, ***and ****). All statistical calculations were performed with GraphPad Prism (Version 7).

4.5. References

1. Couzin-Frankel, J., Breakthrough of the year 2013. Cancer immunotherapy. *Science* **2013,** *342* (6165), 1432-3.
2. Chen, Daniel S.; Mellman, I., Oncology Meets Immunology: The Cancer-Immunity Cycle. *Immunity* **2013,** *39* (1), 1-10.
3. Ribas, A.; Wolchok, J. D., Cancer immunotherapy using checkpoint blockade. *Science* **2018,** *359* (6382), 1350-1355.
4. Smith, M.; García-Martínez, E.; Pitter, M. R.; Fucikova, J.; Spisek, R.; Zitvogel, L.; Kroemer, G.; Galluzzi, L., Trial Watch: Toll-like receptor agonists in cancer immunotherapy. *OncoImmunology* **2018,** *7* (12), e1526250.
5. Geisse, J.; Caro, I.; Lindholm, J.; Golitz, L.; Stampone, P.; Owens, M., Imiquimod 5% cream for the treatment of superficial basal cell carcinoma: results from two phase III, randomized, vehicle-controlled studies. *J. Am. Acad. Dermatol.* **2004,** *50* (5), 722-733.
6. Dockrell, D. H.; Kinghorn, G. R., Imiquimod and resiquimod as novel immunomodulators. *J. Antimicrob. Chemother.* **2001,** *48* (6), 751-755.
7. Dowling, D. J., Recent Advances in the Discovery and Delivery of TLR7/8 Agonists as Vaccine Adjuvants. *ImmunoHorizons* **2018,** *2* (6), 185-197.
8. Rook, A. H.; Gelfand, J. M.; Wysocka, M.; Troxel, A. B.; Benoit, B.; Surber, C.; Elenitsas, R.; Buchanan, M. A.; Leahy, D. S.; Watanabe, R.; Kirsch, I. R.; Kim, E. J.; Clark, R. A., Topical resiquimod can induce disease regression and enhance T-cell effector functions in cutaneous T-cell lymphoma. *Blood* **2015,** *126* (12), 1452-1461.
9. Goldstein, D.; Hertzog, P.; Tomkinson, E.; Couldwell, D.; McCarville, S.; Parrish, S.; Cunningham, P.; Newell, M.; Owens, M.; Cooper, D. A., Administration of imiquimod, an interferon inducer, in asymptomatic human immunodeficiency virus-infected persons to determine safety and biologic response modification. *J. Infect. Dis.* **1998,** *178* (3), 858-861.
10. Lynn, G. M.; Laga, R.; Darrah, P. A.; Ishizuka, A. S.; Balaci, A. J.; Dulcey, A. E.; Pechar, M.; Pola, R.; Gerner, M. Y.; Yamamoto, A.; Buechler, C. R.; Quinn, K. M.; Smelkinson, M. G.; Vanek, O.; Cawood, R.; Hills, T.; Vasalatiy, O.; Kastenmüller, K.; Francica, J. R.; Stutts, L.; Tom, J. K.; Ryu, K.; Esser-Kahn, A. P.; Etrych, T.; Fisher, K. D.; Seymour, L. W.; Seder, R. A., In vivo characterization of the physicochemical properties of polymer-linked TLR agonists that enhance vaccine immunogenicity. *Nat. Biotechnol.* **2015,** *33* (11), 1201-1210.
11. Thomas, S. N.; Vokali, E.; Lund, A. W.; Hubbell, J. A.; Swartz, M. A., Targeting the tumor-draining lymph node with adjuvanted nanoparticles reshapes the anti-tumor immune response. *Biomaterials* **2014,** *35* (2), 814-824.
12. Rueda, F.; Eich, C.; Cordobilla, B.; Domingo, P.; Acosta, G.; Albericio, F.; Cruz, L. J.; Domingo, J. C., Effect of TLR ligands co-encapsulated with multiepitopic antigen in nanoliposomes targeted to human DCs via Fc receptor for cancer vaccines. *Immunobiology* **2017,** *222* (11), 989-997.
13. Rahimian, S.; Fransen, M. F.; Kleinovink, J. W.; Christensen, J. R.; Amidi, M.; Hennink, W. E.; Ossendorp, F., Polymeric nanoparticles for co-delivery of synthetic long peptide antigen and poly IC as therapeutic cancer vaccine formulation. *J. Controlled Release* **2015,** *203*, 16-22.
14. Rosalia, R. A.; Cruz, L. J.; van Duikeren, S.; Tromp, A. T.; Silva, A. L.; Jiskoot, W.; de Gruijl, T.; Löwik, C.; Oostendorp, J.; van der Burg, S. H.; Ossendorp, F., CD40-targeted dendritic cell delivery of PLGA-nanoparticle vaccines induce potent anti-tumor responses. *Biomaterials* **2015,** *40*, 88-97.
15. Bulbake, U.; Doppalapudi, S.; Kommineni, N.; Khan, W., Liposomal Formulations in Clinical Use: An Updated Review. *Pharmaceutics* **2017,** *9* (2).
16. Schwendener, R. A., Liposomes as vaccine delivery systems: a review of the recent advances. *Ther. Adv. Vaccines* **2014,** *2* (6), 159-182.
17. Mahjub, R.; Jatana, S.; Lee, S. E.; Qin, Z.; Pauli, G.; Soleimani, M.; Madadi, S.; Li, S.-D., Recent advances in applying nanotechnologies for cancer immunotherapy. *J. Controlled Release* **2018,** *288*, 239-263.
18. Tabatabaei Mirakabad, F. S.; Nejati-Koshki, K.; Akbarzadeh, A.; Yamchi, M. R.; Milani, M.; Zarghami, N.; Zeighamian, V.; Rahimzadeh, A.; Alimohammadi, S.; Hanifehpour, Y.; Joo, S. W., PLGA-Based Nanoparticles as Cancer Drug Delivery Systems. *Asian Pac. J. Cancer Prev.* **2014,** *15* (2), 517-535.
19. Zupančič, E.; Silva, J.; Videira, M. A.; Moreira, J. N.; Florindo, H. F., Development of a Novel Nanoparticle-based Therapeutic Vaccine for Breast Cancer Immunotherapy. *Procedia Vaccinol.* **2014,** *8*, 62-67.

20. Kim, H.; Niu, L.; Larson, P.; Kucaba, T. A.; Murphy, K. A.; James, B. R.; Ferguson, D. M.; Griffith, T. S.; Panyam, J., Polymeric nanoparticles encapsulating novel TLR7/8 agonists as immunostimulatory adjuvants for enhanced cancer immunotherapy. *Biomaterials* **2018,** *164*, 38-53.
21. Widmer, J.; Thauvin, C.; Mottas, I.; Nguyen, V. N.; Delie, F.; Allémann, E.; Bourquin, C., Polymer-based nanoparticles loaded with a TLR7 ligand to target the lymph node for immunostimulation. *Int. J. Pharm.* **2018,** *535* (1), 444-451.
22. Ilyinskii, P. O.; Roy, C. J.; O'Neil, C. P.; Browning, E. A.; Pittet, L. A.; Altreuter, D. H.; Alexis, F.; Tonti, E.; Shi, J.; Basto, P. A.; Iannacone, M.; Radovic-Moreno, A. F.; Langer, R. S.; Farokhzad, O. C.; von Andrian, U. H.; Johnston, L. P. M.; Kishimoto, T. K., Adjuvant-carrying synthetic vaccine particles augment the immune response to encapsulated antigen and exhibit strong local immune activation without inducing systemic cytokine release. *Vaccine* **2014,** *32* (24), 2882-2895.
23. Oliveira, C. L.; Veiga, F.; Varela, C.; Roleira, F.; Tavares, E.; Silveira, I.; Ribeiro, A. J., Characterization of polymeric nanoparticles for intravenous delivery: Focus on stability. *Colloids Surf., B.* **2017,** *150*, 326-333.
24. Mottas, I.; Bekdemir, A.; Cereghetti, A.; Spagnuolo, L.; Yang, Y.-S. S.; Müller, M.; Irvine, D. J.; Stellacci, F.; Bourquin, C., Amphiphilic nanoparticle delivery enhances the anticancer efficacy of a TLR7 ligand via local immune activation. *Biomaterials* **2019,** *190-191*, 111-120.
25. Havel, H. A., Where Are the Nanodrugs? An Industry Perspective on Development of Drug Products Containing Nanomaterials. *AAPS J.* **2016,** *18* (6), 1351-1353.
26. Bobo, D.; Robinson, K. J.; Islam, J.; Thurecht, K. J.; Corrie, S. R., Nanoparticle-Based Medicines: A Review of FDA-Approved Materials and Clinical Trials to Date. *Pharm. Res.* **2016,** *33* (10), 2373-87.
27. Zhang, X., Gold Nanoparticles: Recent Advances in the Biomedical Applications. *Cell Biochem. Biophys.* **2015,** *72* (3), 771-775.
28. Argyo, C.; Weiss, V.; Bräuchle, C.; Bein, T., Multifunctional Mesoporous Silica Nanoparticles as a Universal Platform for Drug Delivery. *Chem. Mater.* **2014,** *26* (1), 435-451.
29. Möller, K.; Bein, T., Degradable Drug Carriers: Vanishing Mesoporous Silica Nanoparticles. *submitted* **2019**.
30. Bunker, B. C., Molecular mechanisms for corrosion of silica and silicate glasses. *J. Non-Cryst. Solids* **1994,** *179*, 300-308.
31. Vallet-Regí, M.; Colilla, M.; Izquierdo-Barba, I.; Manzano, M., Mesoporous Silica Nanoparticles for Drug Delivery: Current Insights. *Molecules* **2018,** *23* (1).
32. Heidegger, S.; Gößl, D.; Schmidt, A.; Niedermayer, S.; Argyo, C.; Endres, S.; Bein, T.; Bourquin, C., Immune response to functionalized mesoporous silica nanoparticles for targeted drug delivery. *Nanoscale* **2016,** *8* (2), 938-48.
33. Cauda, V.; Schlossbauer, A.; Kecht, J.; Zürner, A.; Bein, T., Multiple Core-Shell Functionalized Colloidal Mesoporous Silica Nanoparticles. *J. Am. Chem. Soc.* **2009,** *131* (Copyright (C) 2012 American Chemical Society (ACS). All Rights Reserved.), 11361-11370.
34. Niedermayer, S.; Weiss, V.; Herrmann, A.; Schmidt, A.; Datz, S.; Muller, K.; Wagner, E.; Bein, T.; Bräuchle, C., Multifunctional polymer-capped mesoporous silica nanoparticles for pH-responsive targeted drug delivery. *Nanoscale* **2015,** *7* (17), 7953-64.
35. Cauda, V.; Schlossbauer, A.; Kecht, J.; Zürner, A.; Bein, T., Multiple Core−Shell Functionalized Colloidal Mesoporous Silica Nanoparticles. *J. Am. Chem. Soc.* **2009,** *131* (32), 11361-11370.
36. Helft, J.; Böttcher, J.; Chakravarty, P.; Zelenay, S.; Huotari, J.; Schraml, Barbara U.; Goubau, D.; Reis e Sousa, C., GM-CSF Mouse Bone Marrow Cultures Comprise a Heterogeneous Population of CD11c(+)MHCII(+) Macrophages and Dendritic Cells. *Immunity* **2015,** *42* (6), 1197-1211.
37. Schlossbauer, A.; Kecht, J.; Bein, T., Biotin-avidin as a protease-responsive cap system for controlled guest release from colloidal mesoporous silica. *Angew. Chem. Int. Ed.* **2009,** *48* (17), 3092-3095.
38. Fisher, T. Avidin-Biotin Interaction. https://www.thermofisher.com/de/de/home/life-science/protein-biology/protein-biology-learning-center/protein-biology-resource-library/pierce-protein-methods/avidin-biotin-interaction.html (accessed Sat. 23 Feb 2019).
39. Pugliese, L.; Coda, A.; Malcovati, M.; Bolognesi, M., Three-dimensional Structure of the Tetragonal Crystal Form of Egg-white Avidin in its functional Complex with Biotin at 2·7 Å Resolution. *J. Mol. Biol.* **1993,** *231* (3), 698-710.
40. Cauda, V.; Engelke, H.; Sauer, A.; Arcizet, D.; Bräuchle, C.; Rädler, J.; Bein, T., Colchicine-loaded lipid bilayer-coated 50 nm mesoporous nanoparticles efficiently induce microtubule depolymerization upon cell uptake. *Nano Lett.* **2010,** *10* (7), 2484-92.
41. Huh, S.; Wiench, J. W.; Yoo, J.-C.; Pruski, M.; Lin, V. S. Y., Organic Functionalization and Morphology Control of Mesoporous Silicas via a Co-Condensation Synthesis Method. *Chem. Mater.* **2003,** *15* (22), 4247-4256.

42. Kecht, J.; Schlossbauer, A.; Bein, T., Selective Functionalization of the Outer and Inner Surfaces in Mesoporous Silica Nanoparticles. *Chem. Mater.* **2008,** *20* (23), 7207-7214.
43. Kobler, J.; Möller, K.; Bein, T., Colloidal Suspensions of Functionalized Mesoporous Silica Nanoparticles. *ACS nano* **2008,** *2* (4), 791-799.
44. Held, P., Fluorimetric Quantitation of Protein using the Reactive Compound Fluorescamine. *Nat. Methods / Application Notes* **2006**.
45. Niedermayer, S.; Weiss, V.; Herrmann, A.; Schmidt, A.; Datz, S.; Müller, K.; Wagner, E.; Bein, T.; Bräuchle, C., Multifunctional polymer-capped mesoporous silica nanoparticles for pH-responsive targeted drug delivery. *Nanoscale* **2015,** *7* (17), 7953-7964.
46. Kobold, S.; Wiedemann, G.; Rothenfußer, S.; Endres, S., Modes of action of TLR7 agonists in cancer therapy. *Immunotherapy* **2014,** *6* (10), 1085-1095.
47. Liu, R.; Zhang, Y.; Zhao, X.; Agarwal, A.; Mueller, L. J.; Feng, P., pH-Responsive Nanogated Ensemble Based on Gold-Capped Mesoporous Silica through an Acid-Labile Acetal Linker. *J. Am. Chem. Soc.* **2010,** *132* (5), 1500-1501.
48. Baldwin, R. L., How Hofmeister ion interactions affect protein stability. *Biophys. J.* **1996,** *71* (4), 2056-2063.
49. Cacace, M. G.; Landau, E. M.; Ramsden, J. J., The Hofmeister series: salt and solvent effects on interfacial phenomena. *Q. Rev. Biophys.* **1997,** *30* (3), 241-277.
50. Deckwer, M., Hofmeistersche Reihen. In *RÖMPP Lexikon Biotechnologie und Gentechnik*, Georg Thieme Verlag: 1999; Vol. 2, p 376.
51. Kniep, R.; Jaenicke, L.; Winter, R.; Fischer-Henningsen, D.; Lippert, B.; Gottschild, D.; Umbrecht, H.; Zahn, T., Wissenschaft Aktuell. *Chem. Unserer Zeit* **1996,** *30* (1), 46-51.
52. Kennedy, R. M., Hydrophobic chromatography. *Methods Enzymol.* **1990,** *182*, 339-43.
53. Porath, J.; Sundberg, L.; Fornstedt, N.; Olsson, I., Salting-out in Amphiphilic Gels as a New Approach to Hydrophobia Adsorption. *Nature* **1973,** *245* (5426), 465-466.
54. Dunn, T. B., Normal and pathologic anatomy of the reticular tissue in laboratory mice, with a classification and discussion of neoplasms. *J. Natl. Cancer Inst.* **1954,** *14* (6), 1281-433.
55. Vallhov, H.; Gabrielsson, S.; Strømme, M.; Scheynius, A.; Garcia-Bennett, A. E., Mesoporous Silica Particles Induce Size Dependent Effects on Human Dendritic Cells. *Nano Lett.* **2007,** *7* (12), 3576-3582.
56. Geisow, M. J.; Evans, W. H., pH in the endosome: Measurements during pinocytosis and receptor-mediated endocytosis. *Exp. Cell Res.* **1984,** *150* (1), 36-46.
57. van Rijt, S. H.; Bölükbas, D. A.; Argyo, C.; Wipplinger, K.; Naureen, M.; Datz, S.; Eickelberg, O.; Meiners, S.; Bein, T.; Schmid, O.; Stoeger, T., Applicability of avidin protein coated mesoporous silica nanoparticles as drug carriers in the lung. *Nanoscale* **2016,** *8* (15), 8058-8069.
58. Oh, J. Y.; Kim, H. S.; Palanikumar, L.; Go, E. M.; Jana, B.; Park, S. A.; Kim, H. Y.; Kim, K.; Seo, J. K.; Kwak, S. K.; Kim, C.; Kang, S.; Ryu, J.-H., Cloaking nanoparticles with protein corona shield for targeted drug delivery. *Nat. Commun.* **2018,** *9* (1), 4548.
59. Zhang, R.; Smith, J. D.; Allen, B. N.; Kramer, J. S.; Schauflinger, M.; Ulery, B. D., Peptide Amphiphile Micelle Vaccine Size and Charge Influence the Host Antibody Response. *ACS Biomater. Sci. Eng.* **2018,** *4* (7), 2463-2472.
60. Wilson, J. T.; Keller, S.; Manganiello, M. J.; Cheng, C.; Lee, C.-C.; Opara, C.; Convertine, A.; Stayton, P. S., pH-Responsive Nanoparticle Vaccines for Dual-Delivery of Antigens and Immunostimulatory Oligonucleotides. *ACS nano* **2013,** *7* (5), 3912-3925.
61. Duperret, E. K.; Liu, S.; Paik, M. J.; Trautz, A.; Stoltz, R.; Liu X.; Ze K.; Perales-Puchalt A.; Reed C.; Yan J.; Xu X.; Weiner D. B., A designer cross-reactive DNA immunotherapeutic vaccine that targets multiple MAGE-A family members simultaneously for cancer therapy. *Clin. Cancer Res.* **2018**.
62. Liu, L. N.; Shivakumar, R.; Allen, C.; Protocols, F.-J. C., Delivery of whole tumor lysate into dendritic cells for cancer vaccination. *Electroporation Protocols* **2008**.
63. Chang, J.-H.; Tsai, P.-H.; Chen, W.; Chiou, S.-H.; Mou, C.-Y., Dual delivery of siRNA and plasmid DNA using mesoporous silica nanoparticles to differentiate induced pluripotent stem cells into dopaminergic neurons. *J. Mater. Chem. B* **2017,** *5* (16), 3012-3023.
64. Zhao, Y.; Trewyn, B. G.; Slowing, I. I.; Lin, V.-S., Mesoporous silica nanoparticle-based double drug delivery system for glucose-responsive controlled release of insulin and cyclic AMP. *J. Am. Chem. Soc.* **2009,** *131* (24), 8398-8400.
65. Colilla, M.; González, B.; Vallet-Regí, M., Mesoporous silica nanoparticles for the design of smart delivery nanodevices. *Biomater. Sci.* **2013,** *1* (2), 114-134.
66. Cha, B. G.; Jeong, J. H.; Kim, J., Extra-Large Pore Mesoporous Silica Nanoparticles Enabling Co-Delivery of High Amounts of Protein Antigen and Toll-like Receptor 9 Agonist for Enhanced Cancer Vaccine Efficacy. *ACS Cent. Sci.* **2018,** *4* (4), 484-492.

4.6. Appendix

Comparison of thermogravimetric analysis data of unfunctionalized, phenyl$_{in}$-functionalized and phenyl$_{in}$-carboxyl$_{out}$-MSNs shows successful implementation of a relative phenyl content of 15% (Figure S 4-1).

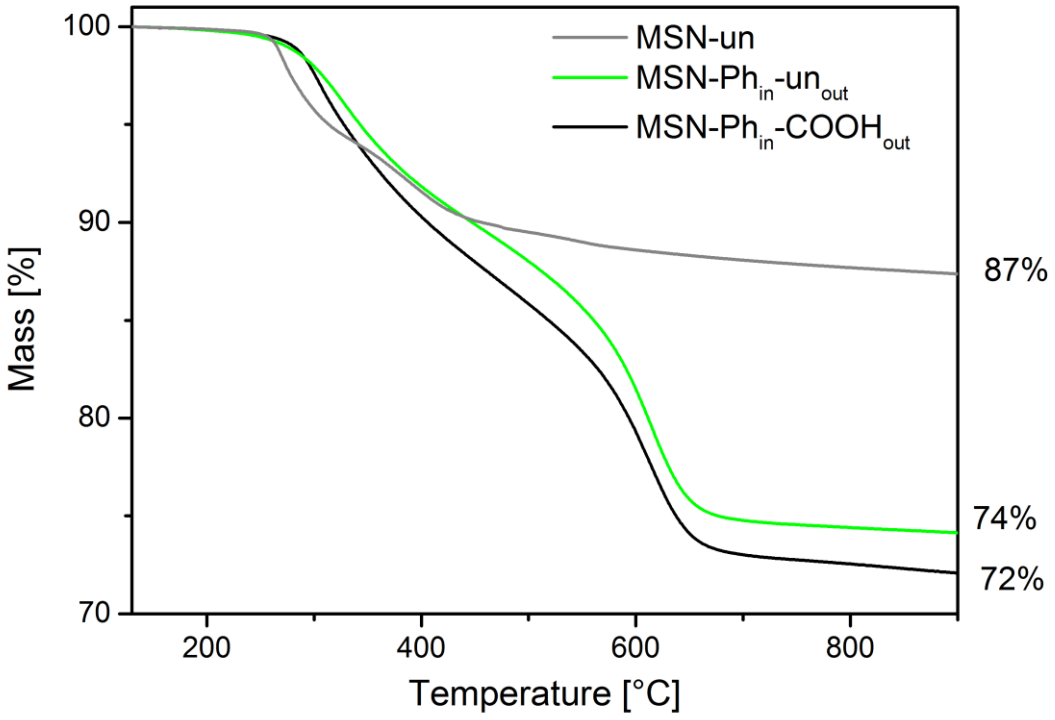

Figure S 4-1. TGA measurements of unfunctionalized MSNs (grey curve), only phenyl-functionalized MSNs (green curve) and MSN-Ph$_{in}$–COOH$_{out}$ (black curve).

The additional mass loss of sample MSN-Ph$_{in}$–un$_{out}$ was used to determine the degree of phenyl functionalization inside the pores. This was calculated according to Equation S 1 with the additional mass loss of 13% for MSN-Ph$_{in}$–un$_{out}$. The estimated degree was determined to be 10.4%, indicating that not all PhTES used in the synthesis was incorporated into the silica nanoparticles (theoretical value of organic functionalization: 17%).

$$Mass\ loss\ (TGA) = \frac{x \cdot M_w('phenyl')}{x \cdot M_w('phenyl') + (100 - x)M_w(SiO_2)}$$

Equation S 1. Calculation to determine estimated percentage of incorporated phenyl groups into MSNs. x (%): estimated degree of organic functionalization. M_w('phenyl') = 77.1 g/mol. $M_w(SiO_2)$ = 60.1 g/mol

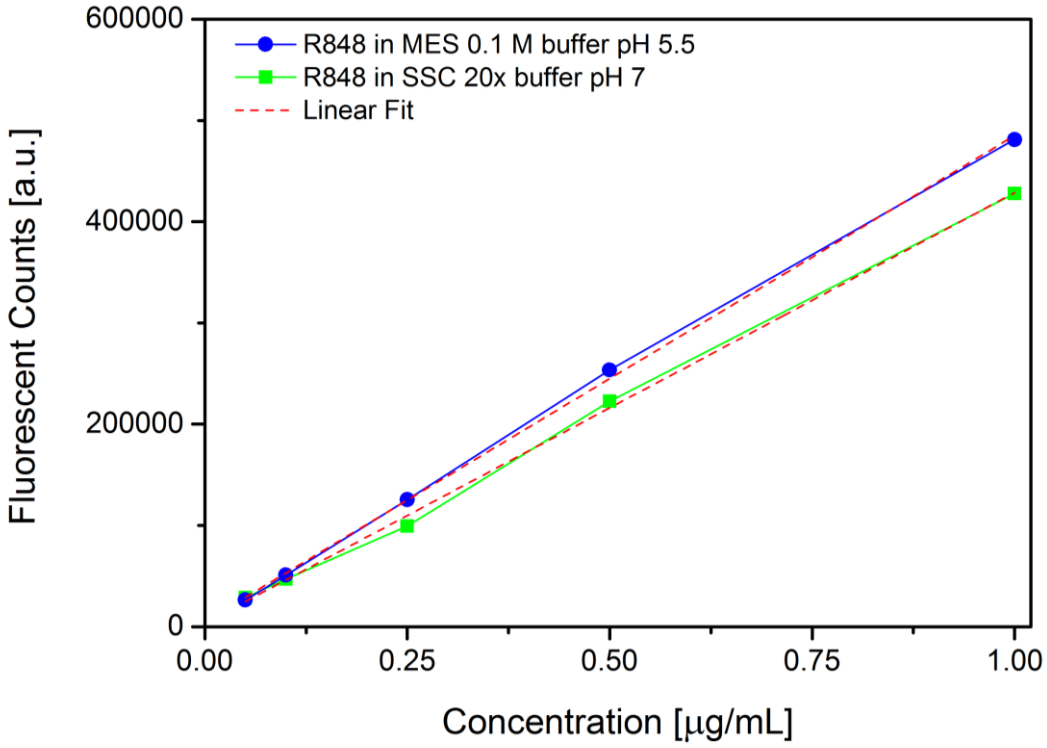

Figure S 4-2. Calibration curves of resiquimod in MES and SSC20x buffer.

Quantification of the released amount of R848 was determined after reaching the saturation plateau as shown in Figure 4-6. Subsequently, emission scans of the resulting R848 concentrations were recorded as well as concentration ranges in the respective buffers. The amount of released resiquimod was calculated by applying the respective linear equation (Figure S 4-3).

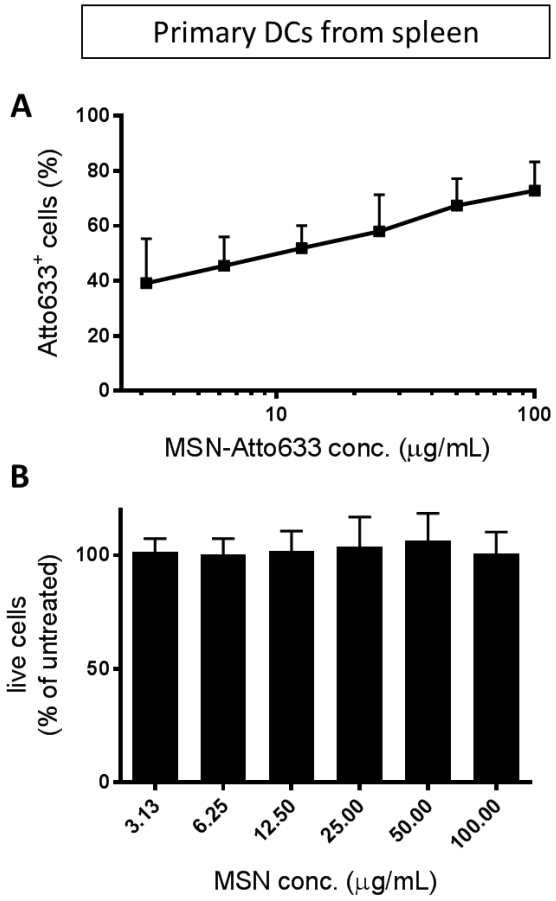

Figure S 4-3. Uptake and toxicity of MSN in splenocytes. (A, B) Total mouse splenocytes were incubated with increasing concentrations of MSN-Atto633 for 24 h and analyzed by flow cytometry. Dead cells were excluded with the help of a Zombie dye and the dendritic cell population was characterized by $CD19^{-}CD3^{-}CD11c^{+}$ cells. The graphs show the mean and SD of a minimum of three independent experiments.

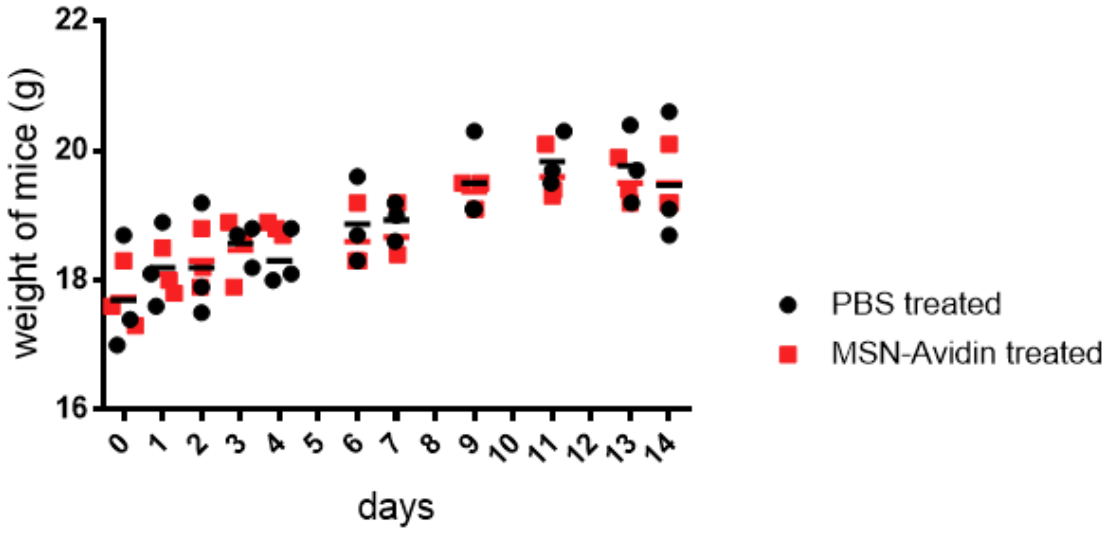

Figure S 4-4. Mice injected with MSN gained weight comparable to control group. 1 mg of MSNs were subcutaneously injected into the right hind limb of mice and the weight of the mice was measured at indicated time points over a period of 14 days.

CHAPTER 5

Clickable Multifunctional Large-Pore Mesoporous Silica Nanoparticles as Nanocarriers

5. Clickable Multifunctional Large-Pore Mesoporous Silica Nanoparticles as Nanocarriers

This chapter was published as:

Hsin-Yi Chiu[§], Dorothée Gößl[§], Lisa Haddick, Hanna Engelke and Thomas Bein, *Chem. Mater*. **2018**, *30*, 644-654.

[§] These authors contributed equally.

Abstract

Large-pore mesoporous silica nanoparticles (LP-MSNs) with defined particle size (< 200 nm) are promising carrier systems for the cellular delivery of macromolecules. Ideal nanocarriers should be adaptable in their surface properties to optimize host-guest interactions; thus, surface functionalization of the nanovehicles is highly desirable. In this study, we synthesized various monofunctional LP-MSNs by incorporating different organic groups into the silica framework *via* a co-condensation approach. Further, we applied a delayed co-condensation strategy to create spatially segregated core-shell bifunctional LP-MSNs. Diverse particle morphologies were obtained by adding different organosilanes to the silica precursor solution. The effect of organosilanes in the co-condensation process on particle size and pore structure formation is also discussed. Surface functional groups were then used for binding stimuli-responsive linkers. These were finally exploited for copper-free click chemistry for cargo conjugation to create a delivery system with controlled cargo release. Model cargo release experiments in buffer using these new multifunctional LP-MSNs demonstrate their ability in controlled cargo uptake and release and their potential for biomolecule delivery.

5.1. Introduction

Since the discovery of periodically ordered mesoporous silica MCM-41 in 1992,[1-2] scientists have spent great efforts on tailoring physical and chemical properties (i.e., particle size and morphology, pore size and structure, surface functionalities, etc.) of mesoporous silica materials and have accommodated a variety of cargos in the mesopores for the study of guest-host interactions.[3-5] Nanosized mesoporous silica materials (mesoporous silica nanoparticles, MSNs) feature several favorable properties, for example, high surface area and pore volume, ease of surface functionalization and biocompatibility, which make them suitable nanocarriers for biomedical applications.[6-7] Furthermore, mesoporous silica particles can be used as templates to create polymer capsules for targeted drug delivery.[8-9]In the past decade, multifunctional MSNs have been developed for controlled release as well as targeted delivery of various therapeutics such as anti-cancer drugs, antibiotics, etc. either *in vitro* or *in vivo*.[6-7, 10] However, most of the drug delivery tasks were achieved using small-pore (≤ 4 nm) MSNs. As the development of siRNA and protein therapies has dramatically advanced in recent years,[11-13] the interest in developing MSNs for drug delivery purposes has turned toward synthesizing large pores for accommodating sizable biomolecules while simultaneously retaining particle sizes smaller than 200 nm for better cellular uptake or an increased EPR (enhanced permeability and retention) effect.[14-16] Numerous research articles regarding the synthesis of large-pore MSNs with suitable particle sizes have been published in the past years. Recently, Zhang *et al.* reported a synthesis using cetyltrimethylammonium p-toluenesulfonate (CTATos) as surfactant in near-neutral precursor solutions, resulting in wide-pore stellate MSNs.[17] The pore size distribution of these stellate MSNs ranging from 10 – 20 nm and their defined particle size of around 100 nm present an ideal platform for the cellular delivery of large-sized biomacromolecules. One significant achievement of this

synthesis method is that it can be used for large-scale production. Up to now, most of the reports regarding the synthesis of stellate MSNs have focused on the discussion of the pore-forming mechanism and particle size control. While the functionalization and the influence of organosilanes on particle characteristics is well studied for small-pore MSNs, only few studies have addressed the functionalization of these stellate MSNs (either by post-synthetic grafting or only shell functionalization) for optimized biomedical applications[18-19] None of them has discussed the impact of different organosilanes in the precursor solution on stellate particle morphology when undergoing silica co-condensation.

To engineer MSNs suitable for nanomedicine, molecular surface modification offers several advantages: hydrophobicity or hydrophilicity as well as the surface charge can be adjusted towards the respective guest molecules, thus ensuring optimal uptake and release properties. Furthermore, a site-specific surface decoration with functional groups allows for the independent attachment of diverse linker or targeting molecules, thus creating multifunctional delivery agents. Postsynthetic grafting and co-condensation are two common methods to implant functional groups into the framework of MSNs. Post-synthetic grafting is more commonly used for functionalizing large-pore stellate MSNs because grafting does not or only negligibly impair the particle morphology or pore structure. However, challenges of post-synthetic grafting include (i) achieving site-specific localization of two or more different functional groups on the MSN surface and (ii) controlling the degree of functional groups incorporated into the silica framework. On the other hand, a co-condensation approach provides a facile route to attain a controlled degree and spatially selective functionalization in the MSN particles. In addition, the functional groups are more homogeneously distributed throughout the pore structure when performing a co-condensation synthesis. However, for this approach to result in well-defined MSNs, high concentrations and/or highly charged organosilanes are typically not applicable.

In this study, we first synthesized various monofunctionalized MSNs via the co-condensation approach. We discuss the prominent impact of 3-aminopropyl triethoxysilane (APTES) (when used together with tetraethyl orthosilicate (TEOS) as silica precursors) on the final pore structure and the particle size of MSNs. We further employed our delayed co-condensation strategy[20-21] to synthesize site-specific (spatially selective) core-shell bi-functional LP-MSNs. Aza-dibenzocyclooctyne (DBCO)-derivatives were attached to the inner surface of MSNs to enable copper-free click chemistry reactions for the conjugation of azide-terminated cargos. In combination with different stimuli-responsive linkers (e.g., redox-sensitive disulfide bridged and pH-sensitive acetal linkers) between DBCO moieties and the MSN surface, we were able to control the cargo uptake and trigger the release in specific buffer solutions. We envision these multifunctional LP-MSNs (Scheme 1) to be promising nanocarriers for encapsulation and controlled release of various therapeutics in a spatiotemporal manner.

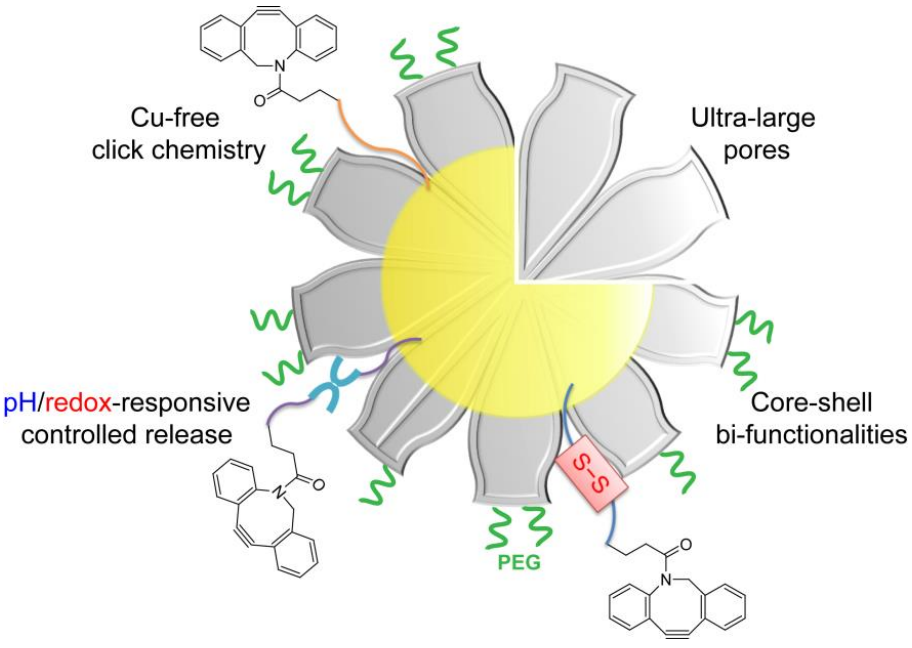

Scheme 1 Schematic illustration of the multifunctional large-pore MSNs established in this study for different applications.

5.2. Results and Discussion

Synthesis of Monofunctional MSNs *via* a Co-Condensation Method

We first chose three commonly used organosilanes carrying thiol, phenyl or amino groups for the functionalization of MSNs. Thiol and amino groups are frequently used in secondary cross-linking reactions while phenyl groups are capable of increasing the hydrophobicity of the silica surface. The three different organosilanes 3-mercaptopropyl triethoxysilane (MPTES), 3-aminopropyl triethoxysilane (APTES) and phenyltriethoxysilane (PTES) were mixed with tetraethyl orthosilicate (TEOS), respectively, and introduced as silica precursors in the co-condensation procedure. A fraction between 5 % and 10 % of the total amount of silica was substituted by the respective organosilane (see Table 2). Un-functionalized MSNs (pure silica, un-MSN) were also synthesized as control group (experimental details are described in the section of Materials and Methods).

According to the TEM micrographs (Figure 5-1a-c), the resulting samples un-MSN, thiol-functionalized MSNs (MSN-SH) and phenyl-functionalized MSNs (MSN-Ph) all show a stellate silica framework with conical pore structure, with MSN-SH and MSN-Ph exhibiting a less dense central backbone and a smaller particle size than un-MSN. The SEM images (Figure 5-1 e-g) further illustrate the flower-shaped morphologies of these stellate MSNs containing irregular pores. In contrast, amino-functionalized MSNs (MSN-NH_2) present a very different particle morphology (Figure 5-1d, 1h), i.e. a denser silica structure with small pores and a large particle size of around 200 nm.

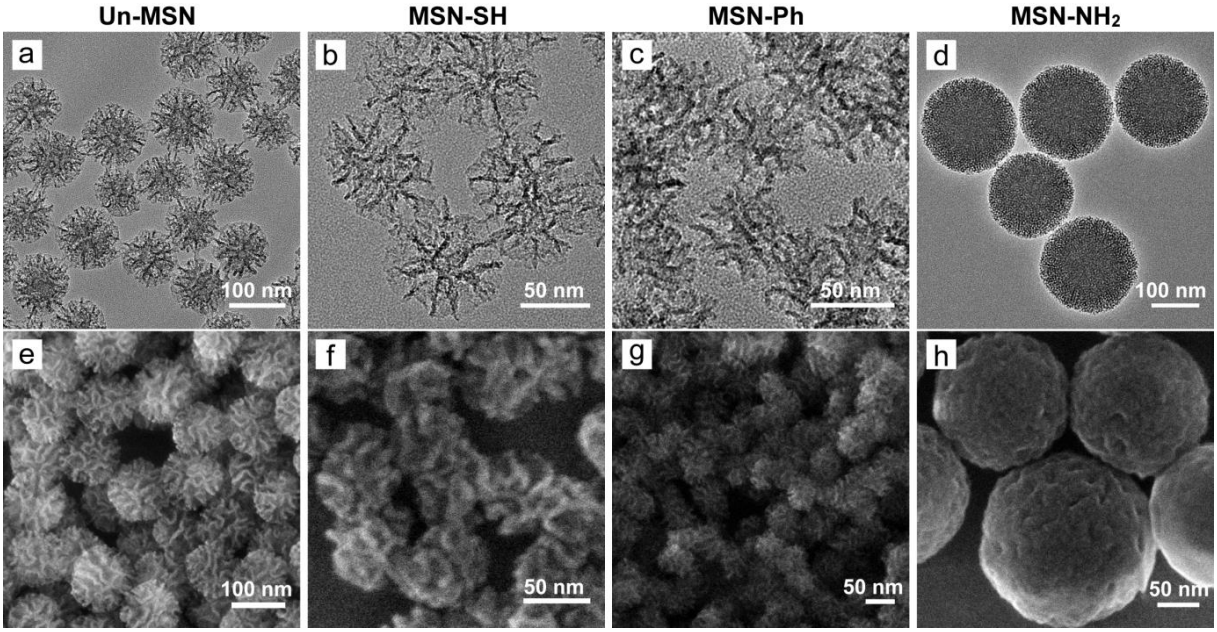

Figure 5-1. TEM and SEM micrographs of MSNs functionalized with different organic groups. (a),(e) Un-functionalized MSNs. (b), (f) Thiol-functionalized MSNs. (c), (g) Phenyl-functionalized MSNs. (d), (h) Amino-functionalized MSNs.

N_2 sorption (Figure 5-2a-b) analysis indicates high surface areas (around 520 – 890 m^2/g) and wide pore size distributions (3 – 30 nm) in samples un-MSN, MSN-SH and MSN-Ph (for detailed information, please see Table 1). In accordance with TEM images, N_2 sorption analysis shows that both MSN-SH and MSN-Ph have wider pore size distributions and larger pore volumes than un-MSN. We note that the pore volume was evaluated at a relative pressure of $p/p_0 = 0.99$ and includes a small contribution of textural porosity (inter-particle volume) due to the small particle size. The results of the N_2 sorption also reveal that the MSN-NH_2 sample has a low surface area of only 285 m^2/g, a low pore volume and a narrow pore size distribution (3 – 4 nm), correlating with the TEM picture. IR spectroscopy shows the typical Si-O-Si asymmetric stretching vibration at 1240 – 1050 cm^{-1} (full range spectra in Figure S 5-1a). Additionally, an absorption band at 1629 cm^{-1} of the bending mode of water adsorbed on the surface of MSNs clearly appears in un-MSN, MSN-SH and MSN-NH_2 indicating that these MSNs are hydrophilic. The signals of the ring C=C stretching mode at 1431 cm^{-1} and two aromatic ring C-H stretching modes at 3059 cm^{-1} and 3079 cm^{-1} (indicated

by *) can be observed in the MSN-Ph spectrum (Figure 5-2c, blue trace). Sample MSN-NH_2 (Figure 5-2 c, green trace) shows the absorbance of the symmetric NH_3^+ vibration at 1532 cm^{-1} and of saturated primary amines at 1627 cm^{-1} (indicated by *, this band overlaps with the physisorbed water in MSNs).

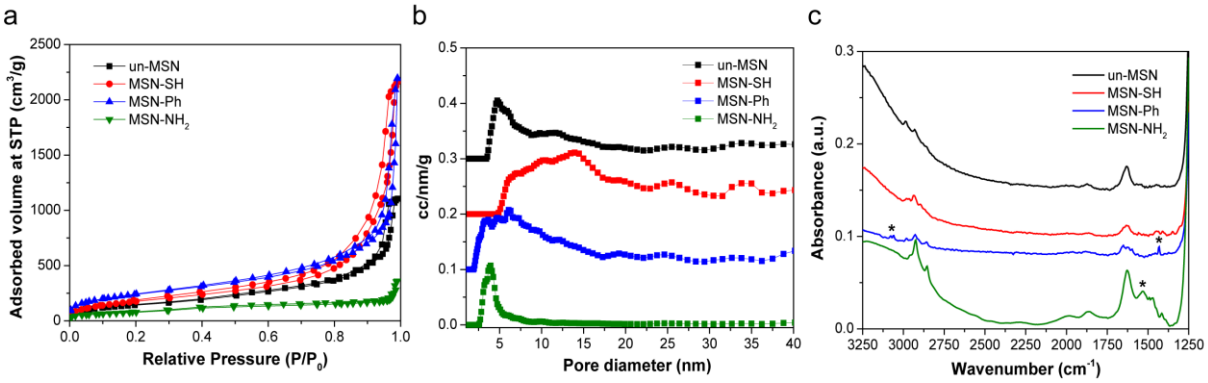

Figure 5-2. N_2 sorption (a) isotherms, (b) pore size distributions and (c) IR spectra of MSNs. The signals of the ring C=C stretching mode at 1431 cm-1 and two aromatic ring C-H stretching modes at 3059 cm-1 and 3079 cm-1 (indicated by *) can be observed in the MSN-Ph spectrum (blue trace). The signal at 1627 cm-1 (indicated by *) in the MSN-NH2 spectrum (green trace) indicates the presence of saturated primary amines. For clarity, the pore size distribution curves in (b) are shifted along the y-axis by a value of 0.1 and the IR spectra in (c) are shifted along the y-axis by 0.05.

Table 5-1. Characterization of MSN samples.

Sample	DFT[1] Pore size distribution (nm)	Pore volume[2] (cm^3/g)	BET surface area (m^2/g)	Particle size[3] (nm)	IEP (pH)	Zeta Potential at pH 7 (mV)
Un-MSN	4.5 - 22	1.6	521	135 ± 53	3.6	-35
MSN-SH	6.0 - 30	3.2	671	117 ± 52	2.3	-30
MSN-Ph	3.5 - 22	2.4	885	50 ± 10	3.3	-28
MSN-NH_2	3.0 - 4.5	0.3	285	216 ± 56	5.6	-31

[1] Data were acquired from the adsorption branch of the isotherms. [2] The total pore volume was determined at p/p_0 = 0.99. [3] Un-MSN, MSN-SH and MSN-NH_2 were measured by DLS, MSN-Ph was analyzed by TEM.

The amino groups in this sample also increased the isoelectric point (IEP) of the particles (IEP = pH 3.6 for un-MSN; IEP = pH 5.6 for MSN-NH_2). Thiol groups of sample MSN-SH can be detected by Raman spectroscopy (appendix Figure S 5-1) showing the S-H stretching mode at 2581 cm^{-1}. Thermogravimetric analysis (TGA, appendix Figure S 5-2) also demonstrates the inclusion and the different stability of the functional groups. The decomposition of SH, Ph and NH_2 groups can be observed in a dominant weight change at 341 °C, 631 °C and 302 °C in the samples MSN-SH, MSN-Ph and MSN-NH_2, respectively. The TGA mass losses and estimated degree of organic functionalizations of the samples are listed in Table S1.

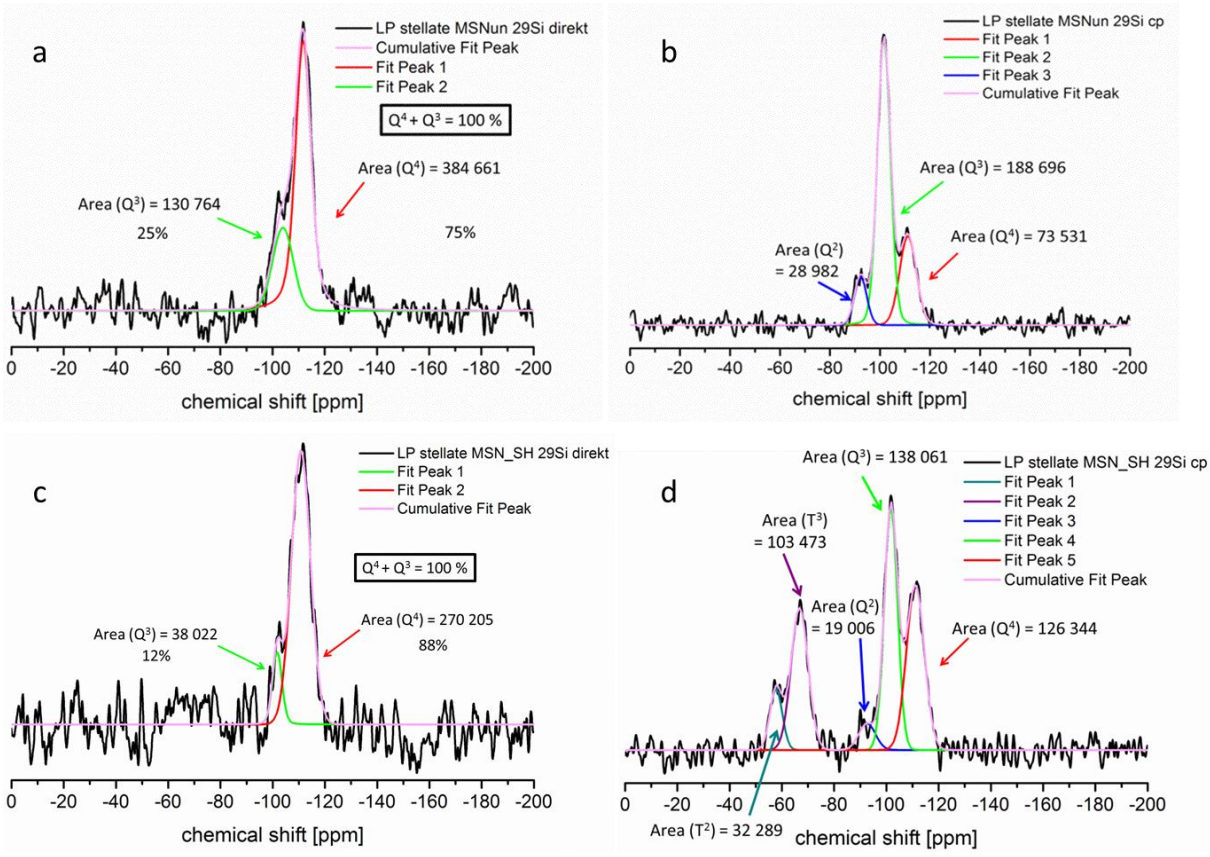

Figure 5-3. ^{29}Si MAS-NMR spectra (a) un-MSN (direct excitation), (b) un-MSN (cross-polarized), (c) MSN-SH (direct excitation), (d) MSN-SH (cross-polarized). Spectra (a)- (c) were fitted with a Voigt function and spectra (d) with a Gauss function (fits in color, data in black). The numbers in spectra (a) and (c) represent the calculated relative condensation degrees.

^{29}Si solid state NMR (ssNMR) measurements prove the successful integration of the organic groups (cross-polarized measurements) and show high condensation degrees of all four

samples (measured with direct excitation) (Figure 5-3 and Figure S 5-8). All spectra show peaks at around -110 ppm (Q^4) and -101 ppm (Q^3) [$Q^n = Si(OSi)_n(OH)_{4-n}$, n = 2-4], corresponding to fully condensed silica and silica with one terminal hydroxyl group, respectively. From the directly polarized spectra the relative degrees of condensation (percentage of Q^4 relative to the total area following the formula $Q^4 + Q^3 = 100\%$) were calculated to be 75% for un-MSN and 88% for MSN-SH (Figure 5-3, as well as 73% for MSN-NH_2 and 79% for MSN-Ph, Figure S 5-8in the SI). Using indirect polarization *via* the hyperpolarization of ^1H nuclei and subsequent $^1H \rightarrow {}^{29}Si$ cross-polarization, geminal hydroxyls (Q^2) at around -92 ppm and T^n-sites can also be observed in the spectra. Those T^n-sites are generated by the incorporated organosiloxanes. Their chemical shifts are commonly around 40 ppm higher than the ones for Q^n-sites.[22-23]

These results show that organosilanes can be successfully introduced into the silica framework of large-pore stellate MSNs *via* a co-condensation synthesis. MPTES and PTES had only a moderate influence on the stellate formation, while APTES strongly modified the co-condensation process, resulting in a highly divergent silica structure. Factors that affect particle morphology and pore structure such as surfactants, catalyst agents, ratio between reactants, temperature, reaction time, stirring rate, etc. are well-studied in the literature. In contrast, only few papers have discussed the influence of organosilanes on the MSN morphology.[24-25]

Influence of Organosilanes on Pore Structure Formation

To investigate the influence of organosilanes on the pore structure formation during co-condensation, we measured the pH values (at room temperature) of the precursor solutions of all samples (Table 2).

Table 5-2. pH values of synthetic precursor mixtures.

Sample	Silica precursors[1] (mol%)	pH value of surfactant solution[2]	pH value[3] after silane addition	pH value[4] after 30 min of silane addition
Un-MSN	100% TEOS	9.68	9.30	9.0
MSN-SH	90% TEOS + 10% MPTES	9.70	9.28	9.01
MSN-Ph	90% TEOS + 10% PhTES	9.65	9.31	9.03
MSN-NH_2	95% TEOS + 5% APTES	9.70	10.06	9.43

[1] 100 mol% = 9.6 mmol. [2] Surfactant solution: 13.7 g of H_2O + 0.263 g of CTATos + 0.047 g of TEA. [3] All pH values were measured after 2 min of silane addition at room temperature. [4] All pH values were measured at room temperature.

The surfactant solution containing CTATos, triethanolamine and water has a pH value of about 9.7. Upon addition of TEOS, the pH value dropped to 9.3. After stirring the reaction solution for 30 minutes, part of the silicon alkoxides are hydrolyzed and condensed, and the pH value dropped further down to 9.0. When 10 mol% of TEOS was replaced by MPTES or PTES, these pH values remained nearly unchanged. However, the addition of APTES led to a higher pH value (pH 10.06) in the reaction mixture due to the basic property of the amino groups. Zhang *et al.* proposed a mechanism for the large-pore stellate MSN synthesis: they propose that at near neutral conditions the counterions Tos^- (X^-) compete with the negatively charged silicates (I^-) for the positively charged surfactant micelles (S^+). Consequently, more Tos^- ions are included in the silica structure resulting in less dense silica particles and larger pores.[17] Following this argument we propose that the increasing pH caused by the addition of APTES enhances the affinity between negatively charged silicates (I^-) and positively charged surfactant micelles (S^+) and thus results in expelling the counterion Tos^- (X^-). Accordingly, a denser particle structure with smaller pores results. Similar observations were reported in a

recently published paper from our group showing that CTATos does not influence the pore radius in comparison to the commonly used CTAC template when the synthesis was performed at the high pH of about 12.[21]

In a previous publication,[26] we demonstrated the possibility to create multiply functionalized or even core-shell MSN particles, the latter by performing a time-delayed co-condensation with more than one organosilane (e.g., APTES + PTES) at high pH. Here, we applied a similar strategy for incorporating either PTES and APTES or PTES and MPTES simultaneously in the co-condensation processes to establish dual-functionalized stellate particles. According to Figure S 5-3, multiply functionalized MSNs were successfully synthesized. The aminogroup-containing dual functionalized MSN-Ph/NH_2 particles resemble the mono-functionlized MSN-NH_2 particles in that both of them consist of a comparably dense silica framework with a narrow pore size distribution. The reaction solution of the MSN-Ph/NH_2 particles still has a high pH value of about 9.92 compared to 10.06 in the mono-functionalized MSN-NH_2 solution, containing only half of the amino concentration, likely causing again the dense silica structure. However, the smaller APTES concentration now results in almost twice the surface area of MSN-NH_2. On the other hand, the mixed MSN-Ph/SH particles resemble their mono-functionalized parent samples MSN-Ph and MSN-SH, with pore size, pore volume and particle size of MSN-Ph/SH falling between those of MSN-Ph and MSN-SH.

Synthesis of Core-Shell Bifunctional Stellate MSNs Using the Delayed Co-Condensation Approach

To synthesize core-shell MSNs having two functional groups precisely localized at either the internal or the external surfaces, we applied the delayed co-condensation procedure. 3-cyanopropyltriethoxysilane (CPTES, 5 mol% of total silane content) was used for co-

condensation with TEOS to generate a nitrile-containing particle core while MPTES (1 mol% of total silane content) and TEOS were used to generate thiol groups on the outer surface. A shell of pure TEOS was condensed in-between to create an interlayer between the cyano- and mercapto-regions. TEM and SEM micrographs (Figure 5-4 a-b) of the resulting $core_{CN}$-$shell_{SH}$ particles (MSN-CN_{in}-SH_{out}) show a similar stellate morphology, particle size and pore structure as the un-MSNs particles.

According to N_2 sorption analysis, MSN-CN_{in}-SH_{out} particles possess a high surface area of 573 m^2/g and a wide pore size distribution of about 2.5 – 12 nm (Figure 5-4 c). The incorporated nitrile groups can be seen in the IR spectrum (Figure 5-4d, blue trace) at 2256 cm^{-1} representing the stretching vibration of aliphatic nitriles. The nitrile groups in MSN-CN_{in}-SH_{out} could be converted into carboxylic groups by heating the sample in a hydrochloric acid solution (appendix Figure S 5-4a). The obtained MSN-$COOH_{in}$-SH_{out} sample shows strong COO^- asymmetric stretching vibrations at 1556 cm^{-1} in the IR spectrum (Figure 5-4 d, magenta trace). To verify the presence of thiol groups on the outer surface, we applied a thiol-disulfide exchange reaction. Incubating MSN-CN_{in}-SH_{out} particles with cystamine in carbonate-bicarbonate buffer resulted in amino groups being anchored on the outer surface of the MSNs. This exchange reaction is evidenced by a dramatic increase in the zeta potential of the particles (Figure 5-4e). External mercapto-groups can be exploited for ligand attachment, e.g., PEGylation of the particles. PEG anchored to the external surface of MSNs has been reported to enhance the particle circulation time in the blood stream as well as to prevent particle degradation.[27-28] To assemble the potential nanocarriers MSN-$COOH_{in}$-PEG_{out} for biomedical application, we attached PEG polymers to the outer surface of the MSN-$COOH_{in}$-SH_{out} particles *via* a mercapto-reactive maleimide-PEG linker (appendix Figure S 5-4b). The corresponding weight increase of the PEGylation can be seen in TGA measurements (Figure 5-4f).

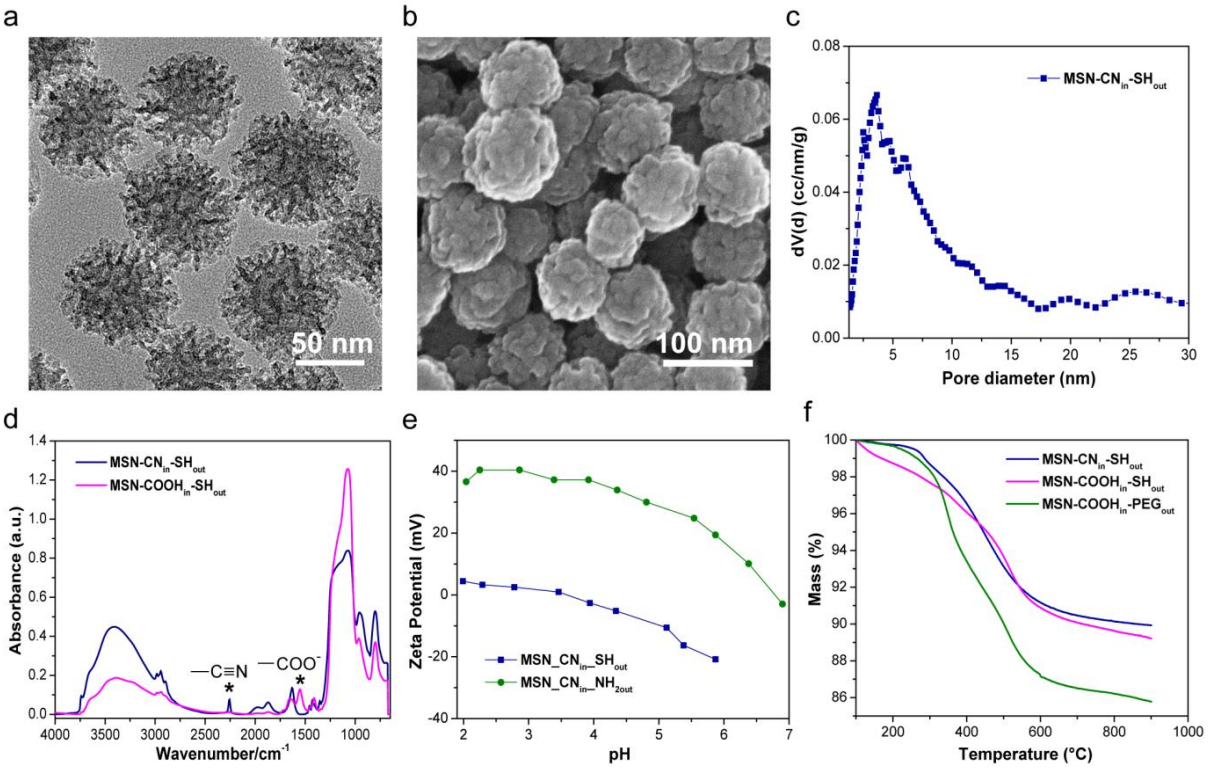

Figure 5-4. Characterization of core-shell MSNs. (a) TEM and (b) SEM images of MSN-CN_{in}-SH_{out} particles. (c) N_2 sorption-based pore size distribution obtained from the adsorption branch and calculated using NLDFT mode. (d) IR spectra. Blue: MSN-CN_{in}-SH_{out}, magenta: MSN-$COOH_{in}$-SH_{out}. (e) Zeta potential of MSN-CN_{in}-SH_{out} (blue) and MSN-CN_{in}-NH_{2out} (green). (f) Thermogravimetric analysis of MSN-CN_{in}-SH_{out} (blue), MSN-$COOH_{in}$-SH_{out} (magenta) and MSN-$COOH_{in}$-PEG_{out} (green).

Copper-Free Click Chemistry for Cargo Immobilization Using Stimuli-Responsive Linkers for Controlled Release

Several strategies have been described to modify functional groups in MSNs for cargo immobilization and controlled release. Recently, we reported on NTA (nitrilotriacetic acid)-modified MSNs chelating metal ions (Ni^{2+}, Zn^{2+} and Ca^{2+}) capable of a controlled binding and pH dependent release of His-tagged fluorescence nanobodies (chromobodies). These constructs enabled the direct transport of nanobodies into living cells for antigen visualization in real time.[29] The MSNs used in the above study were similar to the multifunctional large-pore stellate MSNs discussed in this report. Here, we present an alternative strategy for ligand coupling with the functional groups in these particles. We couple DBCO to the interior surface of the MSNs to enable a copper-free click chemistry for guest molecule conjugations. DBCO was developed independently by the van Delft group in 2009 and the Popik group in 2010 to enhance the reaction kinetics of strain-promoted azide-alkyne cycloaddition (also referred to as copper-free click chemistry).[30-31] Copper-free click chemistry mediated by DBCO derivatives became popular recently in bio-orthogonal conjugation applications for their high selectivity and reactivity toward azide-functionalized molecules under physiological conditions.[32-35] The absence of metal catalysts in the reaction solutions also renders this type of click chemistry strategy more favorable for biological applications.

In our study, two different DBCO derivatives (DBCO-NHS ester and DBCO-S-S-NHS ester) were used to functionalize the internal surface of MSN-$COOH_{in}$-PEG_{out}. After a series of surface modifications (Figure 5-5 a), we fabricated two types of DBCO-modified MSNs in which MSN-$(S\text{-}S\text{-}DBCO)_{in}$-$PEG_{out}$ contains redox-sensitive disulfide bridges between the mesopore surface and DBCO groups, while MSN-$DBCO_{in}$-PEG_{out} contains no stimuli-responsive linkers. Azide-terminated TAMRA dye was chosen as model cargo to carry out the

copper-free click reaction with MSN-(S-S-DBCO)$_{in}$-PEG$_{out}$ and MSN-DBCO$_{in}$-PEG$_{out}$. To evaluate the cargo immobilization efficacy of the DBCO-modified MSNs, time-based release experiments of the fluorescent TAMRA dye were performed in PBS at 37 °C.

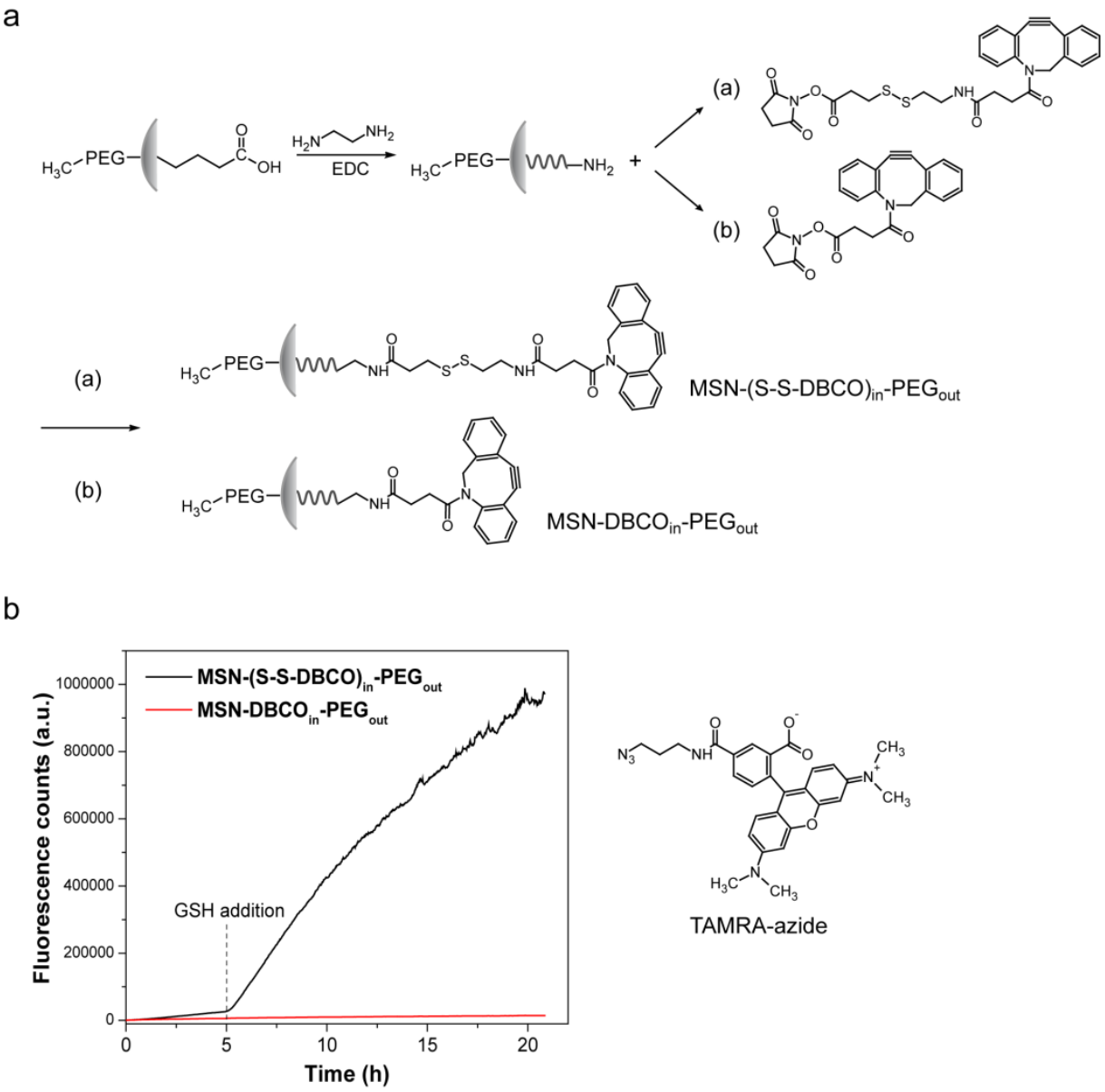

Figure 5-5. (a) Preparation of DBCO-modified MSNs. (b) Time-based release of TAMRA dyes from DBCO-modified MSNs. Azide-terminated TAMRA dye served as model cargo to be immobilized into DBCO-modified MSNs *via* copper-free click chemistry. After 5 h of release experiment initiation, glutathione (10 mM in the final concentration) was introduced to the two samples, respectively. The glutathione-added samples were incubated at 37 °C under shaking (500 rmp) for 5 min before the continuous release experiment.

In brief, 0.5 mg of TAMRA dye-coupled MSNs in 200 µl PBS was loaded into a custom-made Teflon cap fitting on a fluorescence cuvette. The cap was sealed with a dialysis

membrane (MWCO 14,000 g/mol) which was permeable for small dye molecules but not for MSNs. The released dye in the fluorescence cuvette (filled with 3 mL PBS) was recorded by a spectrofluorometer with λ_{ex} = 545 nm and λ_{em} = 565 nm. According to Figure 5-5 b, the two MSN samples showed no spontaneous release and thus an efficient coupling of the TAMRA dye to the MSN host during the first 5 h. Upon addition of the reducing agent glutathione at this point (GSH, 10 mM in the final solutions) to the particle solutions and incubation of the samples at 37 °C shortly for 5 min, the TAMRA dye was quickly released from the MSN-(S-S-DBCO)$_{in}$-PEG$_{out}$ sample, whereas no release was observed from the MSN-DBCO$_{in}$-PEG$_{out}$ sample. This result demonstrates that DBCO-modified MSNs are capable of conjugating azide-terminated molecules and are able to immobilize them stably within the particle interior. By introduction of a stimuli-responsive linker between the silica surface and the cargo conjugating moiety, a controlled release of the cargo from MSNs can be achieved.

As an alternative to the redox-sensitive disulfide bridge, we employed a pH-responsive linker between the MSN surface and the dye cargo to allow a stimuli-responsive cargo release. The pH-sensitive hydrolysis of the acetal linker 3,9-bis(3-aminopropyl)-2,4,8,10-tetraoxaspiro[5.5]undecane (called AK linker) was previously reported in the literature.[36-37] We modified the MSN-COOH$_{in}$-PEG$_{out}$ particles by attaching the amino terminus of the AK linker to the carboxy groups in the inner particle surface and then conjugated an amino-reactive NHS-DBCO moiety to the residual amino group of the AK-linker (Figure 5-6 a). TAMRA dyes were then again coupled to these MSN-(AKL-DBCO)$_{in}$-PEG$_{out}$ samples via copper-free click chemistry. The dye attachment and pH-sensitive release was studied with fluorescence spectroscopy as described above. As illustrated in Figure 5-6 b, TAMRA dyes were stably attached in the mesopores of MSN-(AKL-DBCO)$_{in}$-PEG$_{out}$ without premature leakage when kept in a buffer solution at pH 7. However, the subsequent exchange of the

medium with a pH 5 buffer triggered the TAMRA dye release due to the AK linker hydrolysis.

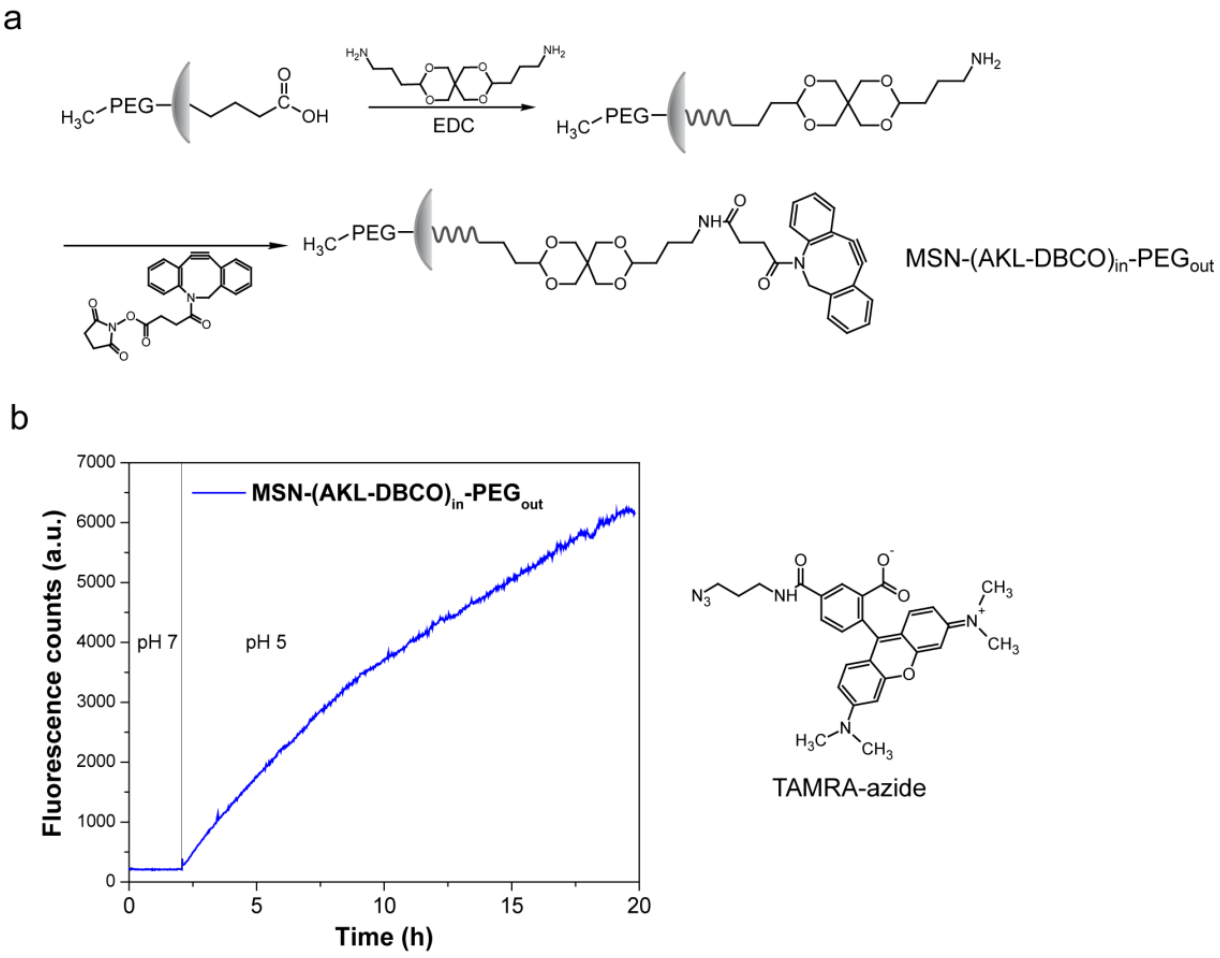

Figure 5-6. (a) Preparation of DBCO-modified MSNs with pH-responsive acetal linker (AKL). (b) Time-based release of TAMRA dyes from AKL-DBCO-modified MSNs. 2 h after release of TAMRA dyes in a pH 7 buffer, the sample was collected by centrifugation and re-dispersed in a pH 5 buffer for the following release experiment.

These release experiments demonstrate that DBCO derivatives are efficient elements for cargo conjugation on functionalized MSNs. Moreover, the sequential MSN modification with DBCO and stimuli-responsive linkers has no significant influence on the pore size distribution of our large-pore nanoparticles (Figure S 5-5a). The successful modification with DBCO and the stimuli-responsive linker is seen in TGA results, which show an increasing mass loss after each reaction step (Figure S 5-5b). Detailed information about DBCO-modified MSNs is listed in Figure S 5-5c.

Finally, we investigated the intracellular release of MSN-TAMRA in HeLa cells. For the cell experiments we chose MSN-S-S-DBCO-TAMRA because the endosomal release can be triggered externally *via* chloroquine shock. The successful cellular uptake of MSN-S-S-DBCO-TAMRA is shown in the fluorescence microscopy image in Figure 5-7.

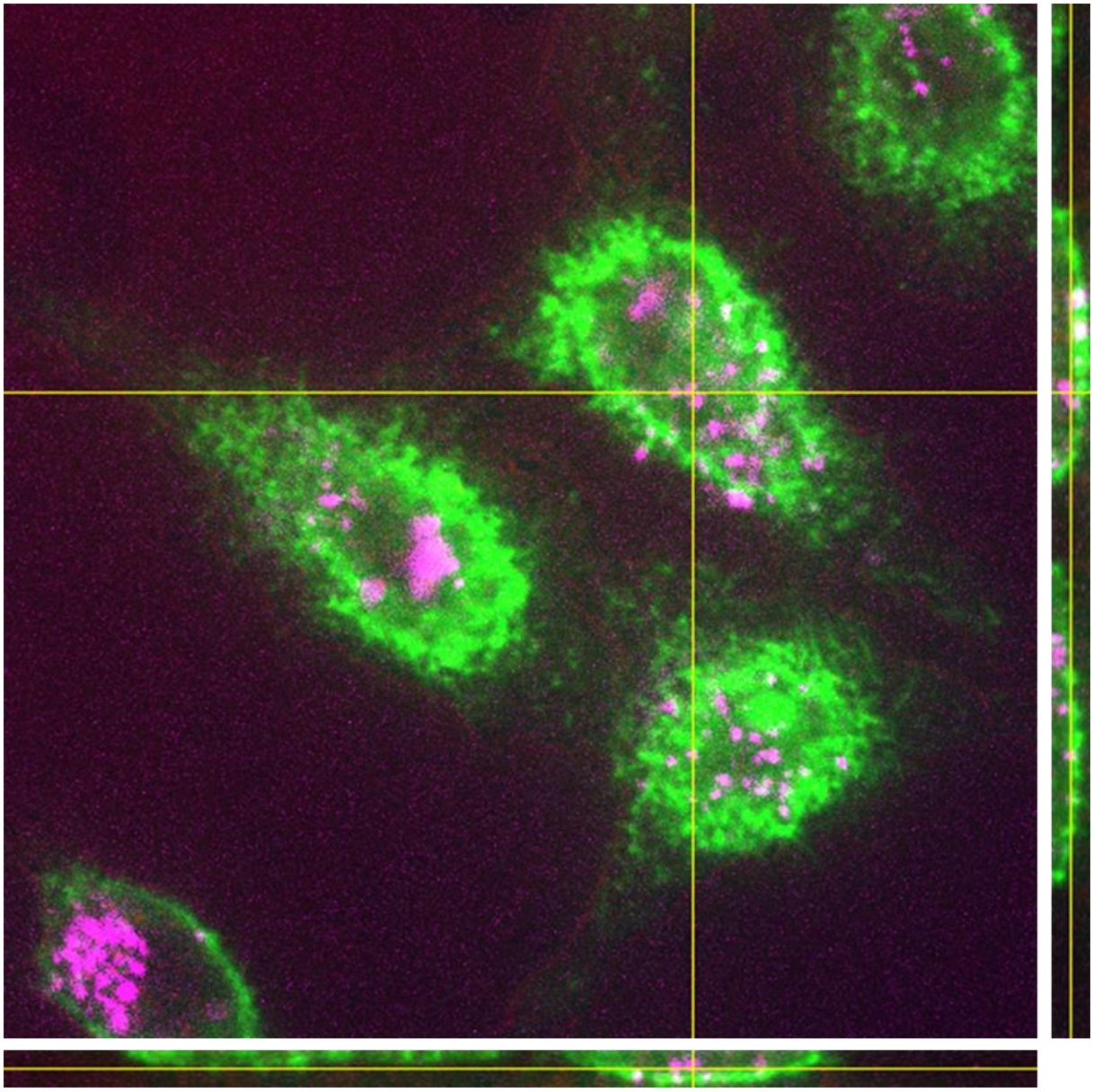

Figure 5-7. Fluorescence microscopy image of MSN-S-S-DBCO-TAMRA (magenta) taken up by HeLa cells (membranes in green). The orthogonal views on the side show successful uptake of MSNs.

No release of TAMRA is visible due to the fact that the releasing agent GSH is mainly present in the cytosol and not in the rather oxidizing environment of the endosome, which contains the MSNs. A chloroquine shock after 36 h released the particles from the endosome into the

cytosol, where GSH induced release of TAMRA from the particles. The resulting spread of the released dye within the cell is displayed in Figure 5-8 b. The control particles MSN-S-S-DBCO-TAMRA without chloroquine shock did not show released dye (Figure 5-8(a)).

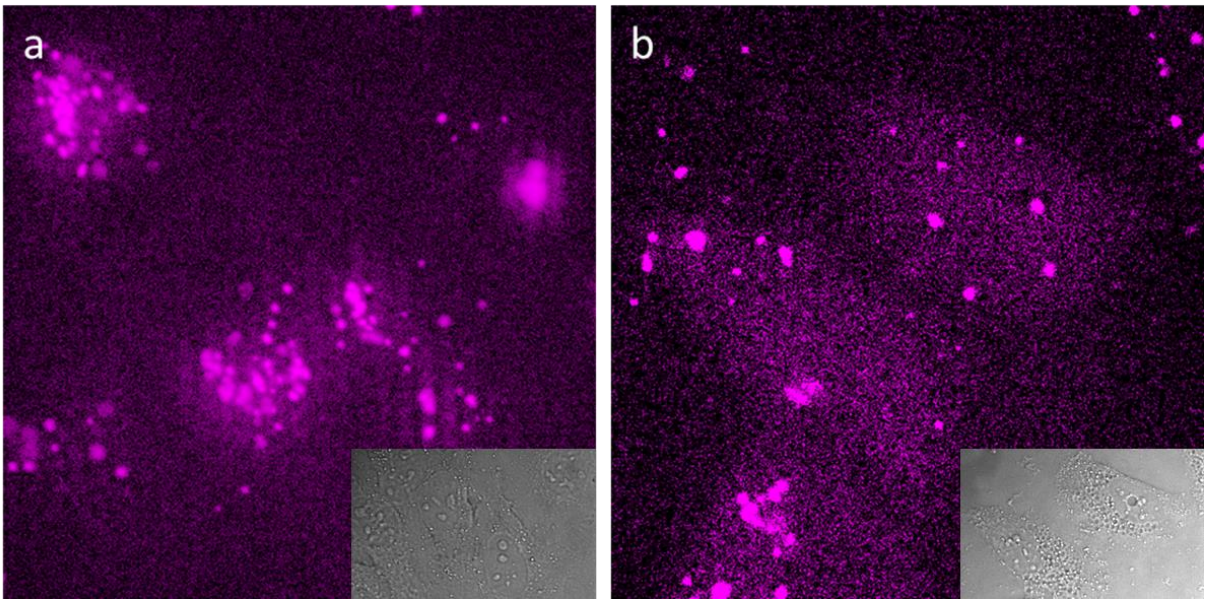

Figure 5-8. Fluorescence microscopy images of (a) MSN-S-S-DBCO-TAMRA and (b) MSN-S-S-DBCO-TAMRA after chloroquine shock; insert: respective transmitted light images. The staining in (b) results from TAMRA released from the particle and spreading within the cell.

5.3. Conclusion

In summary, we tailored the surface properties of large-pore stellate MSNs *via* co-condensation and postsynthetic modification into multifunctional MSNs that render promising nanocarriers for potential biomolecule delivery. Various organic functional groups were incorporated into the silica framework by co-condensing organosilanes with TEOS. We note that the acidity or basicity of an organosilane which might alter the pH value of reaction solution (e.g., ATPES) should be used with care because they can modify the large-pore stellate particle morphology formation and result in different silica structures. A delayed co-condensation approach was used to spatially control the localization of functional groups in the mesoporous nanoparticle, hence creating a core-shell bi-functional stellate MSN structure. In addition, we demonstrated the feasibility of both external and internal MSN surface

modification. DBCO derivatives were employed for copper-free click chemistry in combination with redox-sensitive disulfide bridged or pH-sensitive acetal linkers in our multifunctional MSN system to result in controlled cargo release. The synergy of surface adaptability and large pore radius in these stellate silica nanoparticles provides a promising outlook for applications in biomolecule delivery. This prospect was also demonstrated in our recent paper where similar large-pore stellate MSNs were used for the intracellular delivery of chromobodies.[29]

.

5.4. Experimental Part

Materials. Tetraethyl orthosilicate (TEOS, Aldrich, ≥ 99%), phenyltriethoxysilane (PTES, Aldrich, > 98%), (3-mercaptopropyl)triethoxysilane (MPTES, Aldrich, ≥ 80%), 3-aminopropyltriethoxysilane (APTES, Aldrich, 99%), Cell Counting Kit-8 (CCK-8, Dojindo), 3-cyanopropyltriethoxysilane (CPTES, ABCR, 97%), cetyltrimethylammonium p-toluenesulfonate (CTATos, Sigma), triethanolamine (TEA, Aldrich, 98%), cystamine dihydrochloride (Aldrich), ethanol (EtOH, Aldrich, absolute), hydrochloric acid (HCl, Aldrich, 37%), methoxypolyethylene glycol maleimide (PEG, MW 5000, Sigma), ethylenediamine dihydrochloride (Aldrich), dibenzocyclooctyne-S-S-N-hydroxysuccinimidylester (DBCO-S-S-NHS ester, Aldrich), dibenzocyclooctyne-N-hydroxysuccinimidyl ester (DBCO-NHS ester, Aldrich), 3,9-bis(3-aminopropyl)-2,4,8,10-tetraoxaspiro[5.5]undecane (AK linker, TCI), 5-carboxytetramethylrhodamine azide (5-TAMRA Azide, Baseclick), L-glutathione reduced (GSH, Sigma), N-(3-dimethylaminopropyl)-N-ethylcarbodiimide (EDC, Alfa Aesar, 98%), saline-sodium citrate buffer (SSC buffer, Sigma), sodium carbonate (Sigma), sodium bicarbonate (Sigma), Dulbecco's phosphate-buffered saline (PBS, Gibco). Bi-distilled water was obtained from a Millipore system (Milli-Q Academic A10).

MSN Synthesis. Un-functionalized MSNs (un-MSN) were synthesized based on an adapted recipe reported in the literature.17 In brief, TEA (0.047 g, 0.32 mmol), CTATos (0.263 g, 0.58 mmol) and H2O (13.7 g, 0.77 mmol) were mixed in a 100 mL round bottom and stirred vigorously (1250 rpm) at 80 °C until the surfactant solution became homogeneous. TEOS (2.013 g, 9.6 mmol) was then added to the surfactant solution, and the mixture was continuously stirred at 80 °C for 2 h. The molar ratio of the above-mentioned mixture is TEOS : CTATos : TEA : H_2O = 1 : 0.06 : 0.033 : 80. The as-synthesized particles were collected by centrifugation (7197 *g*, 20 min) and were immediately template extracted (see

below). For functionalized MSNs (MSN-R), TEOS and organosilanes (RTES) were mixed in molar ratios as described in Table 2 (the total silane content remained at 9.6 mmol) for silica co-condensation. All other procedures were the same as in the un-MSN synthesis.

Core-shell bi-functional (MSN-CN_{in}-SH_{out}) MSNs were synthesized through a delayed co-condensation approach. TEOS (1.71 g, 8.2 mmol) and CPTES (116 mg, 0.48 mmol; 5 mol%) were mixed and added to the surfactant solution (as described in the previous section), and the mixture was stirred (1250 rpm) at 80 °C for 1 h. Afterwards, 201 mg of TEOS (0.96 mmol) was separated into 4 aliquots and added to the mixture every 3 minutes. The solution was further stirred for 1 h at 80 °C. A mixture of TEOS (20.1 mg, 0.096 mmol) and MPTES (28.6 mg, 0.096 mmol, 1 mol%) was then added to the solution to generate the outer shell of MSNs. The resulting solution was continuously stirred at 80 °C for 1 h. The as-synthesized particles were collected by centrifugation (7197 *g*, 20 min) and were subsequently template extracted.

Template Extraction. To remove the organic surfactant from MSNs, 1 g of the as-synthesized particles were heated in an ethanolic solution (150 mL) containing 3 g of ammonium nitrate at 90 °C under reflux for 1 h, cooled and collected by centrifugation (7197 *g*, 20 min) and extracted by a second reflux at 90 °C using a 2 M HCl/ethanolic solution (150 mL) for 1 h. Afterwards, samples were washed in the sequence of EtOH, H_2O, EtOH (100 mL per wash) and were finally kept in 20 mL of EtOH. Particles were collected by centrifugation (7197 *g*, 20 min) after each template extraction and washing step.

Buffer Preparation.

Carbonate-Bicarbonate Buffer, pH 9

2 mL of 200 mM of sodium carbonate (2.2 g of sodium carbonate was dissolved in 100 mL H_2O) was slowly added to 23 mL of 200 mM of sodium bicarbonate (1.68 g of sodium bicarbonate was dissolved in 100 mL H_2O) to adjust the pH value to 9.0. By filling the buffer

volume to 50 mL with H_2O the final carbonate-bicarbonate concentration of 100 mM was obtained.

0.1 M MES Buffer, pH 4.7

4-Morpholineethanesulfonic acid (1.95 g, 10 mmol) was dissolved in 100 mL of H_2O. 2 M NaOH was added dropwise to adjust the pH value to 4.7.

Modification of Core-Shell Bifunctional MSNs.

Hydrolysis of MSN-CN_{in}-SH_{out}. 200 mg of MSN-CN_{in}-SH_{out} was dispersed in 20 mL of H_2O, and 60 mL of HCl (37 %) was added carefully. The sample was heated to reflux (90 °C) for 3 h and then cooled down in ambient environment. Afterwards 40 mL H_2O was added and the solution was stirred at RT overnight. 100 mL of H_2O was added to further dilute the solution before centrifugation (7197 *g*, 20 min) for particle collection. The resulting MSN-$COOH_{in}$-SH_{out} particles were washed with SSC buffer (pH 7), H_2O and EtOH (50 mL per wash), and were kept in EtOH (10 mL). Centrifugation (7197 *g*, 20 min) was applied after each washing step for particle collection.

Modification of MSN-CN_{in}-SH_{out} with Cystamine. The thiol groups on the outer shell of MSN-CN_{in}-SH_{out} could be converted to amino groups by disulfide exchange of MSN-CN_{in}-SH_{out} with cystamine. In brief, cystamine dihydrochloride (22.5 mg, 0.1 mmol) was dissolved in 1 mL of H_2O as cystamine coupling solution. 10 mg of MSN-CN_{in}-SH_{out} was dispersed in 900 µL of H_2O and then mixed with 100 µL of 100 mM carbonate-bicarbonate buffer and 1 mL of cystamine coupling solution. The mixture was stirred at RT for 2 h followed by washing steps (twice with H_2O and twice with EtOH (5 mL per wash), followed by centrifugation (16873 *g*, 5 min) to remove excess of cystamine and the side product 2-mercaptoethylamine. The resulting MSN-CN_{in}-NH_{2out} particles were suspended in 5 mL EtOH. During the modification processes, particles were collected by centrifugation (16873 *g*, 5 min) in 1.5 mL Eppendorf tubes after reaction and each washing step.

PEGylation of MSN-COOH$_{in}$-SH$_{out}$. 10 mg of MSN-COOH$_{in}$-SH$_{out}$ and 10 mg of maleimide-terminated PEG were mixed in 6 mL of SSC buffer in a 10 mL-glass bottle. The mixture was stirred at RT overnight. The resulting MSN-COOH$_{in}$-PEG$_{out}$ particles were washed with 10 mL of H_2O three times to remove excess free PEG molecules and were kept in 10 mL of H_2O. Centrifugation (16873 *g*, 5 min) was used to collect the particles after reaction and after each washing step.

Modification of MSN-COOH$_{in}$-PEG$_{out}$ to MSN-DBCO$_{in}$-PEG$_{out}$/MSN-(S-S-DBCO)$_{in}$-PEG$_{out}$. To modify MSN-COOH$_{in}$-PEG$_{out}$ with DBCO-S-S-NHS ester or DBCO-NHS ester, conversion of MSN-COOH$_{in}$-PEG$_{out}$ to MSN-NH$_{2in}$-PEG$_{out}$ was required. Ethylenediamine was used to convert COOH groups to NH_2 groups, the procedure was following the protocol described in the literature.[38] Briefly, ethylenediamine dihydrochloride (1.33 g, 10 mmol) was dissolved in 10 mL of 0.1 M MES buffer (pH 4.7) to generate 1 M ethylenediamine coupling buffer in a 30 mL-glass bottle. The amount of 4 mg of MSN-COOH$_{in}$-PEG$_{out}$ was dispersed in the ethylenediamine coupling buffer (10 mL) followed by addition of EDC (20 mg, 128.8 µmol, 2 mg/ml in the reaction solution) and the mixture was stirred at RT overnight. The resulting MSN-NH$_{2in}$-PEG$_{out}$ particles were collected by centrifugation (16873 *g*, 5 min) and were washed with 4 mL H_2O three times to remove residual chemicals.

DBCO-S-S-NHS ester and DBCO-NHS ester were dissolved in DMSO in the concentration of 10 mM to serve as stock solutions, respectively. 2 mg of MSN-NH$_{2in}$-PEG$_{out}$ particles were mixed with 1 mg of DBCO-S-S-NHS ester (170 µl from stock solution) or 1 mg of DBCO-NHS ester (240 µl from stock solution) in 1 mL PBS. The mixtures were shaken at RT for 3 h followed by washing steps (washed with 2 mL H_2O, 2 mL EtOH and 2 mL DMSO). Centrifugation (16873 *g*, 5 min) was performed for particle collection after each washing step. The resulting MSN-DBCO$_{in}$-PEG$_{out}$ and MSN-(S-S-DBCO)$_{in}$-PEG$_{out}$ particles were stored in DMSO at the concentration of 1 mg/ml.

Conversion of MSN-COOH$_{in}$-PEG$_{out}$ to MSN-(AKL-DBCO)$_{in}$-PEG$_{out}$. A mixture of 4 mg of MSN-COOH$_{in}$-PEG$_{out}$, 5 mg of AK linker (18 µmol) and 5 µl of EDC (4.3 mg, 28 µmol) were dispersed in 1 mL SSC buffer in a 10 mL-glass bottle and were stirred at room temperature overnight. The resulting MSN-AKL$_{in}$-PEG$_{out}$ particles were collected by centrifugation (16873 *g*, 5 min), washed with 10 mL SSC buffer and dispersed in 4 mL EtOH. 2 mg of MSN-AKL$_{in}$-PEG$_{out}$ particles in 1 mL EtOH were mixed with 1 mg of DBCO-NHS ester (240 µl from stock solution) in a 1.5 mL- Eppendorf tube and the sample was shaken at RT for 2 h. The resulting MSN-(AKL-DBCO)$_{in}$-PEG$_{out}$ particles were washed with 2 mL EtOH three times and stored in DMSO at the concentration of 1 mg/ml.

MSN Characterization. For transmission electron microscopy (TEM), samples were prepared by drying a diluted MSN suspension (in ethanol) on a carbon-coated copper grid at room temperature for several hours. The measurement was performed at 200 kV on a Jeol JEM-2010 instrument with a CCD detection system. Scanning electron microscopy (SEM) was performed at 30 kV on a Helios NanoLab G3 UC instrument (FEI, USA) equipped with a TLD detector. Diluted MSN suspensions (in ethanol) were dried on a carbon-coated copper grid at room temperature for several hours. Nitrogen sorption analyses were performed on a Quantachrome Instrument NOVA 4000e at 77 K. Sample outgassing was performed at 120 °C under vacuum (10 mTorr) 16 h before measurement. Pore size distribution curves were calculated by non-local density functional theory (NLDFT) procedures provided by Quantachrome based on the adsorption branch of N_2 on silica. A Thermo Scientific Nicolet iN10 IR-microscope was used to record infrared spectra of dried sample powders in reflection-absorption mode with a liquid-N_2 cooled MCT-A detector. Raman spectroscopy was performed on a Bruker Equinox 55 with a Nd:YAG laser having a wavelength of 1064 nm at a laser power of 100 mW and 3000 scans. Dynamic light scattering (DLS) and zeta potential measurements were performed on a Malvern Zetasizer-Nano instrument

equipped with a 4 mW He-Ne laser (633 nm) and an avalanche photodiode. DLS measurements were directly recorded in diluted suspensions of the particles at a concentration of 1 mg/ml in ethanol. Zeta potential measurements were performed with an add-on Zetasizer titration system (MPT-2) based on diluted NaOH and HCl as titrants, and the samples were prepared by adding 1 mg of the particles to 10 mL bi-distilled water. Thermogravimetric analyses (TGA) of the powder samples (20 mg) were recorded on a Netzsch STA 440 C TG/DSC with a heating rate of 10 °C/min up to 900 °C in a stream of synthetic air of about 25 mL/min. Solid state NMR measurements (cross-polarized ^{13}C and ^{29}Si and direct ^{29}Si excitation) were performed on a Bruker Avance III-500 spectrometer (11,74 Tesla) in a 4 mm (respectively 2.5 mm) ZrO_2 rotor with a spinning rate of 10 kHz (respectively 20 kHz). The resulting spectra were fitted with a Gauss or a Voigt function with Origin Pro 9.0. The preparation of all cell experiments took place in a Hera-Safe cell culture unit and Hera Cell incubators from Heraeus. Fluorescence microscopy was performed with a Zeiss Observer SD spinning disk confocal microscope using a Yokogawa CSU-X1 spinning disc unit and an oil objective (63x magnification) and BP 525/50 (WGA488) and LP 690 (TAMRA) emission filters. A 488 nm and a 564 nm laser was used for excitation. CCK-8 assays were performed with a microplate reader (SPARK 10M, Tecan Austria GmbH) and evaluated with Excel 2010.

Release experiments. MSNs modified with DBCO-functional groups in the inner surface ($MSN\text{-}DBCO_{in}\text{-}PEG_{out}$ / $MSN\text{-}(S\text{-}S\text{-}DBCO)_{in}\text{-}PEG_{out}$ / $MSN\text{-}(AKL\text{-}DBCO)_{in}\text{-}PEG_{out}$) were used in the release experiments. 5-TAMRA azide was used as model cargo to carry out the copper-free click chemistry conjugation with DBCO modified MSNs. For dye loading, 0.5 mg of MSNs and 200 µg of 5-TAMRA azide (5 mg/ml in DMSO) were mixed in 1 mL PBS in an 1.5 mL-Eppendorf tube. The samples were incubated at 37 °C under shaking. After 2 h, TAMRA dye conjugated MSN samples were washed with 1 mL PBS three times to remove

free dyes in the solution. Centrifugation (16873 *g*, 5 min) was applied after each washing step for particle collection. MSN-TAMRA particles were re-dispersed in 200 µl PBS.

Cuvette release experiments. To show the successful release of the bound cargo, the MSN-TAMRA particles were transferred to a custom made Teflon cap fitting on a fluorescence cuvette. The cap was sealed with a dialysis membrane (ROTH Visking type 8/32, MWCO 14,000 g/mol) and placed on the top of a fluorescence cuvette filled with 3 mL PBS. Time-based fluorescence release experiments were performed at 37 °C on a PTI spectrofluorometer equipped with a xenon short arc lamp (UXL-75XE USHIO) and a photomultiplier detection system (Model 810/814). The excitation wavelength was set to λ = 545 nm and the emission fluorescence intensity was recorded at λ = 565 nm. All slits were adjusted to 2.0 mm. To trigger the stimuli-responsive dye release, 22 µl of 100 mM GSH in PBS was added to MSN-DBCO-TAMRA and MSN-S-S-DBCO-TAMRA samples (each sample contains 200 µl volume), respectively to achieve a final GSH concentration of 10 mM. The samples were incubated at 37 °C under shaking (500 rpm) for 5 min. The MSN-AKL-DBCO-TAMRA sample was transferred to an Eppendorf tube and the particles were collected by centrifugation (16873 *g*, 5 min). Afterwards, the sample was re-dispersed in 200 µl of acetate buffer (pH 5) and was transferred back to the Teflon cap for the release experiment. All samples were sealed with the dialysis membranes and the release setups were reassembled. The fluorescence cuvettes for MSN-DBCO-TAMRA and MSN-S-S-DBCO-TAMRA samples were filled up with PBS containing 10 mM of GSH, while the fluorescence cuvette for MSN-AKL-DBCO-TAMRA sample was filled with acetate buffer (pH 5). Fluorescence spectra (λ_{ex} = 545 nm, λ_{em} = 565 nm) were recorded continuously overnight. Quantification of the released dye was performed with the help of a calibration curve (Figure S 5-7).

Cell experiments. HeLa cells were cultured in DMEM supplemented with 10% FBS and 1% PenStrep at 37°C/5% CO_2. For fluorescence microscopy experiments 5000 HeLa cells in

300 µl DMEM were seeded in ibiTreat 8-well slides (ibidi). One day after seeding 2 µg of MSN-S-S-DBCO-TAMRA were added and incubated overnight. Chloroquine shock was performed 36 h after incubation by replacing the medium with medium containing 500 µM chloroquine. After 10 min chloroquine was removed by replacing the medium with normal DMEM. Release was imaged 6 h after chloroquine treatment. For uptake images WGA488 was added immediately before imaging. A wash with DMEM after one minute of incubation removed unbound WGA.

5.5. References

1. Kresge, C. T.; Leonowicz, M. E.; Roth, W. J.; Vartuli, J. C.; Beck, J. S., Ordered mesoporous molecular sieves synthesized by a liquid-crystal template mechanism. *Nature* **1992,** *359,* 710-712.
2. Beck, J. S.; Vartuli, J. C.; Roth, W. J.; Leonowicz, M. E.; Kresge, C. T.; Schmitt, K. D.; Chu, C. T. W.; Olson, D. H.; Sheppard, E. W.; McCullen, S. B.; Higgins, J. B.; Schlenker, J. L., A new family of mesoporous molecular sieves prepared with liquid crystal templates. *J. Am. Chem. Soc.* **1992,** *114,* 10834-10843.
3. Vallet-Regi, M.; Rámila, A.; del Real, R. P.; Pérez-Pariente, J., A New Property of MCM-41: Drug Delivery System. *Chem. Mater.* **2001,** *13,* 308-311.
4. Lai, C. Y.; Trewyn, B. G.; Jeftinija, D. M.; Jeftinija, K.; Xu, S.; Jeftinija, S.; Lin, V. S., A mesoporous silica nanosphere-based carrier system with chemically removable CdS nanoparticle caps for stimuli-responsive controlled release of neurotransmitters and drug molecules. *J. Am. Chem. Soc.* **2003,** *125,* 4451-4459.
5. Díaz, J. F.; Balkus, K. J., Enzyme immobilization in MCM-41 molecular sieve. *J. Mol. Catal. B: Enzym.* **1996,** *2,* 115-126.
6. Argyo, C.; Weiss, V.; Bräuchle, C.; Bein, T., Multifunctional Mesoporous Silica Nanoparticles as a Universal Platform for Drug Delivery. *Chem. Mater.* **2014,** *26,* 435-451.
7. Slowing, II; Vivero-Escoto, J. L.; Wu, C. W.; Lin, V. S., Mesoporous silica nanoparticles as controlled release drug delivery and gene transfection carriers. *Adv. Drug Delivery. Rev.* **2008,** *60,* 1278-1288.
8. Cui, J.; Rose, R. D.; Alt, K.; Alcantara, S.; Paterson, B. M.; Liang, K.; Hu, M.; Richardson, J. J.; Yan, Y.; Jeffery, C. M.; Price, R. I.; Peter, K.; Hagemeyer, C. E.; Donnelly, P. S.; Kent, S. J.; Caruso, F., Engineering Poly(ethylene glycol) Particles for Improved Biodistribution. *ACS Nano* **2015,** *9,* 1571-1580.
9. Suma, T.; Cui, J.; Mullner, M.; Fu, S.; Tran, J.; Noi, K. F.; Ju, Y.; Caruso, F., Modulated Fragmentation of Proapoptotic Peptide Nanoparticles Regulates Cytotoxicity. *J. Am. Chem. Soc.* **2017,** *139,* 4009-4018.
10. Mamaeva, V.; Sahlgren, C.; Linden, M., Mesoporous silica nanoparticles in medicine--recent advances. *Adv. Drug Delivery Rev.* **2013,** *65,* 689-702.
11. Gavrilov, K.; Saltzman, W. M., Therapeutic siRNA: principles, challenges, and strategies. *Yale J. Biol. Med.* **2012,** *85,* 187-200.
12. Leader, B.; Baca, Q. J.; Golan, D. E., Protein therapeutics: a summary and pharmacological classification. *Nat. Rev. Drug Discov.* **2008,** *7,* 21-39.
13. Carter, P. J., Introduction to current and future protein therapeutics: a protein engineering perspective. *Exp. Cell Res.* **2011,** *317,* 1261-1269.
14. Knezevic, N. Z.; Durand, J. O., Large pore mesoporous silica nanomaterials for application in delivery of biomolecules. *Nanoscale* **2015,** *7,* 2199-2209.
15. Moreira, A. F.; Dias, D. R.; Correia, I. J., Stimuli-responsive mesoporous silica nanoparticles for cancer therapy: A review. *Microporous Mesoporous Mater.* **2016,** *236,* 141-157.
16. Yao, V. J.; D'Angelo, S.; Butler, K. S.; Theron, C.; Smith, T. L.; Marchio, S.; Gelovani, J. G.; Sidman, R. L.; Dobroff, A. S.; Brinker, C. J.; Bradbury, A. R.; Arap, W.; Pasqualini, R., Ligand-targeted theranostic nanomedicines against cancer. *J. Controlled Release* **2016,** *240,* 267-286.
17. Zhang, K.; Xu, L. L.; Jiang, J. G.; Calin, N.; Lam, K. F.; Zhang, S. J.; Wu, H. H.; Wu, G. D.; Albela, B.; Bonneviot, L.; Wu, P., Facile large-scale synthesis of monodisperse mesoporous silica nanospheres with tunable pore structure. *J. Am. Chem. Soc.* **2013,** *135,* 2427-2430.
18. Li, Y.; Hei, M.; Xu, Y.; Qian, X.; Zhu, W., Ammonium salt modified mesoporous silica nanoparticles for dual intracellular-responsive gene delivery. *Int. J. Pharm.* **2016,** *511,* 689-702.
19. Xiong, L.; Du, X.; Shi, B.; Bi, J.; Kleitz, F.; Qiao, S. Z., Tunable stellate mesoporous silica nanoparticles for intracellular drug delivery. *J. Mater. Chem. B* **2015,** *3,* 1712-1721.
20. Kecht, J.; Schlossbauer, A.; Bein, T., Selective Functionalization of the Outer and Inner Surfaces in Mesoporous Silica Nanoparticles. *Chem. Mater.* **2008,** *20,* 7207-7214.
21. Möller, K.; Bein, T., Talented Mesoporous Silica Nanoparticles. *Chem. Mater.* **2016,** *29,* 371-388.
22. Kobayashi, T.; Singappuli-Arachchige, D.; Wang, Z.; Slowing, I. I.; Pruski, M., Spatial distribution of organic functional groups supported on mesoporous silica nanoparticles: a study by conventional and DNP-enhanced ^{29}Si solid-state NMR. *Phys.Chem.Chem.Phys.* **2017,** *19,* 1781-1789.
23. Kobler, J.; Möller, K.; Bein, T., Colloidal Suspensions of Functionalized Mesoporous Silica Nanoparticles. *ACS Nano* **2008,** *2,* 791-799.

24. Huh, S.; Wiench, J. W.; Yoo, J.-C.; Pruski, M.; Lin, V. S. Y., Organic Functionalization and Morphology Control of Mesoporous Silicas via a Co-Condensation Synthesis Method. *Chem. Mater.* **2003,** *15,* 4247-4256.
25. Kobler, J.; Möller, K.; Bein, T., Colloidal suspensions of functionalized mesoporous silica nanoparticles. *ACS Nano* **2008,** *2,* 791-799.
26. Cauda, V.; Schlossbauer, A.; Kecht, J.; Zurner, A.; Bein, T., Multiple core-shell functionalized colloidal mesoporous silica nanoparticles. *J. Am. Chem. Soc.* **2009,** *131,* 11361-11370.
27. He, Q.; Zhang, Z.; Gao, F.; Li, Y.; Shi, J., In vivo biodistribution and urinary excretion of mesoporous silica nanoparticles: effects of particle size and PEGylation. *Small* **2011,** *7,* 271-280.
28. Cauda, V.; Argyo, C.; Bein, T., Impact of different PEGylation patterns on the long-term bio-stability of colloidal mesoporous silica nanoparticles. *J. Mater. Chem. B* **2010,** *20,* 8693-8699.
29. Chiu, H. Y.; Deng, W.; Engelke, H.; Helma, J.; Leonhardt, H.; Bein, T., Intracellular chromobody delivery by mesoporous silica nanoparticles for antigen targeting and visualization in real time. *Sci. Rep.* **2016,** *6,* 25019.
30. Debets, M. F.; van Berkel, S. S.; Schoffelen, S.; Rutjes, F. P.; van Hest, J. C.; van Delft, F. L., Aza-dibenzocyclooctynes for fast and efficient enzyme PEGylation via copper-free (3+2) cycloaddition. *Chem. Commun.* **2010,** *46,* 97-99.
31. Kuzmin, A.; Poloukhtine, A.; Wolfert, M. A.; Popik, V. V., Surface functionalization using catalyst-free azide-alkyne cycloaddition. *Bioconjug. Chem.* **2010,** *21,* 2076-2085.
32. Bouvet, V.; Wuest, M.; Wuest, F., Copper-free click chemistry with the short-lived positron emitter fluorine-18. *Org. Biomol. Chem.* **2011,** *9,* 7393-7399.
33. Koo, H.; Lee, S.; Na, J. H.; Kim, S. H.; Hahn, S. K.; Choi, K.; Kwon, I. C.; Jeong, S. Y.; Kim, K., Bioorthogonal copper-free click chemistry in vivo for tumor-targeted delivery of nanoparticles. *Angew. Chem. Int. Ed. Engl.* **2012,** *51,* 11836-11840.
34. Lee, S. B.; Kim, H. L.; Jeong, H. J.; Lim, S. T.; Sohn, M. H.; Kim, D. W., Mesoporous silica nanoparticle pretargeting for PET imaging based on a rapid bioorthogonal reaction in a living body. *Angew. Chem. Int. Ed. Engl.* **2013,** *52,* 10549-10552.
35. Jeon, J.; Kang, J. A.; Shim, H. E.; Nam, Y. R.; Yoon, S.; Kim, H. R.; Lee, D. E.; Park, S. H., Efficient method for iodine radioisotope labeling of cyclooctyne-containing molecules using strain-promoted copper-free click reaction. *Bioorg. Med. Chem.* **2015,** *23,* 3303-3308.
36. Schlossbauer, A.; Dohmen, C.; Schaffert, D.; Wagner, E.; Bein, T., pH-responsive release of acetal-linked melittin from SBA-15 mesoporous silica. *Angew. Chem. Int. Ed. Engl.* **2011,** *50,* 6828-6830.
37. Liu, R.; Zhang, Y.; Zhao, X.; Agarwal, A.; Mueller, L. J.; Feng, P., pH-responsive nanogated ensemble based on gold-capped mesoporous silica through an acid-labile acetal linker. *J. Am. Chem. Soc.* **2010,** *132,* 1500-1501.
38. Hermanson, G. T., *Bioconjugate Techniques*. 2nd ed.; Elsevier Science: 2008.

5.6. Appendix

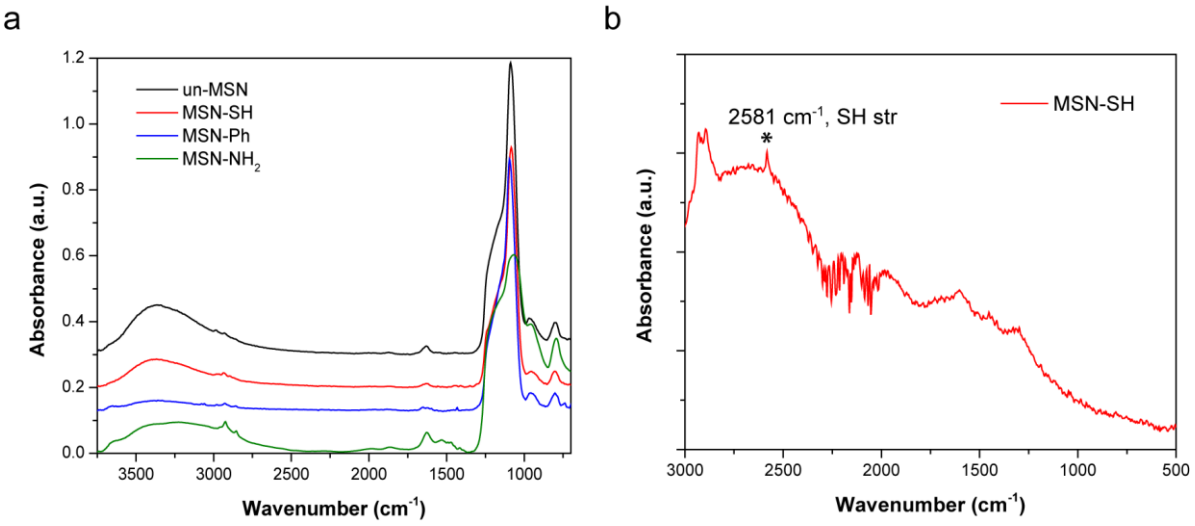

Figure S 5-1. (a) Full range infrared spectra of MSNs. All curves are shifted along the y-axis by 0.1 units for clarity. (b) Raman spectrum of MSN-SH. The spectrum obtained from a Nd:YAG laser (= 1064 nm) at a laser power of 100 mW and 3000 scans.

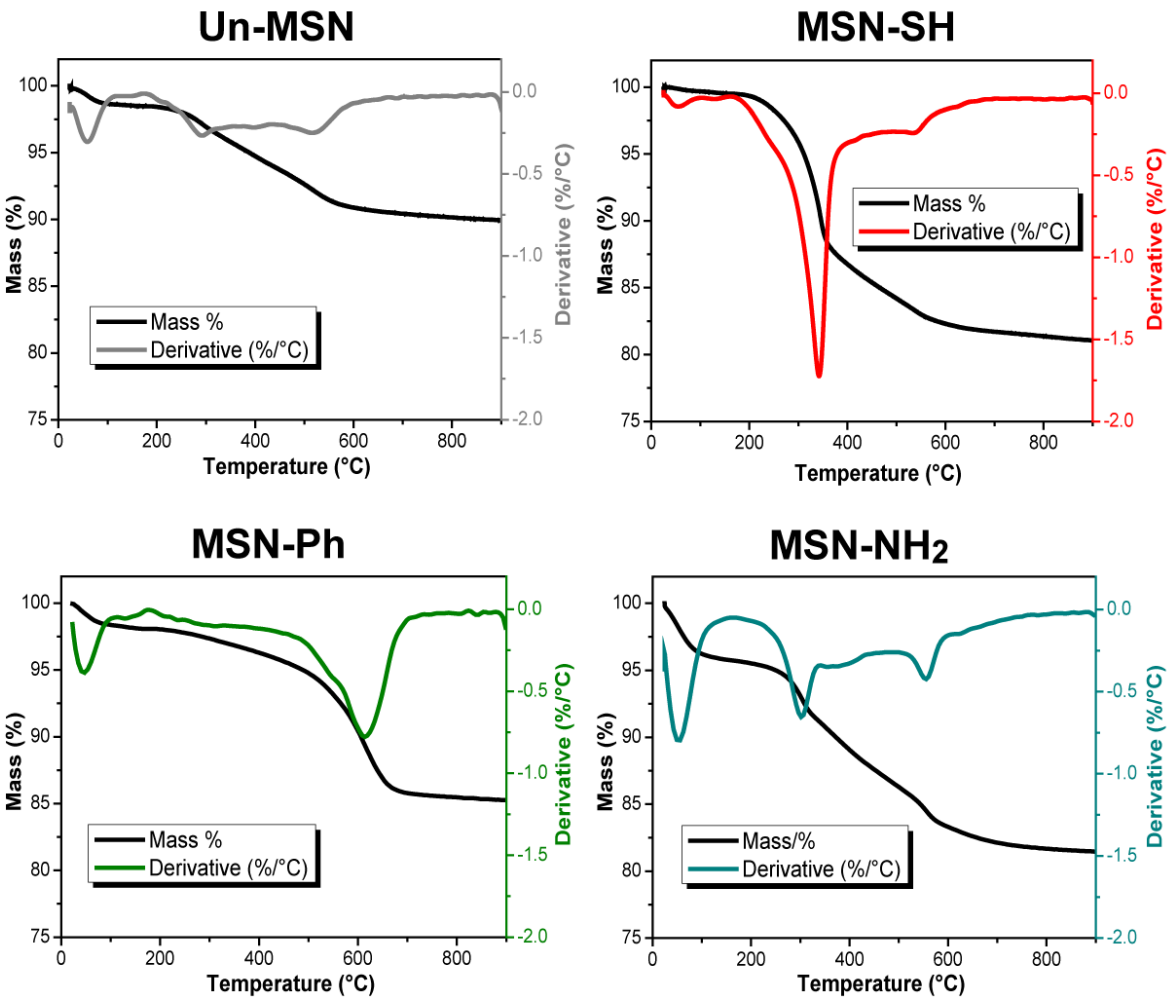

Figure S 5-2. Thermogravimetric analysis of MSNs functionalized with different organic groups.

Table S 5-1. TGA mass losses and the estimated degree of organic functionalizations of the functionalized MSNs.

Sample	Formulation of functional group (R)	Molecular weight of functional group (MW_R)	TGA mass loss[a] (%)	Estimated degree of organic functionalization[b] (%)
MSN-SH	C_3H_6SH	75.2	18.6	15.4
MSN-Ph	C_6H_5	77.1	13.1	10.5
MSN-NH_2	$C_3H_6NH_2$	58.1	15.0	15.4

[a] Calculated based on the mass differences between 150 °C and 900 °C.

[b] Calculated based on the formulation:

$$Mass\ loss\ (\%) = \frac{x \times MW_R}{x \times MW_R + (100 - x)MW_{SiO2}}$$

,x (%) = degree of organic functional groups.

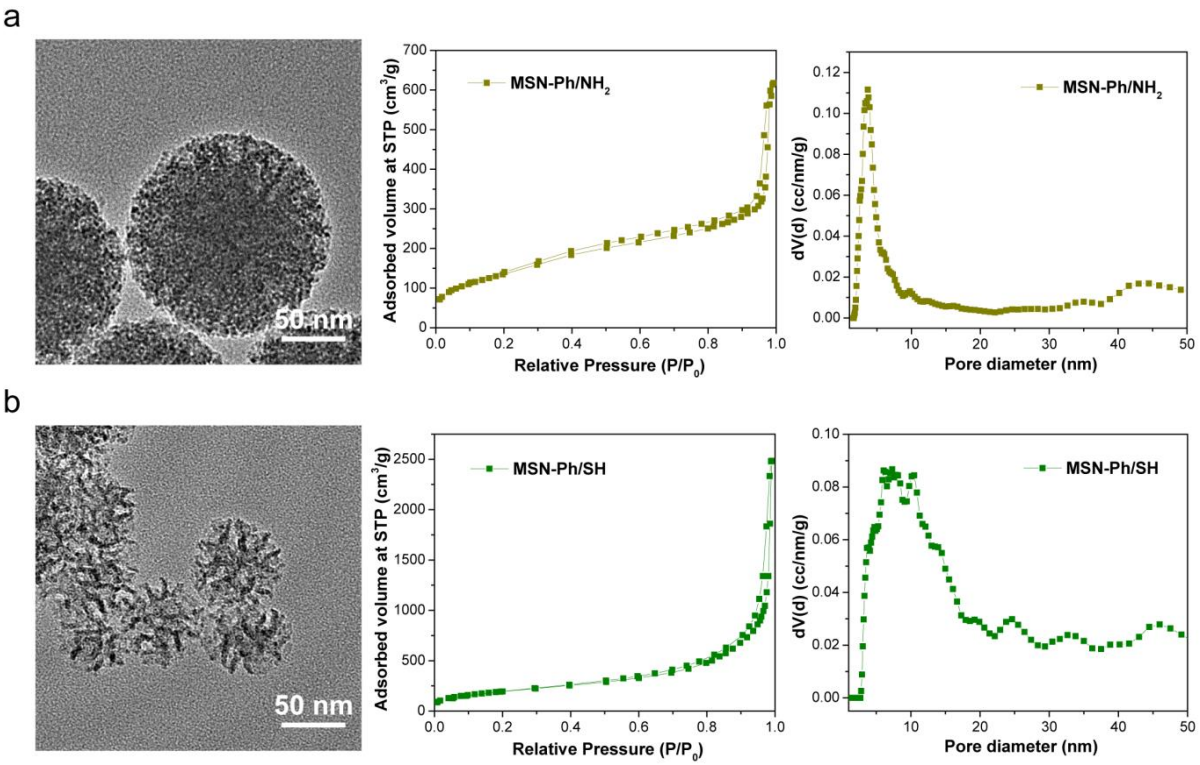

Figure S 5-3. Characterization of (a) MSN-Ph/NH_2 and (b) MSN-Ph/SH. From left to right: TEM images, N_2 sorption isotherms and NLDFT pore size distributions obtained from adsorption branches.

Table S 5-2. Synthesis and characterization information of MSN-Ph/NH_2 and MSN-Ph/SH.

Sample	Precursors	DFT Pore size distribution (nm)	Pore volume (cm^3/g)	BET surface area (m^2/g)	Particle size (nm)	pH value after silane addition
MSN-Ph/NH_2	95 mol% TEOS 2.5 mol% PTES 2.5 mol% APTES	2.5-5.0	0.9	496	190 ± 54	9.92
MSN-Ph/SH	90 mol% TEOS 5 mol% PTES 5 mol% MPTES	3.5-22	2.6	712	73 ± 15	9.33

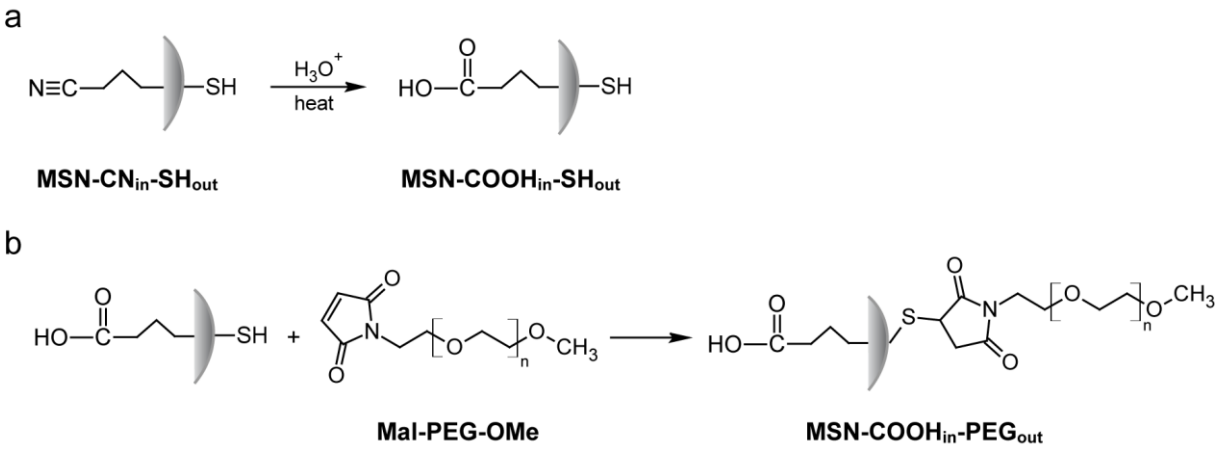

Figure S 5-4. Surface modification of core-shell MSNs. (a) Hydrolysis of MSN-CN_{in}-SH_{out} particles in acidic condition at 90 °C. (b) PEGylation of MSN-$COOH_{in}$-SH_{out}.

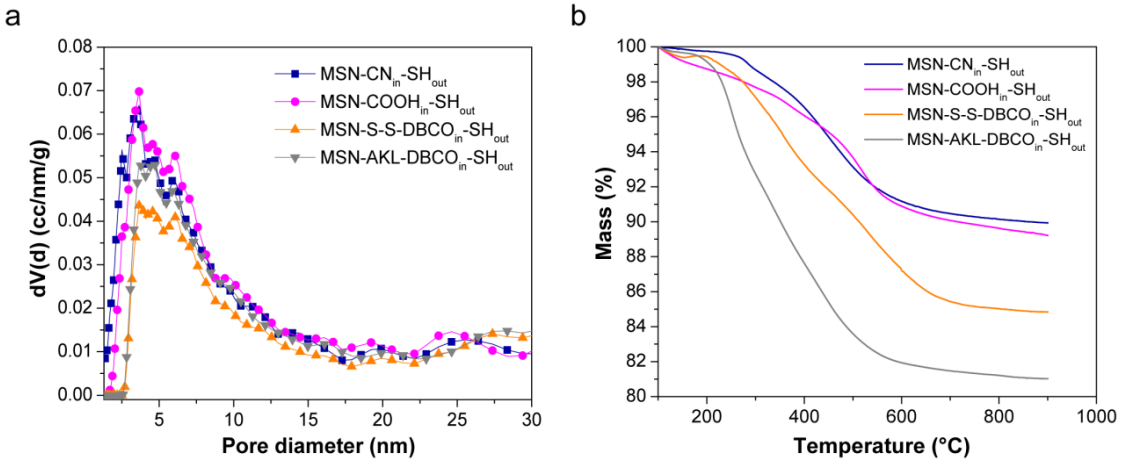

c

Sample	Pore size distribution (nm)	Pore volume (cm^3/g)	Surface area (m^2/g)	TGA mass loss at 900 °C (%)
MSN-**CN$_{in}$**-SH$_{out}$	2.5-12	1.5	573	10.1
MSN-**COOH$_{in}$**-SH$_{out}$	3.0-12	1.5	535	10.8
MSN-**S-S-DBCO$_{in}$**-SH$_{out}$	3.5-12	1.2	339	15.2
MSN-**AKL-DBCO$_{in}$**-SH$_{out}$	3.5-12	1.4	416	19

Figure S 5-5. Characterization of core-shell MSNs. (a) NLDFT pore size distribution of core-shell MSNs calculated from adsorption branches of N_2 sorption isotherms. (b) Thermogravimetric analysis. (c) Summary of the core-shell MSNs characterization. The TGA mass loss was calculated based on the mass differences between 100 °C and 900 °C.

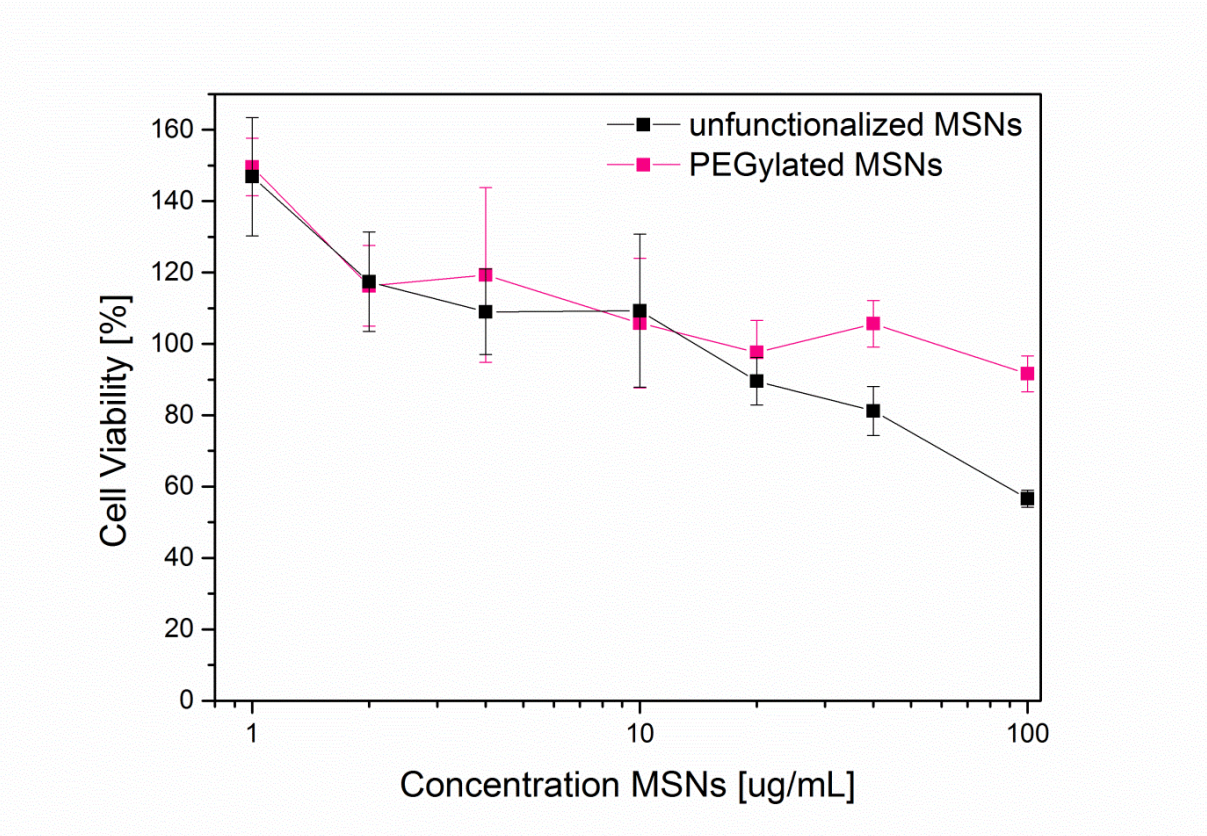

Figure S 5-6. Cytotoxicity of MSNs. CCK-8 assay for cytotoxicity studies of unfunctionalized and PEGylated core-shell MSNs after 24 h incubation on HeLa cells.

The CCK-8 (Cell Counting Kit 8) was used to determine the cytotoxicity of the here used large-pore MSNs. HeLa cells were seeded on a 96-well microplate (5 x 10^3 cells per well) in DMEM (100 µL $well^{-1}$) and incubated at 37 °C and 5% CO_2. 24h after cell seeding, 10 µL of MSNs (with various particle concentrations) were added to each well. The control group consisted of 10 µL water and was used as reference (100%). The cells were incubated with MSNs for 24 h. Afterwards 10 µL of CCK-8 solution were added to each well of the plate and after incubating the plate for another 4 h, the absorbance at 450 nm was measured in a microplate reader (SPARK 10M, Tecan Austria GmbH) with 600 nm as reference wavelength. Experiments were performed in triplicates. Error bars show the standard deviations.

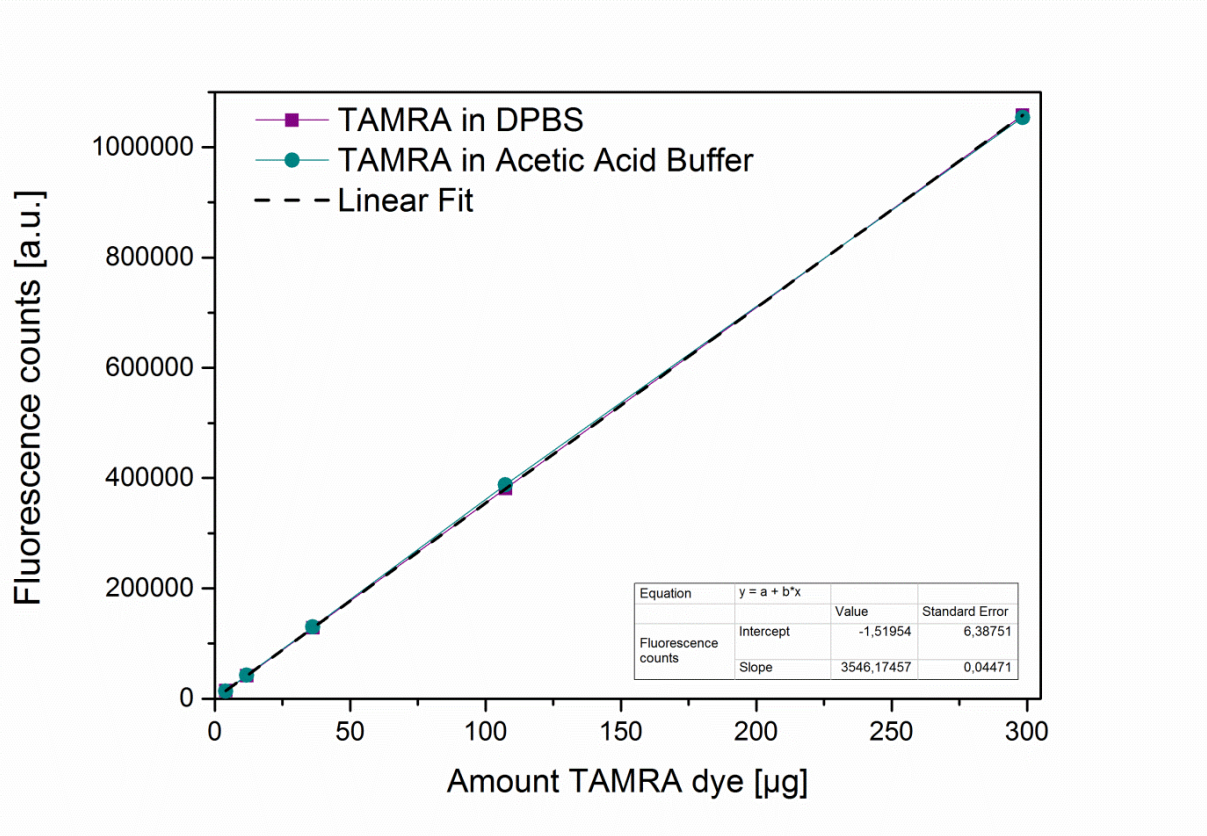

Figure S 5-7. Calibration curve of TAMRA dye for quantification of released amount. Different molar concentrations of TAMRA dye are measured with a fluorescence spectrometer and fitted linearly. As expected, TAMRA does not show a pH-dependent fluorescence.

To make sure that the successful click reaction is not hindered due to lack of TAMRA supply, we used TAMRA dye in excess. The supernatants were measured before and after the click reaction to determine the percentage of loaded dye. For MSN-AKL-DBCO-TAMRA 2% of the dye was loaded into the pores (100% correlates to 200 µg TAMRA dye used in the solution for the click reaction). After hydrolysis of the AK-linker, 60% of TAMRA dye were released. In the pores of MSN-S-S-DBCO-TAMRA, 10% of the provided dye was loaded and 57% thereof was released after reductive cleavage of the disulfide-bridges.

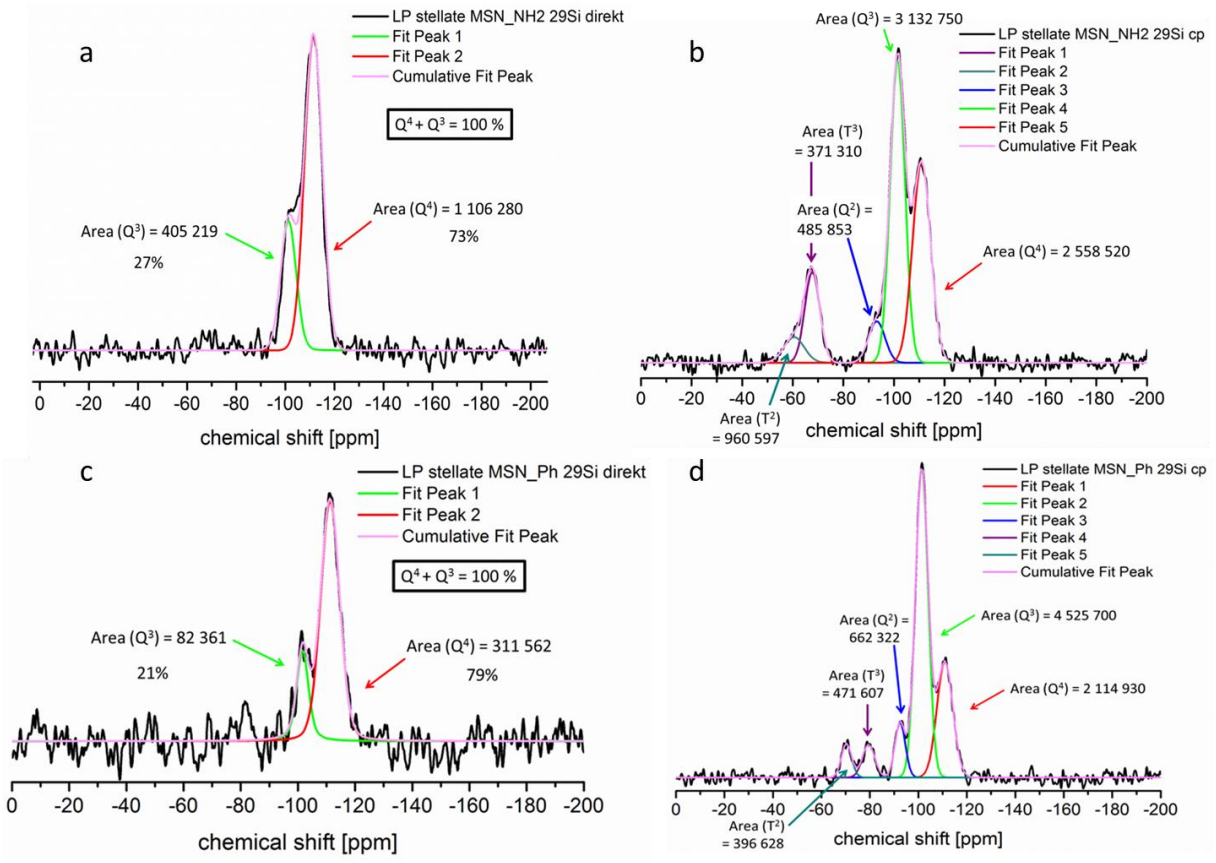

Figure S 5-8. ^{29}Si MAS-NMR spectra (a) MSN-NH_2 (direct excitation), (b) MSN-NH_2 (cross-polarized), (c) MSN-Ph (direct excitation), (d) MSN-Ph (cross-polarized).

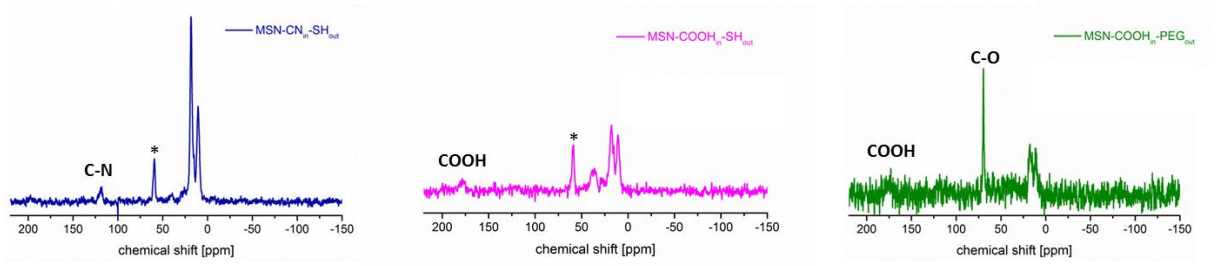

Figure S 5-9. 13C MAS-NMR spectra (a) MSN-CNin-SHout (blue), (b) MSN-COOHin-SHout (magenta) and (c) MSN-COOHin-PEGout (green). Hydrolysis of the cyano-groups (indicated with C-N at 118 ppm, blue spectrum) results in the resonance of carboxyl groups (COOH) appearing at 180 ppm (magenta and green spectra). Successful attachment of the PEG linker can be seen by C-O resonances appearing at 70 ppm (green spectrum). The asterisked peaks denote residual surfactants. The other resonances are assigned to functionalized silanes of the MSNs.

CHAPTER 6

Highly Active Enzymes Immobilized in Large Pore Colloidal Mesoporous Silica Nanoparticles

6. Highly Active Enzymes Immobilized in Large Pore Colloidal Mesoporous Silica Nanoparticles

This chapter was published as:

Dorothée Gößl, Helena Singer, Hsin-Yi Chiu, Alexandra Schmidt, Martina Lichtnecker, Hanna Engelke, Thomas Bein, *New J. Chem.* **2019**, *43*, 1671 – 1680. Reproduced with permission from the Centre National de la Recherche Scientifique (CNRS) and the The Royal Society of Chemistry.

Cover image by Christoph Hohmann, Nanosystems Initiative Munich (NIM)

Abstract

Various bio-applications of mesoporous materials (e.g., the immobilization of enzymes or the delivery of biomolecules such as siRNA) require large pores for the successful adsorption of the rather large molecules of interest and protecting the fragile cargo from external forces such as degradation. We describe the facile synthesis of functionalized mesoporous silica nanoparticles with large pores (LP-MSNs) providing high loading capacity for the immobilization of two differently-sized enzymes. The synthesis procedure yields homogeneous core-shell particles of about 100 nm in size with large mesopores (about 7 nm in diameter) and an azide-functionality inside the pores. The LP-MSNs were synthesized employing a co-condensation approach with the rather large micellar template cetyltrimethylammonium p-toluenesulfonate (CTATos). Due to the azide functionality, the LP-MSNs are suitable for bio orthogonal click chemistry reactions within the porous network. Two different acetylene-functionalized enzymes (sp-carbonic anhydrase (CA) and sp horseradish peroxidase (HRP)) were immobilized in the pores of the obtained LP-MSNs by a copper-catalyzed 1,3 dipolar cycloaddition reaction. The covalent attachment of the enzymes within the mesopores allowed us to investigate the catalytic performance of the enzyme-silica systems. The enzymes are stable after bioconjugation with the silica support and show high catalytic activity over several cycles for the colorimetric reaction of guaiacol (2-methoxyphenol) in case of LP-MSN-HRP and the hydrolysis of 4-nitrophenyl acetate (NPA) by LP-MSN-CA.

6.1. Introduction

Ordered mesoporous silica materials have attracted increasing attention due to the ability to tailor the structural and textural features including particle size, pore size, pore volume and surface area.[1-6] With the possibility to introduce various functionalities into the mesoporous framework, these materials have turned into interesting candidates for various biotechnological applications.[4, 7-10] However, such applications often involve fairly large molecules of more than 5 nm in size that may not fit into the pores of established silica nanoparticles (ca. 4 nm). Additionally, the active molecules need to be immobilized while preserving their function.

Considerable efforts have been made in the past years regarding the control of mesostructural diversity, compositional flexibility and morphology during the synthesis of mesoporous silica nanoparticles (MSNs).[3, 11-13] In recent years the synthesis of well-defined large-pore mesoporous systems with small particle sizes (in the size-range of 100 – 200 nm) for the encapsulation of large biomolecules (i.e. enzymes or siRNA) has been addressed.[14-17] Recently, the group of Zhang published a synthesis route for wide-pore stellate MSNs *via* the use of cetyltrimethylammonium p-toluenesulfonate (CTATos) as template in a near-neutral precursor solution.[18] The resulting stellate particles show a pore size distribution between 10 to 20 nm and a defined particle size of around 100 nm. With those properties they represent an ideal delivery vehicle for the cellular transport of large-sized biomolecules.[19]

Here, we describe a delayed co-condensation approach to create spatially segregated core-shell phenyl- and azide-functionalized large-pore MSNs (LP-MSNs), which serve as a versatile platform for the immobilization of enzymes. Due to their large pores, our functionalized LP-MSNs can be loaded with large bioactive molecules and thus are promising candidates for numerous bio-applications, including biocatalysis.

A promising way to introduce enzymes as biocatalysts in industrial applications is their immobilization onto inorganic mesoporous supports.[2, 20-22] Organo-functionalized nanostructured mesoporous silica materials have attracted great attention among the available inorganic host systems as they offer outstanding properties for the immobilization and encapsulation of biomolecules.[2, 23-24] As the pores of LP-MSNs match the size of enzymes, such silica materials are excellent candidates for enzyme immobilization,[25] yet their potential in this field still needs to be explored. Previous studies on established mesoporous silica materials (e.g. SBA-15) revealed that enzyme confinement within such hosts can increase the stability and reduce denaturation by protein unfolding, one major issue in industrial applications of biocatalysts.[26] However, as a consequence of immobilization onto the solid support, a decrease of the enzymatic activity relative to the free enzyme is often observed in such systems.[27-28] Strong interactions between enzymes and the host materials can be controlled by complementary organo-functionalization of the porous network, resulting in different catalytic activity and loading capacities.[29-31] As the functionalization of the mesoporous framework can be easily modified, the organo-moieties can be adjusted to the requirements of the respective enzyme and the preferred attachment reaction.

Furthermore, the application of mesoporous silica supports allows for the adjustment of pore- and particle size, structural arrangement and surface properties to optimize loading capacity and enzyme activity.[8, 32-33] Lee *et al*. have reviewed different methods of covalent enzyme immobilization onto mesoporous silica supports.[34] Here, we use the flexibility of silica functionalization for loading active enzymes and our newly developed MSNs with large pores to immobilize enzymes while retaining their activity. Additionally, we make use of the demonstrated reusability of immobilized horseradish peroxidase in SBA-16 to be able to study the catalytic behaviour and improved stability over more than one cycle.[35] Previous

studies describe the immobilization of horseradish peroxidase (HRP) onto the surface of mesoporous silica nanoparticles *via* physical adsorption or covalent binding by using the crosslinker glutaraldehyde.[36-37] Due to the fact that glutaraldehyde is toxic and rather unstable in air,[38] here we use a modified azide-alkyne click chemistry approach established by Schlossbauer *et al*. to immobilize enzymes into the LP-MSNs.[39-40] This method is biocompatible and avoids unfavorable pore blocking. The same immobilization technique is also used to covalently bind an essential metalloenzyme, namely carbonic anhydrase, to the pore walls of the mesoporous silica nanoparticles. The immobilization of enzymes in general enables their already mentioned reusability and furthermore their long-term use in bioreactors.[41]

Two different enzymes, namely the lyase carbonic anhydrase (CA) and the peroxidase horseradish peroxidase (HRP), were chosen for this study and were immobilized with an efficient method into the newly developed azide-functionalized LP-MSNs. A novel co-condensation synthesis approach was developed to generate organo-functionalized MSNs with large pores suitable for biocompatible coupling methods. To study the catalytic activity of the immobilized enzymes, two suitable activity assays were performed. In the case of carbonic anhydrase, the catalyzed hydrolysis of the substrate 4-nitrophenol acetate was studied by following the increasing absorbance of yellow 4-nitrophenol at 400 nm over time. For immobilized horseradish peroxidase, the catalyzed oxidation of guaiacol (2-methoxyphenol) was recorded at a wavelength of 470 nm over time. It was shown that the immobilized enzymes exhibited high stability and remained highly active after covalent immobilization in the LP-MSNs.

In this work we combine a simple support synthesis with a very efficient immobilization technique to obtain an active, stable and reusable enzyme-silica system.

6.2. Results and Discussion

Synthesis of large pore MSNs

For the immobilization of alkyne-functionalized enzymes by a bio-orthogonal click chemistry approach, core-shell mesoporous silica nanoparticles with large pores and azide groups on the internal and phenyl groups on the external surface (LP-MSN-N_3) were synthesized using the delayed co-condensation procedure developed in our group following a modified protocol from Zhang et al..[18 46]

In brief, a delayed co-condensation approach was chosen to introduce small amounts (5 mol% of the original TEOS amount) of azide-functionality into the inside of the mesoporous framework of the LP-MSNs and to obtain a homogeneous distribution of organic moieties within the silica material to ensure immobilization of the enzymes only inside the pores of the particles. Higher degrees of organo-modification can result in a reduction of the pore diameter and would thus impede the diffusion of enzyme molecules into the mesoporous channels and increase the likelihood of pore blocking. For the introduction of azide-moieties in the core, the silica source tetraethyl orthosilicate (TEOS) was co-condensed with (3-azidopropyl) triethoxysilane (AzTES, 5 mol% of total silane content) while PhTES (1 mol% of total silane content) and TEOS were used to generate phenyl groups on the external surface. A shell of pure TEOS was condensed in-between to create an interlayer between the two different functional groups. Additionally, we found that the introduction of organo-moieties in the case of azide-silanes has no negative effect on the formation of the mesoporous structure, whereas amine-functionalities easily disrupt the large-pore nanoparticle formation. TEM and SEM micrographs (Figure 6-1a-c) of the resulting core-shell particles (MSN-$N_{3,in}$-Ph_{out}) show a stellate morphology and a conical-like pore structure.

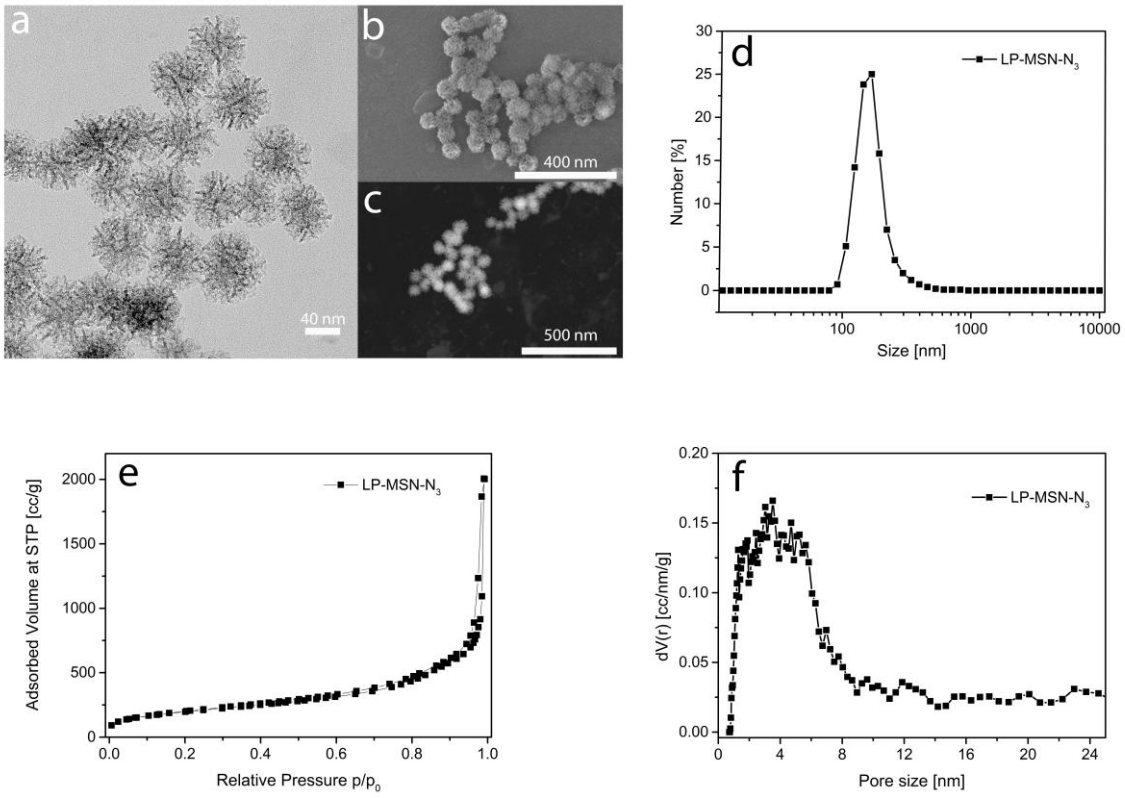

Figure 6-1 Characterization of LP-MSN-N_3. a) Transmission electron microscopy (TEM) image, b) Scanning electron microscopy (SEM) image and c.) Scanning transmission electron microscopy (STEM) image of template-extracted LP-MSN-N_3, d) dynamic light scattering (DLS) data showing a narrow size distribution, e) nitrogen sorption isotherm and f) pore size distribution obtained from nitrogen sorption measurement for LP-MSN-N_3.

Transmission electron microscopy images show spherically shaped nanoparticles with a fairly homogenous particle size distribution within a size range of 60 – 90 nm (Figure 6-1a). The large pores are present in each LP-MSN and evenly distributed over the entire nanoparticle. The particle size distribution data are in good accordance with the values obtained by dynamic light scattering, exhibiting a maximum at 150 nm (Figure 6-1d). We explain the moderately increased apparent size obtained by DLS measurements compared to the TEM measurements with the larger hydrodynamic diameter of the LP-MSN-N3 in comparison to their real size - possibly weak agglomeration is also present. The mesoporous framework is well-defined and clearly present in all particles (Figure 6-1a-c). The pore sizes are in a range of about 6 – 10 nm (deduced from TEM measurements) and consistent with the wide pore

size distribution of about 2.5 – 12 nm obtained from nitrogen sorption measurements (Figure 6-1f). The corresponding sorption data show a hybrid isotherm of type IIb combined with a certain fraction of type IV. The narrow hysteresis can be characterized as an H3 hysteresis loop that results from aggregation and inter-granular pores and thus from a significant degree of textural porosity, indicated by the long tail in the pore size distribution (Figure 6-1f). Monolayer formation of the adsorbate can be observed between p/p0 = 0 and 0.2, followed by multilayer adsorption over a broad range. The apparent lack of saturation (pore filling) at high p/p0 could be due to a broad distribution of textural porosity between the dried particles. The inter-particle voids, which are visible in the micrographs (Figure 6-1a-c), are within a size-range of 10 – 30 nm. Summarizing, we obtained LP-MSNs exhibiting a pore size in the range of mesoporous materials (Figure 6-1f, maximum around 7 nm), with a pore volume of 1.6 cm3/g and a BET surface area of As = 670 m2/g. In addition, infrared spectroscopy was carried out and verified the presence of azide-moieties within the pore system of LP-MSN-N3 (Figure S 6-1).

Immobilization of alkyne-functionalized carbonic anhydrase and horseradish peroxidase onto LP-MSN-N3 via a click chemistry approach

Two different enzymes, namely carbonic anhydrase (CA, 30 000 Da, 4.0x4.2x5.5 nm3)[47] and horseradish peroxidase (HRP, 44 000 Da, 4.0x4.4x6.8 nm3)[48], were immobilized in the mesoporous nanoparticles. Specifically, a modified click chemistry approach was used to immobilize the enzymes within the mesoporous framework of our newly generated LP-MSNs, which required prior alkyne functionalization of the enzyme (for details see Methods section and Scheme 6—1).[39, 42] The latter was achieved by the EDC-activated attachment of 4-pentynoic acid to the amine moieties of CA or HRP, respectively (Scheme 6—1). The reaction took place in MES buffer (pH 6.0) and at 4°C.

Scheme 6—1 Alkyne-functionalization of enzymes

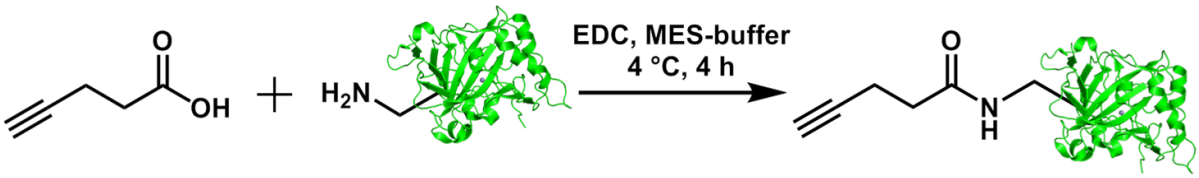

Scheme 1: EDC activated attachment of 4-pentynoic acid to the respective enzyme (carbonic anhydrase or horseradish peroxidase; here shown with bovine carbonic anhydrase II). The reaction was carried out in MES buffer (pH 6.0) at 4 °C. The accession number from the protein data bank (PDB) for the X-ray structure of BCAII is 1V9E.[49]

In a second synthesis step, the LP-MSN-N_3 particles were incubated with the alkyne-functionalized enzymes for 30 minutes to ensure their diffusion into the large mesopores before the click reaction catalysts were added to the reaction mixture, in order to avoid pore blocking (for details see Methods section). Subsequently, a click reaction was performed according to a slightly modified procedure published by Himo *et al.*, employing sodium ascorbate as reducing agent for Cu(II) ($CuSO_4$) (Scheme 6—2).[50] The nanoparticles were washed several times with water in order to remove excess and unbound enzyme molecules.

Scheme 6—2 Covalent attachment of sp-enzymes into LP-MSN-N_3

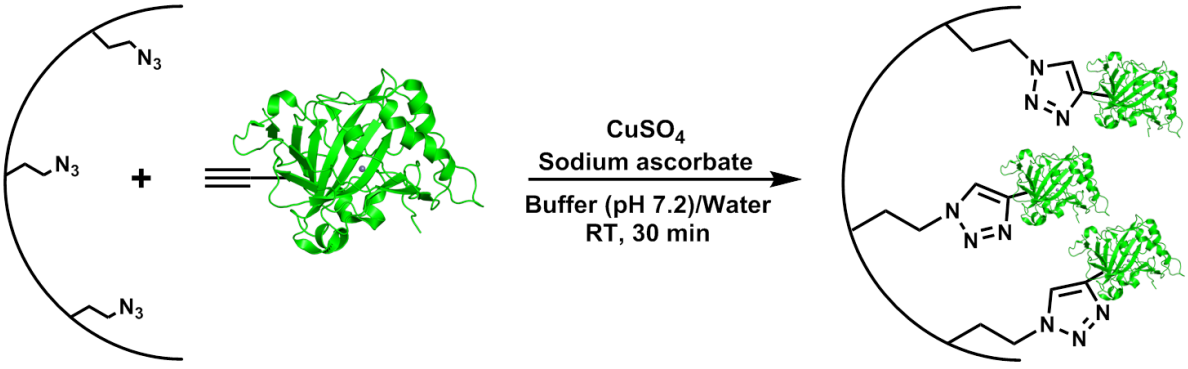

Scheme 2: Scheme for protein immobilization in LP-MSNs using click chemistry. Cu(II) was reduced with sodium ascorbate resulting in Cu(I), the actual catalyst.

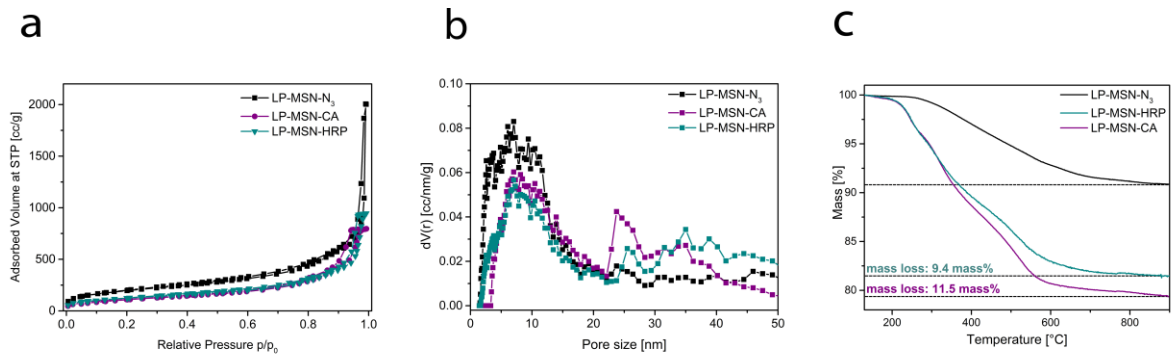

Figure 6-2 Nitrogen sorption data of LP-MSN-N_3 with immobilized enzymes. a) Isotherm of LP-MSN-N_3 (black), LP-MSN-CA (purple) and LP-MSN-HRP (cyan). b) Pore size distribution for LP-MSN-N_3 (black), LP-MSN-CA (purple) and LP-MSN-HRP (cyan). c) Thermogravimetric analysis data of LP-MSN-N_3 (black), LP-MSN-HRP (cyan) and LP-MSN-CA (purple). All TGA curves are normalized to 100% at 130 °C.

All obtained nitrogen sorption data show isotherms that appear as hybrids between type II and type IV isotherms, with a narrow H3 hysteresis loop. After the attachment of sp-enzymes the calculated BET-surface decreased significantly (Figure 6-2a and Table 6-1 respectively). This can be attributed to the uptake and covalent immobilization of the enzyme molecules within the large mesopores of the nanoparticles and the resulting partial pore filling. Accordingly, the pore volume decreased likewise (Figure 6-2b). A strong reduction of the very small pore sizes can be observed. We attribute this to the conical-like shape of the pores: enzymes that diffuse entirely into the pore, block the small end of it and thereby the parts of the pores representing small pore sizes. Carbonic anhydrase shows a stronger reduction of the smaller pore sizes than horseradish peroxidase, possibly due to their different shape: the shape of CA is close to a square and thus, when it gets stuck in a pore due to size limitations, it may block the entire pore uniformly in all directions. HRP is rod-shaped, if it blocks a pore there is space on its sides that allows for BET measurements to still access and probe the pore. We assume that the decrease in pore volume in case of the sample LP-MSN-CA is stronger than in LP-MSN-HRP because a larger amount of sp-CA could be incorporated into the mesoporous framework of our nanoparticles. These results are in good accordance with the thermogravimetric analysis (TGA) data (Figure 6-2c and Table 6-1 for relative mass loss), showing that more carbonic

anhydrase than horseradish peroxidase was immobilized in the LP-MSNs. The higher degree of immobilization of CA as compared to HRP is attributed to its smaller dimension; the enzyme can diffuse more easily into the mesopores without having as much contact with the pore walls and the attached organic moieties, while HRP is bigger and thus has a higher likelihood to touch the pore walls, bind to them and block access to the pore for additional molecules.

Table 6-1 Nitrogen physisorption and thermogravimetric analysis data of LP-MSN-N_3 and LP-MSN-Enzyme.

Sample	BET surface area [m^2/g]	Pore size range [a] [nm]	Pore volume	Relative mass loss [b] [%]
LP-MSN-N_3	670	2.5-12 nm	1.6	9.2 (7.7% for N_3-moieties)
LP-MSN-CA	389	5.5-12 nm	1.2	20.7
LP-MSN-HRP	423	5.3-12 nm	1.4	18.6

[a]DFT pore size range refers to the main range of the pore size distribution. [b]Relative mass loss obtained by TGA; all curves are normalized to 130 °C

From the additional mass loss of 11.5% for the sample LP-MSN-CA compared to LP-MSN-N_3, the amount of attached enzyme can be estimated to be 4.7 µmol per g silica (for calculation see Calculation A 6—1, Appendix), which corresponds to 141 mg carbonic anhydrase per g silica support. The amount was additionally determined via Bradford assay, resulting in 99 mg CA per g silica (see Appendix, Figure S 6-10). This deviation of almost 28% is attributed to additional components in the channels of the mesoporous silica that contribute to weight changes during TGA measurements. The determined amount indicates that 0.5% of all azide-moieties have reacted with sp-CA, as the amount of azide-moieties was estimated to 1.02 mmol per g silica. From the additional mass loss of 9.4% for the sample LP-MSN-HRP compared to the azide-functionalized LP-MSNs, the amount of immobilized horseradish peroxidase can be estimated to 2.6 µmol per g silica (see Appendix, Calculation A

6—1), or to 114 mg HRP per g silica support. The amount determined with the additionally performed Bradford assay (see Appendix, Figure S 6-11) differs very little from the above TGA results and corresponds to 103 mg HRP/ g silica. This indicates that a smaller amount of sp-Horseradish peroxidase molecules was able to diffuse into the large mesopores and reacted with 0.25% of all azide-moieties of LP-MSN-N_3. A probable reason for this is the even larger molecular dimension of horseradish peroxidase (4.0 x 4.4 x 6.8 nm^3),[48] resulting in partial blocking of the pores by immobilized horseradish peroxidase. All nitrogen sorption data are supported by the corresponding thermogravimetric analysis and the calculated relative mass losses that are summarized in Table 6-1. As further proof for the successful attachment of sp-enzymes via click chemistry, vibrational spectroscopy was performed with the respective LP-MSN-enzyme samples (see Figure S 6-3 for CA and Figure S 6-4 for HRP). The symmetric and asymmetric CH_2 stretching vibrations of the enzyme appear in the range of 2960–2871 cm^{-1} in the spectrum of LP-MSN-CA and sp-CA and of LP-MSN-HRP and sp-HRP, respectively. The peak at 2105 cm^{-1} can be attributed to the asymmetric N_3 stretching vibration of LP-MSN-N_3 and can still be observed in LP-MSN-enzyme due to the small fraction of reacted (clicked) azide-moieties. At 1658 cm^{-1} (dashed line) the C=O stretching vibration appears in the spectrum of LP-MSN-CA/HRP, which is attributed to the amide bonds of the attached enzymes. The vibration at 1530 cm^{-1} (second dashed line) is only visible in the spectra of sp-enzyme and LP-MSN-enzyme and represents the N-H bending vibration of the peptide bonds of the enzyme. The peak at 1627 cm^{-1} in the spectrum of LP-MSN-N_3 indicates the presence of traces of water within the sample. Below 1300 cm^{-1}, vibrations of the silica framework appear with strong intensity. Summarizing, the results obtained by nitrogen sorption, thermogravimetric analysis and vibrational spectroscopy all support the successful immobilization of carbonic anhydrase and horseradish peroxidase within the porous network

of LP-MSN-N_3. In the following we address the catalytic properties of the immobilized enzymes.

Catalytic activity determination of immobilized carbonic anhydrase

To characterize the properties of immobilized CA, the catalytic activity of the hydrolysis of 4-nitrophenylacetate (NPA) was studied colorimetrically by measuring the absorbance of the newly formed yellow nitrophenol at 400 nm (Figure 6-3a and Figure S 6-5, Appendix). To ascertain the robust attachment and stability of the enzyme inside the pores, multiple cycles were performed. After cycle 1, the reaction mixture was transferred to small Eppendorf tubes and centrifuged for 5 min (15 °C, 16900 g). The pellet was redispersed in water and centrifuged again. This washing step was conducted two times to remove (un)reacted substrate. Afterwards, the washed particles were redispersed in water and fresh substrate was added for the next cycle. In total eight such cycles with intermediate washing steps were performed (Figure 6-3a). The time-based measurements show a successful conversion of 4-NPA to nitrophenol in all cycles, proving the continuous activity and stability of the immobilized carbonic anhydrase. Due to the washing steps in between the cycles, a certain loss of particles and therefore also enzyme can be seen by a decrease in pellet size and accordingly a decrease in absorbance and slope (Figure 6-3a). The self-hydrolysis of 4-NPA was measured separately (data shown in Figure S 6-6). The self-hydrolysis reaction data were subtracted from the raw data of the enzyme-catalyzed hydrolysis. In Figure 6-3a and Figure S 6-7 the CA activity corrected for self-hydrolysis is shown. For quantitative determination of the reaction rate, the slope of one cycle at a reduced substrate concentration (1mM NPA) was converted into concentration vs. time (Figure S 6-7, Appendix) by using Lambert-Beer's law (ε = 16 300 M^{-1} cm^{-1}).[51] According to Michaelis-Menten kinetics in the limit of low substrate concentrations, the kinetic constant k_{cat}/K_m was determined to be 74 M^{-1} s^{-1}. There are large

differences in the kinetic constants for different CAs reported in the literature.[52] Therefore, it is difficult to compare our result for immobilized bovine carbonic anhydrase to literature values.

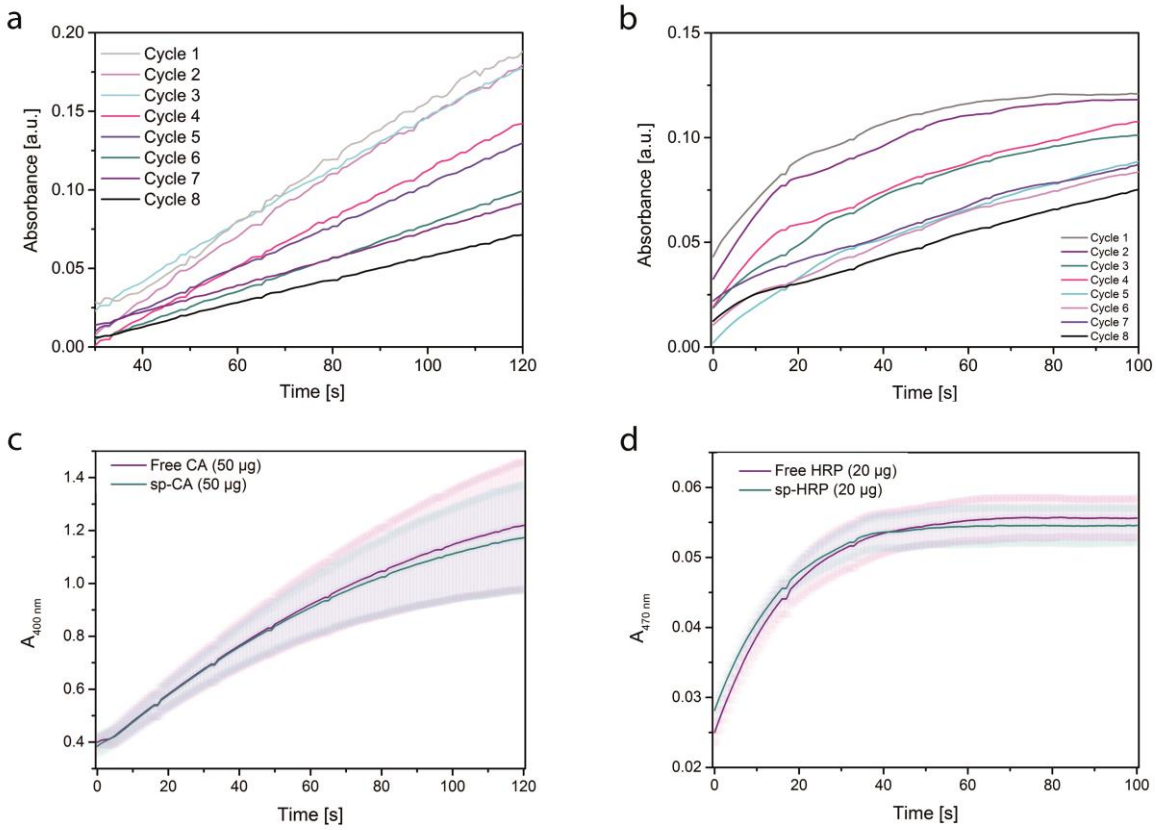

Figure 6-3 Activity determination for LP-MSN-CA and LP-MSN-HRP as well as for free versus alkyne-functionalized enzymes. a) UV-Vis absorption measurement of catalyzed hydrolysis of the substrate 4-nitrophenol acetate (NPA) by LP-MSN-CA within a period of 120 s (interval 1 s) at 400 nm with 10 mM NPA in TRIS buffer (pH 8, 50 mM) over eight cycles. b) Activity determination of LP-MSN-HRP by measuring the absorbance at 470 nm of emerging oxidized guaiacol (2-methoxyphenol) in potassium phosphate buffer (pH 7, 0.2 M) for 100 s (interval 1 s) over eight catalytic cycles. The enzyme's reaction rate was determined from the slope of the first cycle's linear region (gray curve, from 0 s-15 s). c) Catalytic activity of native versus functionalized carbonic anhydrase (assay described in a)). Comparison of catalytic activity of native (free) CA (purple line ± SD light purple area) versus functionalized CA (sp-CA) (cyan line ± SD light cyan area). d) Activity comparison of native versus functionalized horseradish peroxidase (assay described in b)). Activity determination of native (free) HRP (purple line ± SD light purple area) versus sp-HRP (cyan line ± SD light cyan area) by measuring the absorbance of oxidized guaiacol at 470 nm for 100 s.

The resulting activity of immobilized carbonic anhydrase was also determined in international units IU, which is described in the Appendix. The expressed activity of the biocatalyst LP-MSN-CA results in 8.4 units (per 5 mg MSNs) i.e. 1680 units / g support. The corresponding amount of free enzyme shows an activity of 85.6 units and therefore performs one order of

magnitude faster than the immobilized enzyme, which might be attributed to partial blocking of the enzyme due to the statistical attachment of the enzyme molecules inside the pores. All in all, it could be shown that carbonic anhydrase was successfully immobilized inside the large pores of our MSNs and remained there stable and active.

Horseradish peroxidase activity determination

In order to determine the catalytic activity of the MSN-bound HRP molecules, an assay involving the oxidation of guaiacol was performed.[45] Thereby, the catalyzed oxidation of guaiacol was measured by recording the absorption of the produced tetraguaiacol at 470 nm with UV-Vis spectroscopy (Figure 6-3b, for experimental details see Methods section and Figure S 6-8, Appendix). The remaining stability and activity of the immobilized enzyme could be shown over several cycles just as well as in the case of carbonic anhydrase. To determine the reaction rate, the slope in the linear region (0 s - 15 s) of the first cycle's graph (gray graph) was used and converted into concentration vs. time (Figure S 6-9, Appendix) using Lambert-Beer's law (with $\varepsilon = 26.6\ mM^{-1}cm^{-1}$ from Maehly and Chance[45] and d = 1 cm). The rate was calculated to be $2.5 \times 10^4\ M^{-1}\ cm^{-1}$ according to Maehly and Chance.[45] In comparison to the literature value[45] of $3 \times 10^5\ M^{-1}\ cm^{-1}$, our immobilized enzyme performs slower by about one order of magnitude than the free corresponding sp-enzyme. The resulting activity of immobilized horseradish peroxidase (definitions of IU at the end of the Appendix) is 0.86 units (per 0.16 mg MSN) i.e. 5343 units / g support. The corresponding amount of free enzyme shows an activity of 3.7 units, resulting in an only fourfold better performance than our immobilized HRP.

Note that the enzyme concentration used in the calculations is the upper limit. Due to a necessary centrifugation step before the activity assay a small loss of particles and therefore enzyme is inevitable, thus reducing the enzyme concentration. Since the enzyme

concentration is inversely proportional to the calculated reaction rate, our value of the calculated reaction rate represents a lower limit. Additionally, some horseradish peroxidase molecules could be partially hindered or blocked due to the random attachment of the large enzymes into the rather tightly matching pores; the active center might not always be perfectly accessible for the substrates. This may explain the lower reaction rate in comparison to unbound HRP.

To prove that alkyne-functionalisation of the enzymes does not impair their catalytic activity, the activity assays were performed with the native versus alkyne-functionalized enzymes. In both cases (Figure 6-3c and Figure 6-3d) it can be shown that the catalytic performance is maintained after enzyme-functionalization.

6.3. Conclusion

We report a facile delayed co-condensation strategy for the synthesis of spatially segregated core-shell bi-functional large-pore MSNs. This direct approach towards introducing organo-moieties into the mesopores is highly beneficial since different functionalities can be efficiently introduced at controlled concentrations. This method further avoids additional grafting steps that may be difficult with colloidal systems. Our synthesis yields mesoporous silica nanoparticles within a size range of about 100 nm exhibiting large pore sizes of up to 12 nm and carrying azide-functionalities inside the pore system. This organo-functionalization makes the LP-MSNs suitable for a biocompatible modification via click chemistry. We covalently immobilized the two enzymes carbonic anhydrase and horseradish peroxidase in the interior of the LP-MSN-N_3 host.

The lyase carbonic anhydrase (CA) (4.0 x 4.2 x 5.5 nm^3)[47] and the peroxidase horseradish peroxidase (HRP) (4.0 x 4.4 x 6.8 nm^3)[48] were successfully modified with alkyne-linkers to enable grafting through a Cu-catalyzed click reaction. The enzymes were allowed to diffuse into the mesopores before the catalysts for the click reaction were added to the reaction mixture, thus avoiding unfavorable pore blocking and low catalytic activity. We could demonstrate in this study that both enzymes are still highly active in their immobilized state, and that they maintain high activity during activity assays over several cycles.

Overall, we present a spatially structured colloidal MSN-based system with large pores for the immobilization of active biomolecules that holds promise as a versatile platform for numerous applications.

6.4. Experimental Part

Materials. Tetraethyl orthosilicate (TEOS, Aldrich, ≥ 99%), phenyltriethoxysilane (PhTES, Aldrich, > 98%), cetyltrimethylammonium p-toluenesulfonate (CTATos, Sigma), triethanolamine (TEA, Aldrich, 98%), (3-chloropropyl) triethoxysilane (CPTES, Fluka, 95%), diethyl ether (Et_2O, Sigma, >98%), sodium azide (Fluka, 99%), ethanol (EtOH, Aldrich, absolute), conc. hydrochloric acid (HCl, Aldrich, 37%), ammonium nitrate (NH_4NO_3, Sigma, 99%), N-(3-dimethylaminopropyl)-N-ethylcarbodiimide (EDC, Alfa Aesar, 98%), 4-pentynoic acid (Fluka, 97%,), tris(hydroxymethyl) aminomethane (TRIS, Sigma, 99.8 %), 2-(N-morpholino)ethanesulfonic acid (MES, Sigma, 99.5 %), carbonic anhydrase from bovine erythrocytes (Sigma, ≥95% (SDS-PAGE), specific activity ≥3,500 W-A units/mg protein, lyophilized powder), peroxidase from horseradish (Sigma, Type VI-A, essentially salt-free, lyophilized powder, 950-2000 units/mg solid (using ABTS), ≥250 units/mg solid (using pyrogallol)), (+)-sodium L-ascorbate (Sigma, ≥98%), copper(II) sulfate (Sigma, ≥99.99%), disodium hydrogen phosphate (Na_2HPO_4, Sigma, >99%), monosodium hydrogen phosphate (NaH_2PO_4, Sigma, >99%), sodium hydroxide (1 M, Sigma), dipotassium hydrogen phosphate (K_2HPO_4, Sigma, >99%), monopotassium hydrogen phosphate (KH_2PO_4, Sigma, >99%), 4-nitrophenyl acetate (Sigma, esterase substrate), guaiacol (Sigma, oxidation indicator, ≥98.0%), hydrogen peroxide (Sigma, 30 wt%). Unless otherwise noted, all reagents were used without further purification. Bi-distilled water from a Millipore system (Milli-Q Academic A10) was used for all syntheses and purification steps.

Methods. For transmission electron microscopy, samples were investigated with an FEI Titan 80-300 transmission electron microscope (TEM) operating at 300 kV with a high-angle annular dark field detector. A droplet of the diluted MSN solution in absolute ethanol was dried on a carbon-coated copper grid. The TEM, SEM and STEM micrographs in Figure

6-1a-c show template-extracted mesoporous large pore silica particles (LP-MSN-N_3) generated with the above described synthesis procedure (details below). Nitrogen sorption measurements were performed on a Quantachrome Instruments NOVA 4000e and on an Autosorb iQ instrument. All samples with attached enzyme (15 mg each) were treated at 298 K (12 h *in vacuo*), whereas the sample LP-MSN- N_3 was heated to 393 K for 12 h *in vacuo* (10 mTorr) to outgas the samples before nitrogen sorption was measured at 77 K. For calculations of pore sizes and volumes a non-local density functional theory (NLDFT) equilibrium model of nitrogen on silica was used. The obtained physisorption data for LP-MSN-N_3 are shown in Figure 6-1e (nitrogen sorption isotherm) and Figure 6-1f (pore size distribution) and in Figure 6-2a (isotherms) and Figure 6-2b (pore size distribution) for LP-MSN-CA and LP-MSN-HRP. Dynamic light scattering (DLS) measurements were performed on a Malvern Zetasizer-Nano instrument equipped with a 4 mW He-Ne laser (633 nm) and an avalanche photodiode. The hydrodynamic radius of the particles was determined by dynamic light scattering in water. The data are shown in Figure 6-1d. Thermogravimetric analysis of the bulk samples LP-MSN-N_3, LP-MSN-CA and LP-MSN-HRP was performed on a Netzsch STA 440 C TG/DSC with a heating rate of 10 K / min in a stream of synthetic air of about 25 mL/min. The mass was normalized to 100% at 130 °C for all samples and the resulting data are presented in Figure 6-2c. All IR measurements were performed on a Thermo Scientific Nicolet iN10 IR Microscope in reflection-absorption mode with a liquid nitrogen-cooled MCT-A detector. All spectra are background corrected. UV-Vis measurements were performed on a Perkin Elmer Lambda 1050 spectrophotometer with a deuterium arc lamp (UV region) and a tungsten filament (visible region). The detector was an InGaAs integrating sphere detector. Time-based enzyme activity assays were performed in macro PMMA-cuvettes (path length 10 mm). For small sample amounts (2 µl of the sample) a NanoDrop 2000c spectrometer from Thermo Scientific Fisher was employed for UV-Vis measurements.

The absorbance at 280 nm (mode A280) was used to determine carbonic anhydrase concentrations.

Buffer preparation.

MES buffer (0.1 M, pH 6.0). 2-(N-morpholino)ethanesulfonic acid (MES, 9,76 g) was dissolved in water (500 mL). The pH was adjusted to 6.0 using sodium hydroxide (1 M).

Sodium phosphate buffer (5 mM, pH 7.4). Monosodium hydrogen phosphate (2.92 g) and disodium hydrogen phosphate (7.74 g) were dissolved in 10 L of water (5 mM). The pH was fine-adjusted to 7.4 with NaOH or HCl using a pH-meter.

Potassium phosphate buffer (0.2 M, pH 7.0). Monopotassium hydrogen phosphate (13.61 g) and dipotassium hydrogen phosphate (17.40 g) were dissolved in water (500 mL). The pH was fine-adjusted to 7.0 with NaOH or HCl using a pH-meter.

TRIS buffer (0.1 M, pH 8.0). Tris(hydroxymethyl)aminomethane (TRIS, 6.075 g) was dissolved in water (500 mL). The pH was adjusted to 8.0 using HCl (1 M).

Synthesis of alkyne-modified enzymes (sp-enzymes).

Carbonic Anhydrase (sp-CA). To a freshly prepared, cooled solution (4 °C) of carbonic anhydrase (40 mg, M_w = 29000 g/mol, 1.38 µmol) in MES buffer (pH 6, 18.7 mL, 0.1 M), an aqueous solution (1 mL) of 4-pentynoic acid (0.1 M, 9.81 mg, 0.1 mmol) was added. The resulting mixture was vortexed for 2 min and then stored at 4 °C for 15 min. Subsequently, EDC (11.5 mg, 0.07 mmol) was added to the solution. The reaction was vortexed again for 2 min and then kept at 4 °C for 4 h without stirring. Afterwards, the obtained solution was dialyzed in a cold room at 4 °C against sodium phosphate buffer (5 mM, pH 7.4, 10 L) for a period of 24 h. The concentration of sp-CA (3.027 mg/mL) was determined with Nanodrop.

The alkyne-functionalized carbonic anhydrase was used for click reactions without further purification.

Horseradish peroxidase (sp-HRP). Alkyne-functionalized horseradish peroxidase was synthesized according to Gole *et al*. as described above.[42] The concentration of sp-HRP (1,32 mg/mL) was determined with UV-Vis spectroscopy (calibration curve, Figure S 6-2).

Synthesis of (3-azidopropyl) triethoxysilane. (3-Azidopropyl)triethoxysilane was synthesized according to a procedure published by Nakazawa *et al.*.[43] (3-chloropropyl)triethoxysilane (10 g, 41.7 mmol) and sodium azide (10 g, 154 mmol) were heated in anhydrous DMF (100 mL) under inert gas conditions at 90 °C for 4 h. Low boiling materials were removed from the mixture under reduced pressure. The crude oily product was dissolved in diethyl ether, resulting in the precipitation of salts, which were removed by filtration. Et_2O was removed *in vacuo* and the residual oil was distilled (95 °C). (3-azidopropyl)triethoxysilane was obtained as colorless liquid and used without further purification.

Synthesis of azide functionalized large pore mesoporous silica nanoparticles (LP-MSN-N_3). Core-shell bi-functional (MSN-$N_{3,in}$-Ph_{out}) MSNs were synthesized through a delayed co-condensation approach based on an adapted recipe reported in the literature.[18] In brief, TEA (0.047 g, 0.32 mmol), CTATos (0.263 g, 0.58 mmol) and H_2O (13.7 g, 0.77 mmol) were mixed in a 100 mL round bottom flask and stirred vigorously (1250 rpm) at 80 °C until the surfactant solution became homogeneous. TEOS (1.71 g, 8.2 mmol) and AzTES ((3-azidopropyl)triethoxysilane) (120 µL, 0.41 mmol; 5 mol%) were mixed and added to the surfactant solution and the mixture was stirred (1250 rpm) at 80 °C for 1 h. Afterwards, 201 mg of TEOS (0.96 mmol) was separated into 4 aliquots and added to the mixture every 3 minutes. The solution was further stirred for 1 h at 80 °C. A mixture of TEOS (20.1 mg,

0.096 mmol) and PhTES (phenyltriethoxysilane) (22.9 mg, 0.096 mmol, 1 mol%) was then added to the solution to generate the outer shell of the MSNs. The resulting solution was continuously stirred at 80 °C for 1 h. The as-synthesized particles were collected by centrifugation (7197 *g*, 20 min) and were subsequently template extracted (see below).

Template removal from LP-MSN-N_3. The organic template was removed via extraction from LP-MSN-N_3. Thus, 1 g of the as-synthesized particles was heated in an ethanolic solution (150 mL) containing 3 g ammonium nitrate at 90 °C under reflux for 1 h, cooled and collected by centrifugation (7197 *g*, 20 min) and extracted by a second reflux at 90 °C using a 2 M HCl/ethanolic solution (150 mL) for 1 h. Afterwards, samples were washed in the sequence EtOH, H_2O, EtOH (100 mL per wash) and were finally kept in 20 mL EtOH. Particles were collected by centrifugation (7197 *g*, 20 min) after each template extraction and washing step.

Immobilization of alkyne-functionalized carbonic anhydrase in LP-MSN-N_3 (LP-MSN-CA). An ethanolic suspension containing 50 mg LP-MSN-N_3 was centrifuged (10 min, 7197 g), washed with 15 mL sodium phosphate buffer (0.2 M, pH 7.2) and re-dispersed in 2.5 mL sodium phosphate buffer as well as 2 mL water. The suspension was vortexed for 2 minutes and put into an ultrasonic bath for 10 minutes to remove agglomerates. Subsequently, the buffered solution of sp-CA (containing 9 mg, 0.3 µmol sp-CA) was added and the resulting mixture was stirred for 30 minutes at room temperature. In the meantime, sodium ascorbate (1 mg, 5.05 µmol) was added to a solution of Cu(II)SO_4 (1.25 mg, 1 mmol) dissolved in 5 mL water and stirred for 10 min at ambient temperature. 12 µL of this freshly prepared solution was added to the reaction mixture containing LP-MSN-N_3 and sp-CA to catalyze the covalent attachment of the enzyme via click chemistry. The resulting suspension was shaken (600 rpm) for 30 minutes at room temperature. Subsequently, the particles were collected by

centrifugation (10 min, 5500 g, 15 °C) and re-dispersed in 30 mL water. This washing procedure was repeated three times. LP-MSN-CA were obtained as colloidal solution in water and were stored at -20 °C until further use.

Horseradish peroxidase (LP-MSN-HRP). Sp-Horseradish peroxidase was immobilized onto LP-MSN-N_3 via a click chemistry approach according to the synthesis procedure described above for sp-CA. An ethanolic suspension containing 50 mg LP-MSN-N_3 was centrifuged (10 min, 7197 g), washed and re-dispersed as described above. Afterwards, the buffered solution of sp-HRP (containing 9 mg, 0,2 µmol sp-HRP) was added and the mixture was stirred for 30 minutes at room temperature before the freshly prepared catalyst solution consisting of sodium ascorbate and Cu(II)SO_4 (see above) was added. LP-MSN-HRP nanoparticles were obtained as colloidal solution in water after several washing steps.

Catalytic activity determination of LP-MSN-CA. The catalytic activity of LP-MSN-CA was determined by an adapted method published by Shank *et al.*.[44] Fresh solutions of 4-nitrophenyl acetate (NPA, 10 mM, 18.1 mg, 0.1 mmol in 10 mL EtOH) and TRIS buffer (50 mM, pH 8) were prepared shortly before the experiment. 500 µl of an aqueous suspension of LP-MSN-CA (containing 5 mg particles and therefore 0.71 mg carbonic anhydrase, calculated from TGA-data) were mixed in macro PMMA-cuvettes with 400 µL TRIS buffer. Subsequently, 100 µl NPA-solution were added quickly before the time-dependent hydrolysis of the substrate was determined by measuring the absorbance of the formed 4-nitrophenol (400 nm, 120 s and intervals of 1 s). All spectra were background corrected. After a finished cycle, the assay mixture was centrifuged (10 min, 16900 g, 15 °C) and washed with 1 mL water. The washing procedure was repeated three times before the particles were redispersed in 500 µl water and used for the next cycle.

Catalytic activity determination of LP-MSN-HRP. To determine the catalytic activity of immobilized horseradish peroxidase (LP-MSN-HRP) a slightly modified assay following the published protocol of Maehly and Chance was used.[45] All substrate solutions and potassium phosphate buffer (pH 7.0, 0.2 M) were freshly prepared. 5 mg LP-MSN-HRP were resdipersed in 100 µL H_2O and 3 mL buffer as well as 50 µL guaiacol solution (0.5 mM, 2.8 µL in 50 mL water) added and mixed. Subsequently, 20 µL H_2O_2 (12.3 mM) were added, the cuvette once inverted and the time-dependent formation of the coloured product determined by UV-VIS spectroscopy (470 nm, 100 s, intervals of 1 s). All spectra were background corrected.

6.5. References

1. Lu, Y.; Fan, H.; Stump, A.; Ward, T. L.; Rieker, T.; Brinker, C. J., Aerosol-Assisted Self-Assembly of Mesostructured Spherical Nanoparticles. *Nature* **1999,** *398,* 223-226.
2. Hartmann, M., Ordered Mesoporous Materials for Bioadsorption and Biocatalysis. *Chem. Mater.* **2005,** *17,* 4577-4593.
3. Cauda, V.; Schlossbauer, A.; Kecht, J.; Zürner, A.; Bein, T., Multiple Core-Shell Functionalized Colloidal Mesoporous Silica Nanoparticles. *J. Am. Chem. Soc.* **2009,** *131,* 11361-11370.
4. Gao, F.; Botella, P.; Corma, A.; Blesa, J.; Dong, L., Monodispersed Mesoporous Silica Nanoparticles with Very Large Pores for Enhanced Adsorption and Release of DNA. *J. Phys. Chem. B.* **2009,** *113,* 1796-1804.
5. Zhao, D.; Feng, J.; Huo, Q.; Melosh, N.; Fredrickson, G. H.; Chmelka, B. F.; Stucky, G. D., Triblock copolymer syntheses of mesoporous silica with periodic 50 to 300 angstrom pores. *Science* **1998,** *279,* 548-552.
6. Zhao, D.; Huo, Q.; Feng, J.; Chmelka, B. F.; Stucky, G. D., Nonionic Triblock and Star Diblock Copolymer and Oligomeric Surfactant Syntheses of Highly Ordered, Hydrothermally Stable, Mesoporous Silica Structures. *J. Am. Chem. Soc.* **1998,** *120,* 6024-6036.
7. Rosenholm, J. M.; Meinander, A.; Peuhu, E.; Niemi, R.; Eriksson, J. E.; Sahlgren, C.; Linden, M., Targeting of Porous Hybrid Silica Nanoparticles to Cancer Cells. *ACS Nano* **2009,** *3,* 197-206.
8. Zhou, Z.; Taylor, R. N. K.; Kullmann, S.; Bao, H.; Hartmann, M., Mesoporous Organosilicas with Large Cage-Like Pores for High Efficiency Immobilization of Enzymes. *Adv. Mater.* **2011,** *23,* 2627-2632.
9. Mureseanu, M.; Galarneau, A.; Renard, G.; Fajula, F., A New Mesoporous Micelle-Templated Silica Route for Enzyme Encapsulation. *Langmuir* **2005,** *21,* 4648-4655.
10. Lin, Y. S.; Abadeer, N.; Hurley, K. R.; Haynes, C. L., Ultrastable, redispersible, small, and highly organomodified mesoporous silica nanotherapeutics. *J. Am. Chem. Soc.* **2011,** *133,* 20444-20457.
11. Jin, H.; Qiu, H.; Sakamoto, Y.; Shu, P.; Terasaki, O.; Che, S., Mesoporous Silicas by Self-Assembly of Lipid Molecules: Ribbon, Hollow Sphere, and Chiral Materials. *Chem. Eur. J.* **2008,** *14,* 6413-6420.
12. Lin, Y. S.; Haynes, C. L., Impacts of Mesoporous Silica Nanoparticle Size, Pore Ordering, and Pore Integrity on Hemolytic Activity. *J. Am. Chem. Soc.* **2010,** *132,* 4834-4842.
13. Wu, S. H.; Mou, C. Y.; Lin, H. P., Synthesis of Mesoporous Silica Nanoparticles. *Chem. Soc. Rev.* **2013,** *42,* 3862-3875.
14. Han, Y.; Ying, J. Y., Generalized Fluorocarbon-Surfactant-Mediated Synthesis of Nanoparticles with Various Mesoporous Structures. *Angew. Chem. Int. Ed.* **2005,** *44,* 288-292.
15. Möller, K.; Müller, K.; Engelke, H.; Bräuchle, C.; Wagner, E.; Bein, T., Highly efficient siRNA delivery from core-shell mesoporous silica nanoparticles with multifunctional polymer caps. *Nanoscale* **2016,** *8,* 4007-4019.
16. Hartono, S. B.; Gu, W.; Kleitz, F.; Liu, J.; He, L.; Middelberg, A. P. J.; Yu, C.; Lu, G. Q.; Qiao, S. Z., Poly-l-lysine Functionalized Large Pore Cubic Mesostructured Silica Nanoparticles as Biocompatible Carriers for Gene Delivery. *ACS Nano* **2012,** *6,* 2104-2117.
17. Na, H.-K.; Kim, M.-H.; Park, K.; Ryoo, S.-R.; Lee, K. E.; Jeon, H.; Ryoo, R.; Hyeon, C.; Min, D.-H., Efficient Functional Delivery of siRNA using Mesoporous Silica Nanoparticles with Ultralarge Pores. *Small* **2012,** *8,* 1752-1761.
18. Zhang, K.; Xu, L. L.; Jiang, J. G.; Calin, N.; Lam, K. F.; Zhang, S. J.; Wu, H. H.; Wu, G. D.; Albela, B.; Bonneviot, L.; Wu, P., Facile large-scale synthesis of monodisperse mesoporous silica nanospheres with tunable pore structure. *J. Am. Chem. Soc.* **2013,** *135,* 2427-2430.
19. Chiu, H. Y.; Deng, W.; Engelke, H.; Helma, J.; Leonhardt, H.; Bein, T., Intracellular chromobody delivery by mesoporous silica nanoparticles for antigen targeting and visualization in real time. *Sci. Rep.* **2016,** *6,* 25019.
20. Kim, J.; Grate, J. W.; Wang, P., Nanostructures for Enzyme Stabilization. *Chem. Eng. Sci.* **2006,** *61,* 1017-1026.
21. Zhao, X. S.; Bao, X. Y.; Guo, W.; Lee, F. Y., Immobilizing Catalysts on Porous Materials. *Mater. Today* **2006,** *9,* 32-39.
22. Phuoc, L. T.; Laveille, P.; Chamouleau, F.; Renard, G.; Drone, J.; Coq, B.; Fajula, F.; Galarneau, A., Phospholipid-templated silica nanocapsules as efficient polyenzymatic biocatalysts. *Dalton Trans.* **2010,** *39,* 8511-8520.
23. Ispas, C.; Sokolov, I.; Andreescu, S., Enzyme-functionalized Mesoporous Silica for Bioanalytical Applications. *Anal. Bioanal. Chem.* **2009,** *393,* 543-554.

24. Li, Z.; Barnes, J. C.; Bosoy, A.; Stoddart, J. F.; Zink, J. I., Mesoporous Silica Nanoparticles in Biomedical Applications. *Chem. Soc. Rev.* **2012,** *41*, 2590-2605.
25. Zhou, Z.; Hartmann, M., Progress in Enzyme Immobilization in Ordered Mesoporous Materials and Related Applications. *Chem. Soc. Rev.* **2013,** *42*, 3894-3912.
26. Yiu, H. H. P.; Wright, P. A., Enzymes Supported on Ordered Mesoporous Solids: A Special Case of an Inorganic-Organic Hybrid. *J. Mater. Chem.* **2005,** *15*, 3690-3700.
27. Yang, X. Y.; Li, Z. Q.; Liu, B.; Klein-Hofmann, A.; Tian, G.; Feng, Y. F.; Ding, Y.; Su, D. S.; Xiao, F. S., "Fish-in-Net" Encapsulation of Enzymes in Macroporous Cages for Stable, Reusable, and Active Heterogeneous Biocatalysts. *Adv. Mater.* **2006,** *18*, 410-414.
28. Rosales-Hernández, M. C.; Mendieta-Wejebe, J. E.; Correa-Basurto, J.; Vázquez-Alcántara, J. I.; Terres-Rojas, E.; Trujillo-Ferrara, J., Catalytic Activity of Acetylcholinesterase Immobilized on Mesoporous Molecular Sieves. *Int. J. Biol. Macromol.* **2007,** *40*, 444-448.
29. Hudson, S.; Cooney, J.; Hodnett, B. K.; Magner, E., Chloroperoxidase on Periodic Mesoporous Organosilanes: Immobilization and Reuse. *Chem. Mater.* **2007,** *19*, 2049-2055.
30. Lei, C.; Shin, Y.; Liu, J.; Ackerman, E. J., Entrapping Enzyme in a Functionalized Nanoporous Support. *J. Am. Chem. Soc.* **2002,** *124*, 11242-11243.
31. Hoffmann, F.; Cornelius, M.; Morell, J.; Fröba, M., Silica-Based Mesoporous Organic–Inorganic Hybrid Materials. *Angew. Chem. Int. Ed.* **2006,** *45*, 3216-3251.
32. Zhou, Z.; Inayat, A.; Schwieger, W.; Hartmann, M., Improved activity and stability of lipase immobilized in cage-like large pore mesoporous organosilicas. *Microporous Mesoporous Mater.* **2012,** *154*, 133-141.
33. Fried, D. I.; Brieler, F. J.; Fröba, M., Designing Inorganic Porous Materials for Enzyme Adsorption and Applications in Biocatalysis. *ChemCatChem* **2013,** *5*, 862-884.
34. Lee, C.-H.; Lin, T.-S.; Mou, C.-Y., Mesoporous Materials for Encapsulating Enzymes. *Nano Today* **2009,** *4*, 165-179.
35. El-Nahass, M. N.; El-Keiy, M. M.; Ali, E. M. M., Immobilization of horseradish peroxidase into cubic mesoporous silicate, SBA-16 with high activity and enhanced stability. *Int. J. Biol. Macromol.* **2018,** *116*, 1304-1309.
36. Pitzalis, F.; Monduzzi, M.; Salis, A., A bienzymatic biocatalyst constituted by glucose oxidase and Horseradish peroxidase immobilized on ordered mesoporous silica. *Microporous Mesoporous Mater.* **2017,** *241*, 145-154.
37. Chang, Q.; Tang, H., Immobilization of horseradish peroxidase on NH2-modified magnetic Fe3O4/SiO2 particles and its application in removal of 2,4-dichlorophenol. *Molecules* **2014,** *19*, 15768-15782.
38. Takigawa, T.; Endo, Y., Effects of Glutaraldehyde Exposure on Human Health. *J. Occup. Health* **2006,** *48*, 75-87.
39. Schlossbauer, A.; Schaffert, D.; Kecht, J.; Wagner, E.; Bein, T., Click Chemistry for High-Density Biofunctionalization of Mesoporous Silica. *J. Am. Chem. Soc.* **2008,** *130*, 12558-12559.
40. Fried, D. I.; Schlossbauer, A.; Bein, T., Immobilizing Glycopyranose on Mesoporous Silica via "Click-Chemistry" for Borate Adsorption. *Microporous Mesoporous Mater.* **2011,** *147*, 5-9.
41. Yoshimoto, M.; Walde, P., Immobilized carbonic anhydrase: preparation, characteristics and biotechnological applications. *World J. Microbiol. Biotechnol.* **2018,** *34*, 151.
42. Gole, A.; Murphy, C. J., Azide-Derivatized Gold Nanorods: Functional Materials for "Click" Chemistry. *Langmuir* **2007,** *24*, 266-272.
43. Nakazawa, J.; Stack, T. D., Controlled Loadings in a Mesoporous Material: Click-on Silica. *J. Am. Chem. Soc.* **2008,** *130*, 14360-14361.
44. Shank, R. P.; McComsey, D. F.; Smith-Swintosky, V. L.; Maryanoff, B. E., Examination of Two Independent Kinetic Assays for Determining the Inhibition of Carbonic Anhydrases I and II: Structure–Activity Comparison of Sulfamates and Sulfamides. *Chem. Biol. Drug. Des.* **2006,** 113-119.
45. Maehly, A. C.; Chance, B., The assay of catalases and peroxidases. *Methods Biochem. Anal.* **1954,** *1*, 357-424.
46. Chiu, H.-Y.; Gößl, D.; Haddick, L.; Engelke, H.; Bein, T., Clickable Multifunctional Large-Pore Mesoporous Silica Nanoparticles as Nanocarriers. *Chem. Mater.* **2018,** *30*, 644-654.
47. Krishnamurthy, V. M.; Kaufman, G. K.; Urbach, A. R.; Gitlin, I.; Gudiksen, K. L.; Weibel, D. B.; Whitesides, G. M., Carbonic Anhydrase as a Model for Biophysical and Physical-Organic Studies of Proteins and Protein−Ligand Binding. *Chem. Rev.* **2008,** *108*, 946-1051.
48. Hudson, S.; Cooney, J.; Magner, E., Proteins in mesoporous silicates. *Angew. Chem., Int. Ed. Engl.* **2008,** *47*, 8582-8594.

49. Saito, R.; Sato, T.; Ikai, A.; Tanaka, N., Structure of bovine carbonic anhydrase II at 1.95 A resolution. *Acta Crystallogr., Sect. D: Biol. Crystallogr.* **2004,** *60*, 792-795.
50. Himo, F.; Lovell, T.; Hilgraf, R.; Rostovtsev, V. V.; Noodleman, L.; Sharpless, K. B.; Fokin, V. V., Copper(I)-catalyzed synthesis of azoles. DFT study predicts unprecedented reactivity and intermediates. *J. Am. Chem. Soc.* **2005,** *127*, 210-216.
51. Verpoorte, J. A.; Mehta, S.; Edsall, J. T., Esterase Activites of Human Carbonic Anhydrases B and C. *J. Biol. Chem.* **1967,** *242*, 4221-4229.
52. Ozdemir, E., Biomimetic CO2Sequestration: 1. Immobilization of Carbonic Anhydrase within Polyurethane Foam. *Energy Fuels* **2009,** *23*, 5725-5730.

6.6. Appendix

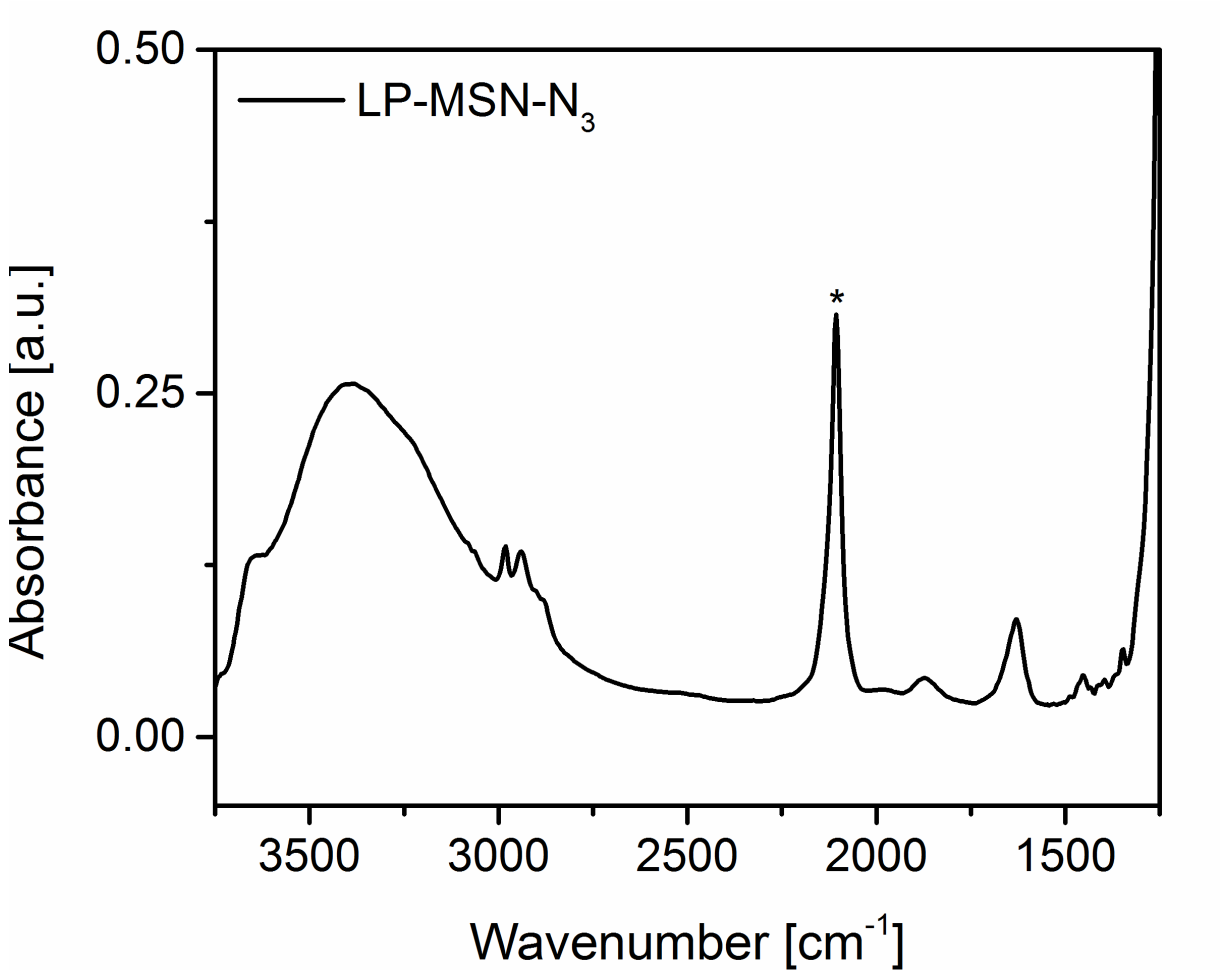

Figure S 6-1 Infrared spectrum of LP-MSN-N_3. The asterisked peak indicates the typical vibration arising from the azide-functionality.

IR spectroscopy was carried out to verify the presence of azide moieties in LP-MSN-N_3. The asymmetric CH_2 stretching vibrations of the azidopropyl-moieties are visible between 2990 cm^{-1} and 2940 cm^{-1}. Furthermore, the CH_2 bending vibration appears at 1451 cm^{-1}. The asterisked strong vibration at 2105 cm^{-1} is attributed to the stretching vibration of the N_3-groups. The vibration at 1633 cm^{-1} appears with lower intensity and can be attributed to the vibrations of residual amounts of water in the sample. Vibrations of the silica framework are visible below 1300 cm^{-1} with strong intensities.

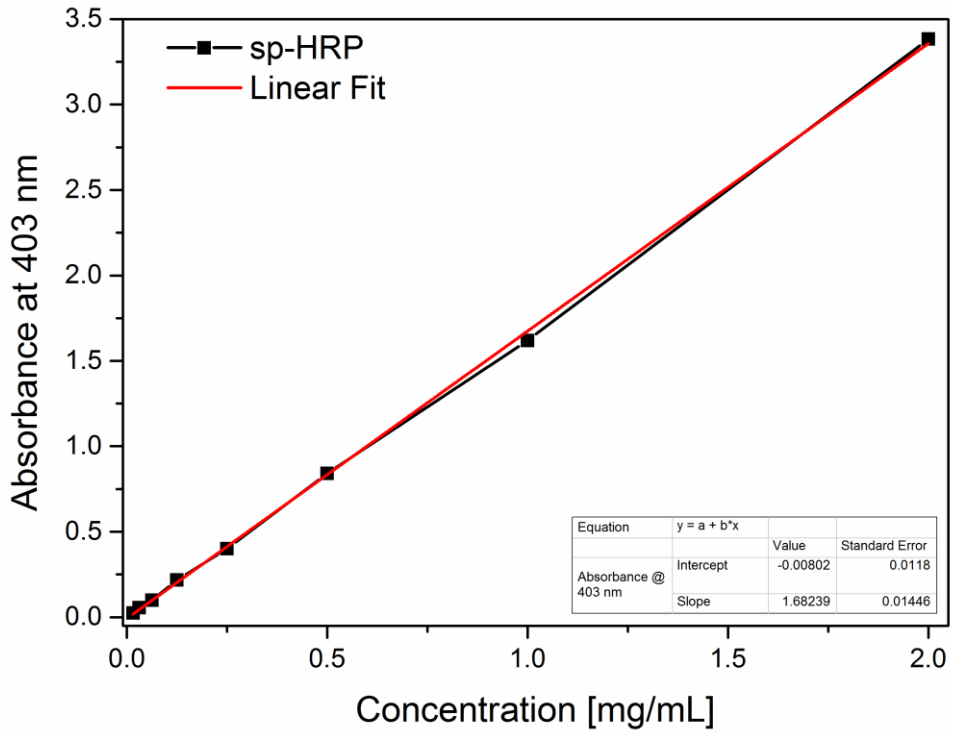

Figure S 6-2 Calibration curve of sp-HRP. Absorbance of different concentrated solutions of alkyne-functionalized horseradish peroxidase was measured at 403 nm *via* UV-Vis and fitted linearly with Origin 9.0 (inserted box).

To estimate the amount of sp-enzyme attached on the solid support, thermogravimetric analyses of the samples LP-MSN-N_3, LP-MSN-CA and LP-MSN-HRP were performed (Figure 6-2c). From the additional mass loss of 11.5% for the sample LP-MSN-CA the amount of attached enzyme can be estimated to be 4.7 µmol per g silica (for calculation see Calculation A 6—1 below). This indicates that 0.5% of all azide moieties have reacted with sp-CA, as the amount of azide-moieties was estimated to be 1.02 mmol per g silica. From the additional mass loss of 9.4%, the amount of immobilized HRP can be estimated to be 2.6 µmol per g silica (see Calculation A 6—1) and the amount of azide-moieties can be estimated at 1.02 mmol per g silica. Horseradish peroxidase is sterically somewhat more demanding than CA due to its larger dimensions (4.0 x 4.4 x 6.8 nm^3)[1] and was only able to react with 0.25% of all azide moieties of LP-MSN-N_3.

Calculation A 6—1 Example for the calculation for thermogravimetric analysis (TGA) of sample LP_MSN-N_3 and LP_MSN-CA

1 g sample LP_MSN-N_3 contains 77 mg azide-residues (mass loss 9.2%, M_w ($C_3H_6N_3$) = 81,05 gmol^{-1} 5:1 M_w (C_6H_5) = 77,1 gmol^{-1}→ mass loss for azide-moieties 7.7%)

$$\frac{77\ mg}{(100\% - 7.7\%)\ g} = 83\ mg\ azide - residues\ /\ g\ silica$$

$$\frac{0.083\ g}{81.05\ \frac{g}{mol}} = 1.02\ mmol\ azide - residues\ /\ g\ silica$$

1 g sample LP_MSN-CA contains 115 mg CA (additional mass loss 11.5%, M_w(CA) = 30 000 gmol^{-1})

$$\frac{115\ mg}{(100\% - 7.7\% - 11.5\%)\ g} = 142\ mg\ CA\ /\ g\ silica$$

$$\frac{0.142\ g}{30\ 000\ \frac{g}{mol}} = 4.7\ \mu mol\ CA\ /\ g\ silica$$

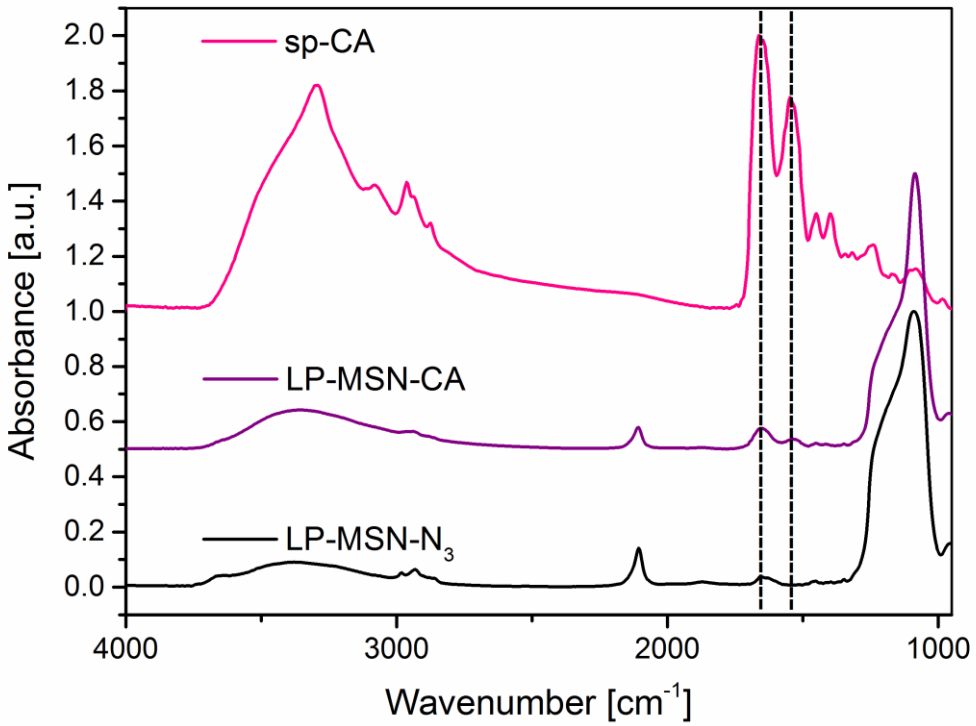

Figure S 6-3 IR spectra of sp-CA (pink), LP-MSN-CA (purple) and LP-MSN-N_3 (black). The spectrum of LP-MSN-CA was shifted along the y-axis by a value of 0.5 and the spectrum of sp-CA by a value of 1.5 for clarity reasons. The peak at 1658 cm^{-1} (dashed line) can be attributed to the C=O stretching vibration and that at 1530 cm^{-1} (dashed line) to the N-H bending vibration of the peptide bonds in sample LP-MSN-CA. Due to the large portion of unclicked azide-groups inside the particles, the N_3-stretching vibration at 2105 cm^{-1} can be seen in both samples – the particles without and with carbonic anhydrase.

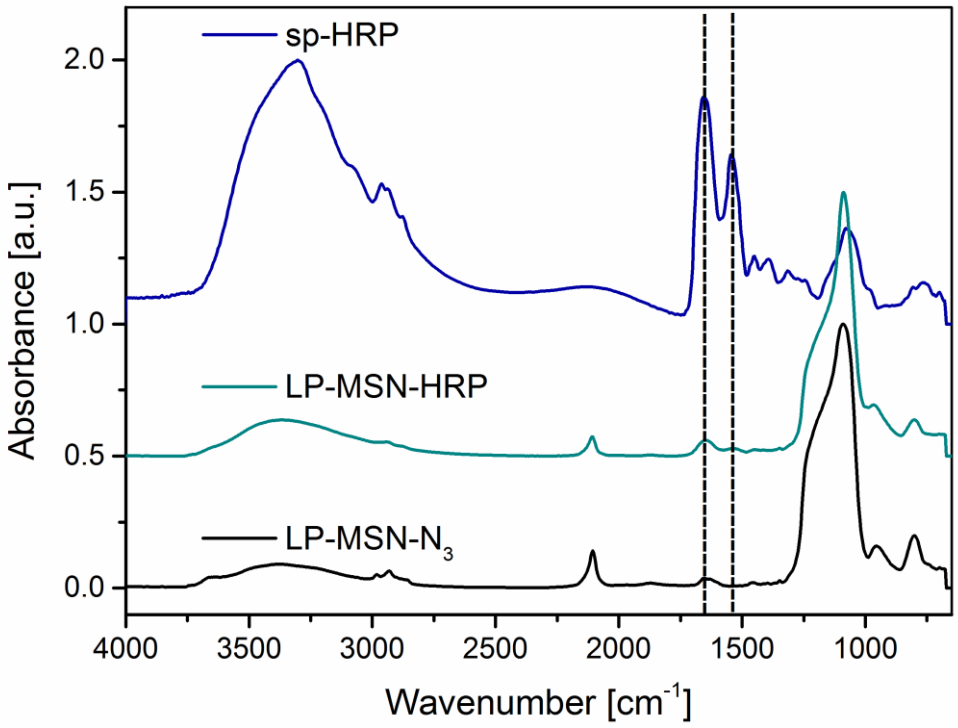

Figure S 6-4 IR spectra of sp-HRP (blue), LP-MSN-HRP (cyan) and LP-MSN-N_3 (black). The spectrum of LP-MSN-HRP was shifted along the y axis by a value of 0.5 and the spectrum of sp-HRP by a value of 1.25 for clarity reasons. The modes at 1658 cm^{-1} (dashed line) can be attributed to the C=O stretching vibration and those at 1534 cm^{-1} (dashed line) to the N-H bending vibration of the peptide bonds in sample LP-MSN-HRP. The stretching of the azide-moieties can also be observed at 2105 cm^{-1} (see explanation above).

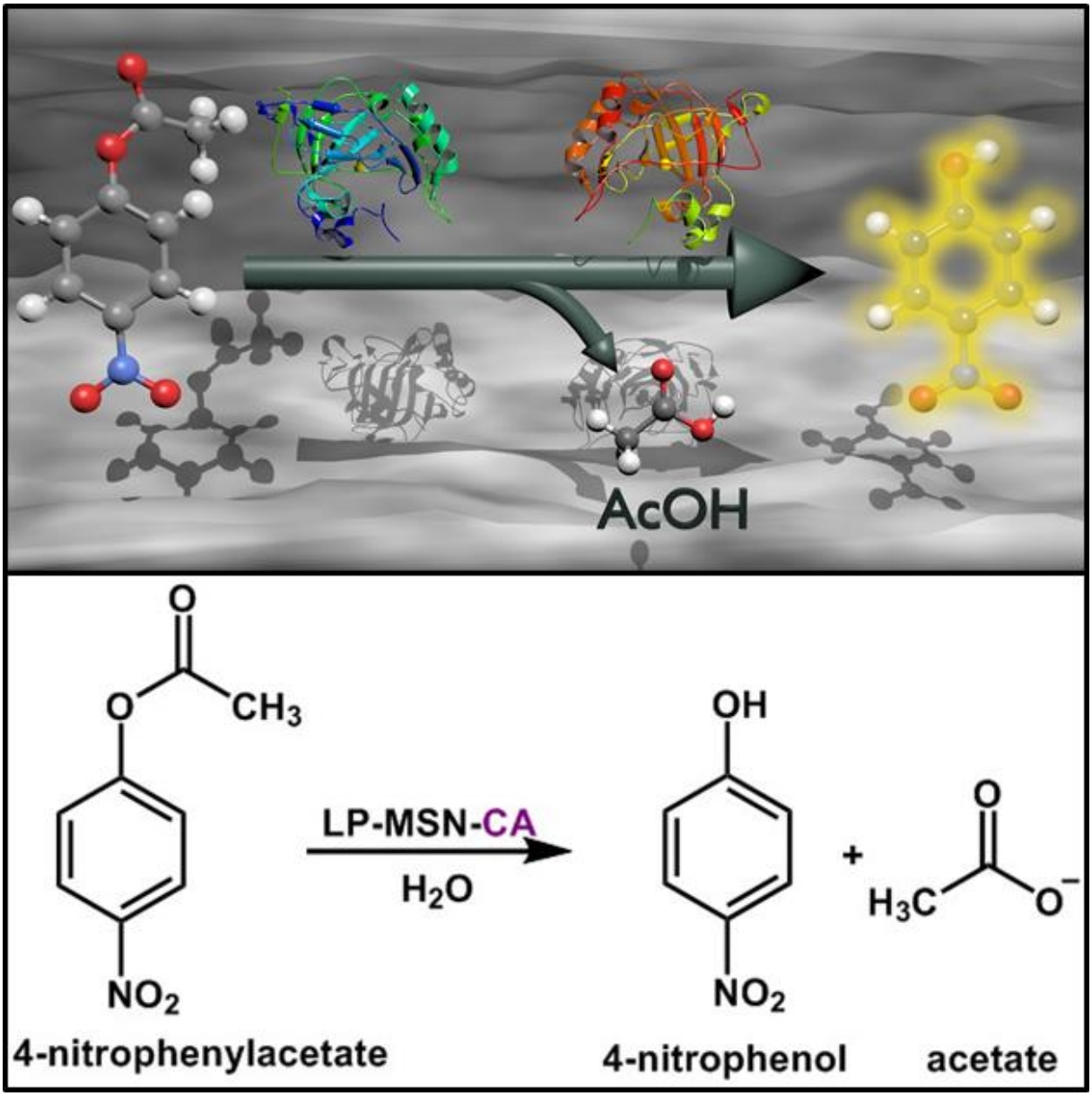

Figure S 6-5 Image and reaction scheme of catalytic activity assay for immobilized carbonic anhydrase. On the left: Sample LP_MSN-CA at the time points t = 0 sec (colourless) and t = 120 sec after the start of the hydrolysis reaction of 4-nitrophenyl acetate (4-NPA) in water and TRIS buffer (pH 8).

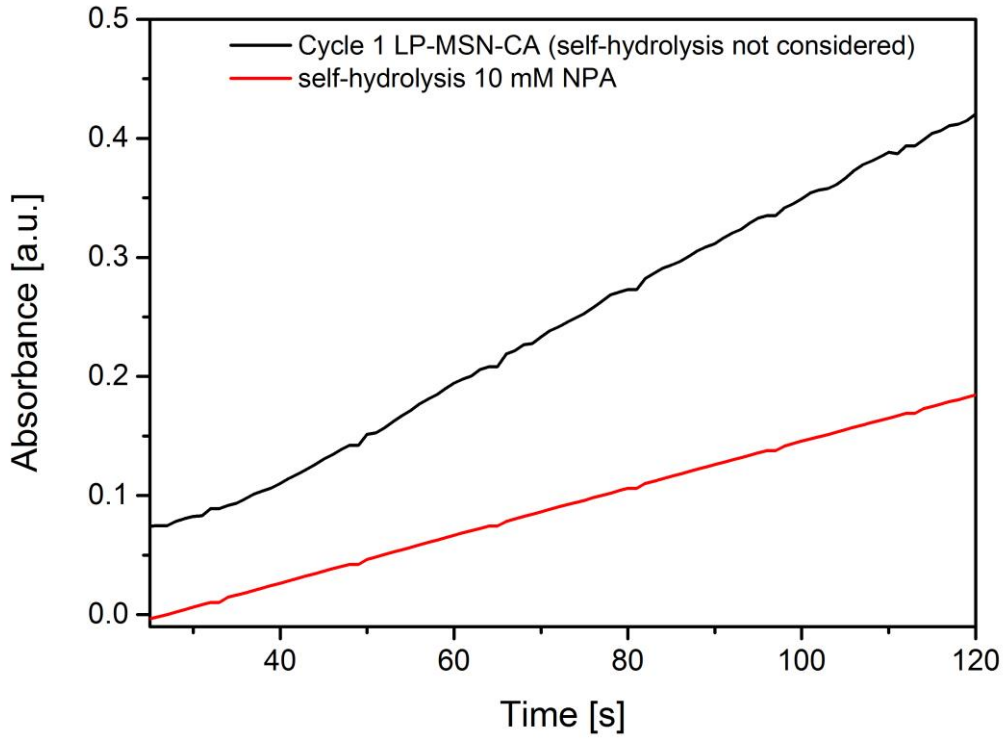

Figure S 6-6 Comparison of 4-NPA's self-hydrolysis and catalytic performance of LP-MSN-CA. UV-Vis absorption measurement of LP-MSN-CA (Cycle 1; black curve) within a period of 120 s at 400 nm with 10 mM NPA and TRIS buffer versus 10 mM NPA only and TRIS buffer (red curve).

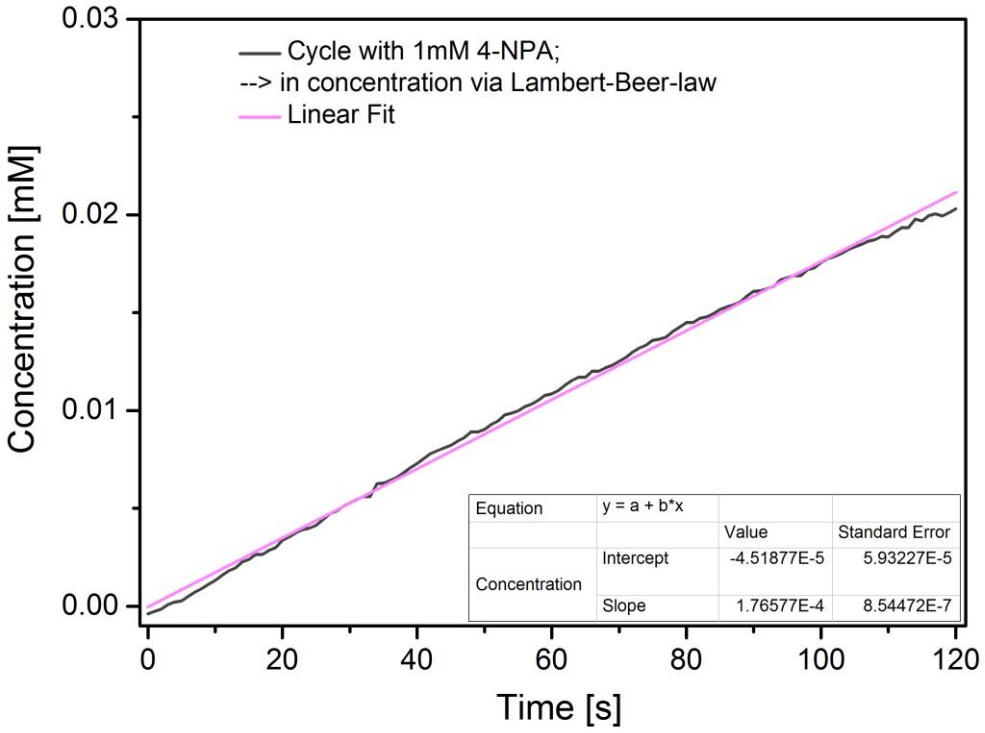

Figure S 6-7 Activity determination for LP-MSN-CA. UV-Vis absorption measurement of LP-MSN-CA within a period of 120 s at 400 nm with 1 mM NPA converted into concentration vs. time via Lambert-Beer law (ε = 16 300 M^{-1} cm^{-1}).[2] The rate of 4-NPA's self-hydrolysis is considered and already subtracted from the measured curve (not shown here).

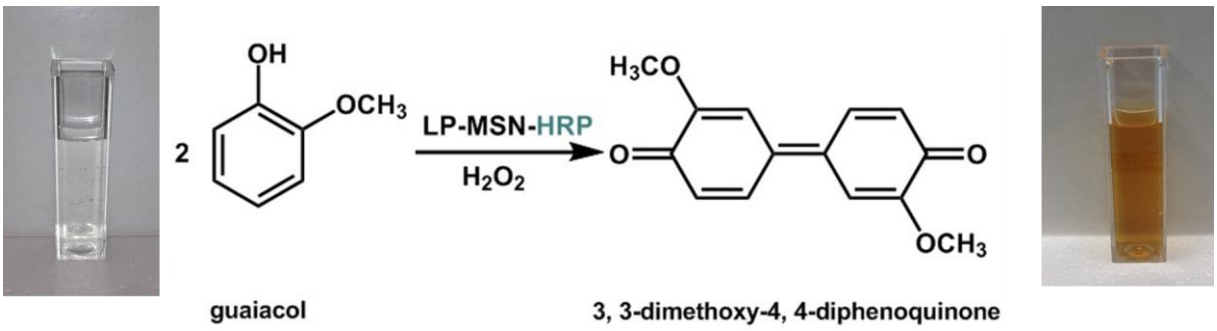

Figure S 6-8 Activity determination for LP-MSN-CA. UV-Vis absorption measurement of LP-MSN-CA within a period of 120 s at 400 nm with 1 mM NPA converted into concentration vs. time via Lambert-Beer law (ε = 16 300 M^{-1} cm^{-1}).[2] The rate of 4-NPA's self-hydrolysis is considered and already subtracted from the measured curve (not shown here).

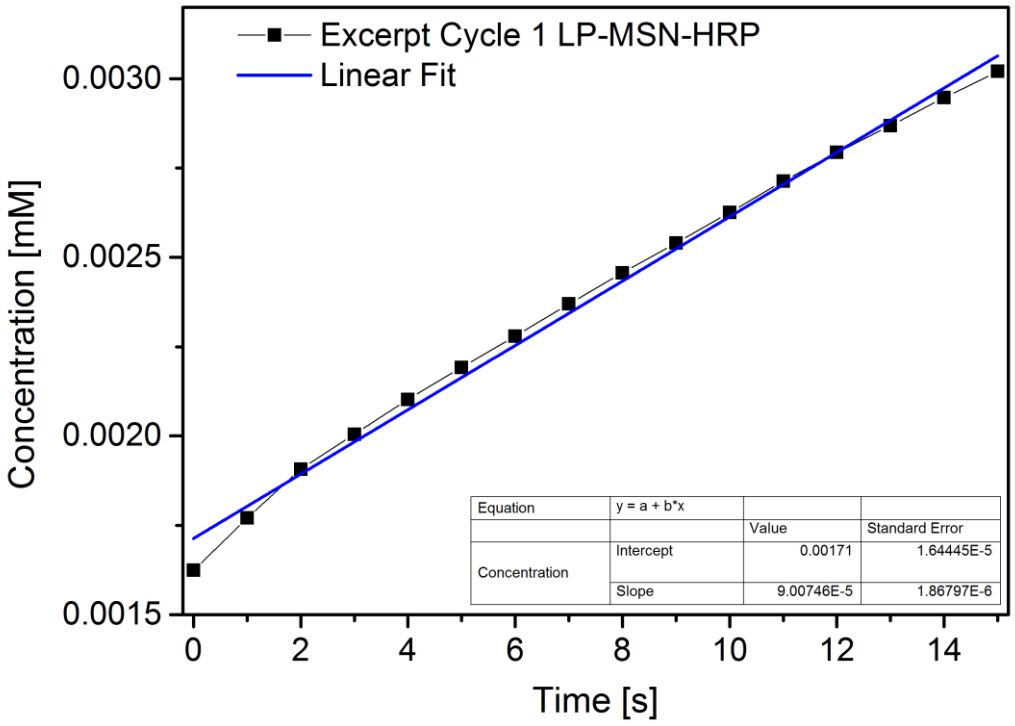

Figure S 6-9 Activity determination for LP-MSN-HRP. Activity determination of LP-MSN-HRP by measuring the absorbance at 470 nm and converting the linear region of the first cycle into concentration via Lambert-Beer law (ε = 26.6 $mM^{-1}cm^{-1}$).[3]

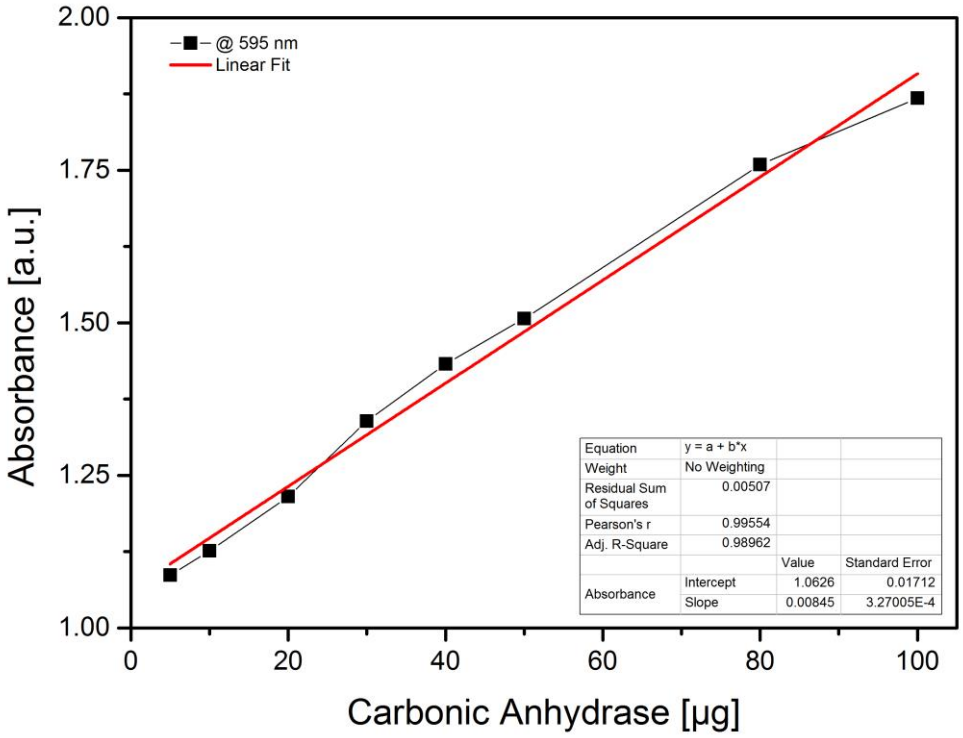

Figure S 6-10 Standard curve of carbonic anhydrase for Bradford assay.[4-5] The amount of immobilized carbonic anhydrase determined via the standard curve (shown above) is 3.4 µmol CA per g silica. In comparison to the via TGA determined amount of 4.7 µmol CA per g silica a deviation of almost 28% is asserted. This deviation is attributed to additional components in the channels of the mesoporous silica that contribute to weight changes during TGA measurements.

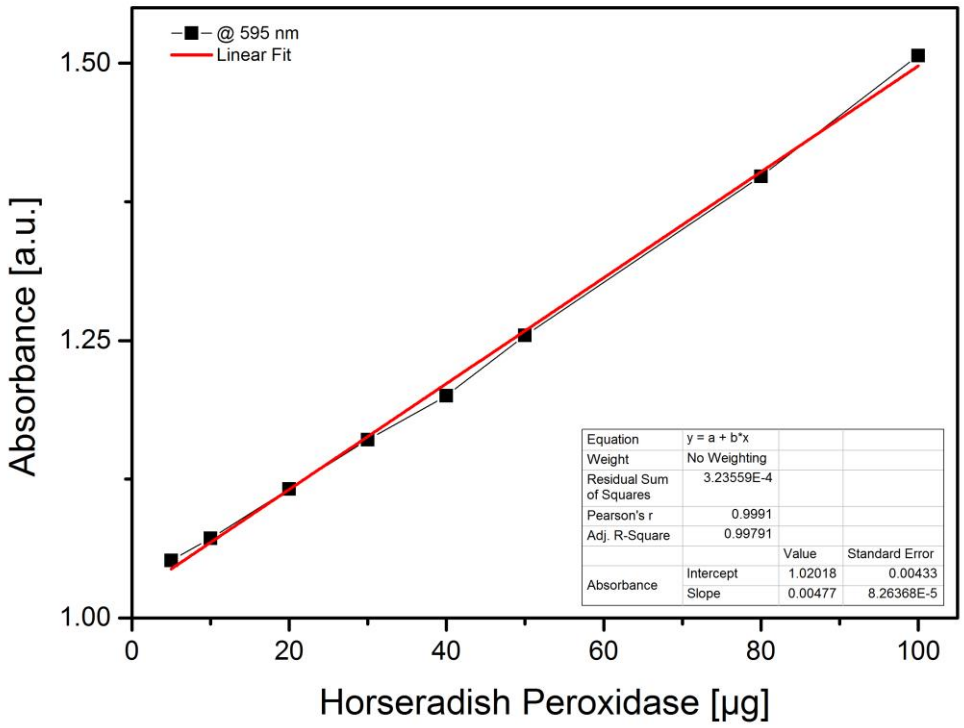

Figure S 6-11 Standard curve of horseradish peroxidase for Bradford assay. In the case of immobilized horseradish peroxidase the amount determined with the Bradford assay differs very little in comparison to carbonic anhydrase. Evaluation of the protein assay results in 2.4 µmol HRP per g silica whereas the amount determined with TGA is 2.6 µmol HRP per g silica which corresponds to a deviation of only ~ 8%.

The expressed activity of the biocatalysts was determined according to the following definitions:

1. Carbonic anhydrase: One international unit of activity (IU) was defined as the amount of enzyme that hydrolyzes 1 µmol of 4-NPA per liter per minute under the conditions described in the manuscript.

   The resulting activity of immobilized carbonic anhydrase is 8.4 units (per 5 mg MSNs), i.e. 1680 units / g support. The respective amount of free enzyme shows an activity of 85.6 units.

2. Horseradish peroxidase: One international unit of peroxidase activity is defined as the amount of enzyme catalyzing the oxidation of 1 µmol of guaiacol per liter per minute under the conditions described in the manuscript.

   The resulting activity of immobilized horseradish peroxidase is 0,86 units (per 0,16 mg

MSN) i.e. 5343 units / g support. The respective amount of free enzyme shows an activity of 3.7 units.

References

1. Hudson, S.; Cooney, J.; Magner, E., Proteins in mesoporous silicates. *Angew. Chem., Int. Ed. Engl.* **2008,** *47*, 8582-8594.
2. Verpoorte, J. A.; Mehta, S.; Edsall, J. T., Esterase Activites of Human Carbonic Anhydrases B and C. *J. Biol. Chem.* **1967,** *242*, 4221-4229.
3. Maehly, A. C.; Chance, B., The assay of catalases and peroxidases. *Methods Biochem. Anal.* **1954,** *1*, 357-424.
4. Bradford, M. M., A Rapid and Sensitive Method for the Quantitation of Microgram Quantities of Protein Utilizing the Principle of Protein-Dye Binding. *Anal. Biochem.* **1976,** *72*, 248-254.
5. Stoscheck, C. M., Quantitation of Protein. *Methods Enzymol.* **1990,** *182*, 50-69.

CHAPTER 7

Biocompatible crosslinked β-cyclodextrin nanoparticles as multifunctional carriers for cellular delivery

7. Biocompatible crosslinked β-cyclodextrin nanoparticles as multifunctional carriers for cellular delivery

This chapter was published as:

Stefan Datz, Bernhard Illes, Dorothée Gößl, Constantin v. Schirnding, Hanna Engelke*, Thomas Bein* *Nanoscale*, **2018**, *10*, 16284-16292. Reproduced with permission from The Royal Society of Chemistry.

Abstract

Nanoparticle-based biomedicine has received enormous attention for theranostic applications, as these systems are expected to overcome several drawbacks of conventional therapy. Herein, effective and controlled drug delivery systems with on-demand release abilities and biocompatible properties are used as a versatile and powerful class of nanocarriers. We report the synthesis of novel biocompatible and multifunctional material, entirely consisting of covalently crosslinked organic molecules. Specifically, β-cyclodextrin (CD) precursors were crosslinked with rigid organic linker molecules to obtain small (~150 nm), thermally stable and highly water-dispersible nanoparticles with an accessible pore system containing β-CD rings. The nanoparticles can be covalently labeled with dye molecules to allow effective tracking in *in vitro* cell experiments. Rapid sugar-mediated cell-uptake kinetics were observed with HeLa cells, revealing exceptional particle uptake within only 30 minutes. Additionally, the particles could be loaded with different cargo molecules showing pH-responsive release behavior. Successful nuclei staining with Hoechst 33342 dye and effective cell killing with doxorubicin cargo molecules were demonstrated in live-cell experiments, respectively. This

novel nanocarrier concept provides a promising platform for the development of controllable and highly biocompatible theranostic systems.

7.1. Introduction

Cancer therapy is currently shifting from a standardized systemic approach to a more personalized and specifically customized disease treatment. Such personalized treatments use multifunctional drugs in combination with carrier systems and are ideally based on molecular-level diagnosis.[1] After decades of research, the demand for innovative biocompatible nanomaterials for the transport of therapeutic agents is still growing. In particular, nanoparticle-based targeting of tumor cells has emerged as a potential therapeutic approach to release effective drug doses within the tumorous tissue.[2-6] Because of the prolonged blood circulation time combined with nonspecific accumulation in tumors through the enhanced permeability and retention (EPR) effect, nanoparticles have been regarded as a suitable candidates in pharmaceutical fields, especially for targeted and personalized cancer therapy. A number of different carrier systems have been investigated in the field of nanobiosciences with differing results in the last decade. Besides inorganic materials, such as mesoporous silica nanoparticles (MSNs),[7-15] periodic mesoporous organosilica nanoparticles (PMOs),[10, 16-20] or metal-based materials, e.g. Au-[21-23] or iron oxide nanoparticles,[24-29] polymeric micelles,[30-32] lipids,[33-35] and DNA origami are other examples for potential drug delivery systems used in fundamental biomedical research,[36-38] However, some of these materials have certain drawbacks, e.g. polymeric micelles and lipids often need specific formulations for different cargos, and may face stability issues. Besides small magnetic iron-oxide based materials, none of the other larger solid nanoparticles, such as silica materials, have reached clinical trials, partially due to concerns about the unknown fate of these particles in the human organism.[39] In contrast to the ever-growing number of sophisticated nanoparticle-based cell-

targeting strategies that effectively target tumor cells *in vitro*, only few studies showed successful tumor-cell specific targeting and controlled cancer cell killing *in vivo*. Even fewer nanoformulations have found their way into clinical studies and practice.[40] Ligand-assisted targeting of cancer cells with nanoparticles *in vivo* through specific receptor-mediated uptake can be limited due to protein corona formation.[41] Therefore, there is a rapidly growing interest in new nanomaterials which can overcome some of the aforementioned limitations. Sugar-based materials are promising candidates since cancer cells are known to have a faster glycolysis metabolism that selectively leads to an increased glucose uptake compared to healthy cells.[42-45]

Here, we present a novel class of biocompatible multifunctional nanomaterials consisting of cross-linked β-cyclodextrin molecules. Cyclodextrins (CDs) are a family of cyclic oligosaccharides composed of six, seven, or eight D(+)-glucose units linked by α-1,4-linkages, which are named α-, β-, and γ-CD, respectively.[46] These different oligosaccharides are frequently used in the medical field because of their biocompatibility and their low toxicity.[47-50] CDs have a hydrophilic exterior and a hydrophobic cavity inside the oligosaccharide rings that can be used to encapsulate different kinds of guest and cargo molecules.[51-54] This encapsulation is based on supramolecular host-guest interactions such as hydrogen bonding, van-der-Waals forces or hydrophobic interactions, and is used in various applications including biomedicine, catalysis, environmental protection and separation processes.[55] Although the use of different CDs in the medical field has been documented for decades, their application is still rather limited due to significant synthetic challenges, hence motivating the development of more specific and controllable CD-containing nanoparticles. Until now, a variety of supramolecular nanoparticles (SNPs) with CD-building blocks have been investigated. However, SNPs are particles in which different building blocks are brought

together by non-covalent interactions resulting in larger assemblies.[56] The assembly is either based on electrostatic interactions or host-guest interactions.[57, 58] The non-covalent interactions limit their use for drug delivery applications, since they might degrade easily before they reach their target. Furthermore, any new guest molecule that is incorporated or loaded into the particle needs to be optimized regarding its interactions with the particle structure. Thus, a covalently crosslinked CD nanoparticle is viewed as an enabling concept that could facilitate a breakthrough for drug delivery applications. Recently, different approaches were used to prepare covalently crosslinked CD molecule-containing materials. One is defined by crosslinking α-CD-poly-ethyleneglycol (PEG) inclusion complexes by using epichlorohydrin. The nanomaterial was obtained after extracting the PEG chains that penetrated the hydrophobic cavity.[59] In another approach, Dichtel *et al.* polymerized β-CD in a nucleophilic aromatic substitution reaction with tetrafluoroterephthalonitrile and obtained mesoporous bulk material that was used to rapidly remove organic micropollutants from waste water.[60] However, no nanoparticles of covalently crosslinked CD molecules were obtained yet.

Here, we combined these different approaches to crosslink β-CD-PEG inclusion complexes with rigid aromatic groups providing for the first time small, dispersible, and thermally stable nanoparticles. These NPs can be covalently labeled with dye molecules exploiting simple click-chemistry to track them effectively in *in vitro* cell experiments. β-CD NPs are rapidly taken up by cancer cells and can efficiently release different cargo molecules. This novel and biocompatible nanocarrier concept provides a promising platform for the development of controllable and efficient theranostic systems.

7.2. Results and Discussion

Highly dispersible and thermally stable β-CD NPs for drug delivery applications were derived from a carefully controlled nucleophilic aromatic substitution reaction with tetrafluoroterephthalonitrile (TFTN, see Figure 7-1A).

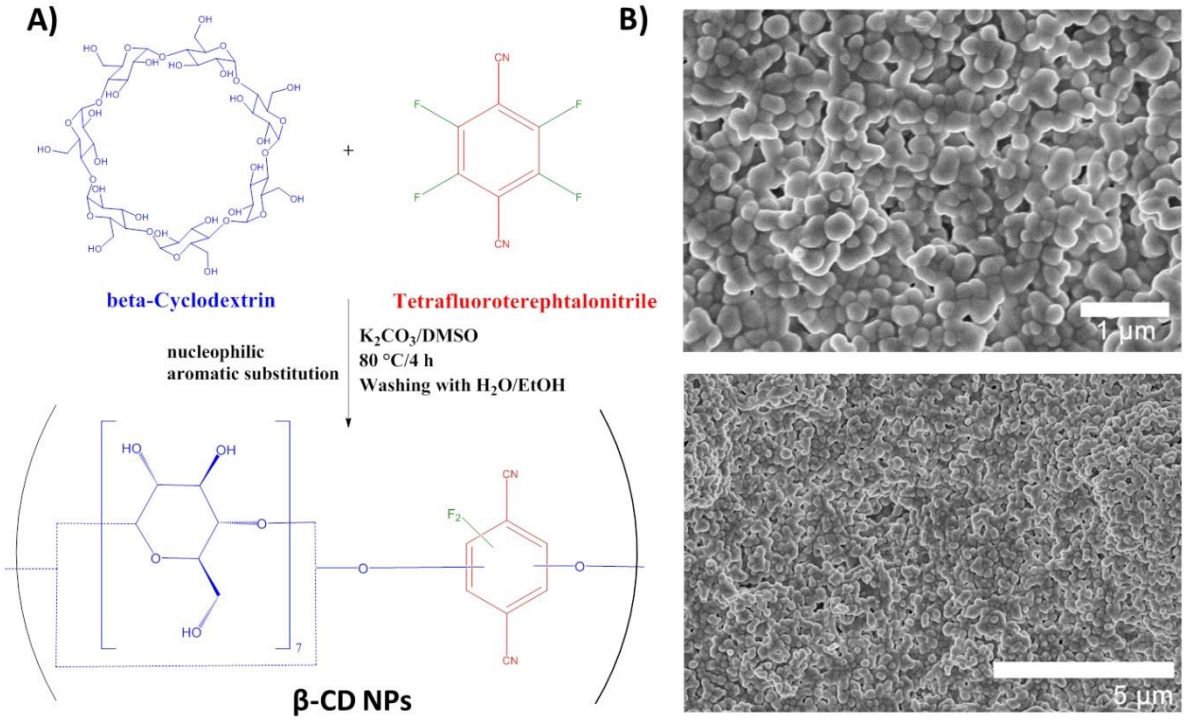

Figure 7-1: Synthesis scheme of β-CD NPs following a nucleophilic aromatic substitution reaction with TFTN (A), SEM images of β-CD NPs showing spherical particles with a narrow particle size distribution (B).

Since cyclodextrins (CDs) are known to form inclusion complexes with certain linear polymer chains such as poly(ethylene glycol) (PEG), this approach was used to create self-assembled aggregates of CD nanostructures.[61] By modifying previously described synthesis procedures, these polyrotaxane structures were reacted with the rigid aromatic linker TFTN to form small and water-dispersible spherical nanoparticles. The β-CD-PEG inclusion complexes self-assembled with the help of CTAB surfactant into spherical nanostructures and were

subsequently polymerized and cross-linked with TFTN in a suspension of K_2CO_3 in dimethylsulfoxide (DMSO) at 80 °C. Several washing steps were essential to remove the excess of precursors, salt and the included PEG chains, resulting in a pale yellow suspension of β-CD NPs with a yield of 25 %. As can be seen in the scanning electron microscopy (SEM) images in Figure 7-1B the obtained nanoparticles exhibit diameters of 150 to 200 nm with a narrow particle size distribution. Additional transmission electron microscopy (TEM) images can be found in the Appendix. Further characterization of the obtained nanomaterial is shown in Figure 7-2. Dynamic light scattering (DLS, Figure 7-2A) measurements reveal a high colloidal stability with hydrodynamic particle diameters of about 180 nm in water, rendering the obtained β-CD NPs useful for cellular delivery applications. Because of their exceptional colloidal stability without agglomeration in aqueous solutions, no additional hydrophilic coating such as PEGylation is necessary to use them in biotheranostics.[62] Infrared spectroscopy (Figure 7-2B) was used to follow the formation of β-CD NPs with TFTN as the rigid organic crosslinker. The strong signal (a) at 1035 cm^{-1} corresponds to characteristic R_3C-OH stretching vibrations due to the oligosaccharide rings of the incorporated β-cyclodextrin compounds. Signal (b) at 1260 cm^{-1} is due to saturated aliphatic C-O-C ether vibrations of the sugar rings and newly formed asymmetric alkyl-aryl-ether =C-O-C vibrations of the crosslinked material. The aromatic system of TFTN incorporated into the nanostructure of β-CD NPs is also confirmed by the signals (c) corresponding to aromatic -C=C- stretching vibrations and (d) corresponding to the strong nitrile vibration. The very broad band (e) around 3200 cm^{-1} is attributed to O-H absorption of the incorporated oligosaccharide building blocks. Additional solid-state nuclear magnetic resonance (ssNMR) characterization reveals the presence of both TFTN and β-cyclodextrin in the crosslinked material (see Appendix). Figure 7-2C displays nitrogen sorption experiments of freeze-dried β-CD NPs and reveals an isotherm with a calculated specific Brunauer-Emmett-Teller (BET)

surface area of about 140 m^2/g. The cumulative pore size distribution (inset) shows pore sizes ranging from 1 to 6.5 nm comprising the majority of the accessible pore volume of 0.26 cm^3/g. Thermogravimetric analysis (TGA) of β-CD NPs (Figure 7-2D) indicates the presence of a thermally stable material up to 285 °C and a complete mass loss of almost 100 % up to 900 °C. Zeta potential measurements show that the nanoparticles have a negative surface charge of about -35 mV at pH 7 due to the free hydroxyl groups of the oligosaccharide compounds. This zeta potential is comparable to other nanocarriers such as unfunctionalized mesoporous silica nanoparticles.[63]

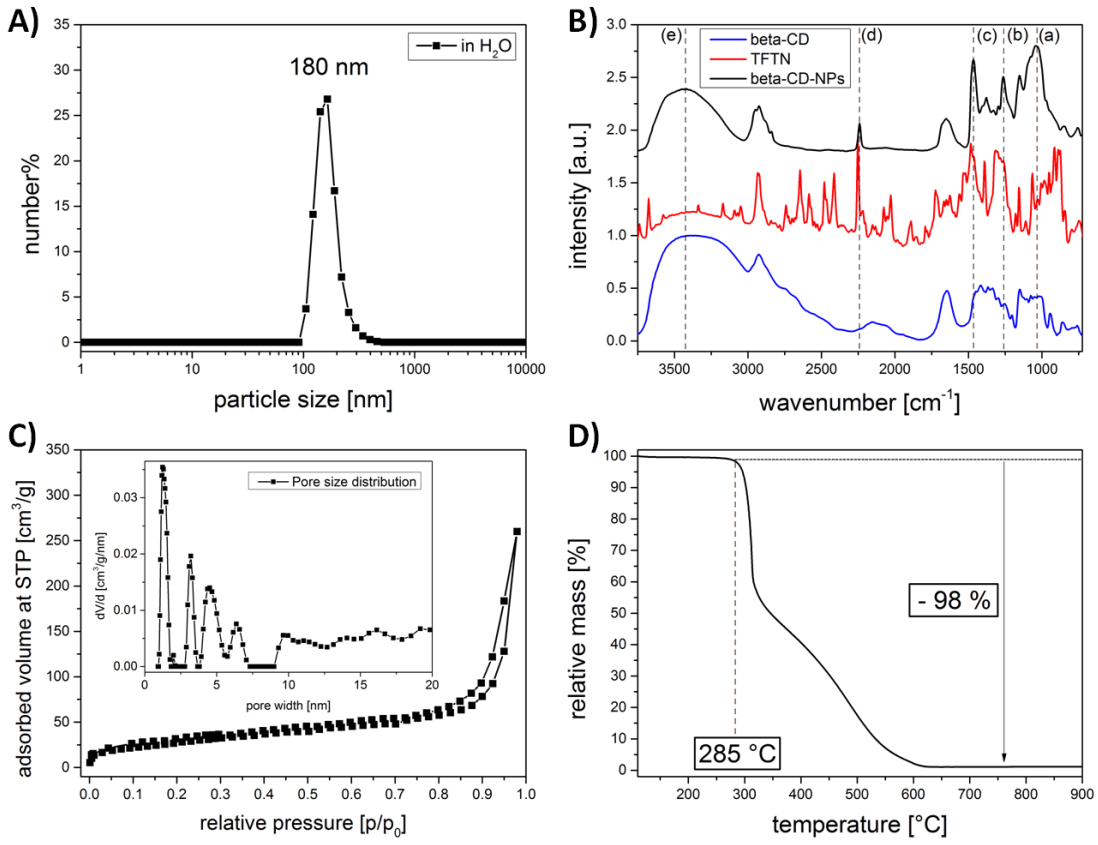

Figure 7-2: Characterization of β-CD NPs. A) Dynamic light scattering (DLS) revealing hydrodynamic particle diameters of about 180 nm in aqueous solution. B) Infrared spectroscopy data of β-CD (blue), TFTN (red) and β-CD NPs (black) with characteristic vibrations. Spectra were normalized and shifted for clarity by 0.75 a.u. along the y-axis. C) Nitrogen sorption isotherm and pore size distribution (inset) of β-CD NPs. D) Thermogravimetric analysis (TGA) up to 900 °C of β-CD NPs.

With this size and zeta potential as well as their porosity maintained even in the (partially collapsed) dry state, the particles reveal promising properties for drug delivery purposes. Therefore, the synthesized nanoparticles were subsequently used for *in vitro* drug delivery experiments. First, the cell uptake kinetics of rhodamine-labeled β-CD nanoparticles was studied on HeLa cells. To obtain labeled nanoparticles, the free nitrile groups of the incorporated organic crosslinker can be used to covalently attach specific dye molecules. Here, the fluorescent tetramethylrhodamine (TAMRA) azide was used under mild reaction conditions in a zinc-catalyzed formation of a tetrazole-ring with the free nitrile groups of β-CD nanoparticles.[64] The formation of the compound was followed with IR spectroscopy (see Appendix). After several washing steps the particles were used for *in vitro* experiments.

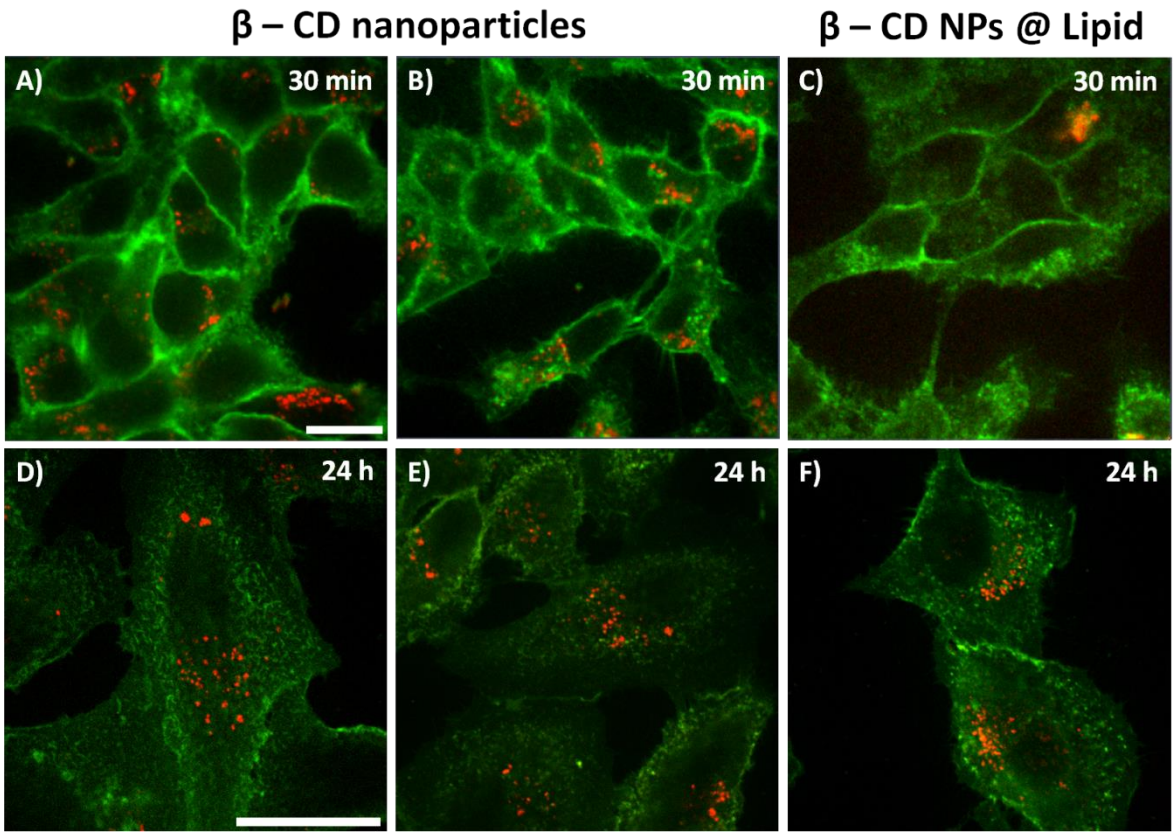

Figure 7-3: Upper panel: *In vitro* cell uptake of rhodamine-labeled β-CD nanoparticles (red) without additional coating (A, B) and with lipid coating (C) after 30 min of incubation on WGA-stained HeLa cells (green). The blurry red spot in C) results from an accumulation of particles on top of the cells. Lower panel: *In vitro* cell uptake of rhodamine-labeled β-CD nanoparticles (red) without additional coating (D, E) and with lipid coating (F) after 24 h of incubation on WGA-stained HeLa cells (green). Scale bar represents 10 μm, respectively.

The upper panel of Figure 7-3 shows representative confocal microscopy images of particle uptake by HeLa cells after just 30 min of incubation. The red-fluorescent material was efficiently internalized by cancer cells - even after very short incubation times of 30 minutes (Figure 7-3 A, B). Compared to the uptake of other nanomaterials, the internalization was very fast, possibly due to the oligosaccharide nature of the particles and sugar-receptor mediated endocytosis.[65, 66] As a reference experiment, the particles were coated with a lipid bilayer in order to compare cell uptake kinetics with as-synthesized β-CD nanoparticles (see Figure 7-3 C and F, synthesis and characterization of lipid coating see Appendix). After 30 min, exclusively uncoated β-CD nanoparticles were taken up by HeLa cells, whereas after 24 h of incubation both particle types are internalized. The experiment leads us to the

assumption that the oligosaccharides are effectively taken up *via* sugar receptors and that the oligosaccharides can be shielded by the lipid coating resulting in slower cell uptake compared to the sugar-receptor mediated endocytosis of the uncoated particles. This suggests that a surface coating for as-synthesized β-CD nanoparticles is counterproductive for cellular uptake.

In order to obtain more insights into the endocytosis pathway of β-CD nanoparticles, an *in vitro* competition experiment was performed. For this purpose, prior to the particle incubation the sugar receptors on the external cell surface of HeLa cells were saturated by adding concentrated aqueous solutions of different mono- and oligosaccharides, namely D-glucose, D-L-arabinose, 2-deoxy-D-glucose and β-cyclodextrin (see Appendix, Figure S 7-3). In all cases the particle uptake was hindered when the receptors were blocked, confirming our hypothesis that the endocytosis of β-CD nanoparticles is mediated *via* a specific sugar-receptor mediated cell uptake.

Next, the drug delivery and release properties of β-CD nanoparticles were evaluated by the loading and release of different guest molecules, namely Hoechst 33342 as nuclei staining dye and doxorubicin as model chemotherapeutic agent. Rhodamine-labeled β-CD NPs were loaded with Hoechst 33342 or doxorubicin and subsequently used for *in vitro* release experiments.

First, we studied loading and release of Hoechst 33342. Strikingly, the benzimidazole-containing compound is effectively loaded and efficiently released after particle endocytosis due to the acidification in the lysosomal compartments that destroys the hydrophobic interaction of Hoechst 33342 and the particle cavities (Figure 7-4). [67, 68] Since Hoechst 33342 is membrane-permeable, it is able to penetrate the lysosomal membrane and to efficiently stain the nuclei of HeLa cells within very short time periods of less than 10 minutes.

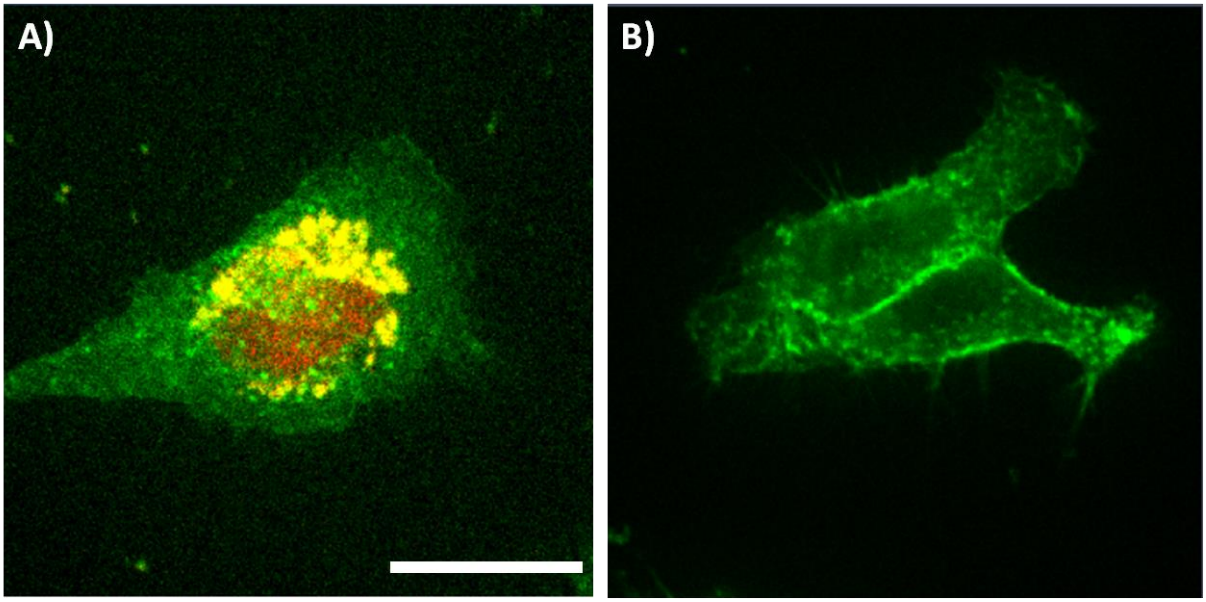

Figure 7-4: *In vitro* HOECHST33342 release on HeLa cells. A) Rhodamin-labelled β-CD NPs (yellow) released HOECHST33342 nuclei staining (red) on WGA-stained HeLa cells (green) after just 2 h of incubation time. B) As a control experiment the supernatant of centrifuged particles (after 2 h) was added to HeLa cells showing no nuclei staining, i.e. no premature release of cargo molecules. Scale bar represents 10 μm.

As a reference experiment, the particle solution used for the cell experiments was centrifuged after 2 h and the supernatant was incubated on HeLa cells. No nuclei staining could be observed. Since Hoechst 33342 is a live cell stain, any molecules in the solution would have stained the nuclei. The absence of any staining resulting from the supernatant demonstrates that no cargo molecules were released prematurely and that the *in vitro* nuclei staining is due to the acidification of nanoparticles in the endosomal compartments that triggers the release of the dye. This rapid and efficient delivery and release of Hoechst 33342 as model cargo suggests that the newly synthesized particles can serve as a promising drug delivery platform with controlled release mechanism.

In order to investigate the ability of our newly developed drug delivery system to transport and release chemotherapeutics and to affect cancer cells with their cargo, we replaced the model cargo Hoechst 33342 with doxorubicin (DOX), a classic cytostatic agent. DOX is known to form inclusion complexes based on hydrophobic interactions with β-cyclodextrin

structures similarly to Hoechst 33342 and should therefore exhibit a similar loading and release behavior. Additionally, it should reveal a pH-responsive release behavior due to enhanced solubility when protonated.[69-71] Hence, the loading and release behavior was first measured with fluorescence spectroscopy in a cuvette experiment.

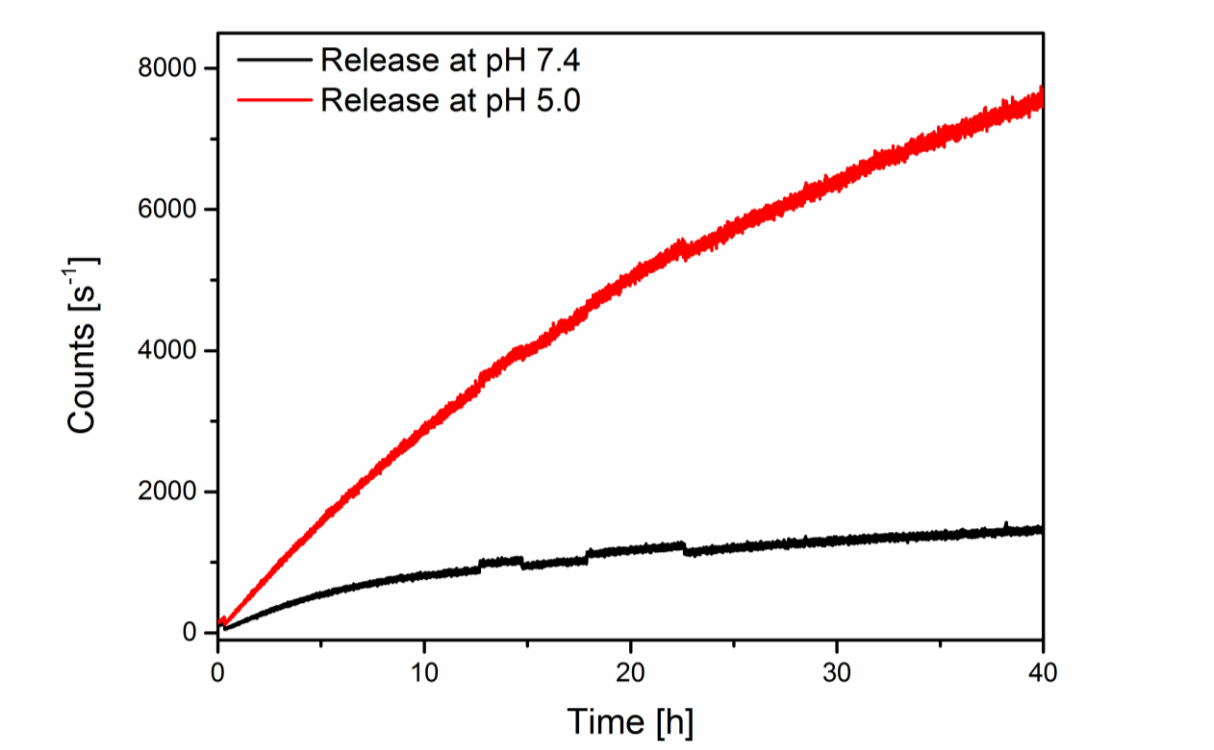

Figure 7-5: Time-based release measurements of doxorubicin at pH 7 (black curve) and pH 5 (red curve) in the fluorescence spectrometer.

For this, we used our custom-made cuvette setup to measure the time-based pH-dependent release of fluorescent doxorubicin.[72] DOX-loaded nanoparticle suspensions were placed into a dialysis membrane-sealed compartment (molecular weight cutoff = 14,000 Da) on top of a solvent-filled cuvette. Only released doxorubicin was able to diffuse through the pores of the membrane and was measured with the fluorescence spectrometer, while the nanoparticles are prevented from diffusing into the cuvette by the dialysis membrane. To prove successful loading without leakage of the cargo, a control experiment was performed in HBSS buffer at pH 7.4. Furthermore, to prove the efficient release of doxorubicin at lower pH, a second experiment was performed in parallel with Citric Acid Phosphate Buffer at pH 5. The

corresponding release curves are shown in Figure 5. They indicate only a small amount of residual DOX released at pH 7.4 and efficient release at pH 5. Next, the effect of DOX-containing particles on HeLa cells was investigated.

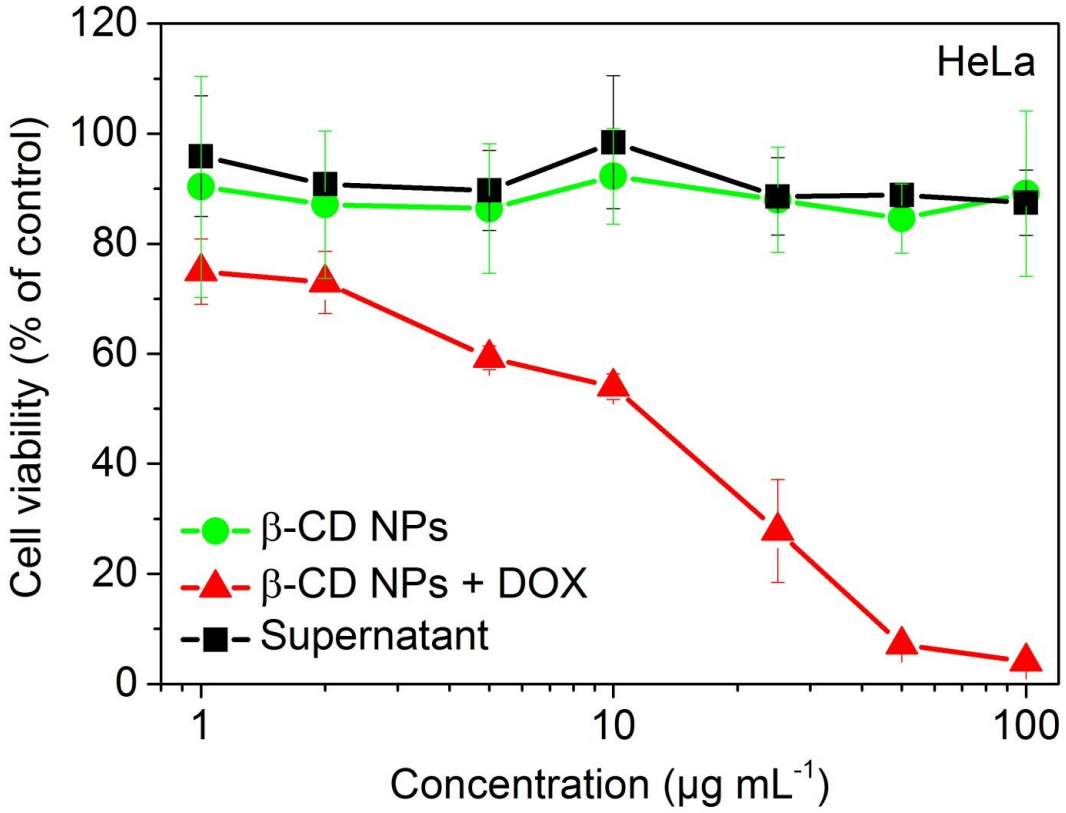

Figure 7-6: Dose-dependent cell-viability study with HeLa cells after 24 h of incubation with β-CD NPs, DOX-loaded β-CD NPs and the supernatant after centrifugation as a reference.

Free DOX is membrane-permeable and is able to induce an uncontrolled cell death within a few hours. Thus, we expected it to escape from the endosomal membrane when released from the particle in the lysosome and to subsequently induce cell death within a few hours after endosomal escape. Indeed, our newly developed β-CD NPs provided intracellular DOX release and caused efficient cell death after 24 h of incubation with a calculated IC_{50} value of 7.23 µg/mL for the DOX-loaded β-CD particles. In addition, the nanoparticles exhibited a high DOX-loading capacity of about 23 wt% (see Appendix, Figure S 7-4). The dose-

dependent cell viability assay demonstrates that DOX was delivered in a controlled manner *via* the particles and released only after endosomal acidification. In contrast, as-synthesized β-CD NPs without any cargo show good biocompatibility in the dose-dependent cell viability studies (Figure S 7-7). As a control experiment the DOX-loaded nanoparticles were centrifuged after 24 h storage and the respective amount of supernatant was incubated on HeLa cells. This control revealed good biocompatibility, i.e. no prematurely released cargo molecules were present. This experiment shows the great potential of β-CD NPs to efficiently deliver chemotherapeutics to cancer cells without premature release. This newly developed biocompatible carrier system provides an attractive platform for cellular delivery applications with exceptionally fast cell uptake kinetics.

7.3. Conclusion

To conclude, we have developed a novel nanomaterial consisting of covalently crosslinked β-cyclodextrin molecules as the main organic component. The obtained nanoparticles are small (~150 nm) and highly dispersible in aqueous solutions. They exhibit very fast cell uptake kinetics due to sugar-receptor mediated endocytosis and can be covalently labeled with dye molecules to effectively track them in *in vitro* experiments. Furthermore, the porous cavities of the particles can be loaded with cargo molecules, which are subsequently released in the endosomal cell compartments due to acidification. This triggered release mechanism allowed us to show efficient nuclei staining with Hoechst 33342 dye and effective cancer cell killing with doxorubicin as cargos, respectively. Thus, the nanoparticles show great potential for future applications as a biocompatible drug carrier system.

7.4. Experimental Part

Materials. β-Cyclodextrin (97 %, Sigma Aldrich), tetrafluoroterephthalonitrile (TFTN, 98 %, Alfa Aesar), polyethylene glycol 2000 (PEG2000, BioUltra, Sigma Aldrich), potassium carbonate (K_2CO_3, 99.5 %, Grüssing GmbH), tetramethylrhodamine 5-carboxamido-(6-azidohexanyl) (TAMRA azide, Base click), doxorubicin hydrochloride (98 % HPLC, Sigma Aldrich), D-glucose (Sigma Aldrich), D-L-arabinose (Sigma Aldrich), 2-deoxy-D-glucose (Sigma Aldrich), Hoechst 33342 trihydrochloride (ThermoFisher Scientific), cetyl trimethylammonium bromide (Sigma Aldrich), wheat germ agglutinin, Alexa Fluor® 488 conjugate (lifeTechnologies), Dulbecco's modified Eagle's medium (DMEM) (lifeTechnologies), Hank´s balanced salt solution (HBSS-buffer, Sigma Aldrich) were used as received. Ethanol (EtOH, absolute, Aldrich), hydrochloric acid (1 M, Bernd Kraft), dimethylsulfoxide (DMSO, anhydrous, >99.9 %, Sigma Aldrich) and dimethylformamide (DMF, >99.9 %, anhydrous, Sigma Aldrich) were used as solvents without further purification. Bidistilled water was obtained from a millipore system (Milli-Q Academic A10).

Characterization. DLS and zeta potential measurements were performed on a Malvern Zetasizer Nano instrument equipped with a 4 mW He-Ne-Laser (633 nm) and an avalanche photodiode detector. DLS measurements were directly recorded in diluted colloidal suspensions of the particles at a concentration of 1 mg/mL. Zeta potential measurements were performed using the add-on Zetasizer titration system (MPT-2) based on diluted NaOH and HCl as titrants. For this purpose, 1 mg of the particles was diluted in 10 mL bi-distilled water. Thermogravimetric analyses (TGA) of the bulk-extracted samples (approximately 10 mg) were recorded on a Netzsch STA 440 C TG/DSC. The measurements proceeded at a heating rate of 10 °C/min up to 900 °C in a stream of synthetic air of about 25 mL/min. Nitrogen sorption measurements were performed on a Quantachrome Instrument NOVA 4000e at -

196 °C. Sample outgassing was performed for 12 hours at a vacuum of 10 mTorr at 120 °C. Pore size and pore volume were calculated by a QSDFT equilibrium model of N_2 on carbon, based on the adsorption and desorption branch of the isotherms. A BET model was applied in the range of 0.05 – 0.20 p/p_0 to evaluate the specific surface area. Infrared spectra of dried sample powder were recorded on a ThermoScientific Nicolet iN10 IR-microscope in reflection-absorption mode with a liquid-N_2 cooled MCT-A detector. Cross-polarized ^{13}C-MAS NMR measurements were performed on a Bruker DSX Avance500 FT spectrometer (11.74 T) in a 4 mm ZrO_2 rotor. The spinning rate was 10 kHz and a total number of 256 scans was recorded. The used contact time was 2 ms and the recycle delay was 1 s. Scanning electron microscopy (SEM) was performed on a FEI Helios instrument at an acceleration voltage of 2.5 kV. For this purpose the samples were put on an adhesive graphite film and sputtered twice with carbon with a BALTEC MED 020 Coating System. Transmission electron microscopy (TEM) data were obtained with a FEI Titan Themis 60–300 microscope at an acceleration voltage of 80 kV. UV/Vis measurements were performed on a Perkin Elmer Lambda 1050 UV-Vis/NIR spectrophotometer with a deuterium arc lamp and a tungsten filament equipped with a 150 mm integrating sphere and an InGaAs detector. Time-based fluorescence release experiments were performed at 37 °C on a PTI spectrofluorometer equipped with a xenon short arc lamp (UXL-75XE USHIO) and a photomultiplier detection system (Model 810/814).

Synthesis of β-CD NPs. In a 40 mL polypropylene reactor, 400 mg β-cyclodextrin (0.35 mmol), 200 mg tetrafluoroterephthalonitrile (TFTN, 1.00 mmol), 600 mg K_2CO_3 (4.34 mmol), 50 mg polyethylene glycol (PEG_{2000}) and 50 mg cetyltrimethylammonium bromide (CTAB, 0.14 mmol) were mixed with 15 mL anhydrous DMSO. The mixture was sonicated (15 min) and subsequently stirred at 900 rpm and 80 °C for 3 h. The orange suspension was cooled to room temperature and 15 mL bidistilled water and 15 mL

hydrochloric acid (1 M) were slowly added to the reaction mixture. After centrifugation for 15 minutes at 7830 rpm (7197 rcf) the isolated light yellow solid was washed extensively with water (2 x 40 mL), HCl (1 M, 2 x 40 mL) and ethanol (2 x 40 mL) followed by centrifugation steps (15 min, 7197 rcf), respectively. Finally, the pale yellow powder was dispersed in 10 mL bidistilled water and used for further characterization (150 mg, 25 % yield).

Rhodamine-labelling of β-CD NPs. 1 mg of β-CD NPs in ethanolic solution were mixed with 2 µL TAMRA-azide (2 mg/mL in anhydrous DMF) and a catalytic amount of zinc(II) acetate dihydrate. The mixture was shaken at 37 °C for 12 h and afterwards washed extensively with ethanol and water (centrifugation steps: 14,000 rpm, 16,837 rcf, 4 min) until no fluorescence could be detected in the supernatant. Finally, the particles were redispersed in 1 mL H_2O and used for *in vitro* uptake experiments.

Cargo loading of β-CD NPs. An aqueous solution of 1 mg/mL β-CD NPs was centrifuged (14,000 rpm, 16,837 rcf, 4 min), washed once with 500 µL HBSS buffer and redispersed again in a mixture containing 500 µL HBSS buffer with either 5 µL doxorubicin hydrochloride (100 mg/mL in DMSO) or 500 µL Hoechst 33342 (10 mg/mL in water), respectively. The nanoparticles were incubated for 3 h and subsequently washed extensively with HBSS buffer (14,000 rpm, 16,837 rcf, 4 min) until no fluorescence could be detected in the supernatant. Finally, the loaded nanoparticles were redispersed in 1 mL HBSS buffer and used for further *in vitro* release experiments. As a reference sample the particles were centrifuged (14,000 rpm, 16,837 rcf, 4 min) after certain time points and the corresponding amount of supernatant was used on HeLa cells.

Lipid preparation. The following lipids were used: DOPC (1,2-dioleoyl-*sn*-glycero-3-phosphocholine, Avanti Polar Lipids), DOTAP (1,2-dioleoyl-3-trimethylammonium propane, Avanti Polar Lipids). The amount of 2.5 mg of the individual lipids was dissolved in a 1 mL

mixture of 40 %vol absolute ethanol and 60 %vol MQ water (conc. 2.5 mg/mL). The amount of 1 mg of nanoparticles in aqueous solution was centrifuged (4 min, 8609 rcf, at 15 °C) and redispersed in 100 µL of the above DOTAP solution. Upon addition of 900 µL MQ water (pH adjusted to 9.4 with sodium hydroxide) the formation of the first SLB layer on the external surface of the nanoparticles was induced. After centrifugation (4 min, 8609 rcf, at 15 °C) and redispersion in 100 µL of a 1:1 mixture of the above DOPC/DOTAP solutions, the formation of a second layer around the nanoparticles was induced by adding 900 µL HBSS buffer.

Cell Culture. HeLa cells were grown in Dulbecco's modified Eagle's medium (DMEM) (lifeTechnologies) supplemented with 10 % fetal bovine serum (FBS) and incubated at 37 °C under a 5 % CO_2 humidified atmosphere. For live cell imaging the cells were seeded on ibidi 8-well µ-slides 24 h before adding particles, at a cell density of 5000 cells per well.

Uptake studies and *in vitro* Cargo release. The cells were incubated with 2 µL or 5 µL of a 1 mg/mL β-CD NPs solution for 0.5 – 24 h prior to the measurements at 37 °C under a 5% CO_2 humidified atmosphere. During the measurements all cells were kept on a heated microscope stage at 37 °C under a 5% CO_2 humidified atmosphere. For imaging, the cells were stained with 1 µL of a WGA solution and were incubated for 2-5 min at 37°C in a 5% CO_2 humidified atmosphere and then washed twice with DMEM. In addition to the uptake studies, the supernatant of the stock solution was similarly investigated for fluorescence and nucleus staining. The subsequent imaging was performed as described in the spinning disk confocal microscopy section.

Spinning disc confocal microscopy. Confocal microscopy for live-cell imaging was performed on a setup based on the Zeiss Cell Observer SD utilizing a Yokogawa spinning disk unit CSU-X1. The system was equipped with a 1.40 NA 63x Plan apochromat oil immersion objective from Zeiss. For all experiments the exposure time was 0.2 s and z-stacks

were recorded. Hoechst 33342 was imaged with light at 405 nm and a power density of approximately 0.16 W/mm^2, WGA was imaged at 488 nm with approximately 0.48 W/mm^2, and Rhodamin was excited at 561 nm with 11 mW/mm^2. In the excitation path a quad-edge dichroic beamsplitter (FF410/504/582/669-Di01-25x36, Semrock) was used. Separate images for each fluorescence channel were acquired using two separate electron multiplier charge coupled device (EMCCD) cameras (PhotometricsEvolveTM).

Cuvette release experiments. To show the successful uptake and release of the cargo, the doxorubicin loaded particles were transferred to a custom made Teflon cap fitting on a fluorescence cuvette. The cap was sealed with a dialysis membrane (ROTH Visking type 8/32, MWCO 14,000 g/mol) and placed on top of a fluorescence cuvette filled with 3 mL of HBSS buffer to show the successful uptake of doxorubicin and with 3 mL of citric acid phosphate buffer at pH 5 to prove the pH-dependent release. The excitation wavelength was set to λ = 488 nm and the emission fluorescence intensity was recorded at λ = 590 nm. All slits were adjusted to 2.0 mm. The measurement was continuously run for more than 40 hours (Figure 7-5).

Cell viability studies. For MTT-Assays we seeded 5000 HeLa cells per well containing 100 µL of high glucose DMEM medium and treated them with particles 24 h after seeding. After 24 h of incubation the cells were washed twice with HBSS buffer. 100 µL of 3-(4,5-dimethylthiazol-2-yl)-2,5-diphenyltetrazolium bromide (MTT, 0.5 mg/mL in DMEM) was added to each well of the nanoparticle-treated cells and incubated for further 2 h. Unreacted MTT and medium were removed and the 96-well plates were stored at -80 °C for at least 1 h. Then, 100 µL DMSO was added to each well. The absorbance was read out by a Tecan plate reader at 590 nm with a reference wavelength of 630 nm. All studies were performed in

triplicates. The IC_{50} and the standard mean deviations were calculated using the Origin 9.0 software.

7.5. References

1. R. Kojima, D. Aubel and M. Fussenegger, *Curr. Opin. Chem. Biol.*, 2015, **28**, 29-38.
2. C. Argyo, V. Weiss, C. Bräuchle and T. Bein, *Chem. Mater.*, 2014, **26**, 435-451.
3. M. W. Ambrogio, C. R. Thomas, Y.-L. Zhao, J. I. Zink and J. F. Stoddart, *Accounts of Chemical Research*, 2011, **44**, 903-913.
4. Y. Wang, Q. Zhao, N. Han, L. Bai, J. Li, J. Liu, E. Che, L. Hu, Q. Zhang, T. Jiang and S. Wang, *Nanomedicine: NBM*, 2015, **11**, 313-327.
5. S. Singh, V. K. Pandey, R. P. Tewari and V. Agarwal, *Nanoparticle Based Drug Delivery System: Advantages and Applications*, 2011.
6. R. Singh and J. W. Lillard, *Exp. Mol. Pathol.*, 2009, **86**, 215-223.
7. V. Cauda, H. Engelke, A. Sauer, D. Arcizet, C. Bräuchle, J. Rädler and T. Bein, *Nano Lett.*, 2010, **10**, 2484-2492.
8. S. A. Mackowiak, A. Schmidt, V. Weiss, C. Argyo, C. von Schirnding, T. Bein and C. Bräuchle, *Nano letters*, 2013, **13**, 2576-2583.
9. S. Niedermayer, V. Weiss, A. Herrmann, A. Schmidt, S. Datz, K. Müller, E. Wagner, T. Bein and C. Bräuchle, *Nanoscale*, 2015, **7**, 7953-7964.
10. J. Croissant, A. Chaix, O. Mongin, M. Wang, S. Clément, L. Raehm, J.-O. Durand, V. Hugues, M. Blanchard-Desce, M. Maynadier, A. Gallud, M. Gary-Bobo, M. Garcia, J. Lu, F. Tamanoi, D. P. Ferris, D. Tarn and J. I. Zink, *Small*, 2014, **10**, 1752-1755.
11. B. Rühle, P. Saint-Cricq and J. I. Zink, *ChemPhysChem*, 2016, **17**, 1769-1779.
12. S. H. van Rijt, D. A. Bölükbas, C. Argyo, S. Datz, M. Lindner, O. Eickelberg, M. Königshoff, T. Bein and S. Meiners, *ACS nano*, 2015, **9**, 2377-2389.
13. Y. Zhao, J. L. Vivero-Escoto, I. I. Slowing, B. G. Trewyn and V. S. Y. Lin, *Expert Opin. Drug Delivery*, 2010, **7**, 1013-1029.
14. Q. Zheng, Y. Hao, P. Ye, L. Guo, H. Wu, Q. Guo, J. Jiang, F. Fu and G. Chen, *J. Mater. Chem. B*, 2013, **1**, 1644-1648.
15. S. Datz, C. Argyo, M. Gattner, V. Weiss, K. Brunner, J. Bretzler, C. von Schirnding, A. A. Torrano, F. Spada, M. Vrabel, H. Engelke, C. Bräuchle, T. Carell and T. Bein, *Nanoscale*, 2016, **8**, 8101-8110.
16. J. Croissant, X. Cattoen, M. W. Man, A. Gallud, L. Raehm, P. Trens, M. Maynadier and J. O. Durand, *Adv. Mater.*, 2014, **26**, 6174-6180.
17. J. G. Croissant, S. Picard, D. Aggad, M. Klausen, C. Mauriello Jimenez, M. Maynadier, O. Mongin, G. Clermont, E. Genin, X. Cattoen, M. Wong Chi Man, L. Raehm, M. Garcia, M. Gary-Bobo, M. Blanchard-Desce and J.-O. Durand, *J. Mater. Chem. B*, 2016, **4**, 5567-5574.
18. J. Croissant, M. Maynadier, A. Gallud, H. Peindy N'Dongo, J. L. Nyalosaso, G. Derrien, C. Charnay, J.-O. Durand, L. Raehm, F. Serein-Spirau, N. Cheminet, T. Jarrosson, O. Mongin, M. Blanchard-Desce, M. Gary-Bobo, M. Garcia, J. Lu, F. Tamanoi, D. Tarn, T. M. Guardado-Alvarez and J. I. Zink, *Angew. Chem. Int. Ed.*, 2013, **52**, 13813-13817.
19. C. Mauriello-Jimenez, N. Knezevic, Y. Galan-Rubio, S. Szunerits, R. Boukherroub, F. Teodorescu, J. G. Croissant, O. Hocine, M. Seric, L. Raehm, V. Stojanovic, D. Aggad, M. Maynadier, M. Garcia, M. Gary-Bobo and J.-O. Durand, *J. Mater. Chem. B*, 2016, DOI: 10.1039/C6TB01915C.
20. S. Datz, H. Engelke, C. v. Schirnding, L. Nguyen and T. Bein, *Microporous Mesoporous Mater.*, 2016, **225**, 371-377.
21. G. Ajnai, A. Chiu, T. Kan, C.-C. Cheng, T.-H. Tsai and J. Chang, *J. Exp. Clin. Med.*, 2014, **6**, 172-178.
22. R. Arvizo, R. Bhattacharya and P. Mukherjee, *Expert Opin. Drug Delivery*, 2010, **7**, 753-763.
23. E. C. Dreaden, L. A. Austin, M. A. Mackey and M. A. El-Sayed, *Ther. Delivery*, 2012, **3**, 457-478.
24. A. Baeza, E. Guisasola, E. Ruiz-Hernández and M. Vallet-Regí, *Chem. Mater.*, 2012, **24**, 517-524.
25. Q. A. P. a. J. C. a. S. K. J. a. J. Dobson, *J. Phys. D: Appl. Phys.*, 2003, **36**, R167.
26. W. Guo, C. Yang, H. Lin and F. Qu, *Dalton Transactions*, 2014, **43**, 18056-18065.
27. S. Laurent, D. Forge, M. Port, A. Roch, C. Robic, L. Vander Elst and R. N. Muller, *Chem. Rev.*, 2008, **108**, 2064-2110.
28. T. T. T. N'Guyen, H. T. T. Duong, J. Basuki, V. Montembault, S. Pascual, C. Guibert, J. Fresnais, C. Boyer, M. R. Whittaker, T. P. Davis and L. Fontaine, *Angew. Chem. Int. Ed.*, 2013, **52**, 14152-14156.
29. B. Rühle, S. Datz, C. Argyo, T. Bein and J. I. Zink, *Chem. Commun.*, 2016, **52**, 1843-1846.
30. A. Kumari, S. K. Yadav and S. C. Yadav, *Colloids Surf., B.*, 2010, **75**, 1-18.
31. W. B. Liechty, D. R. Kryscio, B. V. Slaughter and N. A. Peppas, *Annu. Rev. Chem. Biomol. Eng.*, 2010, **1**, 149-173.
32. K. S. Soppimath, T. M. Aminabhavi, A. R. Kulkarni and W. E. Rudzinski, *J. Controlled Release*, 2001, **70**, 1-20.

33. S. Kalepu, M. Manthina and V. Padavala, *Acta Pharm. Sin. B*, 2013, **3**, 361-372.
34. A. Puri, K. Loomis, B. Smith, J.-H. Lee, A. Yavlovich, E. Heldman and R. Blumenthal, *Crit. Rev. Ther. Drug Carrier Syst.*, 2009, **26**, 523-580.
35. H. Shrestha, R. Bala and S. Arora, *J. Pharm.*, 2014, **2014**, 10.
36. R. Ranjbar and M. S. Hafezi-Moghadam, *Electronic Physician*, 2016, **8**, 1857-1864.
37. P. W. K. Rothemund, *Nature*, 2006, **440**, 297-302.
38. Q. Zhang, Q. Jiang, N. Li, L. Dai, Q. Liu, L. Song, J. Wang, Y. Li, J. Tian, B. Ding and Y. Du, *ACS nano*, 2014, **8**, 6633-6643.
39. S. Hedgire, S. McDermott and M. Harisinghani, in *Nanomedicine-Basic and Clinical Applications in Diagnostics and Therapy*, Karger Publishers, 2011, vol. 2, pp. 96-105.
40. T. Lammers, F. Kiessling, W. E. Hennink and G. Storm, *J. Controlled Release*, 2012, **161**, 175-187.
41. A. Salvati, A. S. Pitek, M. P. Monopoli, K. Prapainop, F. B. Bombelli, D. R. Hristov, P. M. Kelly, C. Åberg, E. Mahon and K. A. Dawson, *Nat. Nanotechnol.*, 2013, **8**, 137-143.
42. R. A. Gatenby and R. J. Gillies, *Nat. Rev. Cancer*, 2004, **4**, 891-899.
43. R. A. Cairns, I. S. Harris and T. W. Mak, *Nat. Rev. Cancer*, 2011, **11**, 85-95.
44. P. P. Hsu and D. M. Sabatini, *Cell*, 2008, **134**, 703-707.
45. R. J. DeBerardinis, J. J. Lum, G. Hatzivassiliou and C. B. Thompson, *Cell Metab.*, 2008, **7**, 11-20.
46. J. Szejtli, *Chem. Rev.*, 1998, **98**, 1743-1754.
47. F. Acartürk and N. Çelebi, *Cyclodextrins in pharmaceutics, cosmetics, and biomedicine: current and future industrial applications*, 2011, 45-64.
48. H. Arima, K. Motoyama and T. Irie, *Cyclodextrins in pharmaceutics, cosmetics, and biomedicine: Current and future industrial applications*, 2011, 91-122.
49. E. Bilensoy, *Cyclodextrins in pharmaceutics, cosmetics, and biomedicine: current and future industrial applications*, John Wiley & Sons, 2011.
50. A. A. Hincal, H. Eroğlu and E. Bilensoy, *Cyclodextrins in Pharmaceutics, Cosmetics, and Biomedicine: Current and Future Industrial Applications*, 2011, 123-130.
51. T. Auletta, M. R. de Jong, A. Mulder, F. C. J. M. van Veggel, J. Huskens, D. N. Reinhoudt, S. Zou, S. Zapotoczny, H. Schönherr, G. J. Vancso and L. Kuipers, *J. Am. Chem. Soc.*, 2004, **126**, 1577-1584.
52. W. C. Cromwell, K. Bystrom and M. R. Eftink, *J. Phys. Chem.*, 1985, **89**, 326-332.
53. M. R. Eftink, M. L. Andy, K. Bystrom, H. D. Perlmutter and D. S. Kristol, *J. Am. Chem. Soc.*, 1989, **111**, 6765-6772.
54. B. V. K. J. Schmidt, M. Hetzer, H. Ritter and C. Barner-Kowollik, *Prog. Polym. Sci.*, 2014, **39**, 235-249.
55. E. M. Del Valle, *Process Biochem.*, 2004, **39**, 1033-1046.
56. L. G. Suárez, W. Verboom and J. Huskens, *Chem. Commun.*, 2014, **50**, 7280-7282.
57. S. Yu, Y. Zhang, X. Wang, X. Zhen, Z. Zhang, W. Wu and X. Jiang, *Angew. Chem. Int. Ed.*, 2013, **52**, 7272-7277.
58. M. E. Davis, *Mol. Pharm.*, 2009, **6**, 659-668.
59. W. Zhu, K. Zhang, Y. Chen and F. Xi, *Langmuir*, 2013, **29**, 5939-5943.
60. A. Alsbaiee, B. J. Smith, L. Xiao, Y. Ling, D. E. Helbling and W. R. Dichtel, *Nature*, 2015.
61. G. Wenz, B.-H. Han and A. Müller, *Chem. Rev.*, 2006, **106**, 782-817.
62. J. V. Jokerst, T. Lobovkina, R. N. Zare and S. S. Gambhir, *Nanomedicine (London, England)*, 2011, **6**, 715-728.
63. A. L. B. de Barros, K. S. de Oliveira Ferraz, T. C. S. Dantas, G. F. Andrade, V. N. Cardoso and E. M. B. d. Sousa, *Mater. Sci. Eng. C.*, 2015, **56**, 181-188.
64. S. Vorona, T. Artamonova, Y. Zevatskii and L. Myznikov, *Synthesis*, 2014, **46**, 781-786.
65. A. Moore, R. Weissleder and A. Bogdanov, *JMRI*, 1997, **7**, 1140-1145.
66. F. Osaki, T. Kanamori, S. Sando, T. Sera and Y. Aoyama, *J. Am. Chem. Soc.*, 2004, **126**, 6520-6521.
67. M. Xue, X. Zhong, Z. Shaposhnik, Y. Qu, F. Tamanoi, X. Duan and J. I. Zink, *J. Am. Chem. Soc.*, 2011, **133**, 8798-8801.
68. H. Meng, M. Xue, T. Xia, Y.-L. Zhao, F. Tamanoi, J. F. Stoddart, J. I. Zink and A. E. Nel, *J. Am. Chem. Soc.*, 2010, **132**, 12690-12697.
69. L. Lu, X. Shao, Y. Jiao and C. Zhou, *J. Appl. Polym. Sci.*, 2014, **131**, n/a-n/a.
70. L. Y. Qiu, R. J. Wang, C. Zheng, Y. Jin and L. Q. Jin, *Nanomedicine*, 2010, **5**, 193-208.
71. T. Yousef and N. Hassan, *J. Inclusion Phenom. Macrocyclic Chem.*, 2016, DOI: 10.1007/s10847-016-0682-4, 1-11.
72. V. Cauda, H. Engelke, A. Sauer, D. Arcizet, C. Bräuchle, J. Radler and T. Bein, *Nano Lett.*, 2010, **10**, 2484-2492.

7.6. Appendix

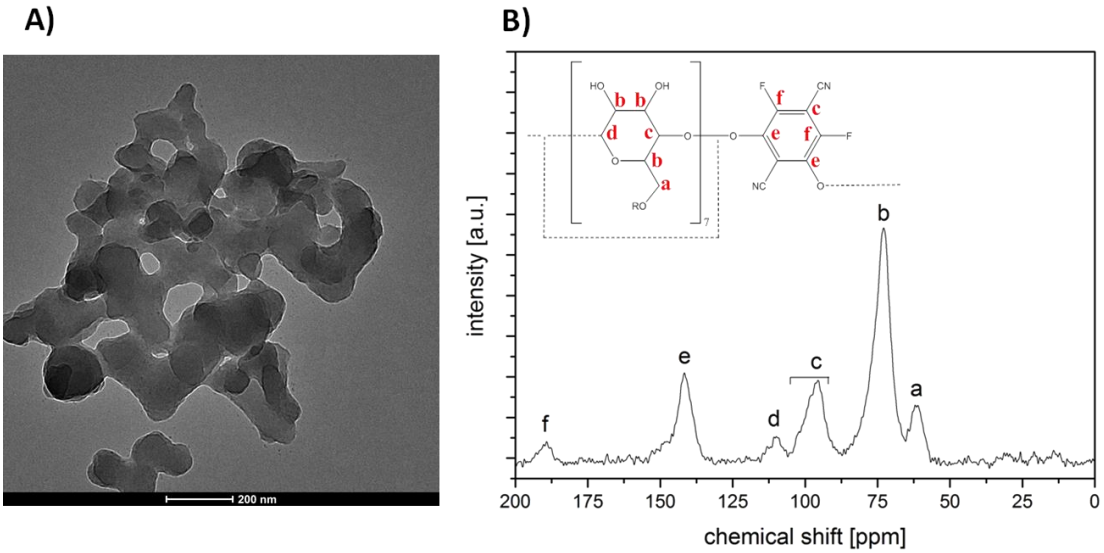

Figure S 7-1: A) Transmission electron microscopy (TEM) image of spherical β-CD NPs revealing a narrow particle size distribution around 100 nm. B) ^{13}C-MAS solid-state nuclear magnetic resonance (ssNMR) spectrum of β-CD NPs indicating the successful incorporation of the oligosaccharide compounds and the rigid organic linker into the crosslinked material.

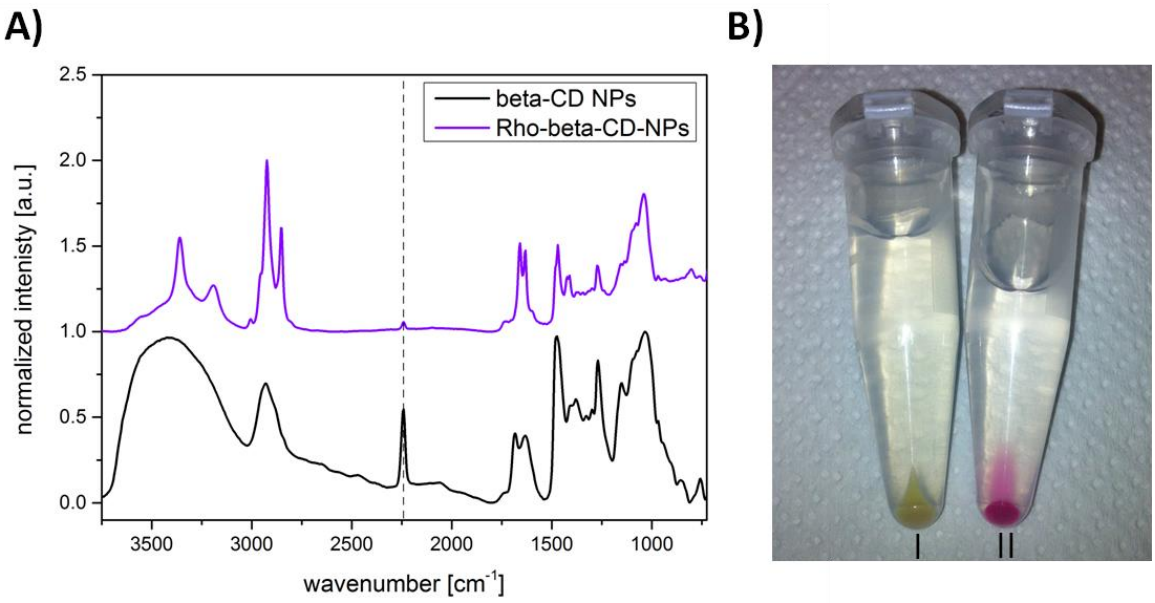

Figure S 7-2: A) IR spectroscopy data of as-synthesized β-CD NPs (black) and rhodamine-labeled nanoparticles (violet). The successful attachment can be followed by the vanishing nitril stretching vibration at 2245 cm^{-1} due to the covalent binding of the dyes azide groups to form tetrazole rings in a 1,3-dipolar cycloaddition. Spectra were normalized and shifted due to clarity reasons by 1.0 along the y-axis. B) Photograph of 1 mg of as-synthesized pale yellow β-CD NPs (I) and pink labeled Rho-β-CD NPs (II) in water after centrifugation, respectively.

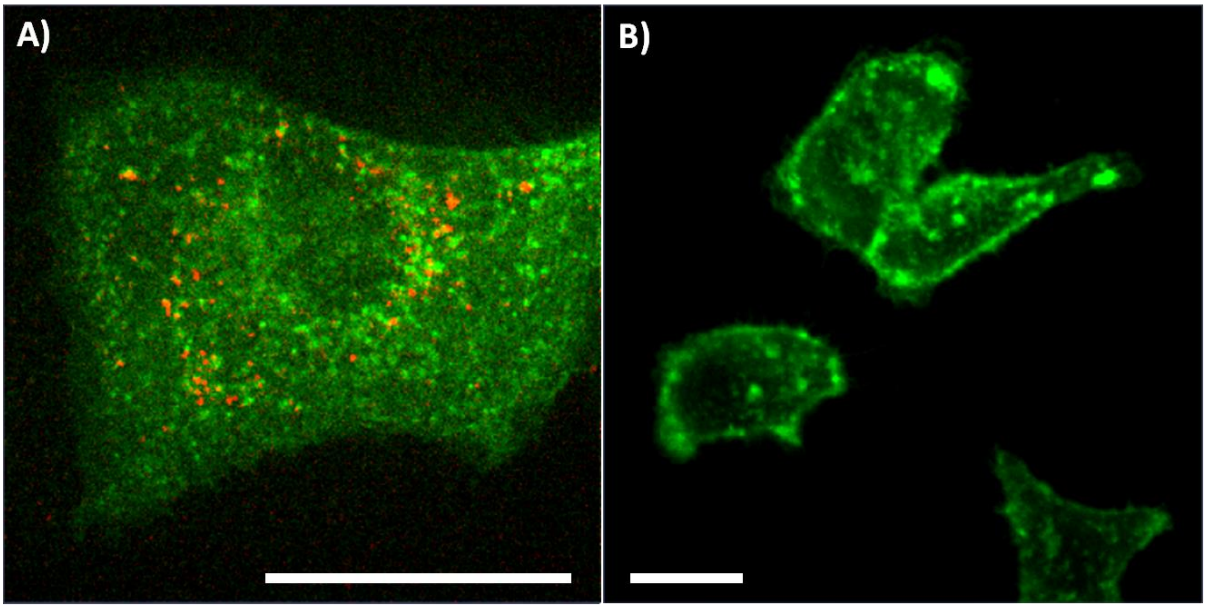

Figure S 7-3. Fluorescence microscopy of HeLa cells incubated with rhodamine-labeled β-CD NPs (red) after 30 min (A), or pretreated with free inhibitors (e.g. β-cyclodextrin) for 30 min and incubated with rhodamine-labeled β-CD NPs for 30 min afterwards (B). Cell membranes are stained with WGA (green). Scale bar represents 10 µm, respectively.

To test the targeting of sugar receptors with β-CD nanoparticles on HeLa cells, the receptors were either blocked or kept free. The functionality was evaluated in a receptor competition experiment (Figure S3). For this purpose, one part of the HeLa cells was pre-incubated with 5 µL of an inhibitor solution (10 mM aqueous solutions of D-glucose, D-L-arabinose, 2-deoxy-D-glucose or β-cyclodextrin, respectively), to block the receptors, for 30 min at 37 °C under a 5% CO_2 humidified atmosphere. Then the HeLa cells were incubated with 5 µg of rhodamine-labeled β-CD-NPs for 30 min at 37 °C under a 5% CO_2 humidified atmosphere. For staining the cell membrane, the cells were incubated with WGA for 2 min. The cells were washed three times with PBS, fresh medium was added and subsequently the cells were imaged. Clearly an enhanced sugar receptor-mediated cell uptake can be seen when the sugar receptors are available on the cell surface (A) compared to blocked receptors (B).

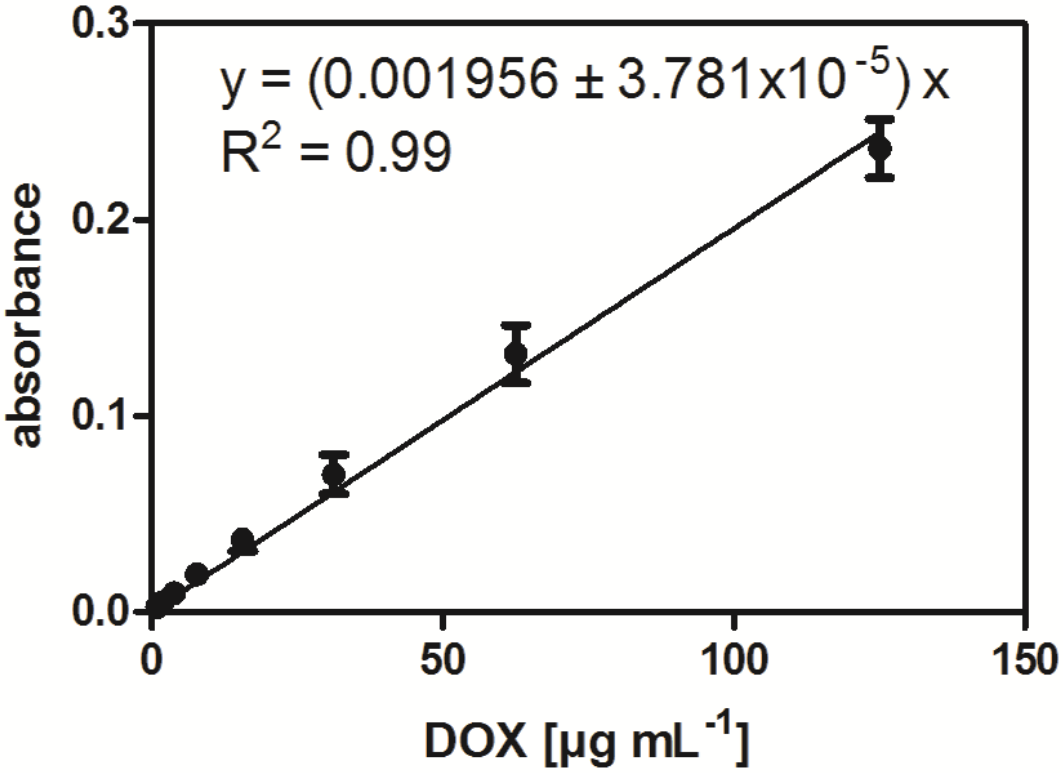

Figure S 7-4: Calibration curve for doxorubicin loading capacity measured at 500 nm.

The concentration of the DOX loading solution was 0.5 mg/mL with 0.5 mg nanoparticles. After several washing steps the supernatants were collected and revealed an added-up absorbance of 0.750±0.008. By using the linear regression fit of the calibration curve (Figure S4), this leads to a DOX content of 383 µg/mL in the collected supernatants. Therefore, the total amount of loaded DOX was 117 µg per 0.5 mg nanoparticles leading to a loading capacity of 23 wt%.

To test the pH-responsive release of Hoechst dye from the nanoparticles, Hoechst-loaded particles were redispersed in 1 ml potassium phosphate buffer at pH 7.4, 6.0, and 4.0, respectively. After a 20-minute incubation period, particle solutions were centrifuged to separate particles and supernatant and the UV-Vis spectrum of the supernatant containing the

released Hoechst dye was measured. Release increased with decreasing pH as shown in Figure S5.

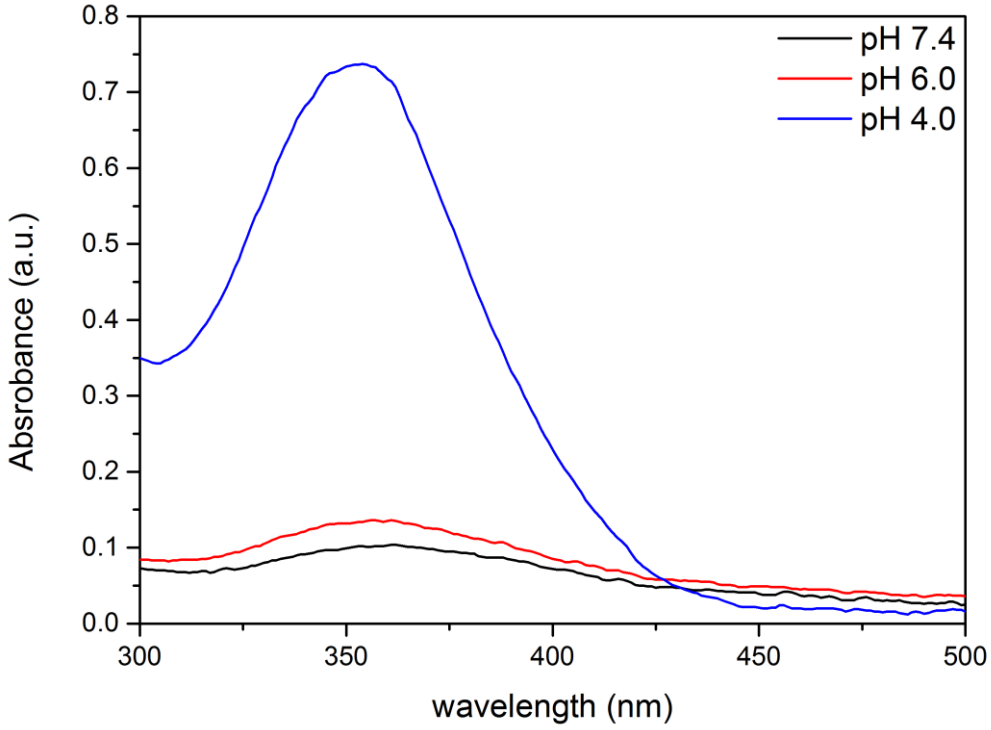

Figure S 7-5: UV-Vis measurement of Hoechst dye released from nanoparticles at different pH values.

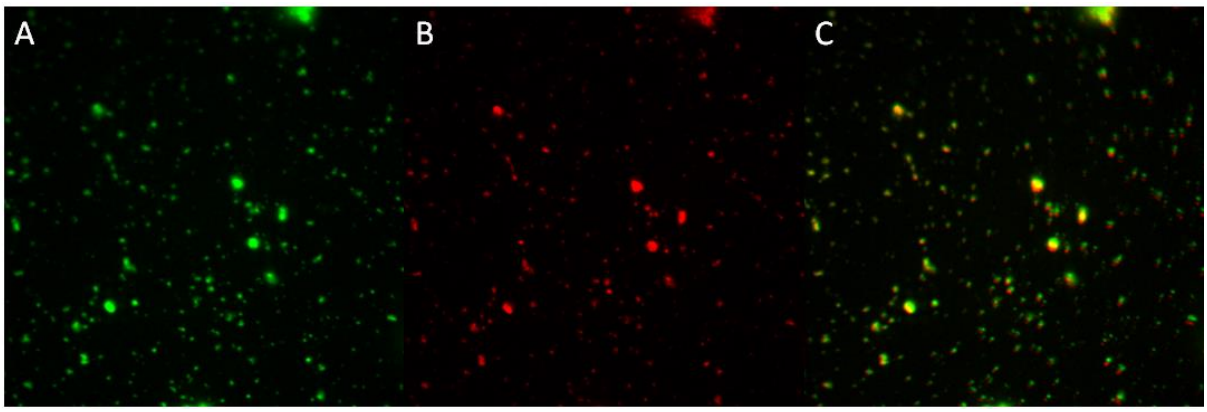

Figure S 7-6: Fluorescence colocalization images of the liposome-coated CD NPs. A) Liposomes labeled with WGA 488, B) CD NPs labeled with TAMRA, C) merged image of both channels.

To investigate if the coating of the particles with liposomes was successful, fluorescence colocalization experiments were performed (Figure S 7-6). For this purpose, β-cyclodextrin particles were stained with TAMRA, a rhodamine dye, and the liposomes were marked with WGA 488. In the case of a successful coating the dyes should be colocalized, while an independent distribution indicates a failure to coat the particles. The images (A, B) show that both the liposomes and particles were stained successfully and the merged image (C) shows that both fluorescent stains are colocalized, proving that the particles were successfully coated with liposomes. The slight offset in the positions of the particles and the liposomes between both channels is caused by the Brownian motion of the particles, while switching to a different excitation wavelength to take the second image. Control experiments confirmed that there is no spectral overlap between both dyes, confirming that the observed colocalization of the signals is caused by the successful coating.

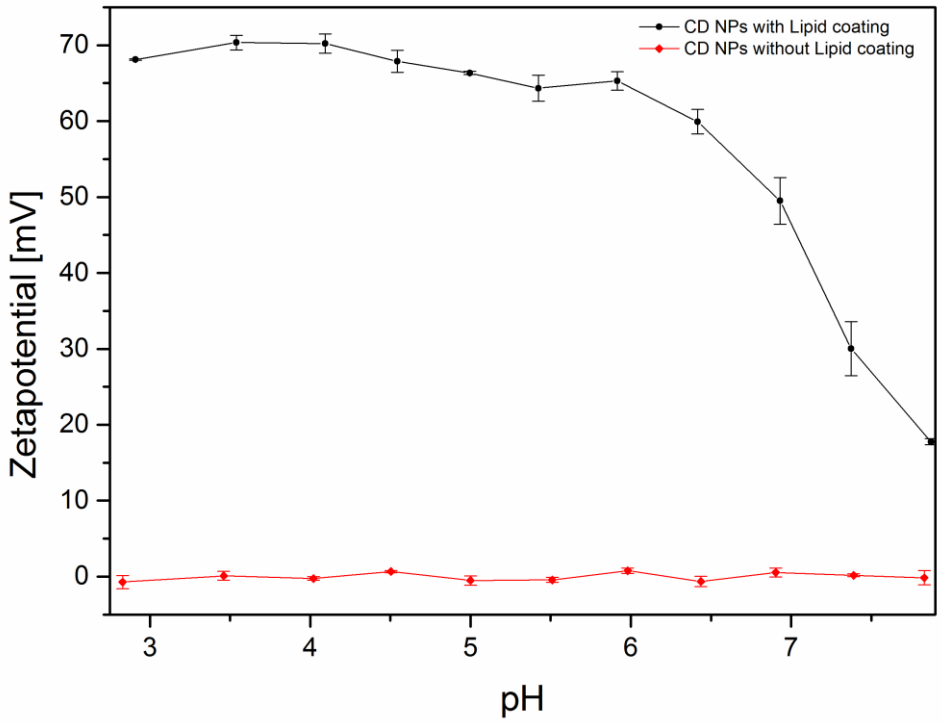

Figure S 7-7: Titration curves of coated and non-coated CD NPs.

A further proof for successful lipid coating is a comparison of the zeta potentials of lipid-coated and non-coated particles (Figure S7). The β-CD-NPs without any coating show a more or less constant zeta potential over the whole pH-range from 3 to 8 of around 0 mV. After successful lipid coating the measured zeta potential increased significantly. This results from the positive charge of the DOTAP lipid and thus confirms successful coating.

CHAPTER 8

Conclusion and Outlook

8. Conclusion and Outlook

This thesis focused on the implementation of well-known tailor-made mesoporous silica nanoparticles (MSNs) in various fields. As a highlight, MSNs were successfully applied as drug delivery vehicle in the field of cancer immunotherapy. Furthermore, the diversity of MSNs could be demonstrated by their use as enzyme support. To expand the horizon of promising nanoparticles, an innovative organic material and its application in cellular delivery was introduced.

The first project described in this work (in chapter 3) is a preceding study of chapter 4. Here, small-pore MSNs with and without a pH-responsive polymer capping system were assessed regarding their biocompatibility, toxicity, and immune-modulatory properties. It was shown that the particles were rapidly and efficiently taken up by specialized antigen-presenting cells (APCs). Furthermore, MSNs did not show any cytotoxicity in the commonly applied concentration range meaning induced apoptosis was only observed when the particles were used in very high concentrations of 200 µg mL^{-1}. To investigate if unloaded particles already induce an immune response, the activation markers, namely co-stimulatory molecule CD80 and proinflammatory cytokines IL-6 and IL-12p70, were measured on different APCs. In both cases no significant upregulation could be observed upon addition of the MSNs to the primary immune cells and thus showing that cargo-free particles could not induce an innate immune response. To prove further that they also have no impact on B and T lymphocytes from the adaptive immune system, the respective early activation marker CD69 was measured and it was shown that neither of them shows an upregulation. Summarizing, the particles represent a non-toxic and non-inflammagenic delivery system which is preferably taken up by specialized antigen-presenting cells. To assess if this MSN system can principally function as carrier for immune-modulatory cargo with regard to cancer immunotherapy applications, the particles were loaded with resiquimod (R848) and coated with the pH-responsive polymer PVP as

capping system. It could be shown that the particles were internalized *via* endocytosis and that the capping system opened up in the local acidic environment allowing R848 release. This was measured with the upregulation of the above mentioned activation markers. In summary, it was demonstrated that MSNs possess indeed the appropriate characteristics for an optimal carrier system of immune-modulatory cargo.

To implement the gained knowledge and explore the possibilities of MSNs as drug delivery system, MSNs were investigated in detail as pH-responsive carrier system for R848 as described in chapter 4. To examine the full potential of the drug delivery system, the aforementioned polymer cap was compared to a protein-based one in respect to their R848 loading and release behaviour. The two different capping systems differed in their opening and closure mechanisms. Whereas the polymer system works reversibly upon pH-dependent (de-) protonation of the PVP groups, the biotin-avidin complex is irreversibly detached through pH-dependent cleavage of the connecting acetal linker. Time-based fluorescence release measurements *in cuvette* demonstrated that the R848 release of the avidin-capped system was superior over that of the PVP-coated MSNs. This was further confirmed in a cell-based assay. Subsequently, the loading behaviour of R848 into MSN-avidin was optimized by introducing phenyl moieties inside the pores and applying SSC20x as loading buffer. The long-term stability and the tight capping of the MSN-avidin system was demonstrated with time-dependent release experiments. This optimized R848 delivery system was further assessed *in vitro* and *in vivo*. Rapid and efficient uptake of unloaded MSN-avidin into dendritic cells (DCs) was observed. Loaded particles induced a potent DC activation as shown in cytokine production and upregulation of co-stimulatory and MHC molecules. Notably, the supernatant of the loaded particles did not induce an immune response, proving the tightness of the capping system. To explore the possibilities of the MSN system further, the antigen OVA peptide was attached to the avidin surface of the loaded particles and the resulting T cell

activation measured. Comparison with free R848 and OVA or the combination thereof, showed that the highest effect in T cell proliferation was achieved through the simultaneous delivery of antigen and adjuvant with the MSN system. To prove that the carrier is applicable *in vivo*, the safety and biodistribution of the avidin-coated MSNs were examined in mice. The particles did not induce any observable toxicity, they were mainly taken up by migratory dendritic cells and delivered to the next draining lymph organ. In sum, it was demonstrated that MSNs hold indeed great promise as carrier system for immune-stimulant R848 and even the simultaneous delivery of adjuvant and antigen. It thus shows high potential to be used in further cancer vaccine applications to achieve a locally induced immune activation while preventing adverse systemic effects. Further work will address the *in vivo* application of the described cancer vaccine system.

Chapter 5 demonstrates the diversity of MSNs regarding their tunable pore size and morphology. Large-pore stellate MSNs (LP-MSNs) with different functionalities were synthesized and the impact of the incorporated organosilanes on the mesopore structure as well as the particle morphology was investigated in detail. Furthermore, an adapted version of the co-condensation method for small-pore particles, was applied to create spatially-segregated core-shell large pore MSNs. To exploit the potential of these multifunctional MSNs, the interior of the pore was functionalized with DBCO derivatives allowing for mild cargo conjugation *via* copper free click chemistry. Attachment of the DBCO molecules was performed with stimuli-responsive linkers, namely the pH-responsive acetal linker described in chapter 4 and a redox-sensitive disulfide linker, to enable triggered release *via* specific buffer or redox conditions. The successful stimuli-responsive release of the model cargo TAMRA dye was proven with *in cuvette* time-based fluorescence experiments as well as *in vitro* fluorescence microscopy experiments. Future work will be dedicated to the conjugation and release of real drugs within the established system.

The described large-pore MSNs offer, in combination with the introduced click-chemistry, new possibilities in immobilizing large biomolecules. These were investigated in chapter 6 of this work. Large-pore MSNs were synthesized with an azide functionality on the inner walls of the pores and a phenyl functionality on the exterior MSN surface to guide the positively charged enzymes horseradish peroxidase and carbonic anhydrase into the pores. Both enzymes were alkyne-functionalized prior to covalent attachment *via* copper-click chemistry on the inner pore walls of the LP-MSNs. The successful immobilization of the biomolecules inside the silica support was characterized with several methods including IR-spectroscopy, gas sorption, and TGA measurements as well as the study of their catalytic behaviour. Here, colorimetric assays were applied for the respective enzymes to monitor their activity over several cycles with simple washing and centrifugation steps in between. It was shown that the enzymes remained stable and active in the pores and thus proving the benefits of covalent immobilization inside a host system like increased stability and efficient workup. A future development based on this work could be to test its application, for example in the removal of toxic phenols from polluted water.

The last chapter of this thesis introduces a novel biocompatible drug carrier which is not based on silica but on crosslinked β-cyclodextrins (CDs). This soft, organic material consists of small nanoparticles with sizes of ~ 150 nm, which are highly water-dispersible. Covalently labeled CD nanoparticles showed rapid uptake in HeLa cells within 30 minutes. Particles coated with a lipid bilayer, in contrast, were not taken up in this short period of time, suggesting a sugar-receptor mediated endocytosis of the CD NPs. Their ability to form inclusion complexes between the cyclodextrin rings and various cargos was demonstrated with the uptake of the nuclei staining dye Hoechst and the chemotherapeutic doxorubicin. Both cargos were efficiently delivered without notable premature leakage. Upon acidification in the endosomes both cargos were successfully released resulting in efficient nuclei staining

or cell death, respectively. Thus, the novel sugar-based material holds great promise as biocompatible drug carrier, which has to be evaluated in further studies.

In summary, the great potential of multifunctional MSNs as carrier system in various fields was illustrated in this work. MSNs with different pore sizes, morphologies, and post-synthetic functionalizations were tailored to meet the requirements of a non-toxic and non-inflammagenic carrier system as well as a support material for large biomolecules. The promising potential as stimuli-responsive drug delivery system was shown *in vitro* and *in vivo*. Nevertheless, there are still some hurdles to overcome to enable the clinical entry of MSNs as biocompatible drug carrier. One of the great challenges in the transition from laboratory to clinics will be the development of a simple, cheap and reproducible upscaling process of highly functionalized MSNs. Furthermore, more uniform studies have to be performed *in vivo* to assess the fate, toxicity and full impact on and in living organisms of the promising drug vehicles.

To expand the spectrum of promising biocompatible carriers and to view the drug delivery field from a different angle, a novel crosslinked organic carrier system was also introduced with a simple synthesis route devoid of several following functionalization steps and encouraging cellular delivery characteristics.

Overall, this thesis demonstrates the great potential of biocompatible nanocarriers, which still has to be fully exploited in the future.

CHAPTER 9

Publications and Presentations

9. Publications and Presentations

9.1. Publications

1.) Immune response to functionalized mesoporous silica nanoparticles for targeted drug delivery

Simon Heidegger, Dorothée Gößl, Alexandra Schmidt, Stefan Niedermayer, Christian Argyo, Stefan Endres, Thomas Bein, Carole Bourquin, *Nanoscale* **2016**, *8*, 938–948.

2.) Mesoporous silica nanoparticles as pH-responsive drug carrier for R848

Dorothée Gößl[§], Julia Wagner[§], Daniel Hauser, Natasha Ustyanosvkaya, Stefan Datz, Olga Zhuzhgova, Hanna Engelke, Thomas Bein[*], Carole Bourquin[*], *to be submitted*, **2019**.

3.) Clickable Multifunctional Large-Pore Mesoporous Silica Nanoparticles as Nanocarriers

Hsin-Yi Chiu[§], Dorothée Gößl[§], Lisa Haddick, Hanna Engelke and Thomas Bein[*] *Chem. Mater*. **2018**, *30*, 644-654.

4.) Highly Active Enzymes Immobilized in Large Pore Colloidal Mesoporous Silica Nanoparticles

Dorothée Gößl, Helena Singer, Hsin-Yi Chiu, Alexandra Schmidt, Martina Lichtnecker, Hanna Engelke, Thomas Bein, *New J. Chem.* **2019**, *43*, 1671 – 1680.

5.) Biocompatible β-cyclodextrin nanoparticles as multifunctional carriers for cellular delivery

Stefan Datz, Bernhard Illes, Dorothée Gößl, Constantin v. Schirnding, Hanna Engelke*, Thomas Bein* *Nanoscale*, **2018**, *10*, 16284-16292.

6.) Cellular resolution is essential for validation of active targeting of nanoparticles in vivo

Deniz Bölükbas, Stefan Datz, Charlotte Meyer-Schwickerath, Malamati Vreka, Lin Yang, Dorothée Gößl, Theodora Agalioti, Christian Argyo, Sabine van Rijt, Michael Lindner, Oliver

Eickelberg, Tobias Stöger, Otmar Schmid, Georgios Stathopolous, Thomas Bein, Silke Meiners, *submitted* **2019**.

9.2. Presentations

1.) Mesoporous silica nanoparticles as platform for targeted drug delivery

Center for Nanoscience Workshop "Channels and Bridges to the Nanoworld", 2015, Venezia, Italy.

2.) Immune response to functionalized mesoporous silica nanoparticles for targeted drug delivery

28. Deutsche Zeolith-Tagung, 2016, Justus-Liebig-Universität, Gießen, Germany.

3.) Immune response to functionalized mesoporous silica nanoparticles for targeted drug delivery

14th European Symposium on Controlled Drug Delivery, 2016, Egmond aan Zee, Netherlands.

4.) Immune response to functionalized mesoporous silica nanoparticles for targeted drug delivery

Nanosystems Initiative Munich Summer Retreat, 2016, Hersching, Germany.

5.) Immune response to functionalized mesoporous silica nanoparticles for targeted drug delivery

Center for Nanoscience Workshop "Nanoscale Matter – Novel Concepts and Functions", 2016, Venezia, Italy.

6.) Mesoporous silica nanoparticles as drug vehicle for diclofenac

29. Deutsche Zeolith-Tagung, 2017, Dechema-Haus, Frankfurt a.M., Germany.

7.) Mesoporous silica nanoparticles as universal drug delivery vehicle

SFB1032 Summer School, 2017, Herrsching, Germany.

8.) pH-responsive mesoporous silica nanoparticles as delivery system for R848

SFB1032 Adhoc-Workshop, 2018, München, Germany.

9.) Biocompatible crosslinked β-cyclodextrin nanoparticles as multifunctional carriers for cellular delivery

Center for Nanoscience Winter Retreat, 2018, Kleinwalsertal, Germany.

10.) Biocompatible crosslinked β-cyclodextrin nanoparticles as multifunctional carriers for cellular delivery

15th European Symposium on Controlled Drug Delivery, 2018, Egmond aan Zee, Netherlands.

11.) Mesoporous silica nanoparticles as universal drug delivery vehicle

Center for Nanoscience Seminar Science Rocks!, 2018, München, Germany.

12.) Highly active enzymes immobilized in large pore colloidal mesoporous silica nanoparticles

Nanosystems Initiative Munich Conference "The Future of Nanoscience", 2018, Tutzing, Germany.